

Sheffield Hallam University

Free self-assembly of spontaneously chiral, supramolecular structures

DASTAN, Alireza

Available from the Sheffield Hallam University Research Archive (SHURA) at:

<http://shura.shu.ac.uk/18142/>

A Sheffield Hallam University thesis

This thesis is protected by copyright which belongs to the author.

The content must not be changed in any way or sold commercially in any format or medium without the formal permission of the author.

When referring to this work, full bibliographic details including the author, title, awarding institution and date of the thesis must be given.

Please visit <http://shura.shu.ac.uk/18142/> and <http://shura.shu.ac.uk/information.html> for further details about copyright and re-use permissions.

Free Self-assembly of Spontaneously Chiral, Supramolecular Structures

Aireza Dastan

A thesis submitted in partial fulfilment of the requirements of
Sheffield Hallam University
for the degree of
Doctor of Philosophy

October 2017

Abstract

In this thesis, Molecular Dynamics simulations are used to investigate the free self-assembly of supramolecular, chiral structures. The main coarse-grained model used for this is the disc-shaped variant of the Gay-Berne potential. This is parameterised to favour face-face configurations, consistent with chromonic molecules which tend to stack due to their $\pi - \pi$ interactions. Additionally, assemblies formed by mixtures of these discs and a second species, modelled as Lennard-Jones spheres, are investigated. Here, hot-spot zones on the rims of the discs are used to provide strong interactions with the spheres.

Simulations of disc-only systems lead to self-assembly of multi-thread, chiral fibres. Depending on the choice of particle shape and face-face interaction strength, the formed fibres are reproducibly either straight or, for reasons of packing efficiency, spontaneously chiral. As they grow radially, increasing stresses cause chiral fibres to untwist either continuously or via morphological rearrangement. It is also found that, due to the kinetics of fibre initiation, the isotropic solution has to be significantly supercooled before aggregation takes place. As a result, the thermal hysteresis of the formed fibres extends to 10-20% of their formation temperatures. The kinetic barriers to the early stages of growth are investigated by the introduction of a small permanent seed. Depending on the size of the seed, monotonic fibre growth is then observed 5-10% above the normal formation temperatures.

On introducing Lennard-Jones spheres and hot-spot zones at the rims of discs, twisted bilayer ribbons, sandwiching a helicoidal sphere layer, are obtained. Systematic investigation of the effects of hot-spot size on the formation and structural properties of these twisted bilayers is then performed. This shows that lateral growth of these bilayers, and the associated increases in bend stresses, lead to the development of defect lines. For relatively small hot-spot sizes, rope structures with five helical threads of discs wrapped around a sphere core self-assemble. Where such ropes aggregate, geometrical frustration leads to multi-rope structures undergoing morphological rearrangement into double-bilayers. Extending the model by giving the discs double hot-spots leads to the formation of a multi-layer twisted bundle with three different directions of growth and three modes of twist.

If the sizes of the interacting particles are changed, then, further new arrangements result. For thinner discs, a different class of bilayer is found in which the threads in the two leaflets are mutually orthogonal. This is shown to provide a new pathway for formation of tubes by a rolling-up mechanism involving intermediate saddle bilayer and half-pipe structures. The dimensions of such tubes are found to be very sensitive to the extent of the hot-spot. Double-helix structures, involving two helices of discs wrapped around a central thread of sphere, are the other major class of supramolecular assembly adopted by systems involving thinner discs. Finally, the interaction of self-assembled objects, leading to behaviours such as the formation of multi-bilayer structures, is shown to be accessed on the time- and length-scales of this class of computer simulation.

To my inspiring parents, for their endless support and kindness.

Acknowledgements

I would like to thank my supervisor, Prof. Doug Cleaver, not only for his exceptional scientific support, but also for all his suggestions and guidance in other aspects of my life. I am also thankful to my second supervisors Dr. Tim Spencer and Dr. Laurence Ellison. I want to also thank Dr. Sabetta Matsumoto for her time in discussing the structures observed in my research. I wish also acknowledge the support of Unilever Research for funding my studies. The help and support of administration staff of MERI at Sheffield Hallam University, particularly Gail Hallewell and Corrie Houton are acknowledged. I appreciate Laurence for his time in proofreading couple of chapters of this thesis.

It gives me pleasure to thank my friends in the office who shared their time with me and made it a nice place to work. Thanks Nikita, Abubakar and Tunde (Ojo). I also want to thank my best friend, Omid, who always kept me motivated, although he was thousands of kilometres away. I would also like to say a very big thank you to Fatemeh, without whom I could not finish my PhD.

A massive thanks to my family for their support and motivations. I'm really grateful to my sisters, not only for all their helps to their little brother, but also for taking care of 'home', which made me less worried about there.

Finally, I wish to thank my incredibly kind parents for their support, patience and understanding. Without them, I could not achieve all I have. So, thanks Baba & Maman.

Advanced Studies

The following is the chronological list of related course and meetings attended during the PhD studies. The scientific contributions by publication or conference presentation are also listed:

- Alireza Dastan, William J. Frith and Douglas J. Cleaver, “Thermal hysteresis and seeding of twisted fibres formed by achiral discotic particles,” *The Journal of Physical Chemistry B*, 2017, doi: 10.1021/acs.jpcb.7b05316.
- The Topical Research Meeting on Physics in Food Manufacturing, Sheffield Hallam University, Sheffield, January 2017 (Talk).
- CCP5 Annual Meeting, Harper Adams University, Newport, September 2016 (Talk).
- Methods to Simulate Nucleation and Growth from Solution (MSNGS), The University of Sheffield, Sheffield, August 2016 (Talk).
- MERI Research Symposium, Sheffield Hallam University, Sheffield, May 2016 (Talk, Best talk prize).
- The Second CCPBioSim/CCP5 Multiscale Modelling Conference, The University of Manchester, Manchester, April 2016 (Poster).
- Shape up 2015 conference, Technical University Berlin, Berlin, Germany, September 2015 (Poster).
- CCP5/CECAM Summer School, The University of Manchester, Manchester, July 2015 (Poster).
- MERI Research Symposium, Sheffield Hallam University, Sheffield, May 2015 (Poster, Best poster prize).
- The British Liquid Crystal Society (BLCS) Annual Conference, Sheffield Hallam University, Sheffield, March 2015 (Poster).

Table of contents

1	Introduction	1
1.1	Aims and Objectives	2
1.2	Outline of the Thesis	3
2	Self-assembly Processes of Fibres and Tubes	5
2.1	Introduction	5
2.2	Fibre Self-assembly	8
2.2.1	Experimental Background	9
2.2.2	Modelling Background	14
2.3	Self-assembly of Tubes	20
2.3.1	Chiral self-assembly	22
2.3.2	Tube formation by scrolling	28
2.4	Emergence of Twist	31
2.5	Summary	34
3	Computer Simulation Methods	36
3.1	Basics	36
3.2	Integration Algorithms	38
3.3	MD Tricks of the Trade	42
3.3.1	Periodic boundary condition	42
3.3.2	Observable quantities	43
3.3.3	Reduced units	46
3.3.4	Initialization	46
3.3.5	Cut-off radius and neighbour list	47

Table of contents

3.3.6	Thermostat / Barostat	48
3.3.7	Post-processing	52
3.4	Inter-particle Potentials	56
3.4.1	Spherical particle interaction	56
3.4.2	Ellipsoidal particle interaction	57
3.4.3	Disc-sphere interaction	65
3.4.4	Amphiphilic chromonics	67
4	Fibre Self-assembly	72
4.1	Introduction	73
4.2	Effects of Shape and Energy Anisotropies	75
4.3	Thermal Hysteresis and Seeding	86
4.4	Kinetics of Fibre Formation	97
4.5	System Size Effects	103
4.6	Conclusions	117
5	Twisted Ribbon Self-assembly	119
5.1	Introduction	120
5.2	Twisted Bilayers	122
5.2.1	Bilayer formation	123
5.2.2	Extent of solvophilicity effects	133
5.2.3	A bilayer with tears	141
5.3	Multilayer Twisted Bundle	144
5.4	Geometric Frustration	150
5.5	Conclusions	160
6	Tube Self-assembly	163
6.1	Introduction	164
6.2	Tube Formation Pathway	165
6.3	Controlling Tube Size	178
6.4	Conclusions	185

Table of contents

7 Self-assembly of Other Structures	188
7.1 Self-assembly of Double-helix	189
7.2 Multi-bilayer Formation	194
7.3 Flat Bilayer Formation	199
7.4 Self-assembly in Double Hot-spot Systems	201
7.5 Conclusions	203
8 Conclusions and Future Work	205
8.1 Conclusions	205
8.2 Future Work	209
Appendix A Forces and Torques for Intermolecular Potentials	212
A.1 Lennard-Jones Interaction	213
A.2 Disc-disc Interaction	213
A.3 Disc-sphere Interaction	216
Appendix B NOSQUISH Algorithm	219
Appendix C Symmetry Breaking of Disc-Disc Interaction	222
C.1 Internally-Shifted Gay-Berne Potential	222
C.2 Hot-spot for Disc-Disc Interaction	225
Appendix D Videos	228
References	230

Chapter 1

Introduction

A supramolecular structure is a stable aggregate of molecules which are organized through non-covalent bondings. The spontaneous formation of such architectures from their sub-units by hydrogen bonding, electrostatic interaction, $\pi - \pi$ stacking, donor-acceptor effects, and/or other Van der Waals interactions under a precisely-defined set of conditions and without human intervention is called ‘self-assembly’ [1–3]. Such processes are widely observed in nature and may also be harnessed in order to construct artificial nanostructures in a bottom-up fashion. The alternative, engineering from the top-down using methods such as vapour deposition and lithography, is often a complex and costly route for building sub-micron structures [4].

The emergence of key characteristics of biological, self-assembled supramolecular structures, such as the chirality of DNA molecules and the stability of lipid bilayers are therefore of great interest. Understanding of such processes may be brought to bear in areas such as liquid crystals and molecular electronics. Within such systems there are numerous factors at play such as the types of building blocks, the nature of their interactions, the medium in which self-assembly occurs and the various pathways that lead to the formation of the final structure. Therefore it is unsurprising that, despite the significant amount of research focused on the investigation of self-assembly in different systems, there are still many areas that are not well understood.

1.1 Aims and Objectives

Experimental studies often only observe the start and end points of self-assembly, from the building-blocks to the final structure due to limitations in the time- and length-scales they can access. Consequently they cannot unravel the details of the processes involved. Computer simulation techniques can go a long way to filling this knowledge gap by modelling what occurs during the different stages of the self-assembly. Such simulations also improve our understanding of the role that the key constituents of the systems and the prevailing conditions have in controlling the process and influencing the form of the final structure. The work reported here centres on the application of coarse-grained Molecular Dynamics to the understanding of the spontaneous formation of a wide variety of supramolecular structures.

1.1 Aims and Objectives

This research was motivated by a previous simulation study [5] of systems of coarse-grained disc-shaped (discotic) particles, which tend to stack due to their $\pi - \pi$ interaction. This showed the capacity of such systems to investigate self-assembly of supramolecular structures with spontaneous chirality (twisted fibres and twisted bilayers) and indicated that a number of other chiral structures might self-assemble from disc-shaped building-blocks. Therefore, the aims of this study were initially set as follows:

- Develop and extend the coarse-grained models for simulation of free self-assembly in systems consisting of discotic and spherical particles, starting from initial isotropic configurations.
- Perform extensive research on the self-assembly of twisted fibres in order to better understand the effects that various parameters have on the formation pathway and, as a result, the final structure. In addition, to investigate the effect of seeding on the process.
- To understand the mechanisms leading to the formation of twisted ribbon structures in a mixture of amphiphilic discs and spheres and to study the emergent length-scales including the pitch length.

1.2 Outline of the Thesis

- Discover whether the spontaneous formation of tubule structures is accessible to the models developed here and, if so, control the dimensions of the self-assembled tubes.

1.2 Outline of the Thesis

In addition to this brief introduction, this thesis has 7 more chapters.

In Chapter 2, the concepts introduced here are expanded upon and the literature associated with the self-assembly of supramolecular structures is reviewed, with particular emphasis on elongated fibres and tubes. The twisted ribbons, one of the geometries being the focus of this research, are explored as the precursor in a particular pathway for tube formation.

Chapter 3 is dedicated to the numerical methods employed in this thesis. These include different aspects of Molecular Dynamics simulation, the main method used for this study, and details of the intermolecular potentials used. Most of the parameters which are used in the next chapters for identification of different systems are introduced in this chapter.

In Chapter 4, we focus on the self-assembly of fibres formed from discotic building-blocks. The effects of particle shape and energy anisotropy and also the system size on the formed fibres are investigated, while a pathway for the formation of such structures is also suggested. The self-assembling systems are then examined to see whether they are subject to a thermal hysteresis and, if so, to probe the effects of seeding.

From Chapter 5 onwards, we consider bipartite systems consisting of amphiphilic discs partially attracted to the second species which is simple spherical particles. This provides us with an extra set of controlling parameters for tuning the systems toward the self-assembly of structures of interest, and naturally adds to the complexity of simulations.

In Chapter 5, a survey is carried out on the systems assembling twisted bilayers. The aim of this is to gain understanding of the effects of the extent of solvophilicity on the character of the structure. Spontaneous formation of twisted bundles with

1.2 Outline of the Thesis

three different directions of the growth is also investigated in this chapter. A new class of self-assembled object called ‘rope’ structure and its transition to a twisted multilayer object due to geometrical frustration is explored at the end of Chapter 5.

Chapter 6 reports a new pathway for the spontaneous formation of tubes formed in the bipartite disc and sphere systems through a rolling-up approach. It is shown that the size of the self-assembled tube formed by this mechanism is controllable by the particle-scale parameters of the system.

Chapter 7 is a final showcase for the further capabilities of the developed models in terms of accessible self-assembling supramolecular structures. Double-helices, multi-bilayers and flat bilayers are some examples of the assemblies which are briefly presented here.

Finally, Chapter 8 draws the major conclusions from the results presented in this work and suggests some directions for future work.

Chapter 2

Self-assembly Processes of Fibres and Tubes

2.1 Introduction

A particularly fascinating aspect of free self-assembly is that it establishes order from disorder and does so in a huge variety of systems both living and non-living. Self-assembly of peptides, phospholipids, DNA and RNA building blocks into secondary and higher order structures are some well-known examples from the biological world [6]. An every day example of self-assembly among abiotic components is the emergence of nematic order in liquid crystals. Furthermore, self-assembly is not limited to the molecular level, it can take place across a vast range of length scales from the microscopic up to weather systems, planets and galaxies [7].

The structure of the building blocks or monomers is one of the key factors influencing the morphology of self-assembled objects in different systems. The size, shape, flexibility and inter-particle interactions of the primary structures (a term introduced by Hill and coworkers [6]) can be as important as macroscopic parameters such as the concentration of the particles in the supporting medium, temperature and pH of the solvent, etc. As a result, the end product should be viewed as being a function of both microscopic and macroscopic considerations. Although very complex molecules with well-defined composition and shape can, alternatively, be developed

2.1 Introduction

based on sequential formation of covalent connections through synthetic chemistry [2], this area falls outside the scope of the systems considered here. We focus, instead, on molecules which act as the primary building blocks for formation of some final ordered structures through the type of process defined for free self-assembly in the previous chapter.

The shape and morphology of the end products of a molecular self-assembly process cover a diverse range from micelle to lamellar to gyroid. Figure 2.1 shows schematic views of some morphologies observed as the final objects formed by amphiphilic molecules. The word “amphiphile” is used to describe a class of molecules having both hydrophilic (water-loving) and lipophilic (fat-loving) properties. This type of molecule generally has a polar head and an apolar tail which is usually a hydrocarbon chain. Two other words “surfactant” and “lipid” are also used interchangeably with amphiphile in the literature. The simplest amphiphilic structure is the planar bilayer membrane assembly which forms the cell membrane. Alternatively, bilayers can also be used in biosensors to isolate an electrode from ions [8]. Figure 2.2 shows three different mesophases adopted within lipid bilayer structures. The size of hydrophilic headgroups, the temperature and the water content are the main parameters controlling transitions between these phases [4]. Lipid vesicles (Figure 2.1-E) can be employed as vessels for encapsulation which may be used in drug delivery applications. The capability of ordered amphiphilic products to undergo a chemical modification post-assembly process provides an opportunity that they can be used to produce structures whose chemistries are not themselves able to exhibit self-assembly [9, 10]. This ability may find applications in microfluidics, molecular recognition devices and liquid crystalline biomaterials. Also, self assembly is not limited to asymmetrical amphiphilic molecules. Other more symmetrical building blocks can also form ordered structures through appropriate combinations of weak inter-molecular interactions. This can typically be seen in liquid crystal context [11].

The above examples were mentioned to give an overview of some of the structures and potential applications of various final products formed by self-assembling molecules. High aspect-ratio or elongated objects, being a part of this research focus, are the other categories of end products. These elongated structures, which

2.1 Introduction

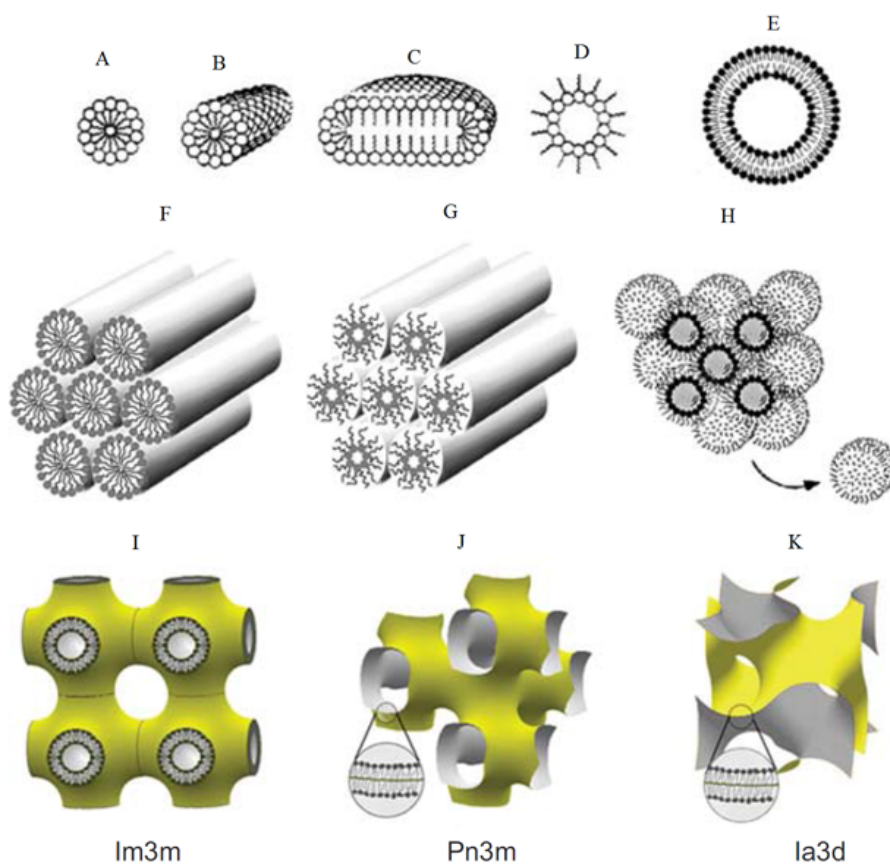


Figure 2.1: Schematic views of different self assembled morphologies observed in amphiphilic systems: A) spherical micelle, B) cylindrical micelle, C) disc, D) inverted micelle, E) liposome, F) hexagonal phase, G) inverted hexagonal phase, H) inverted micellar cubic phase, I) bilayer cubic phase $Im3m$, J) bilayer cubic phase $Pn3m$, and K) bilayer cubic phase $Ia3d$ [12].

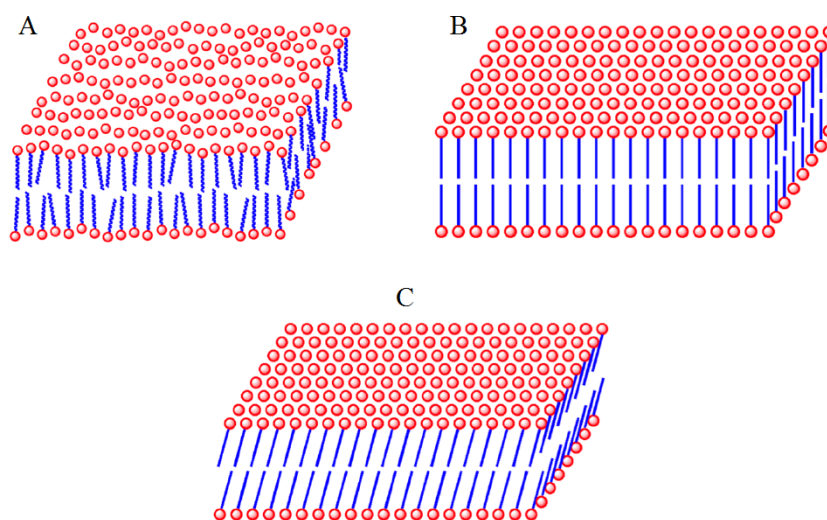


Figure 2.2: Different bilayer structures, A) L_α or smectic A phase, B) The L_β or hexatic smectic B phase, and C) The $L_{\beta'}$ phase in which the molecules are tilted [4].

2.2 Fibre Self-assembly

generally have a cylindrical shape, may be further categorized into “fibres” and “tubes”. Obviously, the latter has a hollow core which is not seen in the former. In the next sections, the self-assembly of these two objects and its associated literature will be discussed. Following this, the background related to the emergence of twist, a geometrical feature which will be observed and addressed in this work, will be presented.

2.2 Fibre Self-assembly

For molecules with aromatic rings, it is believed that the main mechanism promoting aggregation into elongated stacks is the $\pi - \pi$ interaction [13]. This is an attractive force caused by intermolecular overlapping of electron orbitals in π -conjugated systems (the origin of this interaction is still being actively debated in the literature [14–16]). In addition to this, hydrogen bonds and ionic interactions can also contribute to the formation and stabilisation of high aspect ratio objects, i.e. fibres, although their role is less well understood.

In spite of being a phenomenon which is not fully comprehended, there are many areas in which fibre growth plays a key role. These can be categorised into two distinct classes. The first comprises scenarios where fibre formation can be considered as a favourable phenomenon, thereby motivating interest in finding ways to enhance the process in both biological and non-biological contexts to enable secondary applications. Tissue engineering [17, 18], stem cell differentiation [19] and gel development [20–22] are examples from this category. For instance, Figure 2.3 shows a microscopic image of a self-assembled aligned fibre network in a gel. On the other hand, it is believed that fibre formation is a key feature of about 20 known diseases. Here, fibre growth is an unfavourable process that should be stopped or controlled. Fibres in this category, which are named “amyloid” fibres, are insoluble neurotoxic fibrils formed from soluble proteins and resistant to degradation [23]. In a broader sense, amyloid is an *in vivo* or *in vitro* fibre polymerized from peptides into a cross- β structure [24, 25]. Although there are some reports of functional amyloids which contribute to human health or technological applications [26–29], in the human

2.2 Fibre Self-assembly

body, they usually deposit in the tissue and lead to different syndromes, such as Alzheimer's disease, depending on the particular protein or peptide that makes up the building-blocks. The formation of fibres in the brain tissue of a patient who died due to Alzheimer's disease can easily be seen in Figure 2.3.

In the following, some of the experimental and computational literature related to the self-assembly of fibres is reviewed.

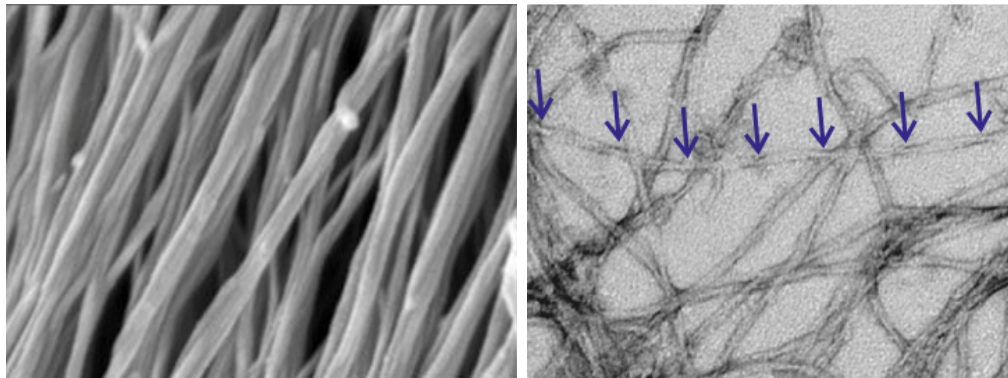


Figure 2.3: Microscopic images of the self-assembled fibres in favourable and unfavourable situations. Left: an aligned fibre network in a gel [22]. Right: brain tissue of a patient who died due to Alzheimer's disease [30].

2.2.1 Experimental Background

The development of an understanding of self-assembled objects has been a cross-disciplinary effort combining elements of biology, synthetic chemistry, physics and engineering.

Regarding the growth process, it is believed that the self-assembly of highly elongated stacks of molecules, be they fibres or tubular elements, is a hierarchical process [31–33]. This means that the highest-order structure is generated via a cascade of lower-order structures which self-assemble in a series of interconnected or cooperative processes. Confirming this hierarchy, in an experimental study by Bromley *et al.* [31] on the formation of α -helical protein fibre through a nucleation and growth mechanism, it was observed that when the peptides are mixed, they rapidly form partly helical dimers with sticky ends. After the mixing phase, a lag phase follows and for a period of about ten minutes, the system, being in aggregation

2.2 Fibre Self-assembly

phase, does not change spectroscopically or visibly. Circular dichroism (CD) spectra data showed that the critical nuclei comprised 6-8 partially folded dimers. After this nucleation, linear fibre formation took place through both longitudinal and radial growth. The suggested pathway for the self-assembly is illustrated in Figure 2.4.

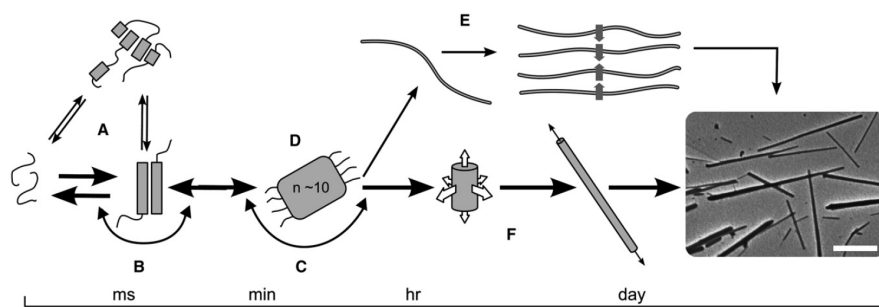


Figure 2.4: Suggested pathway for self-assembly of α -helical protein fibre: A) Two peptides form various oligomers or B) individual peptides incorporate in the self assembly. C) The formed assembly can be energetically favourable or D) only a critical nucleus may be favourable. E) Fibres may grow through bundling or F) by addition of material radially and longitudinally. The right picture is an electron micrograph of the observed fibres [31].

A theoretical model supported by an experimental observation through transmission electron microscopy (TEM) imaging was also presented for the self assembly of chiral rod-like molecules representing peptides [34]. Here, a peptide in β -strand conformation, a chiral rod-shape molecule with donor and acceptor groups on opposing sides and chemically different surfaces, was studied. The chiral rods formed different structures in solution in a hierarchical manner, as shown in Figure 2.5. The monomers formed long twisted tapes (Figure 2.5-c) due to the interactions between donors and receptors. Despite the right-handed chirality of the peptide, the formed tapes were left-handed. The chemical differences between the two sides of molecules and, therefore, the two sides of tape (white and black colors in Figure 2.5), led to different interactions with the solvent, thereby promoting a transition from a twisted tape into helical configuration, as shown in Figure 2.5-c' (approximately, from zero Mean curvature to zero Gaussian curvature). Changing the hydrophobicities of the tape faces (chemical anisotropy) was then found to result in the formation of a double tape or a ribbon. These ribbons stacked and formed fibrils and finally fibres.

2.2 Fibre Self-assembly

The fibril and fibre widths were controlled by balancing the elastic energy cost due to twist with the free energy gain from ribbon-ribbon attraction.

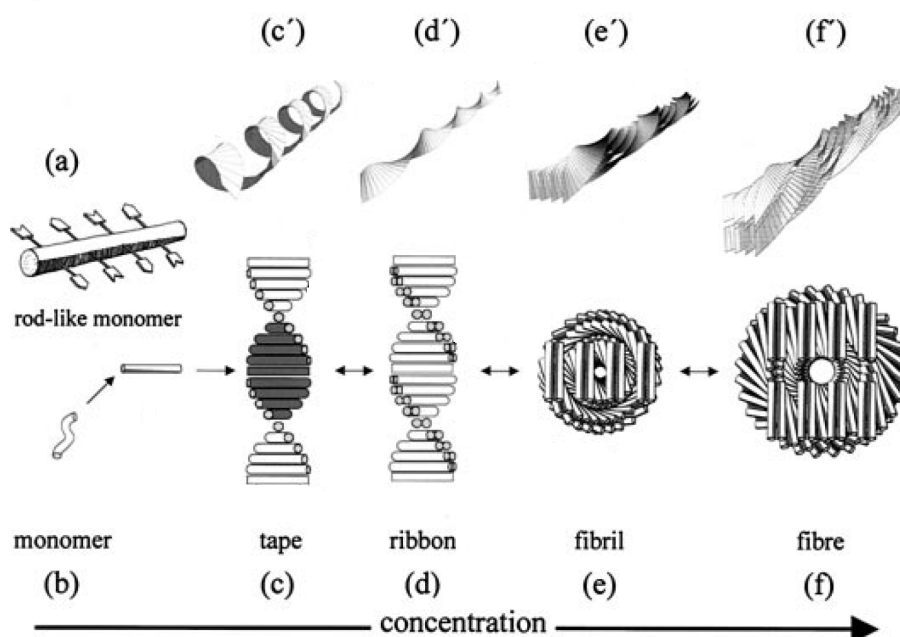


Figure 2.5: Model of the hierarchical self-assembly of chiral rod-like units. Local arrangements (c-f) and the corresponding global equilibrium conformations (c'-f') for the hierarchical self-assembling structures formed in solutions of chiral molecules (a), which have complementary donor and acceptor groups, shown by arrows, via which they interact and align to form tapes (c). The black and the white surfaces of the rod (a) are reflected in the sides of the helical tape (c), which is chosen to curl toward the black side (c'). The outer sides of the twisted ribbon (d), of the fibril (e), and of the fibre (f) are all white. One of the fibrils in the fibre (f') is drawn with darker shade for clarity [34].

Fibre formation from disc-like particles has also been investigated in previous work. Recently, Huang and coworkers [35] have studied the self-assembly of multi-scale fibres using discotic aromatic aramid molecules. They showed that in a dilute solution, the disc-shape molecules self-assemble into nanofibres, while in slightly higher concentration, they form liquid crystalline phase with micro-fibre texture. Increasing the concentration further caused macroscopic rod shape crystals to form. They used a low temperature scanning electron microscope (cryo-SEM), to observe this concentration-dependent phase transition. Small and wide angle X-ray scattering showed that the supramolecular liquid crystals were in the hexagonal columnar phase, each column having a diameter of 9 nm, 3 times the molecule diameter. They also observed that the structure of the formed fibre was independent of the level of water

2.2 Fibre Self-assembly

content in the system. Based on these observations, they suggested a hierarchical mechanism for the self-assembly which is shown in Figure 2.6. It was postulated that, due to the electrostatic interaction and hydrogen bonding, seven planar molecules formed a stable cluster. These clusters were then thought to stack into nano and subsequently micro fibres. This suggested mechanism seems slightly different from what other researchers observed for the formation of fibres in hexagonal arrangement. Other examples will be given later in this section.

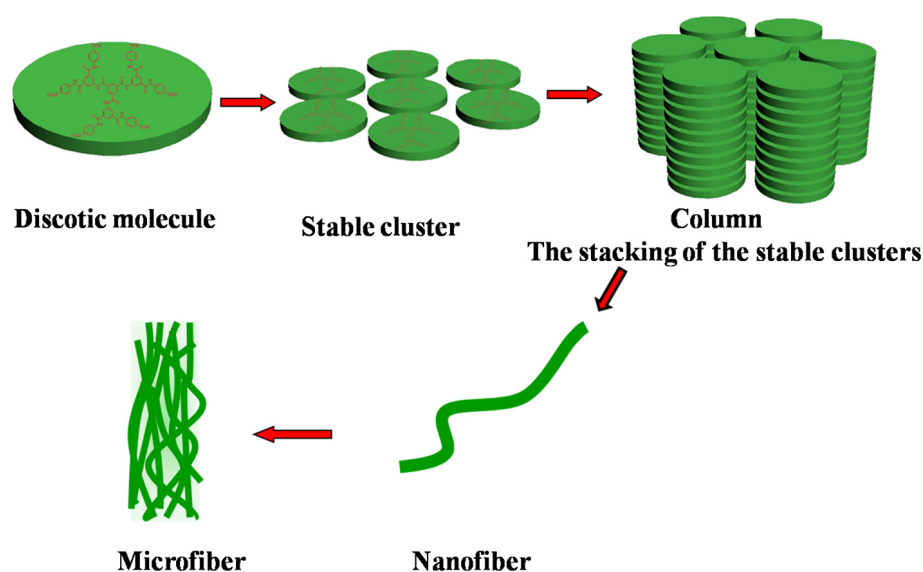


Figure 2.6: Schematic representation of self-assembly of the discotic molecule as suggested by reference [35].

Fibre self-assembly from anisotropic disc-shape molecules was also studied in an earlier work [36]. Here, molecules of phthalocyanine possessing 4 crown ether rings and 8 chiral alkyl side chains were synthesized. Due to their $\pi - \pi$ interactions, in chloroform, these discotic molecules self assembled into left-handed twisted bundles which finally developed into gels. These bundles consisted of two right-handed twisted fibres, each the diameter of a single molecule (see Figure 2.7). According to the CD data, these bundles continued a hierarchy of supercoiled threads with different helicities. It was also observed that, on addition of K^+ ions, although the fibre structures remained unchanged, their helicity disappeared. It was suggested that this tunable chiral material may find application in optoelectronics and sensor devices.

2.2 Fibre Self-assembly

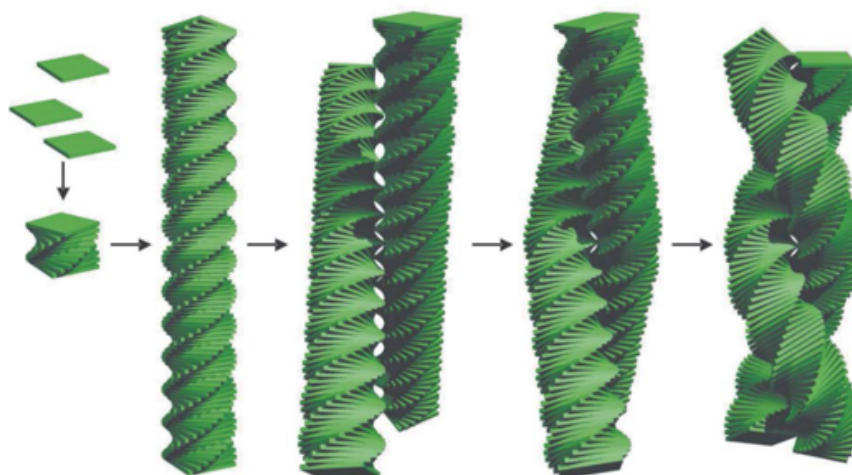


Figure 2.7: Hierarchical self-assembly of crown ether phthalocyanine into right-handed helical arrays, which organize themselves further into left-handed supercoiled structures as suggested by reference [36]. The illustration was taken from reference [33].

Complications which may arise in self-assembly of fibres are exemplified by the study of Gosal and co-workers which found that, depending on pH and concentration, β_2 -Microglobulin may form either worm-like fibrils or long, mature amyloids [37]. Each of these final morphologies was found to involve a distinct kinetic pathway. In one, rod-like fibrils and, eventually, worm-like assemblies were formed by a reversible, non-nucleated mechanism, the end product (the worm-like fibrils) being shown to be a kinetically trapped assembly. In the second, long amyloid fibers were formed by nucleation-driven growth involving a kinetic lag-phase. However, addition of small pre-formed fibers to this system promoted the formation of the long amyloid fibers in conditions that would normally correspond to the first pathway. Thus, seeding was demonstrated to be a viable mechanism for switching between dominant growth pathways, through manipulation of kinetic barriers.

The studies outlined above illustrate that the outcome of fibre self assembly is very sensitive to the choice of molecules and building blocks. Although it is widely accepted that the formation of fibres is a hierarchical process, the details of the initiation and growth mechanisms and also the self-assembled structures are dependent on many parameters such as molecule shape and flexibilities, intermolecular interactions, concentration, solution type and additive components. While the study of the final structures can be performed relatively easily with experimental techniques,

2.2 Fibre Self-assembly

observation of the self-assembly pathway is very challenging, particularly at early stages. On the other hand, computational methods may tackle this limitation and provide a clear image of the growth mechanism. In the following, the literature associated with numerical modelling of fibre formation is discussed.

2.2.2 Modelling Background

Experimental study of self-assembly at the molecular level obviously calls for observation on a very fine resolution in both space and time. Despite recent advances in techniques and devices, such resolution is still unattainable. However, computer simulation can play a significant role in shedding light on such processes. It may also be used as a predictive tool for systems which have not been investigated experimentally. However, for the very same reasons, molecular simulations are restricted to very small windows of time and space. A major challenge for computational researchers is, therefore, to identify which molecular aspects have a meaningful impact on controlling real world phenomena.

Molecular Dynamics (MD), Monte Carlo simulation (MC) [38], and Dissipative Particle Dynamics (DPD) [39] are the most popular computational methods used for studying self-assembly processes. Since the method used in the current research is MD simulation, without ignoring the value of the other techniques, we concentrate here on previous uses of MD, and the details of this method are discussed in Chapter 3.

Full atomistic (FA) and coarse graining (CG) are two approaches for MD simulation. While both of those can investigate system thermodynamics and, more importantly, predict the self-assembly, FA simulation is limited to significantly smaller system sizes and shorter time periods because of higher computational costs. When using CG approaches, on the other hand, making an appropriate choice of model is a substantial issue. Here, a review on previous simulation-based research, performed on the self-assembly of fibres, is presented.

In an effort to gain a better understanding about amyloid fibres, natural peptides, which form amyloid β -type fibres through α -helical intermediates, were investigated

2.2 Fibre Self-assembly

both experimentally and numerically [40]. Here, the authors claimed that the studied aliphatic tripeptid molecules are the shortest ones that can naturally form α -helical structure and, subsequently, amyloid fibre. Circular dichroism and X-ray fibre diffraction showed that the process is a function of peptide concentration in water. FA MD simulation for 20 nano seconds revealed that antiparalell monomers form dimer structures and then by structural alignment, a stable coiled fibre condensed (this was also observed in another computational work by Tamamis *et al* [41]). It was also shown that, due to lower hydrophobicity, shorter peptides have slower formation dynamics compared to longer ones. These simulation results demonstrated that, when isolated protofibril strands form multi-strand fibril aggregates, they achieve a lower free energy. However, the system sizes used (at most 216 molecules) were too small to reveal the formation of helical structures. While, because of the hydrophobic core, the water content inside the formed fibre was very low, a layer of water molecules was observed around the fibre, and it was concluded that in hydrogel, the water is stored between fibres and not within them.

Having gained this insight into amyloid fibres, FA MD simulations were used to investigate the structural stability of different models of Alzheimer's β -amyloid fibrils [42]. In this work, self assembly was not the focus of the work, but, instead, structural models achieved from NMR data were numerically studied. The MD results showed that the initial configurations became twisted and more compact by optimization of side-chain packing. It was also concluded that the investigated fibrils are structurally stable over the course of simulations (10-20 ns) which is the main feature of amyloid fibres.

In another work, the investigation of self assembly and stability of cylindrical nano fibres from peptide amphiphiles (PA) was performed by Yu *et al.* [43] using FA MD and steered molecular dynamics (SMD) simulations. Here, the starting configuration was an artificially constructed micelle. The micelle (solvated in water) consisted of a stack of 10 discs with 5 Å spacing. In each disc, there were 9 radially distributed PA molecules, having inward pointing hydrophobic tails. After a 40 ns equilibration MD run, an SMD simulation was performed on the resultant nano fibre. In SMD [44], a fixed force or velocity is applied to a particular molecule to pull it

2.2 Fibre Self-assembly

out of the structure. This method is usually used to reveal the structural changes in mechanical unfolding or stretching. By performing the SMD simulation and calculating the energy, enthalpy and entropy changes associated with the assembly process, it was concluded that the driving force for the self-assembly was enthalpic, although the electrostatic and van der Waals interactions also contributed to the process. Interestingly, while the charge interactions were concentrated in the PA headgroups, for van der Waals forces, both head and tail attractions were significant.

In another FA simulation, the self assembly of cylindrical fibres from peptide amphiphiles was studied [45]. The investigated amphiphilic rod shape peptides (144 molecules) formed a stable cylindrical fibre having diameter of about 88 \AA , consistent with experimental data. It was found that water and Na^+ ions penetrate into the fibre, but not between the hydrophobic chains. The electrostatic interactions between the peptide and the sodium ions as well as the van der Waals binding between the building blocks were the main stabilizing factors for the fibre. Figure 2.8 illustrates the final fibre structure observed after 40 ns.

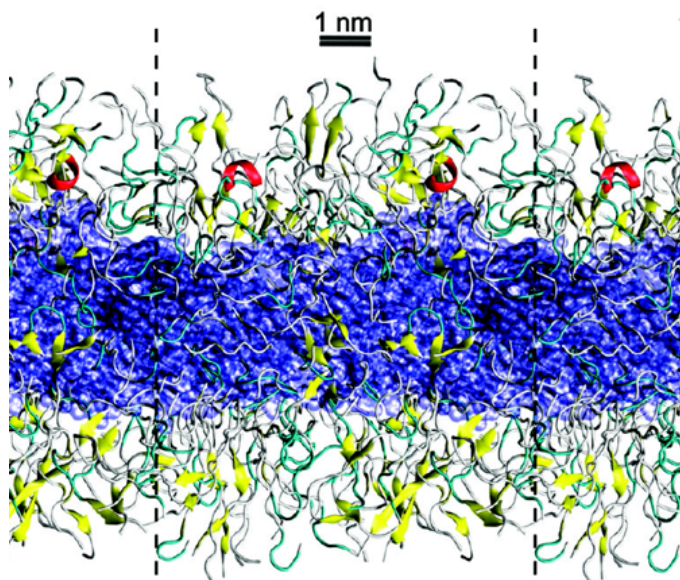


Figure 2.8: Snapshot of the self-assembled PAs simulated in reference [45]. The hydrophobic core is in blue, α -helices are in red, β -sheets are in yellow, turns are in cyan, and coils are in gray. Periodic boundaries are indicated by the dotted lines.

The limitations of the FA approach in simulating larger systems and longer time-scales encourage computational researchers to turn to CG methods to access higher

2.2 Fibre Self-assembly

level effects [46]. By using CG models, in which the whole molecule or a part of it is replaced with a single site, the micrometre and millisecond length- and time-scales, respectively, can be reached. Coarse-grained models were used for simulation of a range of systems to investigate the behaviour of both complicated molecules such as proteins [47, 48] or macrocycles [49, 50] and relatively simpler molecules like water with only 3 atoms [51]. Here, the coarse-grained simulations of fibre self-assembly are briefly reviewed.

Marrink and coworkers [52] developed a novel coarse-grained model for lipid systems. They simulated the free formation of a bilayer structure from isotropic configuration and the achieved data such as area per headgroup, phosphate-phosphate distance, bending modulus and compressibility had a good agreement with experimental results. In another work [53], the self-assembly of PA was numerically studied using the CG MD approach. The results showed that interplay between the hydrophobic interactions of the tails and the hydrogen bonding of the peptide blocks may lead to formation of different assemblies. Spherical micelles, micelles with β -sheets in corona and long cylindrical fibres were some of the morphologies observed in this work.

Fibre self-assembly in a system of 16-residue alanine based peptide (96 molecules) was simulated based on a four-sphere united atom CG model [54]. The discontinuous molecular dynamics (DMD) method, in which the particles interact through a discontinuous potential such as hard-sphere or square-well potential, was applied. A hierarchical mechanism was suggested for fibre formation based on the simulation results. First, the system entered a lag phase in which some amorphous clusters formed. Then, these clusters assembled β -sheets being aligned with each other and formed a small elongated aggregate. This fibril then grew into a longer fibre.

Lee *et al.* [55] also simulated the spontaneous formation of fibres from 140 PAs using CG MD. A four-to-one mapping approach was chosen for coarse graining and the solvent (water) and ions were represented explicitly. A cascade of intermediate aggregates contributed to the formation of the final fibre in 16 μ s of simulation. At the early stage, the hydrophobic tails packed to form spherical micelles interacting with each other through van der Waals forces. In the period 0.1-0.5 μ s, micelles grew

2.2 Fibre Self-assembly

and formed a 3D network. At about $1 \mu\text{s}$, the tails of adjacent micelles merged and a single fibre formed instead of the diffuse network. This transformation from spherical phase to fibrous one was in agreement with experimental observations. After about $10 \mu\text{s}$, all PAs joined the single fibre which had a diameter of about 80 \AA . This size was also in agreement with their previous FA simulation [45]. Figure 2.9 illustrates the growth of the fibre in the investigated system.

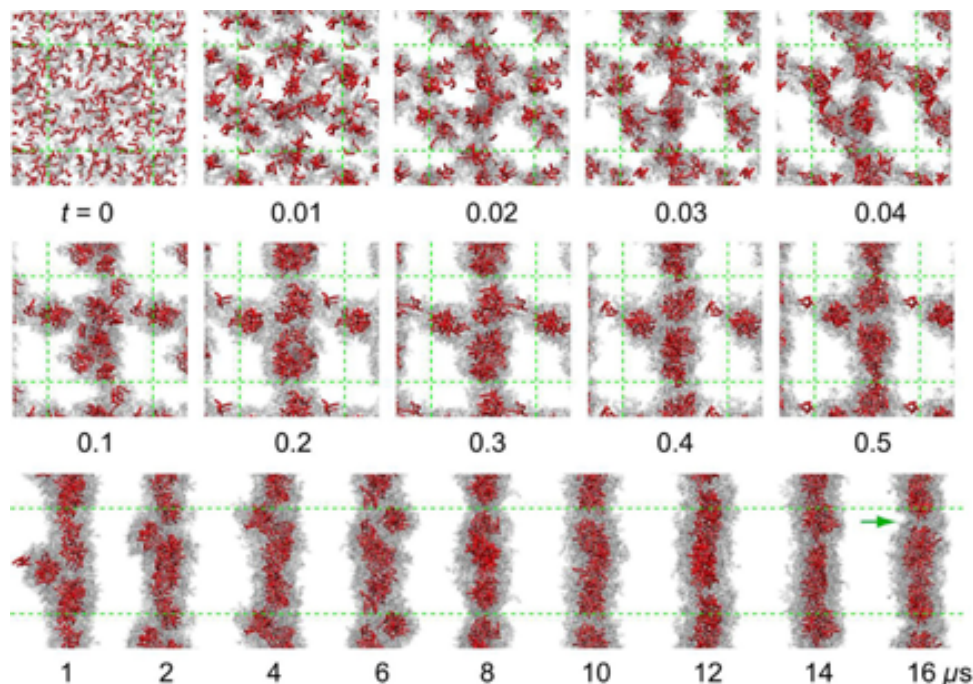


Figure 2.9: Process of PA fibre formation observed in simulations of reference [55]. Hydrophobic tails are shown in red, peptides in gray and periodic boundaries in dotted green lines. Total simulation time was $16 \mu\text{s}$ and the time at which every snapshot was taken is written in the figure.

A CG model was also developed for simulation of collagen-silk-collagen triblock polypeptides [56]. At low pH, this peptide self assembles into nano fibres with lengths of the order of a micrometre. By adopting a CG model derived using structural data from FA MD, formation of a stable stack of β -roll (fibre) with a length being consistent with the experimental data was simulated. The authors, therefore, suggested that the proposed CG model could be used to study folding behaviour of proteins.

Simulation of fibre formation from disc-shaped particles has also been studied by a few researchers. Li *et al.* [57] used a soft anisotropic potential, incorporating the orientation of particles, to run a DPD simulation of the self assembly of discotic

2.2 Fibre Self-assembly

particles. It was found that by increasing the repulsion strength between discs and solvent particles, which is representative of a change in solvent condition such as cooling or adding another solvent, one dimensional stacks of particles form. At lower disc-solvent repulsion, 1200 discs in the system formed some individual threads. At higher repulsion, a straight bundle of about 20-30 threads, packed in a hexagonal configuration, was observed. By increasing the repulsion still further, a twisted fibre also assembled. It was further seen that a higher repulsion parameter leads to formation of several short and thick bundles. It was suggested that this bundle breaking was due to the strong interfacial tension. By a similar method, this same group studied the self-assembly of discs in shear flow [58]. It was shown that, although the shear flow suppresses the formation of fibres from threads, well-structured fibres can still form if the repulsion parameter is set sufficiently high.

Prybytak [5, 32] also performed a detailed study of fibre self assembly from discotic building blocks, represented by Gay-Berne (GB) potential [59], in a solution of spherical Lennard-Jones (LJ) particles. Mimicking the effects of $\pi - \pi$ interactions, the face-face orientation was made more favourable than the edge-edge configuration for the discs. Prybytak showed that, for a given size of discs and spheres, the change of the GB energy anisotropy parameter leads to formation of fibres with different aspect ratios and even helicity. For a severe anisotropy in energy, the formed fibre was straight, while for the other investigated values of the parameter, the assembled fibres were twisted. It was also suggested that the fibre self assembly from discotic particles is a hierarchical process. That is, starting from an isotropic configuration, due to the face-face interaction of particles, some threads of discs form and then these threads interact laterally and make a cluster. This cluster grows both laterally and longitudinally and eventually the final fibre forms. This observation for the hierarchy of fibre assembly from discotic particles is different from the postulation of Huang *et al.* [35] which was discussed in the previous subsection (compare with Figure 2.6). Some structural analysis was performed by Prybytak on the final fibres and it was concluded that, for the twisted fibres, the pitch lengths for the threads packed in a hexagonal configuration along the axis of fibre are all the same, except for the central thread which is straight. It was also shown that the pitch in the

2.3 Self-assembly of Tubes

twisted fibre is a function of particle size and that, the flatter the particle, the longer the pitch length. In general, the behaviour of the system exhibited three distinct regimes according to temperature. At higher temperatures, no fibres form and the particles are distributed in random isolated threads. For a narrow range of temperature, a defect-free and well-structured fibre forms. At temperatures below this range, two or more initial clusters form in the system and, in the course of growth process, these clusters coalesce into a single imperfectly formed fibre. The work of Prybytak showed that the CG GB model has promising features for studying fibre self-assembly from disc-shaped molecules. The present research, being an extension of Prybytak's work, tries to shed more light on the complicated fibre formation process from discotic particles by performing more detailed investigations which will be presented in chapter 4.

2.3 Self-assembly of Tubes

The other class of elongated objects which can be self-assembled and have fascinating applications in different areas is tubule structures. Figure 2.10, for example, shows a microscopic image of a self-assembled nanotube with a hollow morphology. The literature on tube self-assembly indicates that most tubular objects, except carbon nanotubes (CNTs), form from amphiphilic molecules. It was in the 1980's, before the discovery of CNTs, that the self-assembly of lipid nanotubes was reported [60, 61]. The main advantage of lipid-based tubules is bio-compatibility. Consequently, the significant potential application for such tubes is in the capture, transport and controlled release of materials such as drugs. Lipid nanotubes can protect the encapsulated material from the environment. Also, due to their relatively large inner diameter (10-1000 nm), compared with CNTs, they can readily carry larger biomolecules. The elongated nature of tubules makes them well suited for transporting material along nanochannels. Further, lipid tubes with inorganic materials deposited on their outer surface may have enhanced mechanical and chemical properties and, thus, be suitable for a wider range of applications [4]. Research has shown that self-

2.3 Self-assembly of Tubes

assembled tubes may even have applications in molecular electronics as semiconductor components [62].

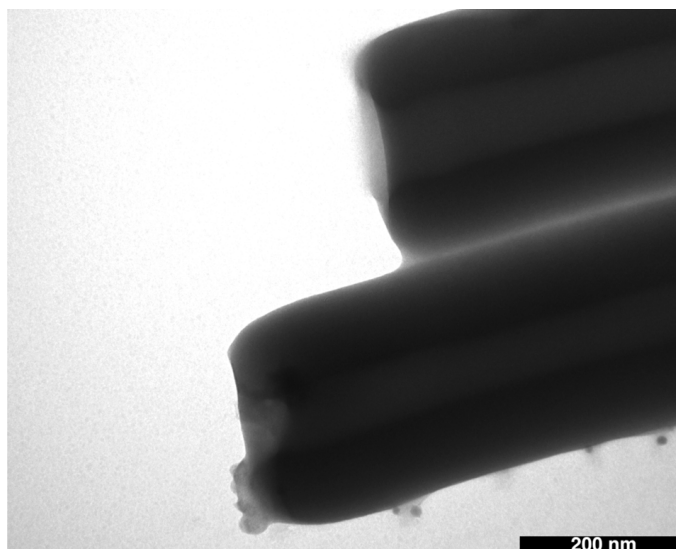


Figure 2.10: Microscopic image of the nanotubes formed from glycolipid in the work of Barclay *et al.* [63].

Whilst micelle- and fibre-forming systems are relatively common, building blocks which self-assemble into tubes are quite scarce. This is due to the highly ordered packing and specific anisotropic intermolecular interactions which are needed to form tubular structures. For example, in the comprehensive work by Kunitake *et al.* [64], the aggregated morphologies of more than 60 synthesised molecules were studied by electron microscopy and, of these, only four lipid molecules were found to form tubular structures with bilayer walls. Among amphiphilic molecules, coil-rod molecules show a greater propensity for tube formation than coil-coil ones with higher chain flexibility and more isotropic interactions [65], although other types of molecules can also self-assemble into tubes. A small number of mechanisms for tubule self-assembly have been suggested in the literature [66], and two of them, namely chiral tubule self assembly and tube formation through scrolling, will be discussed in the following subsections.

2.3 Self-assembly of Tubes

2.3.1 Chiral self-assembly

One of the routes identified for formation of a tubular object is via chiral self-assembly of amphiphilic molecules. Chirality of the building-blocks is believed to be key in this type of tubule formation which usually involves an intermediate helical ribbon structure. The reported cases of chiral self-assembly of tubes were mostly in aqueous solution, although the tube formation from quite thin and narrow ribbons in mineral oil has also been observed[67].

Two pathways for nanotube formation via helical ribbons have been suggested [65]. In one, as illustrated in Figure 2.11a, the width of the ribbon remained constant, but through shortening the helix pitch, a cylinder is formed (this was also observed in reference [68]). In the alternative pathway, whilst maintaining constant pitch, the full tube formed through widening of the helical ribbon (as seen in Figure 2.11b and also captured in reference [69]). It should be noted that there have been far more experimental observations of the latter pathway. However, both pathways are similar in that they require two distinct steps: first, development of a helical ribbon and then evolution into a tube from this ribbon. Understanding the mechanism involved in these two steps is crucial in gaining insight into chiral self-assembly of tubes.

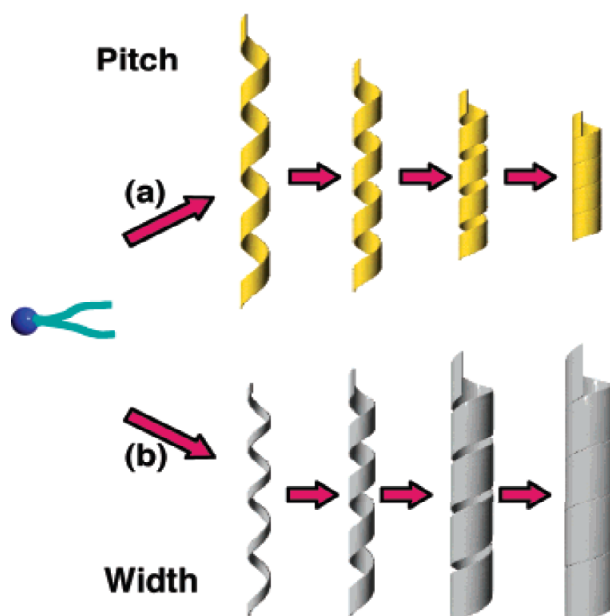


Figure 2.11: Possible formation mechanisms of lipid nanotubes based on chiral molecular self-assembly [65].

2.3 Self-assembly of Tubes

In order to understand the initial phase of tubular growth, having an insight into the self-assembly mechanisms of amphiphilic molecules is important. In most aqueous solutions, strong interactions with water molecules lead to a random dispersion of solvated particles because this minimizes free energy. For the hydrophobic tail of the amphiphilic molecules, however, it is thermodynamically unfavourable to be dispersed in water, because of the disruption caused to the interactions between the water molecules. Therefore, amphiphiles tend to self-assemble into structures which reduce the distortion caused to the aqueous phase. Simultaneously, the hydrophilic head groups, which tend to face out from these structure, minimize the free energy further by enhancing polar interactions with water molecules. Depending on the amphiphile concentration, pH and other thermodynamic properties, these effects can lead to formation of various microphase separated structures [70].

Various theories have tried to explain the origin of helicity in chiral self-assembly and the subsequent tube formation from these helical structures. Most of these theories [71, 72] were shown to be incorrect by experimental observations. However, Helfrich and Prost [73] developed one based on the notion that chiral molecules do not pack parallel to each other, but they adopt a tilt or nonzero twist relative to adjacent particles. The propagation of this twist throughout the membrane, was then shown to create a bending force that helically twists the membrane into a tube. Some of the earlier theories about tube formation from helical intermediates speculated a helical tilt angle of 45° . Although this was consistent with many findings, it was not a universal requirement. For example, it was observed that cholesterol formed metastable helical ribbons with pitch angles of 11° and 54° [74]. However, it should be noted that the tilt angle of 45° suggested by the theories is not necessarily the same as the structural pitch angle [75]. The variation in pitch angle can be explained by considering an anisotropy in the elastic constants of the ribbon. This determines the nature of bending of the bilayer ribbon longitudinally and laterally [68]. This elastic anisotropy also clarifies why shorter ribbons are stabilized into helices which transform into tubes as they grow longer. Another theory [76], supported by experimental work, showed that helical ribbons are not

2.3 Self-assembly of Tubes

necessarily transient structures - for particular parameters they can remain stable rather than forming tubes.

In most experimental investigations of chiral tubule formation, it has been observed that a twisted ribbon (Figure 2.12-A) is a precursor to the intermediate helical ribbon (Figure 2.12-B) [77, 78]. The twisted ribbon is characterized by negative Gaussian curvature, while this is zero in helical ribbons which maintain significant Mean curvature. Studies revealed that the transition from Gaussian curvature to Mean curvature happens as the width of ribbon grows because, although wider ribbons have lower edge energy cost per unit length, the energetic cost of twist significantly increases on widening of the ribbon [78, 79]. This observation implies that there is a correlation between size and morphology of the structures in the chiral tubule assembly pathway. However, it was seen that this structural transition is actually a function of the width to pitch ratio of the ribbon, and that, as this increases the transition happens at smaller widths [78].

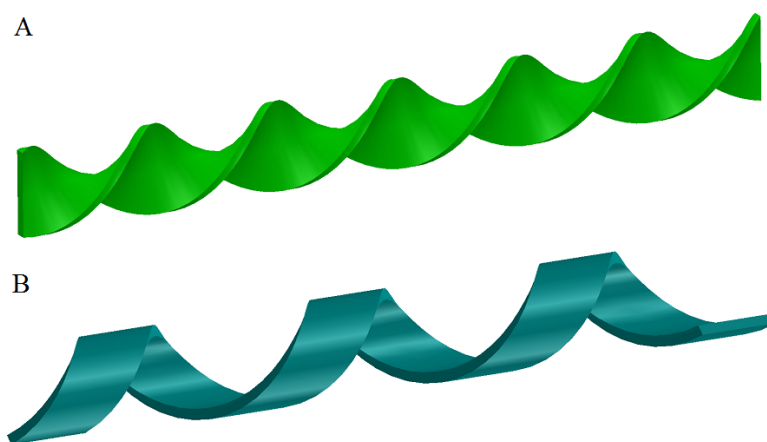


Figure 2.12: Schematic views of A) twisted ribbon and B) helical ribbon.

Figure 2.13 shows a schematic pathway of chiral self-assembly of tubes suggested in reference [79]. In a dilute aqueous solution of a short lipo-amino acid, many twisted ribbons formed from nanofibres in a few hours. The times required for the next transition to helical ribbons and then to tubes were of the order of 4 weeks and 4 months, respectively. This indicates the very slow nature of the tube self-assembly which makes it challenging for a computational investigation.

2.3 Self-assembly of Tubes

As well as chiral molecules, racemic mixture and even achiral building-blocks can also self-assemble into helical tubes [4, 75, 80–82]. Spontaneous symmetry-breaking is the mechanism by which such systems can form helical structures. For example, a transition from L_α phase (Figure 2.2-A) to $L_{\beta'}$ (Figure 2.2-C) leads to asymmetry as the molecules tilt, and this can induce chirality into the bilayer. The work of Thomas and colleagues [83] is an example of chiral multilamellar tube formation from a racemic mixture of diacetylenic phospholipid. More interestingly, it was observed that tube formation is a rapid process which happens in the order of an hour by transition from spherical multilamellar vesicles.

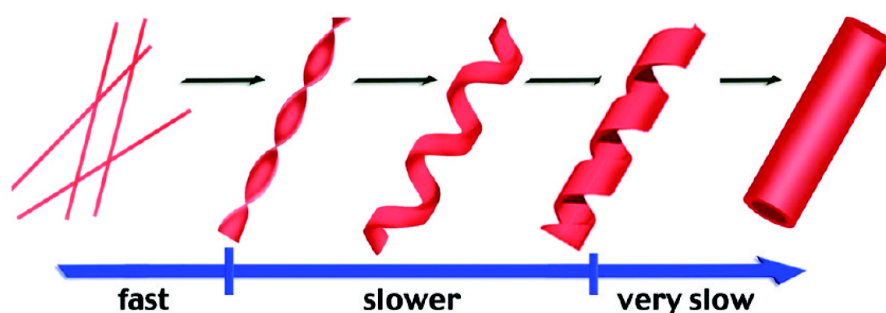


Figure 2.13: Schematic description of transitions in tube formation process as function of time [79].

Due to the very long time scales over which tube self-assembly takes place (of the order of hours and days), to the best knowledge, no FA MD simulations of chiral tube formation have been attempted. However, CG seems to be a better option for tubular self assembly investigation.

Cheng and coworkers [84–86] developed a CG model for an artificial microtubule self assembly investigation. A wedge shape rigid monomer consisting of 35 sites was the building block for their studies (Figure 2.14). Here, 27 sites which built the backbone interacted via the LJ potential and the remaining 8 particles, being attractive components, interacted through a particular soft potential in which a lock-and-key binding mechanism for the vertical interaction was applied. A structure diagram for the formation of different morphologies such as monomers, oligomers, partial rings or arcs, full rings, full tubules, sheets, and filaments based on different potential parameter values was developed in these works. Interestingly, helical tubes

2.3 Self-assembly of Tubes

formed more readily from the building-blocks even though the model had been designed for the purpose of non-helical tube assembly. This observation of chirality from achiral primary structures was also seen in the fibre simulations of Prybytak *et al.* [32]. It was found that, by making the vertical interaction stronger, the pitch of helical tube could be controlled. It was also suggested that there are at least two mechanisms for tubule assembly. The main growth mechanism was the addition of free monomers to the tubule. The other one was through capturing dimers, oligomers and even collisions of clusters. However, this approach in artificial tube formation is different from that which is usually observed in lipid systems in which the intermediate structure is a helical ribbon, as shown, for instance, in Figure 2.13. Figure 2.14 also illustrates a snapshot of the system in which the tubules have different pitch lengths.

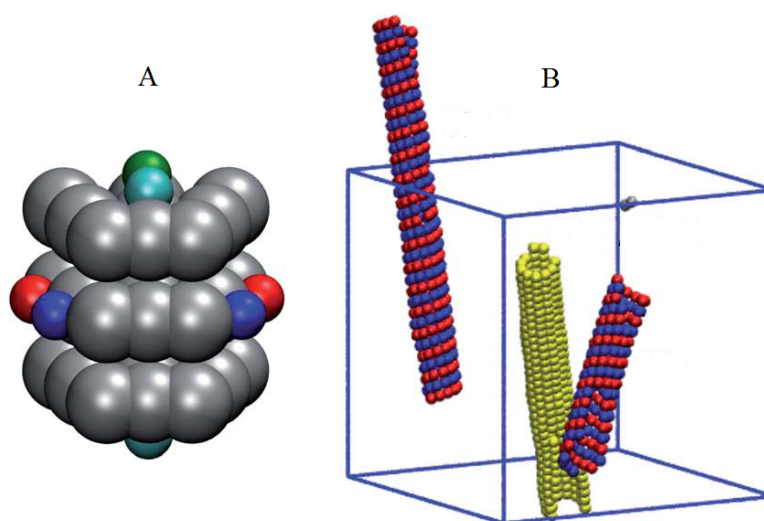


Figure 2.14: A) The 35 site wedge shape rigid monomer. The backbone particles are in grey and the attractive ones are in colour. B) Snapshot of the investigated system in which microtubules with different pitches form. In this figure every monomer is represented by a sphere. Tubes with a pitch of 1 are rendered in yellow, whilst the red and blue tubes have a pitch of 2 [85].

In order to investigate a more realistic building-block rather than the artificially constructed objects used in the aforementioned works, Srinivas and Klein [87] developed a CG model for hexa-peri-hexabenzocoronene (HBC) derivatives which had shown promise in previous experimental works on nanotube self-assembly [62, 88]. The HBC molecule investigated in the experimental work consisted of a central

2.3 Self-assembly of Tubes

planar section comprised of 13 aromatic rings, two hydrophobic chains on one side and two triethylene glycol (TEG) chains on the other side (Figure 2.15). It was seen that in a solution of tetrahydrofuran (THF), nanotubes having a bilayer structure in their walls formed after some hours. In THF/water solution, a helical ribbon was observed and, therefore, it was suggested that the helical ribbon is the intermediate morphology in the tube formation [62]. Mimicking the structure of the HBC molecule, a 25 site model was developed for the CG simulation work, as shown in Figure 2.15. The simulation box consisted of 180 HBC molecules and 21600 CG water sites. It was seen that the HBC molecules initially assembled into small clusters which grew in time. Then, a columnar structure formed from the clusters and finally a structure similar to a twisted ribbon was observed (Figure 2.15). However, tube formation was not seen, possibly due to the limited size and duration of the simulation. The authors suggested that a different level and approach to coarse graining would be needed in order for more features of tube formation to be captured.

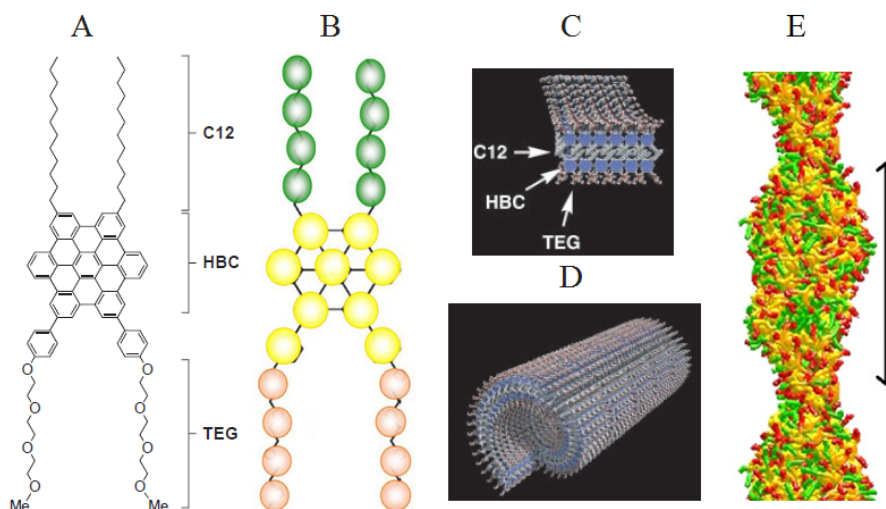


Figure 2.15: A) The investigated HBC molecule with two hydrophobic C12 chains on one side and two TEG chains on the other side. B) The 25 site CG model presented for the HBC molecule. C) Structure of bilayer in the wall of nanotube. D) Schematic representation of the nanotube formed in the experimental work. E) The twisted ribbon observed in the numerical simulation (the arrow shows the pitch length). The pictures were taken from references [62, 87].

2.3 Self-assembly of Tubes

2.3.2 Tube formation by scrolling

Scrolling and rolling is the other mechanism for self-assembly of tubes. For flat membranes, being largely exposed to solution is energetically unfavourable, and therefore, in concentrated solution, they stack and form multi-layer structures. In dilute solutions, however, the membranes can spontaneously scroll to form tubes and reduce surface energy [66, 89]. Figure 2.16 shows the possible mechanism of multi-layer sheet and rolled-up tube formation from linear molecules having aromatic cores and two side chains, as suggested in the work of Chen *et al.* [89]. At low concentrations, the formed single layer sheets were widely dispersed in the domain and, therefore, interactions between them were rare. In order to lower surface energy under these conditions the sheets tended to roll and form scrolled nanotubes. Figure 2.16 also shows an SEM image of the self-assembled tubes in which the scrolled structure is evident. In another experiment [90], formation of 2D flat sheets of laterally grafted amphiphilic rods was observed in aqueous solution. On heating, due to the energy costs of packing frustration of the rod segments of the molecule, the sheets scrolled into a hollow tubular structure. Resting at room temperature for a period of two weeks, the tubes opened completely into sheets, which shows the reversibility of the process.

Not only rod molecules, but also T-shaped rod-coil molecules also showed a transition from flat bilayer sheets to a curved tubular structure, maintaining mean curvature, by rolling [91]. Here, in a mixed experimental and computational study, it was indicated that the structural switch between these two configurations is reversible and can be controlled by slight variation in the coil length of the T-shaped molecule. The motivation for such a transition is the high energetic penalty due to low grafting density at the planar rod-coil interface.

In a series of DPD simulations [92–94], the spontaneously rolling up of sheets to scrolled tubes was investigated for rod-coil molecules. It has been theoretically predicted [95] that tethered sheets with any anisotropy exhibit a tubule phase rather than flat or crumpled phases. Following this prediction, these DPD studies also introduced volume and chemical asymmetries to the side coils of the rods in order to

2.3 Self-assembly of Tubes

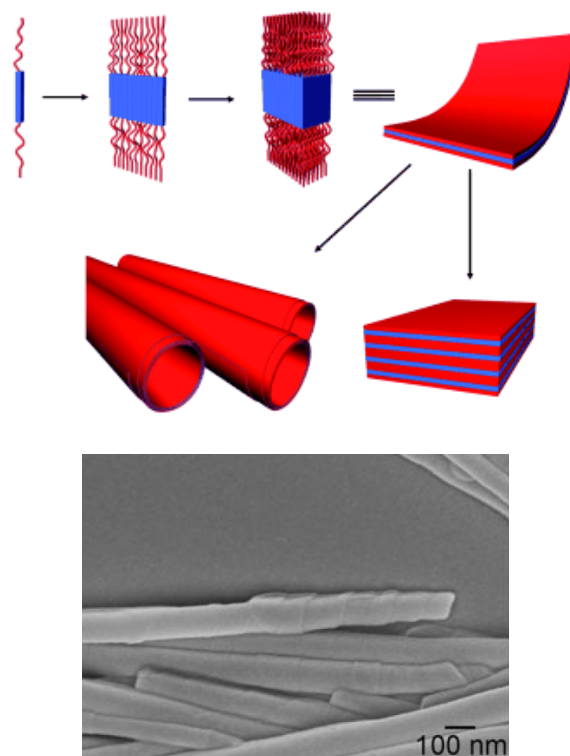


Figure 2.16: Top: possible mechanism for self-assembly of multi-layer sheets and rolled-up tubes from a linear molecule with an aromatic core and 2 side chains. Bottom: SEM image of the rolled-up tubes in low concentration [89].

observe the formation of scrolled structures. Figure 2.17 presents a suggested phase diagram for the formation of curved sheets, tubes and filled scrolls based on the variation of tether coil volume ratio of the two sides (vertical axis) and coil-solvent repulsion strength (horizontal axis). It was also suggested that the size and curvature of the internal cavity of the formed object is closely associated with the fraction of coils mimicking the H-bonds on the partially H-bonded side of the membrane. This anisotropic H-bonding leads to the entropic repulsion on one side of the sheet and consequently the rolling up of the flat ribbon. The curvature of the object exhibited a linear correlation with the H-bonding fraction [93]. Interestingly, the formation of faceted nanotubes (with triangular, square, pentagonal and hexagonal cross-sections) was also simulated by introducing a patterned defect to the membrane [94].

Coarse-grained MD simulations of nanovesicle and nanotubes formation from peptides modelled with the MARTINI force field [96] were performed by Guo *et al.* [97]. Here, it was found that the morphology of the formed nano-structures is

2.3 Self-assembly of Tubes

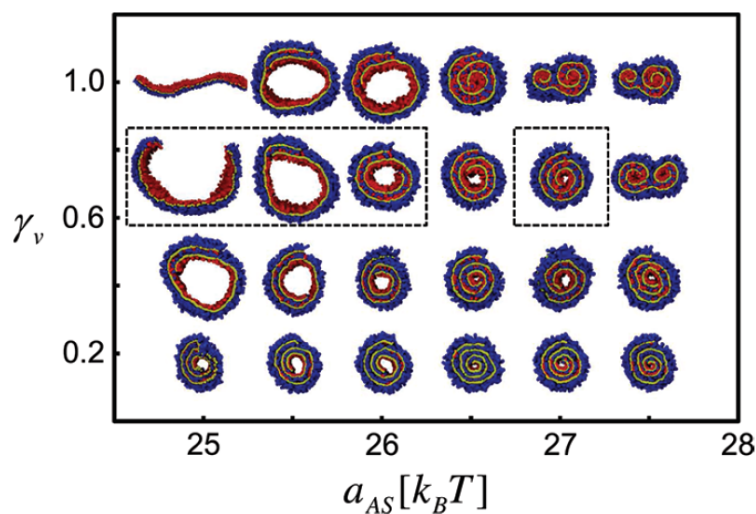


Figure 2.17: Phase diagram for formation of curved sheets, tubes and filled scrolls by variation of tether coil volume ratio (vertical axis) and coil-solvent repulsion strength (horizontal axis) [92].

concentration dependant. At low concentration, only vesicle-like structures formed, whereas higher concentrations promote the self-assembly of nanotubes and bilayers - at the highest investigated concentration, 90% of the formed objects were bilayers. Two pathways for nanotube self-assembly were observed. At moderate concentration, vesicle fusion was the mechanism of the tube formation. Starting from an initially isotropic configuration, bilayers formed in the system very rapidly and, then, by bilayer closure, spherical and ellipsoidal vesicles emerged. Interaction of these vesicles with each other and their fusion led to a shape transformation and, eventually, the appearance of a nanotube. Figure 2.18a shows the time line of this spontaneous process. This vesicle fusion and tube formation was also observed experimentally in concentrated solutions of cationic peptides [98]. For higher concentrations, however, fusion rarely occurred and the bending of the formed bilayer was the main mechanism of tube formation. Figure 2.18b also illustrates some snapshots of the tube assembly through this pathway. Investigation of the total potential energy of different systems revealed that, at moderate concentrations, the nanotube was the most stable structure and, therefore, the system tended to form such an object.

2.4 Emergence of Twist

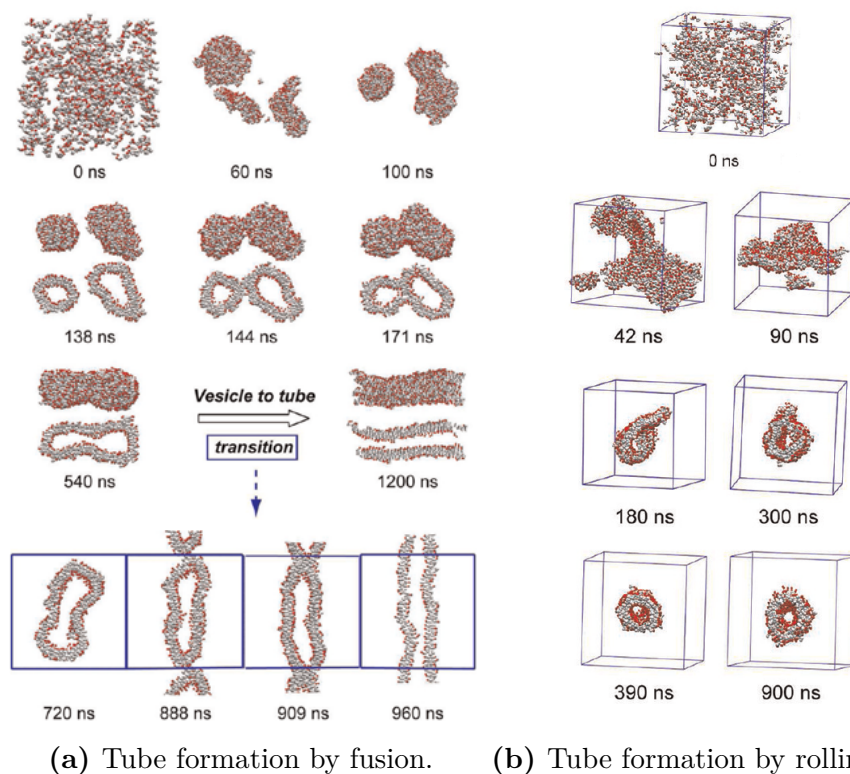


Figure 2.18: Time lines of two pathways for self-assembly of tubes from peptides [97].

2.4 Emergence of Twist

There are several factors which may lead to the emergence of twist in a self-assembled structure. Among them, as exemplified in previous sections, the chirality of the building-blocks is the most common feature which causes the formed object to become helical or twisted. However, in this section, we focus on the situations in which twist emerges from achiral particles. The associated literature is reviewed very briefly to give insight into spontaneous symmetry breaking and formation of twisted structures. The background discussed here is consciously focused on examples related to the aim of this work, which is self-assembly in systems consisting of coarse-grained ellipsoidal particles.

In order to break the symmetry and form a chiral structure, it seems that having an anisotropy is crucial [99]. By learning from nature where, for example, two competing length scales in DNA lead to the helicity of the structure, one may conclude that the anisotropy in the shape of building blocks can be key to this

2.4 Emergence of Twist

process. On this basis, Chakrabarti *et al.* [100] have characterized the global minima for clusters of GB discotic particles using the basin-hopping approach [101]. A range of parameters for this potential was investigated and the associated structures with global minimum energy were identified. For isotropic interactions, in which the face-face and edge-edge configurations are the same, the stable columnar structure has no chirality, suggesting that an anisotropic interaction is also needed for the emergence of twist in this potential. By changing the potential parameters and making the face-face configuration more favourable for interacting discs, twisted stacks of particles were observed. By an increase in the number of simulated particles, a 7-column twisted structure with a straight central thread was found to be the global minimum (Figure 2.19). This chiral structure was the result of close packing of particles and their interdigitation in neighbouring columns. As the interaction was achiral, the energies associated with both left- and right-handed clusters were the same, but with a very high energy barrier in between. The amount of twist (pitch length) was found to change non-monotonically with the aspect ratio of interacting particles and for more rounded discs the twist disappeared and the columns were parallel.

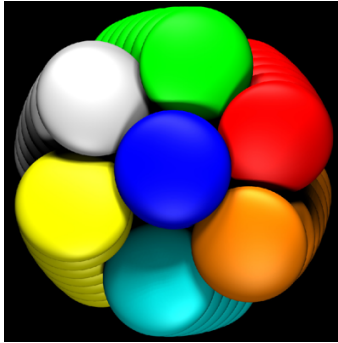


Figure 2.19: The structure with minimum global energy found for a cluster of 49 GB discs having an anisotropy in their interaction energy [100].

A helical structure has also been observed in a columnar mesophase of discotic liquid crystals through MD/MC simulations of GB particles [102]. Two columnar phases, helical columnar C_α and tilted columnar C_β , were found for the first time with a small change in the parametrization of the potential. For the helical mesophase, the column of discs showed a spiral pattern with an axis parallel to the director of

2.4 Emergence of Twist

the system. It was shown that the C_β phase was thermodynamically preferred to C_α , suggesting that the helical columns were entropically more favourable.

Variation of the anisotropy in the interaction of ellipsoidal particles can lead to observation of different structures. In the works of Fejer *et al.* [99, 103], the global minima for clusters of discotic particles interacting with a different potential were determined. Here, the Paramonov-Yaliraki (PY) potential [104], which exhibits more long-range interaction than the GB potential and uses the idea of the directional contact distance of two ellipsoids, was applied. Various intriguing configurations were predicted by this potential for a range of interaction anisotropies. If the side-side configuration of the discs is preferred to the edge-edge one, then the global minimum structure consists of a double-helix in which the short axes of particles have an angle with the axis of helix (Figure 2.20a). For a larger cluster formed from particles with the same parametrization, the structure was not helical any more, but is formed of both stacks and arcs. For the isotropic interaction (uniform well-depth) at each relative orientation, the global minimum is achieved by two half rings in an orthogonal arrangement (Figure 2.20b). The structure resembles the lobes of a ‘tennis ball’. By favouring the face-face orientation, it was observed that the shifted stacked configuration has a lower energy than the perfectly aligned one (in contrast with the GB potential). This symmetry breaking led to observation of a single-thread helical structure in which the helix radius can be controlled by increasing the shape anisotropy (Figure 2.20c). In this configuration, the particles are parallel to the axis of the helix.

Spherical particles with anisotropic interactions can also self-assemble into interesting morphologies. Both GB and PY potentials with similar interaction strength ratios were applied for the investigation of global minimum structures of spherical particles [99]. Although no helical features were observed for the GB potential, the stable cluster for the PY potential consisted of twisted strands. It was noted that by increasing the number of spherical particles in the cluster, a similar structure to that which is observed for GB discs [100] (see Figure 2.19) can be achieved with the PY model.

2.5 Summary

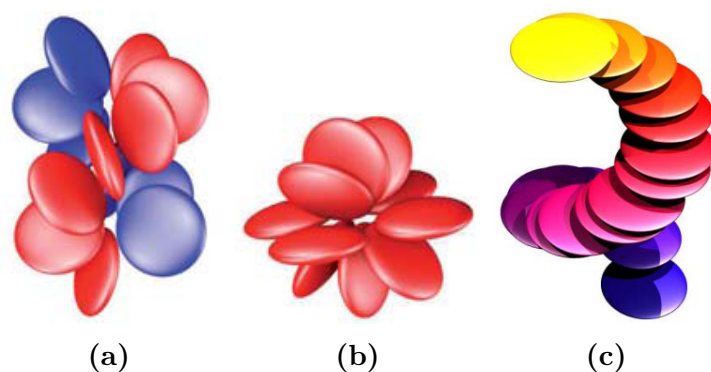


Figure 2.20: Global minimum structures observed for different anisotropies in PY potential. a) Double-helix for discs with edge-edge preference. b) Tennis ball structure for uniform interaction at different configurations. c) Single-thread helix for particles with face-face preference [99, 103].

2.5 Summary

The literature review carried out here reveals that the formation of supramolecular structures is of interest to many researchers including biologists, physicists, chemists and engineers due to their fascinating properties and potential applications. Despite a substantial number of experimental and numerical studies performed in this area, the mechanisms of the initiation of such structures and their subsequent growth, particularly the early stages, where very short time- and length-scales apply, are not well understood. The self-assembly pathways suggested by experimental observations are often speculative, and sometimes different groups have suggested contradictory mechanisms for the same process. We showed that the literature of tubule self-assembly suffers more from a lack of detailed understanding of the formation process than that of fibres. Due to significantly larger time- and length-scales associated with the formation of tubes, only a few numerical investigations were successful in capturing tubule self-assembly and, therefore, these powerful techniques could not appropriately address many of the questions that have been raised by experimental observations.

Here, we use Molecular Dynamics simulations to study the free self-assembly of a variety of supramolecular chiral structures. The advantage of MD is that it provides us with a ‘live’ picture of what is happening in the studied systems and, therefore, a fuller understanding of pathways leading to the formation of final structures. In

2.5 Summary

the next chapter, we focus on the methodology of this research and then we use the developed methods to study the spontaneous formation of various structures.

Chapter 3

Computer Simulation Methods

In this chapter, details of the computer simulation methods used in the current research are presented. As discussed in Chapter 2, Molecular Dynamics (MD) simulation yielded useful outcomes in previous studies of molecular self assembly. It was, therefore, chosen as the main method in the current work. In the following, the related concepts and techniques are discussed.

3.1 Basics

In MD simulations, the governing equations of classical mechanics [105], these being conservation of linear and angular momentums (for rigid body motion), are solved for a system of N particles, subject to a potential energy, U . The conservation of linear momentum is represented by Newton's second law of motion:

$$\mathbf{F} = m \frac{d^2 \mathbf{r}}{dt^2} \quad (3.1)$$

where \mathbf{F} , m and \mathbf{r} are the force vector, mass and position vector of the particle, respectively. The second order time derivative of position term on the right hand side is, in fact, the acceleration of the particle; \mathbf{a} . In this work, for consistency, vector and tensor variables are introduced with bold letters and they are distinguished by

3.1 Basics

their definition. The rotational equivalent of equation (3.1) is:

$$\boldsymbol{\tau} = \mathbf{I} \frac{d\boldsymbol{\omega}^s}{dt} \quad (3.2)$$

where $\boldsymbol{\tau}$ is the torque vector, \mathbf{I} is the moment of inertia tensor, $\boldsymbol{\omega}$ is the rotational velocity vector and superscript s denotes that the rotational velocity is represented in a space-fixed coordinate system.

The general form of the pair potential, U , governing the interaction of sites i and j can be written as:

$$U = U(\mathbf{A}_i, \mathbf{A}_j, \mathbf{r}_{ij}) \quad (3.3)$$

where \mathbf{r}_{ij} is the inter-site vector, $\mathbf{r}_{ij} = \mathbf{r}_i - \mathbf{r}_j$, and \mathbf{A} is an orthogonal rotation matrix used to transform between space-fixed and body-fixed coordinates [105] and its subscript denotes the associated site index. The body-fixed coordinate system is attached to the particle and rotates with it. The rows of each matrix \mathbf{A} are, in fact, the principal axis vectors of each particle. For potentials that are sensitive to the relative orientations of the interacting particles, one, two or three principal axes (rows of matrix \mathbf{A}) may appear in the potential formulation. If the pair potential is a function of only one axis of the particle, for example in the original Gay-Berne potential [59], then the matrix \mathbf{A} in equation (3.3) reduces to that principal axis. By the approach of Allen and Germano [106] for the potential functions having the form of equation (3.3), one can analytically derive the forces and torques acting on each particle:

$$\mathbf{F}_i = -\mathbf{F}_j = -\frac{\partial U}{\partial \mathbf{r}_{ij}} \quad (3.4)$$

$$\boldsymbol{\tau}_i = -\sum_m \mathbf{A}_{im} \times \frac{\partial U}{\partial \mathbf{A}_{im}} \quad (3.5)$$

$$\boldsymbol{\tau}_j = -\sum_m \mathbf{A}_{jm} \times \frac{\partial U}{\partial \mathbf{A}_{jm}} \quad (3.6)$$

where \mathbf{A}_{im} and \mathbf{A}_{jm} are, respectively, the principal axis vectors of particles i and j , which appear in the potential. The term \times indicates the cross product of the two

3.2 Integration Algorithms

vectors. Allen and Germano [106] showed that the forces and torques applied to two interacting particles, i and j should satisfy the following equation:

$$\boldsymbol{\tau}_i + \boldsymbol{\tau}_j + \mathbf{r}_{ij} \times \mathbf{F}_i = \mathbf{0} \quad (3.7)$$

This can be used to verify the derived forces and torques of a new potential or as a measure of the accuracy of calculations during a simulation. Clearly, the rotation matrix \mathbf{A} , is not seen in the potentials that are spherically symmetric (e.g. the Lennard-Jones model [38]) and, therefore, the torques on the particles are zero. Details of the derivation of forces and torques for the potentials used in this work are given in Appendix A.

Given the total force and torque acting on each particle through its interactions with the other particles in the system, integrating equations (3.1) and (3.2) with respect to time allows the system to evolve. The standard method for integrating these ordinary differential equations is to adopt a finite difference approach in which the equations are discretised and time is split into small time steps, Δt . Different algorithms have been developed for this integration, some of which are discussed in the next section.

3.2 Integration Algorithms

In an MD simulation, the particle positions, velocities and other characterising data at a given time, t , are used to determine those same variables at the later time, $t + \Delta t$. Many finite difference algorithms have been developed for achieving this by integration of the governing equations. Verlet, Leap-frog, velocity-Verlet and prediction-correction methods are examples of some of the finite difference algorithms that are widely used in an MD context [38]. Of these, the velocity-Verlet has proved to have good characteristics in terms of simplicity, stability and ability to conserve key observables of the system such as the total energy and linear momentum. The algorithm was firstly developed for translational motion and also extended to deal

3.2 Integration Algorithms

with rotational degrees of freedom of particles [107, 108]. Here, the translational motion velocity-Verlet algorithm is discussed.

The velocity-Verlet algorithm consists of two steps for the velocity, \mathbf{v} , with a force calculation in between. The first step takes the form:

$$\mathbf{v}_i\left(t + \frac{\Delta t}{2}\right) = \mathbf{v}_i(t) + \frac{\Delta t}{2}\mathbf{a}_i(t) \quad (3.8)$$

$$\mathbf{r}_i(t + \Delta t) = \mathbf{r}_i(t) + \Delta t\mathbf{v}_i\left(t + \frac{\Delta t}{2}\right) \quad (3.9)$$

The terms in parentheses denote the time step at which the variable is considered. After calculation of particle positions at the next time step, through equation (3.9), the forces (and torques for rigid body motion) on each particle are calculated based on their new positions (and orientations). This is done by equation (3.4) (and equations (3.5 and 3.6) for torques). At this stage, the potential energy of the system can also be calculated. From here, the second step of the velocity-Verlet algorithm can be performed:

$$\mathbf{v}_i(t + \Delta t) = \mathbf{v}_i\left(t + \frac{\Delta t}{2}\right) + \frac{\Delta t}{2}\mathbf{a}_i(t + \Delta t) \quad (3.10)$$

At this point, the time step is completed and other observables, such as the kinetic energy, can be determined.

Whilst translational motion of particles can be dealt with straightforwardly, taking care of the rotational motion is more complicated. The source of this complexity is the form of the differential equations governing rotational motion, which makes the development of a reliable and stable integration algorithm challenging.

In treating rigid body motion [105], a body-fixed coordinate system, which attaches to the particle and moves and rotates with it, is usually used. As said, transformation between the space-fixed and body-fixed coordinates is achieved through the rotation matrix, \mathbf{A} , whose rows are the principal axes of the particle. This definition also leads to a diagonal tensor for the particle moment of inertia in

3.2 Integration Algorithms

the body-fixed coordinate system. The matrix \mathbf{A} can be defined as:

$$\mathbf{A} = \begin{bmatrix} 1 - 2(q_2^2 + q_3^2) & 2(q_1q_2 + q_0q_3) & 2(q_1q_3 - q_0q_2) \\ 2(q_1q_2 - q_0q_3) & 1 - 2(q_1^2 + q_3^2) & 2(q_2q_3 + q_0q_1) \\ 2(q_1q_3 + q_0q_2) & 2(q_2q_3 - q_0q_1) & 1 - 2(q_1^2 + q_2^2) \end{bmatrix} \quad (3.11)$$

where q_i are the four-component quaternions (also known as Euler parameters) with a unit norm [105]:

$$q_0^2 + q_1^2 + q_2^2 + q_3^2 = 1 \quad (3.12)$$

The quaternions for a particle satisfy the rigid body equation of motion given by [109, 108]:

$$\dot{\mathbf{q}} = \frac{1}{2}\mathbf{Q}\boldsymbol{\omega} \quad (3.13)$$

$$\begin{aligned} \dot{\omega}_x^b &= \frac{\tau_x^b}{\bar{I}_x} + \frac{\bar{I}_y - \bar{I}_z}{\bar{I}_x} \omega_y^b \omega_z^b \\ \dot{\omega}_y^b &= \frac{\tau_y^b}{\bar{I}_y} + \frac{\bar{I}_z - \bar{I}_x}{\bar{I}_y} \omega_z^b \omega_x^b \\ \dot{\omega}_z^b &= \frac{\tau_z^b}{\bar{I}_z} + \frac{\bar{I}_x - \bar{I}_y}{\bar{I}_z} \omega_x^b \omega_y^b \end{aligned} \quad (3.14)$$

where $\mathbf{q} = [q_0 \ q_1 \ q_2 \ q_3]^T$, $\boldsymbol{\omega} = [0 \ \omega_x^b \ \omega_y^b \ \omega_z^b]^T$ (superscript b indicates that the rotational velocities correspond to the body-fixed coordinate system), \bar{I}_j s are the principal moments of inertia of the particle, and

$$\mathbf{Q} = \begin{bmatrix} q_0 & -q_1 & -q_2 & -q_3 \\ q_1 & q_0 & -q_3 & q_2 \\ q_2 & q_3 & q_0 & -q_1 \\ q_3 & -q_2 & q_1 & q_0 \end{bmatrix} \quad (3.15)$$

Several algorithms have been developed for integration of equations of rigid body rotational motion based on the idea of quaternions [107–111]. These algorithms calculate the rotational velocity and orientation of particles at the next time step by implementing variants of equations (3.2) and (3.13). In the present research, all of the

3.2 Integration Algorithms

above-mentioned approaches were implemented and their performances compared for a given system. Results showed that the algorithm suggested by Miller *et al.* [108], which is known as NOSQUISH, has the best performance and stability, particularly for complicated systems for which the other algorithms either failed or showed a significant energy drift. However, NOSQUISH also proved the most complicated and time consuming of the algorithms considered, which makes it computationally expensive. Here, in the trade off between computational cost and accuracy, the latter wins and, therefore, the NOSQUISH algorithm was adopted for integration of rotational equations of motion in the current work. The key equations and concepts of this algorithm are discussed here, but discretisation details are deferred to Appendix B.

The NOSQUISH algorithm [108] is symplectic, which means that it is time reversible and very stable, because it does not need any iteration in its integration scheme. Quaternions, \mathbf{q} , quaternion momenta, $\bar{\mathbf{p}}$, and quaternion torques, $\bar{\boldsymbol{\tau}}$, are the main dynamical variables of the algorithm:

$$\bar{\mathbf{p}} = \begin{bmatrix} \bar{p}_0 \\ \bar{p}_1 \\ \bar{p}_2 \\ \bar{p}_3 \end{bmatrix} = 2\mathbf{Q} \begin{bmatrix} 0 \\ \bar{I}_x \omega_x^b \\ \bar{I}_y \omega_y^b \\ \bar{I}_z \omega_z^b \end{bmatrix} \quad (3.16)$$

$$\bar{\boldsymbol{\tau}} = \begin{bmatrix} \bar{\tau}_0 \\ \bar{\tau}_1 \\ \bar{\tau}_2 \\ \bar{\tau}_3 \end{bmatrix} = 2\mathbf{Q} \begin{bmatrix} 0 \\ \tau_x^b \\ \tau_y^b \\ \tau_z^b \end{bmatrix} \quad (3.17)$$

It should be noted that, as the torques given by equations (3.5 and 3.6) are in the space-fixed coordinate system, they have to be transferred to the body-fixed coordinates in order to be used in equation (3.17). For this, any vector including the torque vector, $\boldsymbol{\tau}$, can be expressed in the body coordinate through a simple transformation:

$$\boldsymbol{\tau}^b = \mathbf{A}\boldsymbol{\tau}^s \quad (3.18)$$

3.3 MD Tricks of the Trade

The system Hamiltonian is given by:

$$H(\bar{\mathbf{p}}, \mathbf{q}) = \sum_{k=0}^3 h_k(\bar{\mathbf{p}}, \mathbf{q}) + \phi(\mathbf{q}) \quad (3.19)$$

where $\phi(\mathbf{q})$ is the potential energy and

$$h_k(\bar{\mathbf{p}}, \mathbf{q}) = \frac{1}{8\bar{I}_k} (\bar{\mathbf{p}}^T \mathbf{P}_k \mathbf{q})^2, \quad k = 0, \dots, 3 \quad (3.20)$$

The term $\mathbf{P}_k \mathbf{q}$ is a vector whose elements are the $(k + 1)^{th}$ column of tensor \mathbf{Q} and \bar{I}_k is the k^{th} principal moment of inertia of the particle, except for \bar{I}_0 which is an arbitrary non-zero constant. The NOSQUISH integration scheme can then be derived from the Hamiltonian given by equation (3.19), as discussed by [108, 112] and presented in Appendix B.

The NOSQUISH algorithm fits well onto the velocity-Verlet scheme considered for translational motion. In the first half of the algorithm, the normal integration time step, Δt , is split into m_{rot} sub-steps. In each sub-step, the quaternions and their momenta are updated. At the end of the first half, the quaternions are updated to the next time step and the quaternion momenta are achieved for the half step, similar to velocity-Verlet in which the positions and velocities are updated to the next step and half step, respectively. At this stage, the force and torque calculations are performed, based on the new positions and orientations. Then the second half of the algorithm is completed by calculation of the quaternion momenta at the next time step. Given updated quaternion momenta, $\bar{\mathbf{p}}$, at the next time step, the rotational velocities of the particle (required for the rotational kinetic energy calculation) can be determined from equation (3.16).

3.3 MD Tricks of the Trade

3.3.1 Periodic boundary condition

Due to the limitations of computational resources, MD simulation of a real-size system having a significant number of particles (of order 10^{23}) is currently impossible.

3.3 MD Tricks of the Trade

Instead, computer simulations are usually performed for $10^2 - 10^6$ particles. For this size of system, particles on the faces of an isolated simulation box would experience totally different forces from those in the bulk. In order to overcome these surface effects, periodic boundary conditions are applied. Here, it is assumed that the cubic simulation box is replicated in the x, y and z directions and that the image particles in the periodic boxes move in exactly the same way as those in the original box. If a particle crosses a boundary and leaves the system, its image enters the domain from the opposite side. In such a system, particles interact according to the minimum image convention [38]. This means that a particle only interacts with the nearest image of a second particle, whether it is in the same box or in an image one. The details of applying periodic boundary condition are discussed elsewhere [38] and, so, are ignored here for the sake of brevity.

3.3.2 Observable quantities

One of the aims of performing a simulation is to measure key observable quantities which characterise the behaviour of the system under investigation. Here, some of those quantities such as energies, temperature, pressure, structural properties, etc. are discussed.

The Hamiltonian of a system is the sum of the potential and kinetic energies of all constituent particles. Conventional MD simulations are performed in microcanonical (constant-NVE) ensemble in which the number of particles (N), volume of the system (V) and total energy (E, Hamiltonian) are constants. In a microcanonical ensemble, the more an algorithm conserves the total energy, the better the performance of that algorithm. The potential energy is the sum of all pairwise potentials in the system and the kinetic energy is the sum of the translational and rotational kinetic energies of the particles:

$$E_{kin} = \sum_{i=1}^N \frac{m_i(\mathbf{v}_i \cdot \mathbf{v}_i)}{2} + \sum_{i=1}^{N_{\text{non-sph}}} \frac{(\bar{\mathbf{I}}_i \boldsymbol{\omega}_i \cdot \boldsymbol{\omega}_i)}{2} \quad (3.21)$$

3.3 MD Tricks of the Trade

where $N_{\text{non-sph}}$ is the number of non-spherical particles for which the rotational motion is considered and $\bar{\mathbf{I}}$ is a diagonal tensor whose elements are the principal moments of inertia of the given particle.

According to the equipartition theorem, the temperature of a system is related to the average energies. That is, each quadratic degree of freedom is associated with an average energy of $k_{\text{B}}T/2$, where k_{B} is Boltzmann's constant. Consequently, the temperature, T , can be calculated by:

$$\langle E_{kin} \rangle = \frac{1}{2}k_{\text{B}}T(N_t^f + N_r^f) \quad (3.22)$$

where E_{kin} is given by equation (3.21), $\langle \rangle$ denotes time averaging [38], and N_t^f and N_r^f are the total numbers of translational and rotational degrees of freedom, respectively:

$$N_t^f = (N - 1)d_t \quad (3.23)$$

$$N_r^f = (N_{\text{non-sph}})d_r \quad (3.24)$$

where d_t and d_r are the translational and rotational degrees of freedom for a single particle, respectively. In a 3D domain, $d_t = 3$. For symmetric potentials such as the original GB model, the rotation around the axis of symmetry of the particle does not represent a degree of freedom and, therefore, the non-spherical particles modelled with the GB potential have only 2 degrees of freedom for rotational motion ($d_r = 2$). However, breaking the symmetry of the potential (see next section) causes rotation around the third axis to also become relevant. In this case, each particle has 3 rotational degrees of freedom ($d_r = 3$). This was not considered in the work of Prybytak [5] for the Tanh potential used in disc-sphere interaction and, therefore, there may be a slight difference between the values of temperature reported here and those of Prybytak's work. In equation (3.23), one degree of freedom in each direction is removed from the system, because net linear momentum is assumed to be zero and, by this, a constraint is applied on the system in each direction.

3.3 MD Tricks of the Trade

The pressure or stress tensor can be calculated through following equation [38]:

$$p_{\alpha\beta} = \frac{1}{V} \left[\sum_{i=1}^N m_i v_{i\alpha} v_{i\beta} + \sum_{i=1}^N \sum_{j>i}^N r_{ij\alpha} F_{ij\beta} \right] \quad (3.25)$$

where V is the volume of the simulation box and F_{ij} is the force due to the interaction between particles i and j . The diagonal elements of the pressure tensor represent the values of the pressure in three different directions. The average of these three elements should match the pressure value given by the virial theorem [38].

The orientational order parameter or, as it is called in liquid crystal context, nematic order parameter, P_2 , is a measure showing how certain particle axes adopt a preferred direction. The nematic order parameter is the largest eigenvalue of the Q-tensor given by:

$$Q_{\alpha\beta} = \frac{1}{2N_{\text{non-sph}}} \sum_{i=1}^{N_{\text{non-sph}}} (3\hat{u}_{i\alpha}\hat{u}_{i\beta} - \delta_{\alpha\beta}) \quad (3.26)$$

where \hat{u}_i is the unit director vector of particle i , δ is the Kronecker delta, and the eigenvector associated to this eigenvalue is the director of the system, \hat{n} .

Another structural observable is radial distribution function, $g(r)$. The radial distribution function indicates how, on average, the particles in a system are radially packed around each other. In fact, $g(r)$ gives the probability of finding a pair of particles at a distance r , relative to the probability expected for a completely random distribution at the same density. In order to calculate the radial distribution function, the domain is divided into a series of thin concentric spherical shells of thickness dr . A histogram based on the separations of particles is constructed for this series of shells. Then, the histogram (number of pair separations in each shell) is normalized by the ideal distribution of particles in that particular shell, and averaged over all particles [38].

In some applications, it is useful to have some information about the distribution of particles with respect to a given axis. This can be achieved by calculating the normal and parallel distribution functions, $g_{\perp}(r)$ and $g_{\parallel}(r)$. To calculate these functions, the separation vector of each pair of particles is projected parallel and

3.3 MD Tricks of the Trade

normal to the given axis which can be, for example, the system director. Then, the parallel and normal distribution functions are calculated, based on these separations, similar to the $g(r)$ calculation. For the parallel and normal distribution function calculations, the domain is divided, respectively, into disc and cylindrical shells whose symmetry axes are the same as the given axis.

3.3.3 Reduced units

In MD simulation, it is a good practice to use reduced units instead of dimensional ones. In CG simulation, using reduced unit means that a particular set of simulation results do not just correspond to a single molecule, but may be valid for a class of building-blocks. The unit reduction is usually performed by choosing characteristic units for length, mass and energy. Provided no mass-dependent potential such as a gravitational field is applied in the domain, the choice of mass for different particles is not important and, therefore, all particle masses are sets to be 1. The characteristic length is generally the value of zero repulsion separation, σ_0 , and in this work the diameter of the discotic particles has been chosen for the length reduction. The potential well-depth for the disc-disc interaction, ϵ_0 , is used to reduce the energy. Therefore, the units of temperature and time are ϵ_0/k_B and $\sqrt{m\sigma_0^2/\epsilon_0}$, respectively. The reduced parameters are always defined by dividing the real value of the parameter by its unit, as mentioned above.

3.3.4 Initialization

At the beginning of every MD simulation, the initial particle positions, orientations and velocities need to be assigned. This can be achieved either from a previous configuration file or by performing an initialization process. For the latter, the particles are usually distributed in the domain according to face-centred cubic (FCC) structure. If there is more than one type of particle in the domain, these are distributed randomly on the lattice points. The orientations of non-spherical particles are set by assigning random values to the Euler angles and, then, the quaternions for every particle are calculated from these random angles [105]. The initial translational

3.3 MD Tricks of the Trade

velocities are set according to the Maxwell-Boltzmann distribution [38]. This is performed based on the initial target temperature of the system. After assigning the velocities, any net linear momentum is removed from the system so as to ensure that a stationary system is simulated. For simplicity, it is assumed that the rotational velocities are zero at the beginning of each initiation simulation.

3.3.5 Cut-off radius and neighbour list

Most separation-dependent potentials tend to zero at relatively long separation and the computational costs related to the pairs at long distance are an overhead for the simulations. Therefore, provided it is not a true long-range interaction (e.g. Coulomb), it is reasonable to cut the long-range tail of the potential to have cost-efficient simulations. That is, in short range potentials such as LJ and GB, where particles have a separation which is greater than a particular radius, the cut-off radius (r_c), their interaction is assumed to be zero [38]. Normally, r_c is chosen as the separation at which the value of the potential is less than 1% of the maximum well-depth. To avoid a jump in the potential at the cut-off radius, the potential itself is shifted up, so that it tends to zero smoothly. Applying the cut-off radius concept can lead to a significant reduction in simulation time, depending on the size of the system.

In order to avoid performing a whole-domain search in the process of identifying the particle pairs that are closer than r_c , which involves detecting particles in an imaginary sphere with radius r_c centred on the current particle, a neighbour list method was developed and used in the current work. In this, a uniform grid of minimum size of r_c is mapped on the simulation box. At every time step, after moving the particles, the host cell for every particle is determined, and simultaneously, the name of each particle residing in a particular cell is added to the list of that cell. Then, in the force loop, this neighbour list is used to determine the particles interacting with the current one. To find all interacting sites closer than r_c to a particular particle, the host cell of that particle plus its neighbour cells (27 cells) are searched. At a constant density, the bigger the size of the system, the more computational

3.3 MD Tricks of the Trade

time can be saved by applying the neighbour list method. For orientation-dependent potentials such as GB, however, a variable cut-off radius concept may lead to even greater reduction in simulation time. Discussion of variable cut-off radius is left for the next section, where the details of GB potentials for anisotropic particles are presented.

3.3.6 Thermostat / Barostat

Conventional MD algorithms lead to a constant-NVE ensemble. However, most real-world systems such as chemical reactions or biological phenomena happen in constant temperature and constant pressure conditions. Several different methods have been proposed for adjusting temperature and pressure in the course of an MD simulation through applying a thermostat and barostat on the system [113–117]. Here, some of those which have been used in the current research are discussed.

Berendsen and coworkers [113] developed a simple thermostat and barostat. The thermostat, being quite straight forward, re-scales the translational and rotational velocities through a scaling factor calculated by:

$$\lambda = \left[1 + \alpha_T \left(\frac{T_0}{T} - 1 \right) \right]^{1/2} \quad (3.27)$$

Here T is the instantaneous temperature, calculated from equation (3.22), and T_0 is the target temperature. It should be noted that the Berendsen thermostat does not produce a canonical ensemble [38].

The isotropic version of the Berendsen barostat is applied through rescaling the cubic simulation box length and the particle positions by:

$$\mu = [1 + \alpha_P(P_0 - P)]^{1/3} \quad (3.28)$$

where P_0 is the target pressure and P is the instantaneous pressure, being the average of the diagonal elements of the pressure tensor given by equation (3.25). The parameters α_T and α_P are the relaxation parameters for the temperature and pressure, respectively and are set to $\alpha_T = 5 \times 10^{-3}$ and $\alpha_P = 10^{-4}$ in this work.

3.3 MD Tricks of the Trade

Another well-known thermostat, which considers an additional dynamical parameter, is known as the Nosé-Hoover thermostat [114]. The original Nosé-Hoover thermostat was developed for translational motion as follows:

$$\begin{aligned}
 \dot{\mathbf{r}}_i &= \frac{\mathbf{p}_i}{m_i} \\
 \dot{\mathbf{p}}_i &= \mathbf{F}_i - \zeta_t \mathbf{p}_i \\
 \dot{\zeta}_t &= \frac{1}{Q_t} \left[\sum_{i=1}^N m_i (\mathbf{v}_i \cdot \mathbf{v}_i) - N_t^f k_B T_0 \right]
 \end{aligned} \tag{3.29}$$

where \mathbf{p} is the linear momentum vector, ζ_t is the thermostat variable for translational motion and Q_t is the thermostat mass.

For rigid body motion, the rotational motion can be thermostated independently as suggested by Kamberaj *et al.* [118]. For this, the governing equations of rotational motion mentioned in section 3.2 are still valid, apart from those given by equation (3.14) which are modified as:

$$\begin{aligned}
 \dot{\omega}_\alpha^b &= \frac{\tau_\alpha^b}{\bar{I}_\alpha} + \frac{\bar{I}_\beta - \bar{I}_\gamma}{\bar{I}_\alpha} \omega_\beta^b \omega_\gamma^b - \zeta_r \omega_\alpha^b, \\
 (\alpha, \beta, \gamma) &= (x, y, z), (y, z, x) \text{ or } (z, x, y)
 \end{aligned} \tag{3.30}$$

The rotational motion thermostat variable, ζ_r , is given by:

$$\dot{\zeta}_r = \frac{1}{Q_r} \left[\sum_{i=1}^{N_{\text{non-sph}}} (\bar{\mathbf{I}}_i \boldsymbol{\omega}_i \cdot \boldsymbol{\omega}_i) - N_r^f k_B T_0 \right] \tag{3.31}$$

where Q_r is the rotational thermostat mass.

The translational and rotational Nosé-Hoover thermostats can be explicitly integrated in a velocity-Verlet scheme as described by Smith [112].

In order to achieve an isothermal-isobaric (constant-NPT) ensemble, a number of different algorithms have been developed. Maintaining a constant pressure in a system requires the size or shape of the simulation box to change. While isotropic barostats keep the cubic shape of the box, anisotropic ones usually change the simulation box lengths and/or angles independently to reach the target pressure. The key idea used in the formulation of the latter cases is that of using a tensorial set of equations instead of an algebraic one. The box shape is defined through a matrix,

3.3 MD Tricks of the Trade

\mathbf{h} , whose columns are the vectors of the simulation box sides. Even in an isotropic system, where the time-average of off-diagonal pressure tensor elements tends to zero, the instantaneous values fluctuate and cause the box shape to distort slightly. Dealing with distorted cells (e.g. applying periodic boundary conditions and the minimum image convention) is highly complex and needs significant computational efforts, so it seems that an “anisotropic orthogonal barostat” which changes the box lengths independently and keeps the angles orthogonal, is quite appropriate.

The MTK thermostat/barostat developed by Martyna *et al.* [116], has been presented as a route to achieving a more precise isothermal-isobaric ensemble. Having three different versions, isotropic, fully flexible shape and hybrid method, also makes the MTK algorithm useful for different applications. The original formulation of this model was for translational motion and only a few groups [118–120] have tried to extend it to rigid body motion in which the rotational degrees of freedom are also considered. Although the origins of fully anisotropic translational/rotational thermostat/barostat in the three mentioned works are the same, their formulations are slightly different. In the work of Kamberaj *et al.* [118], the rotational kinetic energy was included in the calculation of the pressure tensor and the barostat variable was also coupled to the rotational motion, while in the other two papers, the rotational degree of freedom was decoupled from the barostat. In the mentioned works, the barostat variable was thermostated based on the Nosé-Hoover chain algorithm [112].

Here, an anisotropic orthogonal thermostat/barostat based on the MTK algorithm has been developed for rigid body motion. This is the same as the one suggested by Ikeguchi [120], except that, a cell vector is used instead of a cell matrix and the barostat variable is thermostated according to the Nosé-Hoover algorithm. For the length of each side of the cuboid box, L_i , a barostat variable vector is introduced:

$$\begin{aligned}\mathbf{L} &= \begin{bmatrix} L_1 & L_2 & L_3 \end{bmatrix}^T \\ \boldsymbol{\eta} &= \begin{bmatrix} \eta_1 & \eta_2 & \eta_3 \end{bmatrix}^T\end{aligned}$$

3.3 MD Tricks of the Trade

where η_i is the barostat variable in each direction. The governing equations are then as follows:

$$\begin{aligned}
\dot{r}_{i\lambda} &= \frac{p_{i\lambda}}{m_i} + \eta_\lambda r_{i\lambda} \\
\dot{p}_{i\lambda} &= F_{i\lambda} - \frac{d_t}{3N_t^f}(\eta_1 + \eta_2 + \eta_3)p_{i\lambda} - \zeta_t p_{i\lambda} \\
\dot{\omega}_\alpha^b &= \frac{\tau_\alpha^b}{\bar{I}_\alpha} + \frac{\bar{I}_\beta - \bar{I}_\gamma}{\bar{I}_\alpha} \omega_\beta^b \omega_\gamma^b - \frac{d_r}{3N_r^f}(\eta_1 + \eta_2 + \eta_3)\omega_\alpha^b - \zeta_r \omega_\alpha^b, \\
&(\alpha, \beta, \gamma) = (1, 2, 3), (2, 3, 1) \text{ or } (3, 1, 2) \\
\dot{\zeta}_t &= \frac{1}{Q_t} \left[\sum_{i=1}^N m_i (\mathbf{v}_i \cdot \mathbf{v}_i) - (N_t^f + 1)k_B T_0 + \frac{1}{3}W(\eta_1^2 + \eta_2^2 + \eta_3^2) \right] \\
\dot{\zeta}_r &= \frac{1}{Q_r} \left[\sum_{i=1}^{N_{\text{non-sph}}} (\bar{\mathbf{I}}_i \boldsymbol{\omega}_i \cdot \boldsymbol{\omega}_i) - (N_r^f + 1)k_B T_0 + \frac{1}{3}W(\eta_1^2 + \eta_2^2 + \eta_3^2) \right] \\
\dot{\eta}_\lambda &= \frac{1}{W} \left[d_t V (P_{\lambda\lambda} - P_0) + \frac{d_t}{N_t^f} \sum_{i=1}^N m_i (\mathbf{v}_i \cdot \mathbf{v}_i) \right] - \zeta_t \eta_\lambda \\
\dot{L}_\lambda &= \eta_\lambda L_\lambda
\end{aligned} \tag{3.32}$$

where W is the barostat mass, $P_{\lambda\lambda}$ is the diagonal element of the pressure tensor and λ is 1, 2 or 3.

The anisotropic thermostat/barostat, given by equations (3.32), can be simply converted to an isotropic one if, in the equation for the time derivative of barostat variable, $\dot{\eta}_\lambda$, the diagonal elements of the pressure tensor, $P_{\lambda\lambda}$, are replaced by their average (the instantaneous pressure). In this case, the barostat variables for different direction become identical and the side lengths of the simulation box remain equal. The presented MTK thermostat/barostat for rigid body motion is slightly different from those in references [118–120], such that this conversion between anisotropic and isotropic barostat can be easily performed. Discretisation of the MTK algorithm for translational motion in a velocity-Verlet scheme has been discussed by Smith [112], and the same procedure is also applied for the rotational motion in the current work. Here, the Nosé-Hoover thermostat and MTK thermostat/barostat masses were set to $Q_t = Q_r = 5$ and $W = 50$, respectively.

3.3 MD Tricks of the Trade

3.3.7 Post-processing

As the focus of this work is the investigation of self-assembly, it is crucial that we can identify the formed objects in the simulation. Therefore, in the post-processing part of the simulation, object identification needs to be performed. “Thread” and “cluster” are two terms that are used substantially in this text. A strand of discs aligned nearly on top of each other is called a thread. That is, the short axes of particles in a thread are approximately parallel. For some assembled objects, such as a double-helix (see Chapter 7), the discs in a single thread may even have an angle with each other and, in that case, the thread terminology is used to describe a series of particles whose centres form a continuous curve. Two or more threads can laterally join each other and make a cluster. This means that for identification of clusters or other complex objects, first, the threads need to be identified. Figure 3.1 illustrates a cluster of 7 threads which are coloured distinctly. The stacking of particles in each thread and the lateral interdigitation of threads, which form the cluster, can be seen in this figure.

Here, the thread detection is done by simply measuring the pair separation of particles [38]. The pairs that are closer than a certain distance can then be ascribed to a single thread. The anisotropy in the shape of the particles used here eases the thread identification task. By choosing a threshold distance which is intermediate between the thickness and diameter of the discs, we can be sure that the particles in the identified threads are on top of one another, rather than side to side (see Figure 3.1). The threshold distance can be chosen by investigation of radial distribution data. This distance should be selected such that it lies between the first and second distinct peaks of the $g(r)$ graph. The results of this work show that a threshold distance of about 1.5 disc thickness is a good choice for thread identification. Here, it is assumed that the shortest thread consists of at least 2 particles, except where otherwise mentioned.

For cluster identification, another separation threshold needs to be defined. As threads are the building-blocks of a cluster, they need to be searched to identify the laterally close ones which form a cluster. This separation distance should be of the

3.3 MD Tricks of the Trade

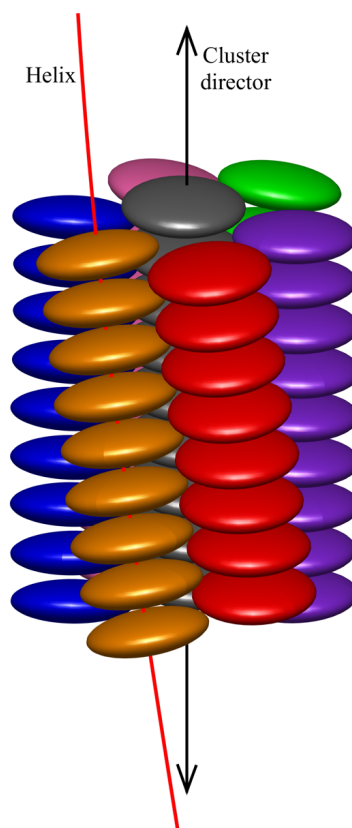


Figure 3.1: A cluster of 7 threads with one straight central thread and 6 helical surrounding threads. Each thread is coloured distinctly for clarity. The director vector of the cluster is shown by an arrow. A helix fitted on one of the threads through the described algorithm is also illustrated. Here, the pitch length is approximately 38 disc diameters.

order of a disc diameter. If a certain number of particles of each thread are found to be at a distance less than the set threshold, those threads are judged to form a cluster. This minimum number of particles is usually set as the minimum number of particles in each thread.

For successful cluster identification, attention to the relative orientation of particles is much more important than is the case in thread detection. Here, this is performed by considering two predefined angles. One is a measure of maximum angle between the thread axes in the cluster. For particles closer than the cluster distance threshold, if the angle between their short axes is less than this predefined angle, then their threads can be members of a single cluster. In Figure 3.1, for example, the short axes of particles in neighbouring threads are nearly parallel (the angle is close to zero). Similarly, in most of the structures studied in this work, the threads are nearly

3.3 MD Tricks of the Trade

parallel to each other, and defining such an angle prevents selection of the threads which are not really in the cluster. The other angle used here is the minimum angle between the short axes of particles in adjacent threads and their separation vector. For perfectly parallel adjacent threads, this angle is about 90 degrees. Having this constraint causes that two threads which are in-line with each other, rather than adjacent, do not form a cluster.

Cluster identification for spherical particles is performed similarly to the thread identification in discotic particles, and just involves defining a maximum pair distance for spheres. This should be slightly larger than their diameter.

Having an identified cluster, we can go on to extract many structural data such as the number of particles, order parameter, moments of inertia, etc. only for the self-assembled object. Cluster identification can also simplify visualization tasks performed in the post-processing part of simulations, e.g., video production.

The principal moments of inertia of an object can yield useful information about its structural details. For a cluster of N particles with unit mass, the eigenvalues of the symmetric inertia tensor I give the principal moments of inertia of the object. The elements of the inertia tensor are defined as:

$$\begin{aligned}
 I_{xx} &= \sum_{i=1}^N (y_i^2 + z_i^2) \\
 I_{yy} &= \sum_{i=1}^N (x_i^2 + z_i^2) \\
 I_{zz} &= \sum_{i=1}^N (x_i^2 + y_i^2) \\
 I_{xy} &= -\sum_{i=1}^N x_i y_i \\
 I_{xz} &= -\sum_{i=1}^N x_i z_i \\
 I_{yz} &= -\sum_{i=1}^N y_i z_i
 \end{aligned} \tag{3.33}$$

where x_i , y_i and z_i are the components of the relative position of particle i with respect to the centre of mass of the object. By normalizing the principal moments

3.3 MD Tricks of the Trade

of inertia with the trace of the above tensor, one may have a better understanding about the character of a growing object.

Pitch measurement

In the self-assembly of chiral structures, one important observable is the object pitch length, which is usually an emergent length scale. Here, we have employed two approaches for measuring pitch length, based on helix fitting and helicoid fitting, respectively.

In the first method, a common axis is assumed, normally the director vector of all particle orientations, which passes through the centre of mass of the cluster. Helices about this axis are then fitted to individual thread loci defined by particle coordinations. The fit parameters for each helix are calculated using an iterative scheme suggested by Eberly [121]. The average value of the measured pitch length of all threads is then reported as the overall pitch length for the investigated object. Figure 3.1 illustrates the director vector of the cluster passing through its centre of mass (the common axis of all helices) and also a helix fitted on one of the threads.

In the second method, which has only been used for the twisted ribbons with layers of spheres (Chapter 5), it is supposed that the twisted sphere layer fits onto a helicoidal surface. The helicoid is a ruled surface, meaning that it can be constructed with straight lines. Using this property, we developed a method for measuring the pitch lengths of the sphere layers formed in the twisted ribbon structures found in this research. The surface is first sliced into several strips with small width (the same as the threshold distance in clustering of spheres) perpendicular to the axis, along which the pitch length is to be measured. A line is then fitted on the centres of the spheres located on each strip. Therefore, the helicoidal sphere surface is reduced into a series of lines perpendicular to the considered axis. The pitch length for the rotation of every pair of successive lines then is measured, based on their angular separation. Finally, these pitch lengths are averaged to give a single value for the pitch length of the structure. This can also be used to measure the pitch lengths along two orthogonal axes, something that cannot be achieved by the first method.

3.4 Inter-particle Potentials

Curvature measurement

The curvature of a surface can be considered as a characteristic feature of that surface. Considering all possible tangent vectors to a surface at a point, the maximum and minimum normal curvatures associated to these tangent vectors are termed the principal curvatures of the surface at that point. The Gaussian and Mean curvatures are, respectively, the product and average of these principal curvatures. In this work, curvature measurement has been performed for the sphere layers of some self-assembled structures. For this, a triangulated surface has been fitted on the sphere layer using CGAL library [122]. Given the positions of the spheres, the number of data points is increased by a particular factor through applying an upsampling procedure and then iterating several passes of smoothing (see the “point set processing” part of the CGAL library). Finally, a surface triangulation is performed for the new data points to fit an estimated surface on the sphere layer (see the “advancing front surface reconstruction” part of the CGAL library). Mean curvature measurements can then be performed for this triangulated surface, using the methods suggested by Meyer *et al.* [123]. The data from the edge triangles are excluded from this in order to avoid spurious contributions to these calculations.

3.4 Inter-particle Potentials

In this section, the soft potentials used in this thesis to represent the inter-particle interactions are presented. If the potential field governing the interaction of particles is identified, the force and torque on each particle can be calculated by equations (3.4 - 3.6). In the following subsections, the different potentials used to represent different types of particle are discussed.

3.4.1 Spherical particle interaction

In the present work, one of the species is represented by spherical particles. These spherical molecules interact with each other via the simple Lennard-Jones (LJ) soft

3.4 Inter-particle Potentials

potential [38]:

$$U^{\text{LJ}} = 4\epsilon_0 \left[\left(\frac{\sigma_0}{r} \right)^{12} - \left(\frac{\sigma_0}{r} \right)^6 \right] \quad (3.34)$$

where ϵ_0 is the potential well-depth, σ_0 is the separation at repulsion, and r is the interparticle distance ($r = |\mathbf{r}_{ij}| = |\mathbf{r}_i - \mathbf{r}_j|$). The term $-\left(\frac{1}{r}\right)^6$ is the long range attractive part of potential and $\left(\frac{1}{r}\right)^{12}$ is the steeply rising repulsive part.

3.4.2 Ellipsoidal particle interaction

The results of Prybytak's work [5] showed that the Gay-Berne (GB) potential [59] can be used to coarse-grain small-molecule building-blocks. This anisotropic potential incorporates the orientation of particles. The shape of the particles in the Gay-Berne potential is an approximation to an ellipsoid of revolution (prolate or oblate). These ellipsoidal particles interact with each other through a 12-6 potential similar to the LJ one, but the effects of orientation are also included. The potential is written as:

$$U^{\text{GB}} = 4\epsilon(\hat{\mathbf{u}}_i, \hat{\mathbf{u}}_j, \mathbf{r}_{ij}) \left[\left(\frac{\sigma_0}{r - \sigma(\hat{\mathbf{u}}_i, \hat{\mathbf{u}}_j, \mathbf{r}_{ij}) + \sigma_0} \right)^{12} - \left(\frac{\sigma_0}{r - \sigma(\hat{\mathbf{u}}_i, \hat{\mathbf{u}}_j, \mathbf{r}_{ij}) + \sigma_0} \right)^6 \right] \quad (3.35)$$

where ϵ and σ are the energy and shape parameter functions, respectively. The unit vectors $\hat{\mathbf{u}}_i$ and $\hat{\mathbf{u}}_j$, are the orientation unit vectors of particles i and j , respectively. In the current work, the particle orientation vector is defined as its third principal axis. Therefore, the elements of this vector are the same as the third row of the rotation matrix, \mathbf{A} , given by equation (3.11).

Cleaver *et al.* [124] extended the original Gay-Berne potential by generalising it to non-identical particles. This extended potential reduces to the standard GB and LJ potentials in the appropriate limits. The generalized Gay-Berne potential is the same as equation (3.35), but with the shape parameter expressed as:

$$\sigma(\hat{\mathbf{u}}_i, \hat{\mathbf{u}}_j, \mathbf{r}_{ij}) = \sigma_0 \left\{ 1 - \frac{\chi}{2} \left[\frac{\left(\frac{\alpha}{r} A + \frac{1}{\alpha r} B \right)^2}{1 + \chi C} + \frac{\left(\frac{\alpha}{r} A - \frac{1}{\alpha r} B \right)^2}{1 - \chi C} \right] \right\}^{(-1/2)} \quad (3.36)$$

3.4 Inter-particle Potentials

where $A = \hat{\mathbf{u}}_i \cdot \mathbf{r}_{ij}$, $B = \hat{\mathbf{u}}_j \cdot \mathbf{r}_{ij}$ and $C = \hat{\mathbf{u}}_i \cdot \hat{\mathbf{u}}_j$. It should be noted that, in other references such as [5, 59, 124], parameters A and B were defined by unit separation vector, $\hat{\mathbf{r}}$, and therefore the form of the above equation seems to be slightly different from those works. However, equation (3.36) was just rearranged in a way that makes the derivation of forces and torques to be more straight forward. The parameters χ and α are measures of the anisotropy in particle shape [124]:

$$\chi = \pm \left[\frac{(l_i^2 - d_i^2)(l_j^2 - d_j^2)}{(l_j^2 + d_i^2)(l_i^2 + d_j^2)} \right]^{1/2} \quad (3.37)$$

$$\alpha^2 = \left[\frac{(l_i^2 - d_i^2)(l_j^2 + d_i^2)}{(l_j^2 - d_j^2)(l_i^2 + d_j^2)} \right]^{1/2} \quad (3.38)$$

where l is the length of particle (in the direction of the axis of revolution) and d is the diameter of the particle. In equation (3.37), the negative sign is only used when the interacting particles are discs and therefore their aspect ratio is less than 1 (this was dropped in reference [124]). For identical interacting particles, the original Gay-Berne potential [59] is recovered, and the two parameters reduce to $\alpha = 1$ and:

$$\chi = \frac{\kappa^2 - 1}{\kappa^2 + 1}$$

where $\kappa = l/d$ is the aspect ratio or shape parameter of the particle. The parameter σ_0 for identical particles is the same as their diameter and for non-identical ones, it can be calculated from [125]:

$$\sigma_0 = \sqrt{\frac{d_i^2 + d_j^2}{2}} \quad (3.39)$$

The generalized Gay-Berne energy parameter function is given by:

$$\epsilon(\hat{\mathbf{u}}_i, \hat{\mathbf{u}}_j, \mathbf{r}_{ij}) = \epsilon_0 [\epsilon_1(\hat{\mathbf{u}}_i, \hat{\mathbf{u}}_j)]^\nu [\epsilon_2(\hat{\mathbf{u}}_i, \hat{\mathbf{u}}_j, \mathbf{r}_{ij})]^\mu \quad (3.40)$$

where ϵ_0 , ν and μ are constants and:

$$\begin{aligned} \epsilon_1(\hat{\mathbf{u}}_i, \hat{\mathbf{u}}_j) &= [1 - (C\chi)^2]^{(-1/2)} \\ \epsilon_2(\hat{\mathbf{u}}_i, \hat{\mathbf{u}}_j, \mathbf{r}_{ij}) &= 1 - \frac{\chi'}{2} \left[\frac{(\frac{\alpha'}{r}A + \frac{1}{\alpha'r}B)^2}{1 + \chi'C} + \frac{(\frac{\alpha'}{r}A - \frac{1}{\alpha'r}B)^2}{1 - \chi'C} \right] \end{aligned} \quad (3.41)$$

3.4 Inter-particle Potentials

Deriving appropriate formulas for χ' and α' is rather less straight forward than it is for those in shape parameter. Cleaver *et al.* [124] suggested that they can be obtained by a curve fitting on the full potential. However, for identical interacting particles, α' goes to unity and:

$$\chi' = \frac{\kappa'^{1/\mu} - 1}{\kappa'^{1/\mu} + 1}$$

where $\kappa' = \epsilon_{\perp}/\epsilon_{\parallel}$. The potential well depths, ϵ_{\perp} and ϵ_{\parallel} , both correspond to configurations in which the orientation vectors of the interacting particles are parallel with each other. The subscripts indicate the relative orientation of particle directors with respect to the separation vector. For ϵ_{\perp} the particle director vector is perpendicular to the separation vector and for ϵ_{\parallel} they are parallel. In fact, κ' is a measure showing the anisotropy in the strength of the potential for different configurations.

The Gay-Berne potential for identical particles can be identified by 4 parameters; κ , κ' , μ and ν . Gay and Berne [59] used the parametrization of $\text{GB}(\kappa, \kappa', \mu, \nu) = \text{GB}(3, 5, 1, 2)$ for a linear array of 4 sites. Luckhurst *et al.* [126] found that in a system of rod shaped molecules interacting through $\text{GB}(3, 5, 2, 1)$, more liquid crystalline mesophases can be achieved. Discotic particles were also studied using $\text{GB}(0.345, 0.2, 1, 2)$ in some previous works [127, 128, 32]. However, Bates and Luckhurst [128] used a slightly different GB potential from equation (3.35) for simulation of discotic particles. This potential is discussed in the following subsection.

Discotic GB potential

The GB potential discussed above can be applied for particles with oblate ellipsoidal Gaussian (discotic) shape, if the appropriate GB parameters, κ , κ' , μ and ν are selected. For a discotic particle, $\kappa < 1$, κ' determines the anisotropy in the attraction between particles in different relative orientations. For $\kappa' > 1$, the edge-edge orientation is more favourable for two interacting molecules, while for $\kappa' < 1$ the particles prefer the face-face configuration. Therefore, the κ' parameter for discs can be defined as $\kappa'_{dd} = \epsilon_{ee}/\epsilon_{ff}$, where the subscript *dd* indicates that this κ' is for the disc-disc interaction, and *ee* and *ff* denote edge-edge and face-face, respectively.

3.4 Inter-particle Potentials

However, Bates and Luckhurst [128] found that equation (3.35) shows unrealistic behaviour at small values of the interparticle separation when it is applied to discs. For example, in the edge-edge configuration, the GB potential given by equation (3.35) tends to infinity only when the molecules completely overlap. For other relative orientations, the potential only tends to infinity at negative separation which is unrealistic. They therefore suggested that if the potential is shifted and scaled by the thickness of discs $\sigma_f = l$, this behaviour can be corrected. Therefore, the discotic version of the GB potential is given by:

$$U^{\text{dd}} = 4\epsilon(\hat{\mathbf{u}}_i, \hat{\mathbf{u}}_j, \mathbf{r}_{ij}) \left[\left(\frac{\sigma_f}{r - \sigma(\hat{\mathbf{u}}_i, \hat{\mathbf{u}}_j, \mathbf{r}_{ij}) + \sigma_f} \right)^{12} - \left(\frac{\sigma_f}{r - \sigma(\hat{\mathbf{u}}_i, \hat{\mathbf{u}}_j, \mathbf{r}_{ij}) + \sigma_f} \right)^6 \right] \quad (3.42)$$

Figure 3.2 shows the potential energy based on equation (3.42) for two different configurations of discotic particles interacting with parameters of GB(0.345, 0.15, 1, 2). As seen, the potential depth in the edge-edge orientation is 0.15 of that in the face-face configuration.

Model verification

In order to verify the validity of results obtained using the developed in-house code for CG MD simulation of GB particles, a comparison with the work of Bates and Luckhurst [128] for pure discotic system was performed. In the reference work, Monte Carlo simulations of GB discs were used to identify the transitions between isotropic, nematic and columnar mesophases at different pressures. A Gay-Berne coarse grained model for triphenylene, being a typical example of a discotic molecule, was developed by Emerson *et al.* [127] and the GB parameters for that molecule were suggested to be GB($\kappa, \kappa', \mu, \nu$) = GB(0.345, 0.2, 1, 2). These parameters for triphenylene were also used by Bates and Luckhurst [128]. Figure 3.3 shows the all-atom representation of triphenylene and also its coarse-grained disc-shape model.

Here, the behaviour of the system was investigated by cooling of a box of 500 discotic particles at three different reduced pressures of 25, 50 and 75. The reduced

3.4 Inter-particle Potentials

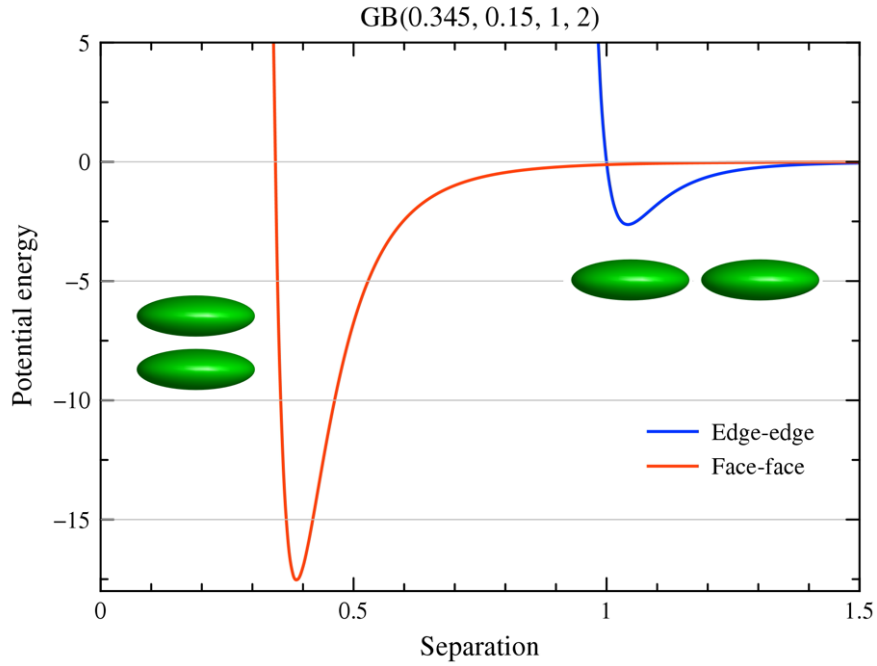


Figure 3.2: Gay-Berne potential for interaction of two discotic particles with parameters of GB(0.345, 0.15, 1, 2) at two different relative orientations. The separation is reduced by the diameter of particles.

temperature decrement was 0.1. A high temperature at which the system was expected to be isotropic, was selected and an NVE simulation performed. The last configuration of this NVE run was then used in the NPT simulation with Brendsen thermostat/barostat as the initial configuration of the system. An equilibration run of 50,000 steps, with time step $\Delta t = 5 \times 10^{-4}$, was performed and followed by a 50,000 Δt production run. For lower temperatures, at which the system was in the nematic or columnar mesophases, the number of equilibration steps was increased by a factor of between 2 and 9. The reported observables were averaged from the results of the production runs obtained at each temperature.

Figure 3.4 shows the orientational order parameter data obtained at each of the investigated pressures. The results of Prybytak [5] and those of Bates and Luckhurst [128] (with 2000 particles) for $P=25$ are also presented. As can be seen, the data from the present work are in good agreement with those of previous works. The jumps in the orientational order parameter are indicative of transitions between the mesophases of a discotic system. Starting from an isotropic configuration at high temperatures, each system goes into a nematic phase in which there is clear

3.4 Inter-particle Potentials

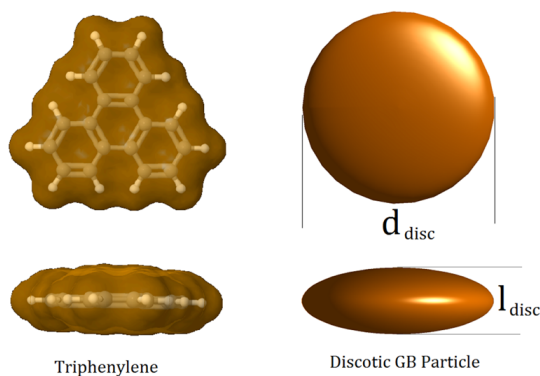


Figure 3.3: Two views of the triphenylene molecule including the electron cloud (left). The symmetric discotic particle which represents a CG model for the $\text{C}_{18}\text{H}_{12}$ molecule (right).

orientational order in the system. On cooling each system further, the columnar phase, in which the particles stack into columns and pack hexagonally, appears. For the highest investigated pressure, $P=75$, at the low temperatures, the orientational order parameter goes to 1, suggestive of a crystalline phase. Investigations showed that the RMS displacement of the particles in the temperatures below $T=3.3$ did not grow in time, again suggesting that the system was in a crystalline phase. This transition can be also identified with a jump in P_2 at a temperature of 3.2 (blue line in the figure). Because this behaviour was not reported in the reference works, there is a possibility that this observation was due the use of the simple isotropic Berendsen barostat. Therefore, the simulations were repeated with the anisotropic MTK thermostat/barostat starting from a nematic configuration. As seen in Figure 3.4 for $P=75$, when the MTK algorithm was applied the crystalline phase was not observed any more. Therefore, it seems that the results achieved by applying the Berendsen thermostat/barostat were not reliable in a highly ordered system.

Two configurations of the system for $P=75$ are illustrated in Figure 3.5 from the cooling sequence achieved using the anisotropic MTK barostat in which the lengths of the box could vary independently. In the columnar phase, the particles were mostly oriented in a single direction which was, in fact, the director of the system.

Figure 3.6 compares the values of simulation box average volume per particle for $P=25$ achieved in the current work and that of Bates and Luckhurst [128]. As seen, the agreement is quite good. The transition points between different mesophases can

3.4 Inter-particle Potentials

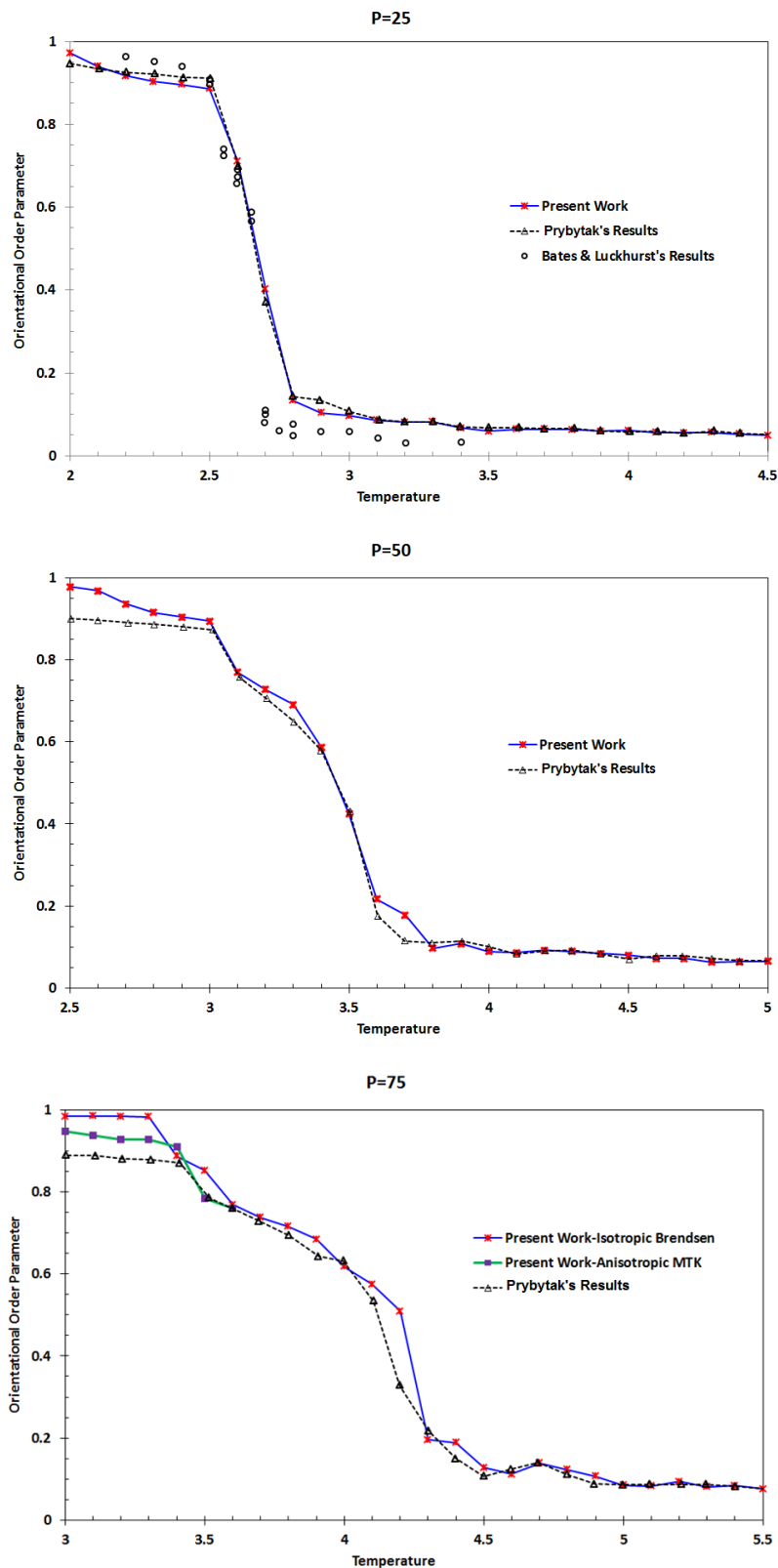


Figure 3.4: The orientational order parameter of pure GB disc systems at $P=25$ (top), $P=50$ (middle) and $P=75$ (bottom). The results of Prybytak [5] and Bates and Luckhurst [128] (if applicable) are also presented for comparison.

3.4 Inter-particle Potentials

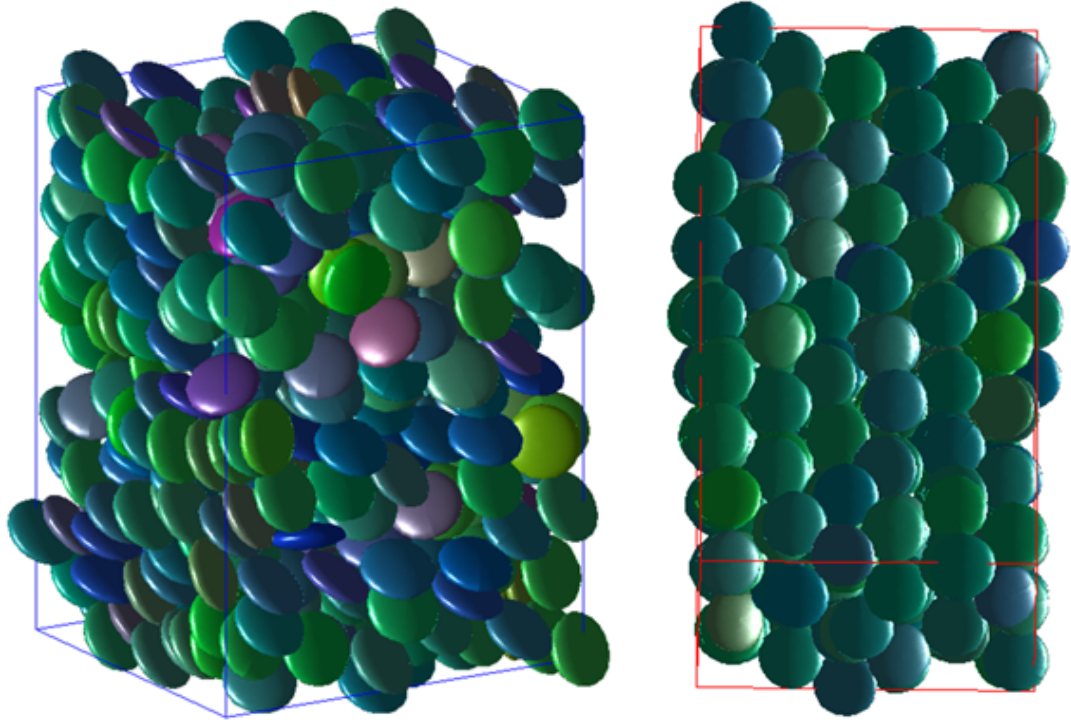


Figure 3.5: Configurations of the system for $P=75$ simulated by anisotropic MTK thermostat/barostat. Left: Nematic phase at $T=3.5$ in which $P_2 = 0.783$, and, Right: columnar phase at $T=3.2$ in which $P_2 = 0.928$. For the right figure, the box is shown roughly along the director vector. Particles are coloured based on their orientation. That is, the unit director vector of each particle, \hat{u} , is mapped to the RGB color-space to give a single color based on particle orientation.

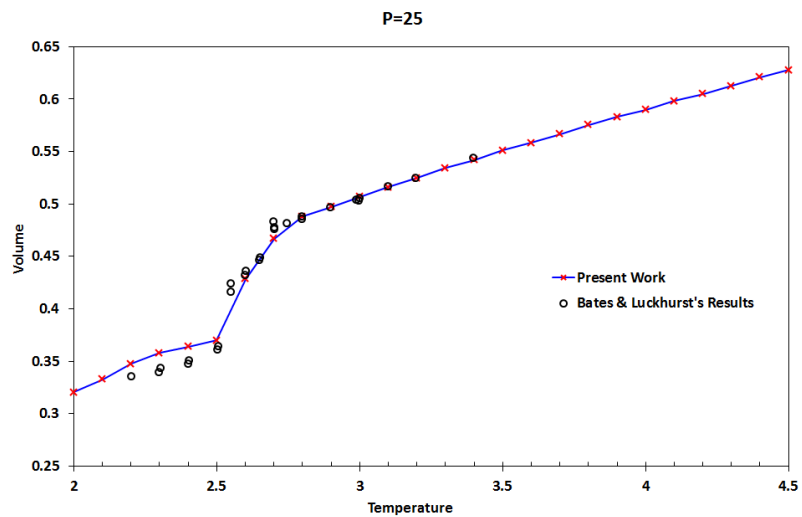


Figure 3.6: The temperature variation of the average volume per particle of the system at $P=25$.

3.4 Inter-particle Potentials

be determined through changes of the slope in this V-T diagram. As expected, the slope of the graph, $\left(\frac{\partial V}{\partial T}\right)_P$, is similar in both isotropic and columnar phases, while in the nematic phase, the slope is significantly larger than that of the two other phases. The steep jump in P_2 in the nematic phase (see Figure 3.4), causes the particles to pack more efficiently, and this is the reason for the difference of slopes in the V-T diagram.

3.4.3 Disc-sphere interaction

The generalized Gay-Berne potential introduced in subsection 3.4.2 can be easily applied for the interaction of discotic (solute) and spherical (solvent) particles as suggested in reference [124]. The governing GB potential for disc-sphere interaction has the same form as that given in equation (3.42), although it should be noted that the shape and energy parameter functions, σ and ϵ are not dependent on the orientation of the spherical particle ($\hat{\mathbf{u}}_i$) any more [124]:

$$\sigma^{ds}(\hat{\mathbf{u}}_j, \mathbf{r}_{ij}) = \sigma_0^{ds} \left[1 - \chi \alpha^{-2} (B^2/r^2)\right]^{(-1/2)} \quad (3.43)$$

$$\epsilon^{ds}(\hat{\mathbf{u}}_j, \mathbf{r}_{ij}) = \epsilon_0^{ds} \left[1 - \chi' \alpha'^{-2} (B^2/r^2)\right]^\mu \quad (3.44)$$

where σ_0^{ds} is calculated by equation (3.39), ϵ_0^{ds} is the potential depth for edge-sphere orientation and:

$$\chi \alpha^{-2} = \frac{l_j^2 - d_j^2}{l_j^2 + d^2} \quad (3.45)$$

$$\chi' \alpha'^{-2} = 1 - \left[\frac{\epsilon_{fs}}{\epsilon_{es}}\right]^{(1/\mu)} \quad (3.46)$$

here, d is the diameter of spherical particle, ϵ_{fs} and ϵ_{es} are the potential depth for face-sphere and edge-sphere orientations, respectively.

Prybytak [5] investigated a system of discotic and spherical particles in order to observe the self assembly of columnar stacks of discs. It was found that using the GB potential given by equation (3.42) led to formation of threads of discs in the system but, due to the high attraction force between spheres and edge of the discs, the spherical particles prevented threads from joining laterally and forming a fibre.

3.4 Inter-particle Potentials

To reduce this attraction, the repulsion term, $(\dots)^{12}$, was scaled up by a constant, $R > 1$. This scaling also causes the zero repulsion separation distance to be shifted, however. As an alternative, in the current work, the disc-sphere GB potential is modified by another constant, $\beta \leq 1$, which scales the potential without shifting the location of minimum depth and zero repulsion separations. The GB potential for disc-sphere interaction is then given by:

$$U^{ds} = 4\beta\epsilon^{ds}(\hat{\mathbf{u}}_j, \mathbf{r}_{ij}) \left[\left(\frac{\sigma_f}{r - \sigma^{ds}(\hat{\mathbf{u}}_j, \mathbf{r}_{ij}) + \sigma_f} \right)^{12} - \left(\frac{\sigma_f}{r - \sigma^{ds}(\hat{\mathbf{u}}_j, \mathbf{r}_{ij}) + \sigma_f} \right)^6 \right] \quad (3.47)$$

Figure 3.7 compares the original disc-sphere GB potential (without modification) and the modified one given by (3.47), for edge-sphere and face-sphere orientations.

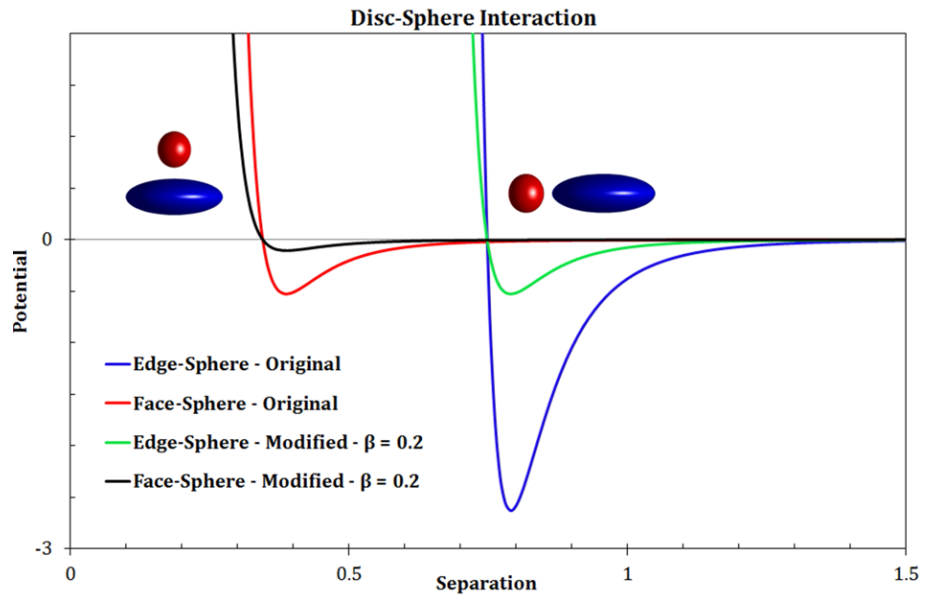


Figure 3.7: A comparison between original GB potential for disc-sphere interaction and the modified one by $\beta = 0.2$. Here $\kappa = 0.345$ and the diameter of sphere is the same as the thickness of the disc. The other parameters are: $\epsilon_0^{ds} = 2.63$, $\sigma_0^{ds} = 0.748$, $\mu = 1$ and $\epsilon_{fs}/\epsilon_{es} = 0.2$. The separation is reduced by the diameter of the disc.

Variable cut-off radius

In section 3.3, the use of a constant cut-off radius for reducing the computational costs of simulation was discussed. Here, a variable version of cut-off distance applicable to

3.4 Inter-particle Potentials

orientation-dependent disc-disc and disc-sphere GB potentials is introduced. As can be seen in Figures 3.2 and 3.7, the potentials for different relative orientations tend to zero at different separation lengths. This means that using a spherical cut-off can lead to calculation of some very weak interactions, for which r_{ij} is substantially larger than the zero repulsion separation. For GB-based interactions, the location at which the potential drops below a certain value for different orientations has a constant distance from the location of zero repulsion distance at that relative orientation. The zero repulsion separation lengths, σ , for the disc-disc and disc-sphere interactions are given by equations (3.36) and (3.43), respectively. Therefore, a variable cut-off radius for each relative orientation can be calculated by:

$$r_c^{var} = \sigma + \sigma_{cut} \quad (3.48)$$

Studying the GB potential curves in more detail reveals that, if the longest characteristic length of the particle is used for unit reduction, then the choice of $\sigma_{cut} \approx 0.6$ results in the potential at $r = r_c^{var}$ being only 1% of the potential well-depth at that orientation. Using this variable cut-off radius instead of constant r_c was found to deliver a time saving of at least 10%.

3.4.4 Amphiphilic chromonics

The presented disc-disc and disc-sphere GB potentials are cylindrically symmetric with respect to the axis of revolution of the disc. That is, there is no preference around the rim of each disc that affects its interactions with neighbour particles. Real-world systems, however, may have different characteristics and, therefore, a certain part of the rim of building-blocks may be more attracted to either the other discs or solvent molecules, due to, e.g., the presence of side groups as polar sites. To model this behaviour, previous studies [5, 129] showed that, with the GB foundation for the interaction of particles still in place, the symmetry can be broken and more complex amphiphilic character can be introduced. Here, this symmetry breaking idea is extended and also some new approaches are introduced toward modelling what we term “amphiphilic chromonics”.

3.4 Inter-particle Potentials

Chromonics are relatively flat molecules, usually with carbon ring core, which tend to stack and form linear aggregates. The face-face interaction of aromatic rings is believed to be the driving factor in this stack-like aggregation which appears in nearly all chromonic phases [130]. Conversely, the term “amphiphilic” is mostly used to describe rod-shaped molecules with solvophilic head groups and solvophobic tails. More generally, however, it deals with molecules with these two regions, whatever their shapes. Therefore, we use amphiphilic chromonics to describe a class of flat molecules in which the symmetry around the normal axis to the plane of the molecule is broken and, therefore, different regions around the rim have different interaction behaviour with other molecules (particularly any solvent). This amphiphilic behaviour can be viewed as mimicking the influence of different functional groups at the peripheries [131–133].

Here, the symmetry of the GB potential around the rim is broken so as to give a coarse-grained model of amphiphilic chromonics. This can, in particular, be done for both disc-sphere and disc-disc interactions. Two new GB-based potentials were developed for breaking the symmetry of disc-disc interaction and are presented in Appendix C. However, these did not undergo systematic study in this thesis work, and their further investigation is left for future research. In the following sub-section, therefore, the symmetry breaking for disc-sphere interaction is discussed by introducing one or more hot-spot regions around the rim. This model is used to generate the results in chapters 5-7 of this thesis.

Disc-sphere symmetry breaking

Based on the ideas presented in reference [129], Prybytak [5] suggested a modification to the energy parameter of disc-sphere interaction through a “Tanh” function. Extending the Tanh potential model discussed by Prybytak, one or more regions of the rim of the discs may act as a solvophilic region (or hot-spot) for spherical particles. In order to achieve such a behaviour, the disc-sphere Gay-Berne potential

3.4 Inter-particle Potentials

given by equation (3.47) takes the form:

$$U^{\text{ds}} = 4\beta\epsilon^{\text{ds}}(\hat{\mathbf{u}}_j, \mathbf{r}_{ij}) \left[\sum_{k=1}^{n^{\text{hs}}} \epsilon_k^{\tanh}(\hat{\mathbf{u}}_k^{\text{hs}}, \mathbf{r}_{ij}) \right] \left[\left(\frac{\sigma_f}{r - \sigma^{\text{ds}}(\hat{\mathbf{u}}_j, \mathbf{r}_{ij}) + \sigma_f} \right)^{12} - \left(\frac{\sigma_f}{r - \sigma^{\text{ds}}(\hat{\mathbf{u}}_j, \mathbf{r}_{ij}) + \sigma_f} \right)^6 \right] \quad (3.49)$$

where the superscript hs denotes the hot-spot and n^{hs} indicates the number of hot-spot regions on the rim of the disc. The energy parameter for each hot-spot is given by:

$$\epsilon_k^{\tanh}(\hat{\mathbf{u}}_k^{\text{hs}}, \mathbf{r}_{ij}) = a_k + b_k \tanh \left[\frac{(D_k/r) - s_k}{l_k} \right] \quad (3.50)$$

here, $\hat{\mathbf{u}}^{\text{hs}}$ is a unit vector pointing to the core of each hot spot region from the centre of the disc, $a = (\epsilon_{\text{max}} + \epsilon_{\text{min}})/2$, $b = (\epsilon_{\text{max}} - \epsilon_{\text{min}})/2$, $D = (\hat{\mathbf{u}}^{\text{hs}} \cdot \mathbf{r}_{ij})$, $s = 1 - 0.02H$ and, finally, H and l control the shape of the resultant energy parameter function. ϵ_{max} and ϵ_{min} are the maximum and minimum values for the Tanh energy parameter given by equation (3.50). Thus, for example, for single hot-spot potential ($n^{\text{hs}} = 1$), in the hot-spot region, the disc-sphere potential given by equation (3.47) is multiplied by ϵ_{max} and outside of this region, it is multiplied by ϵ_{min} . The parameter H sets the extent of the solvophilic region around the rim and is roughly the percentage of the rim of the disc which is attracted to the spheres. The parameter l controls the shape of the crossover between the solvophilic and solvophobic parts. The smaller the value of l , the sharper the crossover. In this work, the first hot-spot region is always located in the direction of the first principal axis of the disc, which is expressed by the first row of the rotation matrix.

Figures 3.8 and 3.9 show contour plots of the Tanh potential for different values of H . The disc-sphere potential with no Tanh energy parameter and the plots for two opposite hot-spots are also presented. Comparing the values of the original disc-sphere GB potential in Figures 3.8A or B and the other cases in which the Tanh potential is applied, it is seen that the maximum absolute value of potential is multiplied by ϵ_{max} .

3.4 Inter-particle Potentials

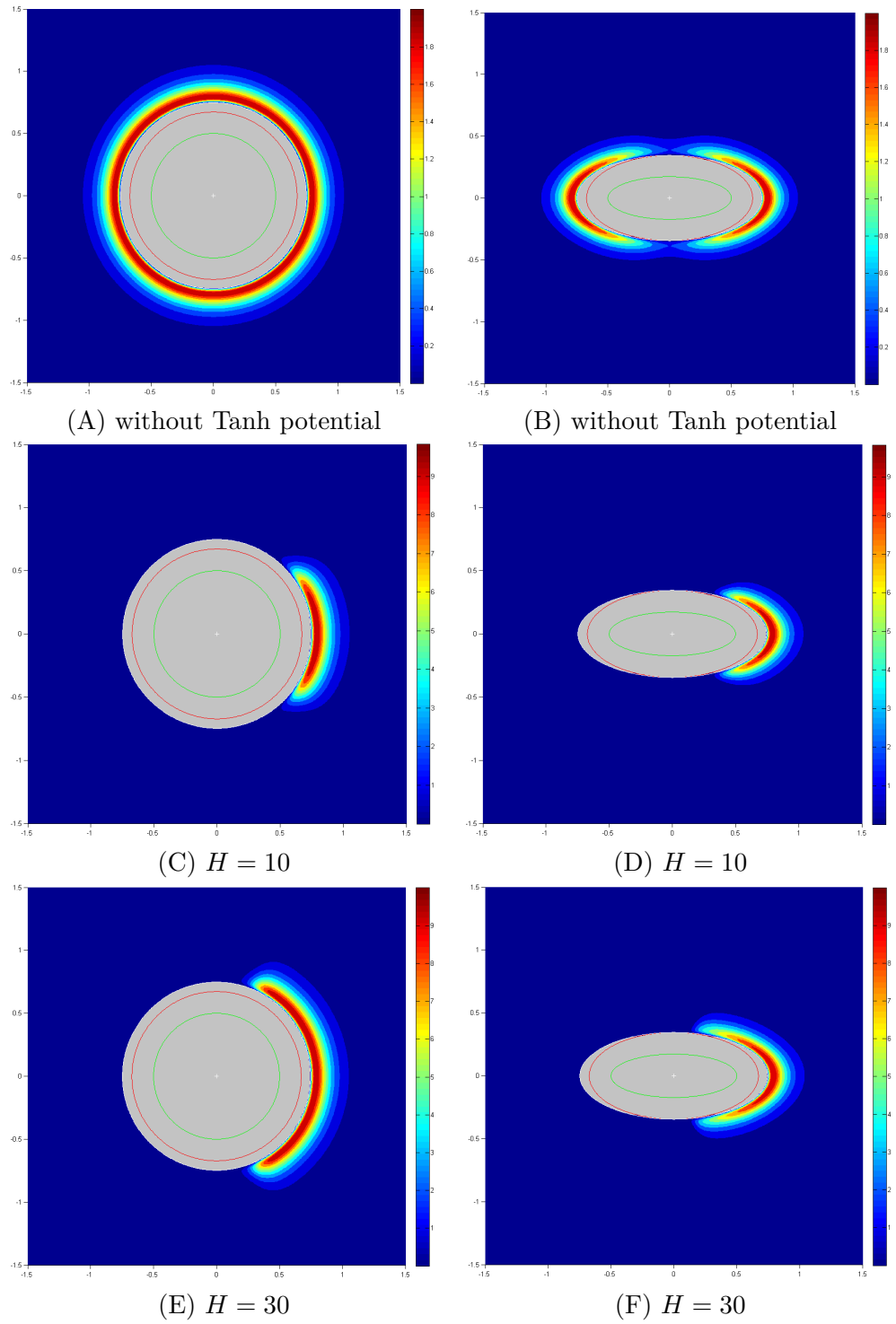


Figure 3.8: Contours of disc-sphere potential field (absolute values) for original GB potential and also Tanh potential with different values of H . In this figure $\kappa = d = 0.345$, $\epsilon_0^{ds} = 2.0$, $\sigma_0^{ds} = 0.748$, $\mu = 1$, $\epsilon_{fs}/\epsilon_{es} = 0.2$, $\beta = 1$, $a = 2.6$, $b = 2.4$ and $l = 0.1$. Green lines show edge of the disc, red lines indicate the centre of the sphere being tangent to the disc surface and white lines shows the zero repulsion separation. The figures at left show the horizontal symmetry plane and the right ones are for vertical symmetry plane of the disc. The repulsion part of the potential being inside the white lines is not shown.

3.4 Inter-particle Potentials

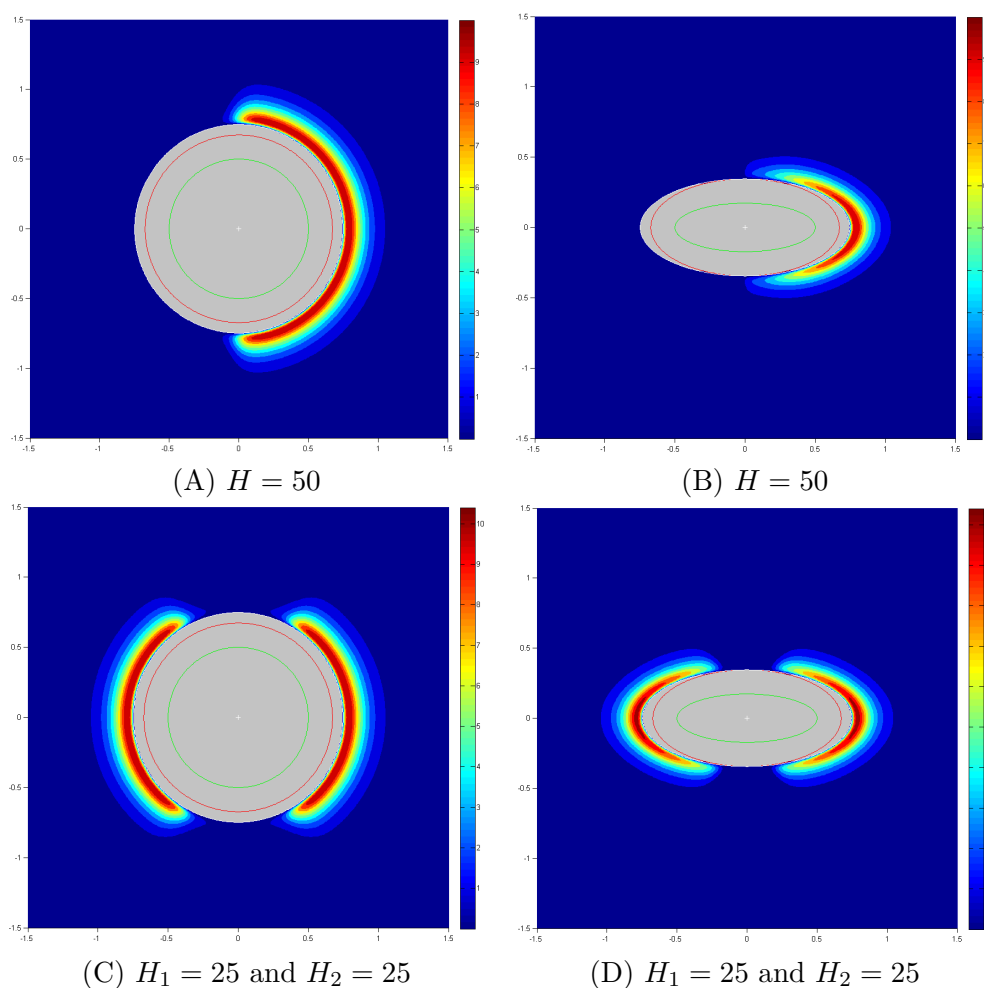


Figure 3.9: See caption of Figure 3.8 for the details. In parts C and D, two equal hot-spots with opposite directions are applied.

In this chapter, we presented the details of the MD simulations which are used as the method of performing the current research. The intermolecular potentials governing the interactions of the coarse-grained particles were also reviewed. Knowing these, together with having an insight into the background associated with the focus of the current work, which was reviewed in the previous chapter, we can move to the result chapters of this thesis. In chapter 4, the self-assembly of fibres is investigated. In the remaining chapters, by considering the Tanh potential for the interaction of discs and spheres, spontaneous formation of several supramolecular structures in amphiphilic chromonics systems is studied.

Chapter 4

Fibre Self-assembly

As we discussed in Chapter 2, there are many aspects of spontaneous fibre formation which are not well understood. Several previous studies of the self-assembly of highly elongated stacks of molecules have described the observed behaviour in terms of a hierarchy of interacting processes [31–33]. In such a hierarchy, the highest-order object is generated via a cascade of lower-order structures which themselves develop through a series of interconnected or cooperative processes. However, within this generic framework, a range of different (or even contradictory) pathways have been suggested for fiber and amyloid growth. As with the kinetic cascades realised to achieve accelerated growth in various bio-mineralisation processes [134], it is inherent in hierarchical self-assembly that the presence of a free energy barrier between each stage introduces possible complexities such as trapping in metastable states or competition between alternative kinetic pathways [135]. Chromonics, having aromatic rings in their molecular structure, are one of the candidates for forming elongated objects, as their $\pi - \pi$ interactions promote stacking. However, being relatively flat and, therefore, having shape anisotropy can also add to the complexity of formation and growth mechanisms. Orientational order metastability is one example of this complexity, discotic colloidal particles forming small ordered strands at the early stages of self-assembly from isotropic solution, regardless of the growth pathway or final structure [136]. The anisotropy in the energy of interaction at different configurations is the other factor which can affect the self-assembly of fibres.

4.1 Introduction

In addition, as the bundle grows, the outer layers of the structure experience different conditions from the inner layers [137]. This difference can become dominant, leading growing structures on pathways which have lower free energy cost.

The aforementioned points regarding fibre self-assembly provide the main motivations for this chapter. Here, we will use MD simulations of simple discotic building blocks in order to access and, so, gain understanding of the competing effects associated with the spontaneous formation of fibres.

4.1 Introduction

The aims of this chapter are to determine whether fibre formation behaviors are accessible, in a reproducible way, to molecular simulation and, if so, to gain clearer insight into the competing kinetic and thermodynamic effects that are apparent from related experimental systems. To this end, the self-assembly is considered of achiral, discotic (oblate ellipsoidal) building-blocks using conventional Molecular Dynamics (MD) simulation described in Chapter 3. In this, computer simulation methods such as meta-dynamics [138] and forward-flux-sampling [139], which have been developed to investigate rare events (such as nucleation) and explore reaction pathways, are consciously avoided. This is because they also prescribe the form of any final aggregate and (importantly) bias any intermediate structures and, thus, the associated hierarchical self-assembly pathways. The study is restricted, therefore, to the more prosaic, but bias-free, procedures adopted in previous simulation studies [32, 140] of fibre-formation from an isotropic precursor phase.

The work presented here builds upon and expands that of Prybytak *et al.* [5, 32], wherein a two-component mixture of GB discs and spherical Lennard-Jones particles was simulated to study fibre self-assembly. All simulations started from an isotropic configuration at high temperatures with no translational and rotational order. After equilibration, this system was “gently” cooled down to lower temperatures, while the temperature was controlled with Nosé-Hoover thermostat. Temperature decrements of 0.1 were used at high temperature, but these were reduced to 0.01 as each fibre-formation temperature was approached. At each temperature, at least 3×10^6 MD

4.1 Introduction

Table 4.1: Disc-disc potential well-depth at edge-edge configuration for some shape parameters κ used in this work.

κ	0.25	0.3	0.345	0.4	0.45
well-depth	4.516	3.3	2.63	2.103	1.785

steps were performed and the observables (number of monomers, dimers, trimers, etc.) were monitored to be sure that they reached a steady state and the system achieved equilibration. It was also found that “direct” cooling of the isotropic system to the temperature at which the fibre forms in a gentle cooling process could lead to the same outcome. In this way, some computational time could be saved, as there was no need for the equilibration at higher temperatures, although without knowing the fibre forming temperature in advance, a trial-and-error procedure was necessary for finding the optimum (highest) temperature at which a defect-free fibre grows. Direct cooling of the system to the temperatures below the optimum range, however, led to formation of defected structures which developed as a result of coalescing of two or more smaller clusters [5]. Both gentle and direct cooling approaches were used in this research.

Here, a range of κ and κ' values have been explored for the GB disc-disc interaction given by equation (3.42), but μ and ν have been fixed at their usual values of 1 and 2, respectively [128]. Both σ_0 and ϵ_0 parameters in the GB disc-disc potential were also set to be 1. The potential well-depth at edge-edge configuration is a function of the shape parameter κ (see Table 4.1), and it increases as the disc becomes thinner. Constant cut-off radius of 1.7 disc diameter was applied for all the simulations presented in this chapter.

Initial investigations of the present research showed that, in order for the modified disc-sphere potential introduced in equation (3.47) to achieve the same results as Prybytak, the modification parameter $\beta = 0.2$ should be used. That is, in the disc-sphere system, the fibres form if the interaction between spheres and discs is kept sufficiently weak. This suggests that, perhaps, the spheres have no effect on fibre formation by discotic particles. To verify this hypothesis, different systems with $\kappa = 0.345$, $\kappa' = 0.15$ and sphere number fractions from 0 to 0.87 at a fixed

4.2 Effects of Shape and Energy Anisotropies

disc number density were considered and the fibre self-assembly in these system were investigated by the direct cooling procedure explained above. The diameter of spheres were set to be the same as the height of the discs which is 0.345. The results showed that the observable quantities of the final formed fibres were, indeed, independent of the number of spheres. There was a negligible increase (about 1%) in formation temperature of the fibre, possibly due to the slight increase of effective density of discs when the number of spheres rose. By an increase in the number of spheres at constant disc density, the pressure in the systems also went up which may have contributed to the small temperature shift. In summary, excluding the spheres had no effect on the fibre formation and led to both greater clarity of interpretation, due to the reduced parameter space of the model, and increased run times, because of the associated computational savings. Therefore, in this chapter, the disc-only systems will be considered. However, as illustrated in Figure 4.1, the disc density had an effect on the fibre formation temperatures. An increase in the building-block density caused the chance of the initiation of growth to go up and, therefore, the fibres formed at higher temperatures. For the results presented in this chapter, simulations are limited to the systems with disc number density of 0.075, except where explicitly mentioned.

In the following, we try to address the issues raised at the beginning of this chapter. The effects of the shape and energy anisotropies on the spontaneous formation of fibres will be investigated. Thermal hysteresis and seeding will also be investigated. Then, the kinetics of the process and its pathway will be discussed. At the end, by considering substantially larger systems, some size-related phenomena will be studied.

4.2 Effects of Shape and Energy Anisotropies

In the simulations presented here, 15 different systems have been considered, characterised by three values of shape anisotropy parameter κ (0.3, 0.345, 0.4) and five values of energy anisotropy parameter κ' (0.05, 0.1, 0.15, 0.2, 0.3). For each of these parameter combinations, a 3d periodic, cubic system of 600 discs has been

4.2 Effects of Shape and Energy Anisotropies

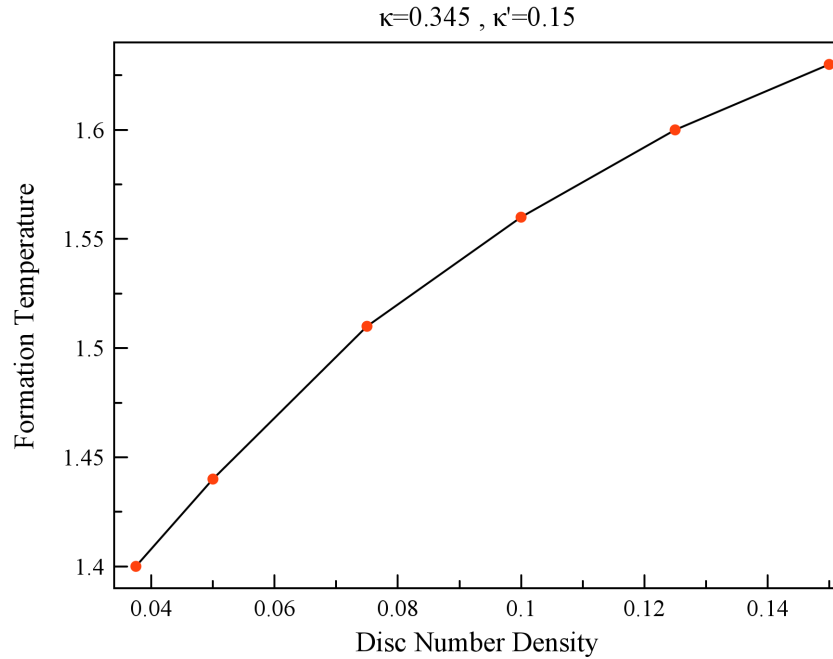


Figure 4.1: Fibre formation temperatures versus disc number density for $\kappa = 0.345$ and $\kappa' = 0.15$.

cooled at a reduced number density of 0.075, that is with a box length of 20 disc diameters. The MD time-step was set to be 10^{-3} units. These simulations resulted in the observation of rapid-fibre-onset temperatures in all cases which are plotted in Figure 4.2. Given that κ' is inversely proportional to the strong face-face interaction strength (the dominant interaction here), it is reasonable that, for fixed κ , these temperatures should follow hyperbolae.

Figure 4.3 shows the time lines of some variables for the system with $\kappa = 0.345$ and $\kappa' = 0.15$ at its fibre forming temperature $T=1.51$. For each investigated system, the simulation at fibre forming temperature can be divided into three distinct phases; 1) pre-assembly phase, at which some small clusters form but they are not sufficiently long-lived and dissolve (few million MD steps not being shown in the figure), 2) growth phase, where one of the formed small clusters grows (about one million steps for the system sizes presented here), and 3) steady-state phase, over which there is no significant change in the observables. The pre-assembly and growth phases will be discussed later in this chapter, but more details of the final fibres and the phenomena

4.2 Effects of Shape and Energy Anisotropies

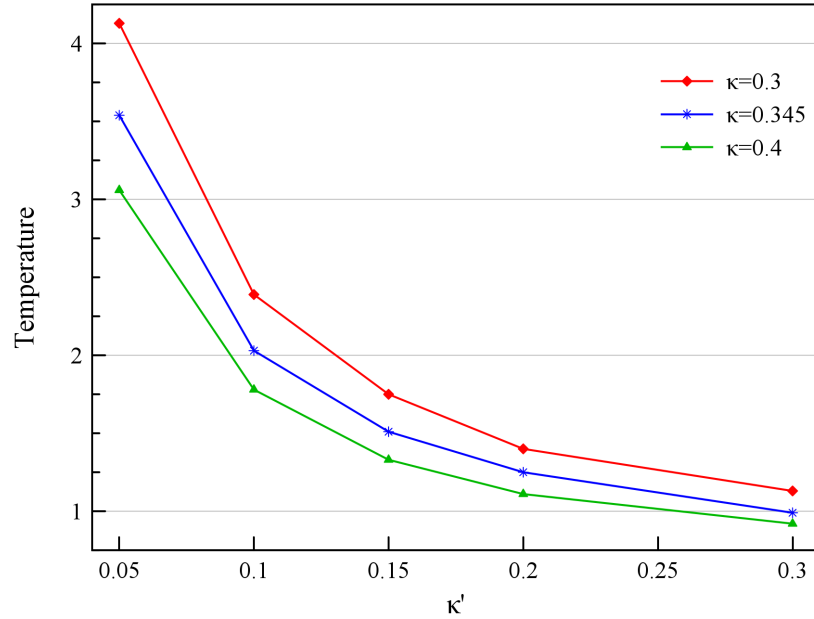


Figure 4.2: Fiber-onset temperatures on cooling from isotropic, for systems with a range of particle shape and energy anisotropies. For each κ value, the system above the associated curve is isotropic.

occurring in the growth phase which led to the observation of these structures will be presented here.

As shown in Figure 4.3, when the fibre initiates and starts the growth phase, it never disperses and the number of particles in the fibre monotonically increases until it consumes almost all of the material in the simulation box and reaches the steady-state size (about 90% of particles form the fibre). The growth happens both longitudinally and radially, which is apparent from the number of threads in the growing fibre. Small variation of number of threads just before the steady-state phase (between 4.5 and 5 million steps) can be related to the fact that some of the initial small threads at the outer layer of the fibre finally unite to become a single thread and cause the total number of threads to slightly drop. The normalized moments of inertia with two large values and a smaller one suggest the formation of an elongated object (each components of moments of inertia was normalized with the sum of all three). This is confirmed by Figure 4.4 showing two views of the formed fibre in this system. The fibre comprised twisted threads and a central straight thread. The spontaneous twist in this fibre resulted when threads attempt to both pack

4.2 Effects of Shape and Energy Anisotropies

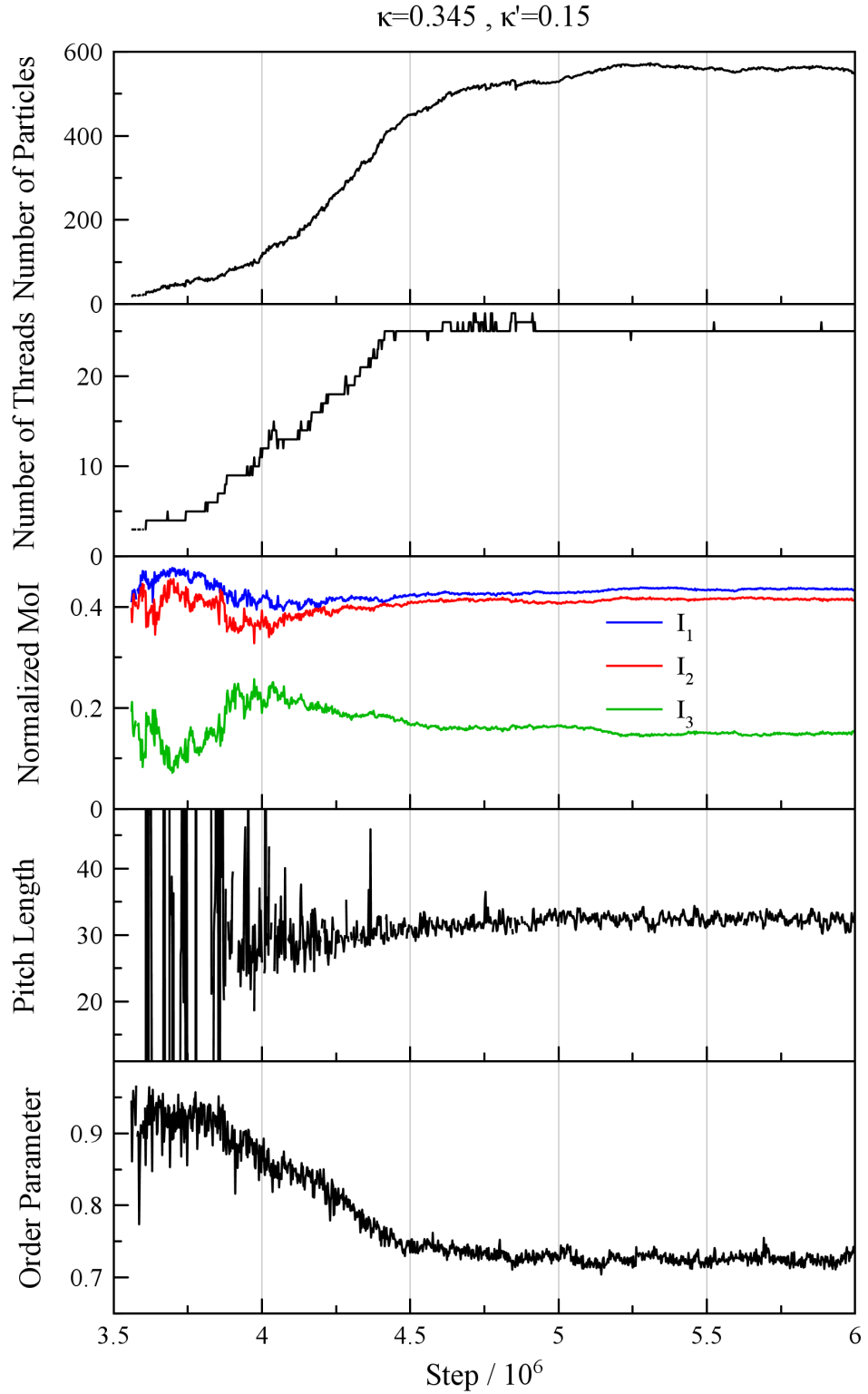


Figure 4.3: Time lines of different parameters measured for the system with $\kappa = 0.345$ and $\kappa' = 0.15$ at fibre forming temperature $T=1.51$. The data are only shown from the beginning of the growth phase.

4.2 Effects of Shape and Energy Anisotropies

hexagonally and interdigitate with their neighbours [5, 32, 100]. Since there are no chiral terms in the inter-particle interactions used in this study, both left-handed and right-handed fibres can be observed with equal likelihood in these simulations. The pitch length of the twisted fibre was also plotted in Figure 4.3 by averaging the pitch of the helices fitted on each thread except the central one. Significant variation of pitch length at the early stages of the growth has two potential reasons. When the cluster is small and the number of particles in each thread is limited, the helix fitting algorithm is not efficient. In addition, at the early stages, the handedness of the fibre is not fixed and its pitch is able to switch between positive and negative values. When the fibre reaches a particular size and the first layer of threads around the central one is complete, the handedness ceases to change. However, a slight increase in the pitch length is observed as the radius of fibre increases. Because the neighbouring threads are interdigitated, the particles in the outer threads have to tilt more in order to maintain the same pitch length as the inner threads. This causes the particle orientations to deviate from the director which is the same as the axis of fibre and, therefore, the orientational order parameter drops as the object grows.

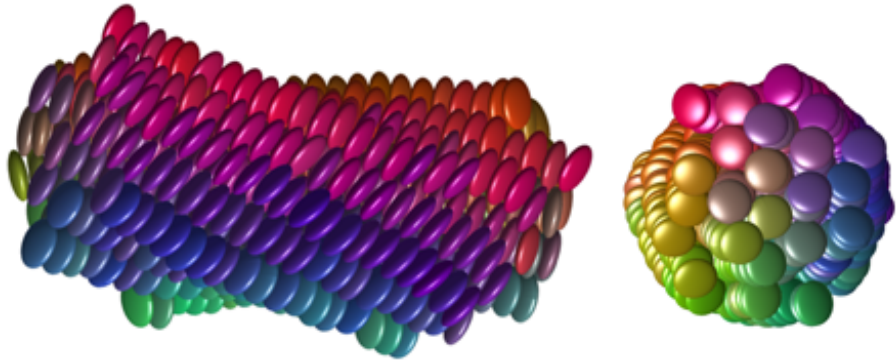


Figure 4.4: Two views of the self-assembled fiber formed at $T=1.51$ ($\kappa = 0.345$, $\kappa' = 0.15$). The discs are color-coded based on their orientations. The slight change of color within individual threads is an indication of twist and writhe in the structure. Both hexagonal local packing of threads and defect-free interdigitation of particles in neighboring threads are apparent.

To further investigate the propensity for fibre formation in these systems, extended runs were performed at $T=1.52$, 1.53 and 1.54 . At $T=1.52$, a dynamic equilibrium persisted for 6×10^6 MD time-steps, after which fibre formation was eventually signalled by a comparatively fast reduction (over $\simeq 10^6$ MD time-steps) in free

4.2 Effects of Shape and Energy Anisotropies

monomers. At $T=1.53$, the isotropic state persisted for nearly 50×10^6 MD time-steps, after which fibre formation was again seen. However, at $T=1.54$, the system remained isotropic throughout a long run of 300×10^6 MD time-steps.

The characteristics discussed above are largely replicated by the other 14 systems studied here. Therefore, they are not described in detail and only the average values of parameters for the fibres at their steady-state phase will be compared. When there is a deviation from the aforementioned points, it will be clearly stated. One example of this deviation is illustrated in Figure 4.5, showing the final structures of formed fibres. For high κ and low κ' , that is more spherical particles with strong face-face interactions, the fibres formed were straight, rather than twisted.

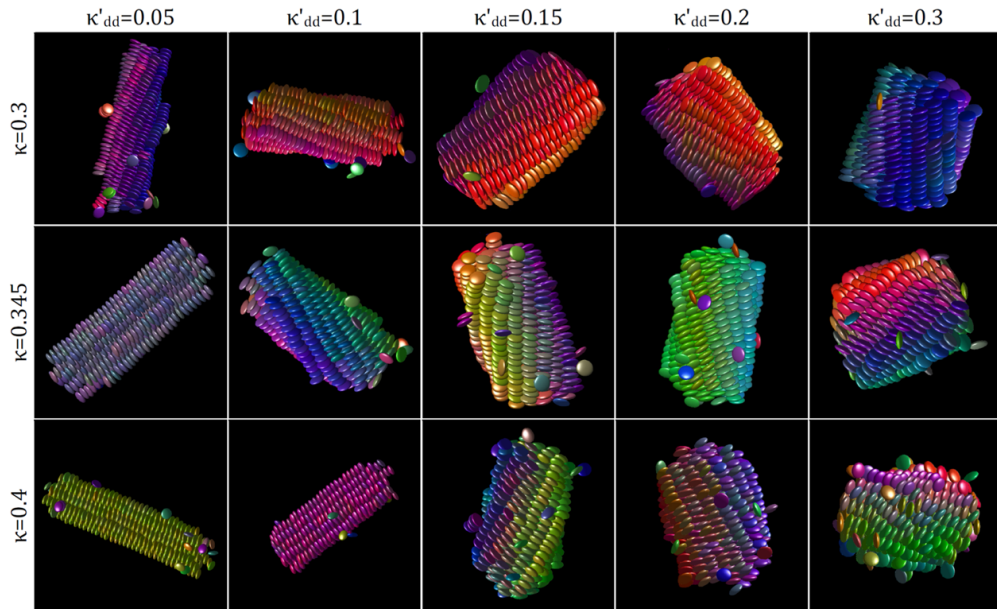


Figure 4.5: Snapshots of the final formed fibers, on cooling from isotropic, for systems with a range of particle shape and energy anisotropies, κ and κ' . For clarity, snapshots are zoomed in to fill each box, rather than all being to scale.

Figure 4.6 illustrates the averaged values of different parameters over the steady state phase of the simulations (last one million steps including 500 configurations). In most cases, the formed fibres consisted of 85-97% of the particles, except for the system with the thickest disc and $\kappa' = 0.3$ in which only 75% of the particles formed the aggregate (Figure 4.6a). There was a slight increase in number of particles for each fibre on weakening the face-face interaction between the discs which is, possibly, due to the fact that fibres with smaller κ' values formed at higher temperature

4.2 Effects of Shape and Energy Anisotropies

(Figure 4.2), and consequently, the particles have more kinetic energy to move around and not to join the growing cluster. Figures 4.6b-4.6d depict that the growth in two directions, lateral and longitudinal, can be controlled with the energy anisotropy parameter, κ' . The aspect ratios of the formed fibres show a clear trend, being long and thin for low κ' but progressively shorter and fatter on increase of this parameter.

Figure 4.6e shows that, as expected, the orientational order parameters for straight fibres (see Figure 4.5) were above 0.95, meaning that the particles were highly aligned with a preferred direction which is the axis of the fibre. By an increase in the κ' parameter, and consequently, the increase in the tilt angles of particles due to their being in threads with larger radius, the order parameter dropped. The P_2 dependency on particle thickness, however, does not follow the expectations. Fibres formed by the thickest particles, $\kappa = 0.4$, had higher order parameters than the thinner particle systems. This deviation can also be seen in the pitch length data (Figures 4.6f). The time lines of order parameter for the systems with $\kappa = 0.4$ (Figure 4.7) show that the monotonic decrease in the growth phase seen in Figure 4.3 was not exhibited by most of the systems with this shape parameter. For the strongest face-face interaction, $\kappa' = 0.05$, the initial cluster was straight and also remained straight within the growth phase - the P_2 value never dropped below 0.9. For $\kappa'=0.3$, the orientational order parameter can be seen to have decayed as the strongly aligned early-stage cluster developed coherent twist and writhe in its constituent threads. Between these two limiting behaviours, however, size-dependent transitional behaviour was apparent - at $\kappa'=0.1$, initial order parameter decay was arrested, reversed, and ultimately exhibited a jump to a high constant value; and at $\kappa'=0.15$ and 0.2 , the order parameter dropped to 0.6-0.7 before recovering to a steady state of 0.8. The graphs labelled Before transition in Figures 4.6e and 4.6f are, in fact, the averaged values before this untwisting transition, and they are consistent with those adopted by thinner discs. This observed behaviour can be explained by the fact that, strains along local thread axes must grow with their writhe radii - Grason has argued that thread stresses in twisted fibres increase as r^4 [137]. In order to maintain axial mechanical stability in these simulations, therefore, central threads necessarily underwent net compression, to balance the extension of the outer threads.

4.2 Effects of Shape and Energy Anisotropies

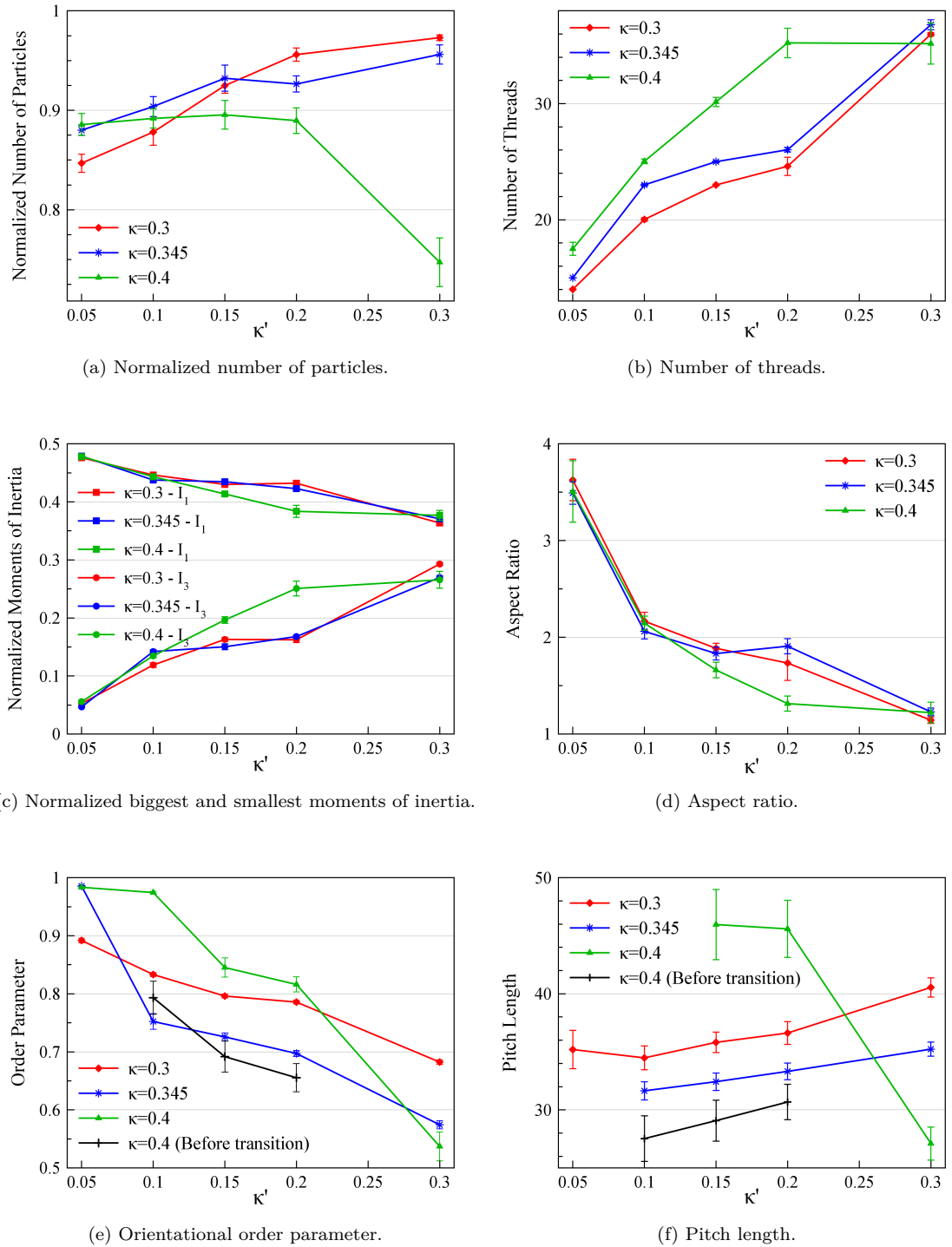


Figure 4.6: Averaged values of different parameters for the investigated systems at their fibre forming temperature. The sampling was performed over the last one million steps (500 configurations) in the steady-state phase. For parts e and f, the “Before transition” graphs for $\kappa = 0.4$, however, achieved by sampling in the growth phase just before the untwisting transition occurs for the growing object. The error bars show \pm Standard Deviation of sampled data.

4.2 Effects of Shape and Energy Anisotropies

Growing tangential strains, correspondingly, caused concerted increase in fibre pitch length and, therefore, its complete ($\kappa'=0.1$) or partially ($\kappa'=0.15$ and 0.2) untwisting.

For the untwisting to happen, particles have to re-locate themselves in the fibre and, therefore, their local packing changes. This can be seen from the $g_{\perp}(r)$ data for different systems with $\kappa = 0.4$ shown in Figure 4.8. For twisted fibres ($\kappa' > 0.1$) The first peak in this graph occurs at about 0.95 disc diameter inter-particle distance, suggesting an interdigitation of neighbouring threads. For $\kappa'=0.3$ with fully twisted fibre, however, the first peak is broader and the second and third ones are more distinct. On the other hand, for the straight fibres, the first peak splits into two; one at about 0.93 and the other at 1.04 disc diameter. This suggests that the local packing of particles is not hexagonal any more - Figure 4.9 shows a view along the axis of a straight fibre in which only 4 threads are interdigitated with a central thread, while the other two neighbours expanded their inter-thread distance with that thread.

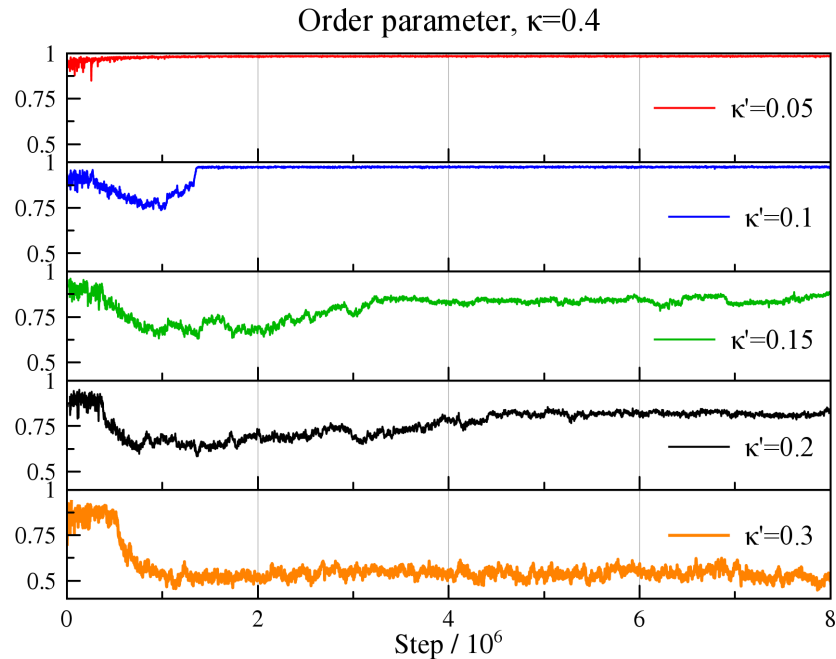


Figure 4.7: Time lines of the orientational order parameter of the particles in the growing fibers formed by $\kappa=0.4$ systems with a range of energy anisotropies, κ' . All graphs are drawn from the beginning of the fibre growth phase and any latency prior to fibre initiation (few millions MD time-steps) is omitted.

4.2 Effects of Shape and Energy Anisotropies

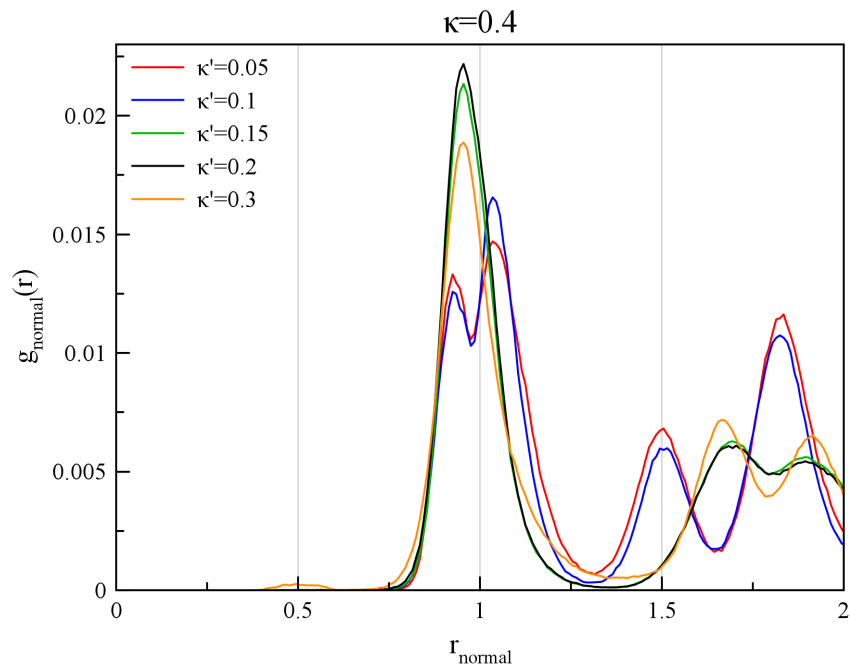


Figure 4.8: $g_{\perp}(r)$ data of the particles forming the fibre for $\kappa=0.4$ systems with respect to the director of fibres. 500 different configurations were sampled for measuring the distribution functions and all of them were normalized such that the area underneath equals one.

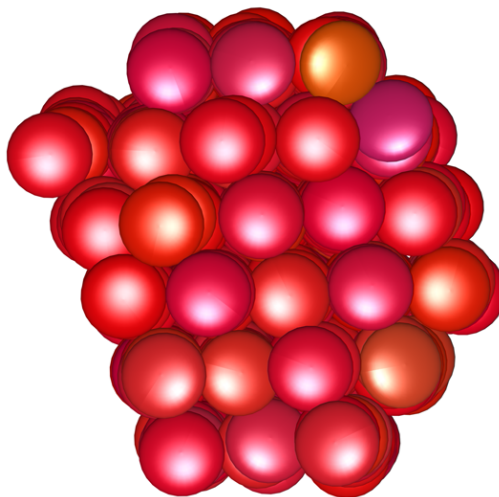


Figure 4.9: Packing of particles in a straight fibre formed in the system with $\kappa = 0.4$ and $\kappa' = 0.1$. For each thread, the neighbouring threads at angles $\pi/3$ and $4\pi/3$ expanded their distances, while the other 4 threads experienced a compression toward the central one.

4.2 Effects of Shape and Energy Anisotropies

Figure 4.10a shows the averaged intra-thread potential energies for the formed fibres in their steady-state phases. The potential energy of each thread is normalized by the number of particles in that thread and then is averaged over all threads of fibre. The intra-thread energies, being mainly due the face-face interactions, show a very clear dependency on both shape and energy anisotropy parameters. For each value of κ' , scaling of the intra-thread energies with the corresponding edge-edge potential well-depths (Table 4.1) causes the values for the three different particle sizes to collapse onto a single graph. This suggests that the averaged intra-thread energies of the fibres are independent of the structure of the object (being straight or twisted), similar to the behaviour of the formation temperature graphs (Figure 4.2).

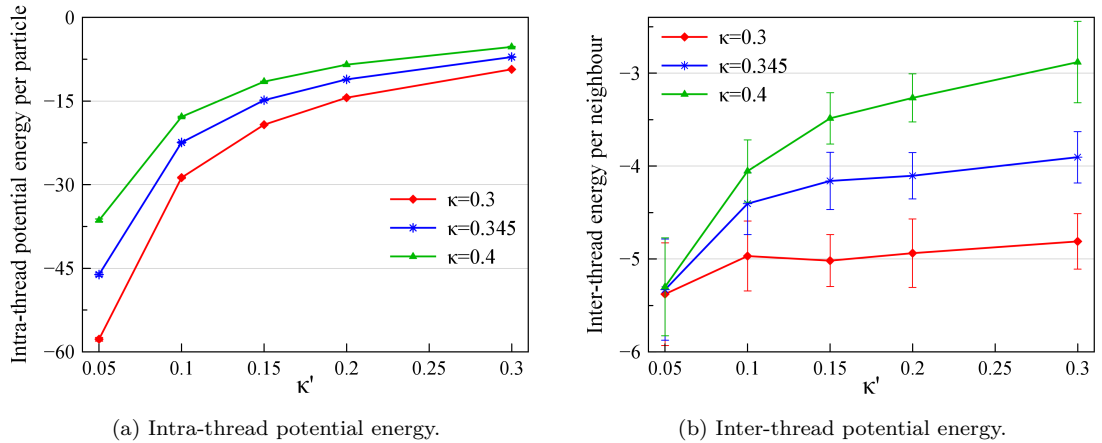


Figure 4.10: Averaged intra- and inter-thread potential energies of the formed fibres at the steady-state phase. The potential energy of each thread is normalized by the number of particles in that thread and then is averaged over all threads of fibre. For inter-thread energies, the second normalization is performed with the number of neighbouring threads. The error bars show \pm Standard Deviation of sampled data.

As discussed, the mechanical properties of threads are significantly dependent on their radii [137]. Therefore, the distribution of energies of threads with respect to their radii in the fibre should give useful information. Figures 4.11-4.13 show the probability plots for finding a thread with particular intra- or inter-thread potential energies at a particular radial distance from the centre of mass of fibre for the 15 different investigated systems at their steady-state phases. The figures depict that the intra-thread energies show an inverse dependence on distance from the centre of fibre. That is, as the fibre grows radially, the longitudinal strains increase and

4.3 Thermal Hysteresis and Seeding

the particles adopt energetically less favourable relative configurations. The largest variation of the intra-thread energy across fibre radius occurs for the $\kappa = 0.4$, $\kappa' = 0.3$ system and is about 15-20%. For straight fibres, however, this radius-dependent change of intra-thread energies is limited to less than 5%. More discussion on the interpretation of these energy plots will be presented in section 4.5.

The variation of inter-thread energies with thread radius, however, was more significant - mostly above 50%. The step-wise character of these distributions is due to the change in the number of interacting neighbour threads with radial position in the fibre. Normalizing the inter-thread energies with the number of neighbouring threads (see Figure 4.14 for $\kappa = 0.4$ system) confirms the significant effect of packing of threads on their energies and, consequently, the fibre structure and stability. Comparing Figures 4.11-4.14 reveals that, for the system size studied here, the interaction of two particular threads is not strongly correlated with their position in the fibre, but the radial location of each thread dictates the total energy that it can achieve by interacting with its neighbours.

The shape and energy anisotropies do have an effect on the inter-thread energy per neighbour, as shown in Figure 4.10b. Thicker particles generally have less strong inter-thread energies - this is consistent with the data of Table 4.1. On increasing the face-face interaction strength (smaller κ' values), however, the inter-thread energy value becomes more negative. This suggests that the inter-thread energy is due to a combination of both face-face and edge-edge interactions.

4.3 Thermal Hysteresis and Seeding

In this section, the reverse process of fibre formation is investigated by the heating up of the fibres formed in systems with $\kappa = 0.345$. One of the motivations for doing such a study is to shed some light on the stability of the fibres on the change of temperature and, thus, the possible hysteresis of the formation. The sensitivity of fibre formation to seeding will also be investigated in this section. The results from the system with $\kappa' = 0.15$ are presented in more detail and then those of other systems are given for comparison.

4.3 Thermal Hysteresis and Seeding

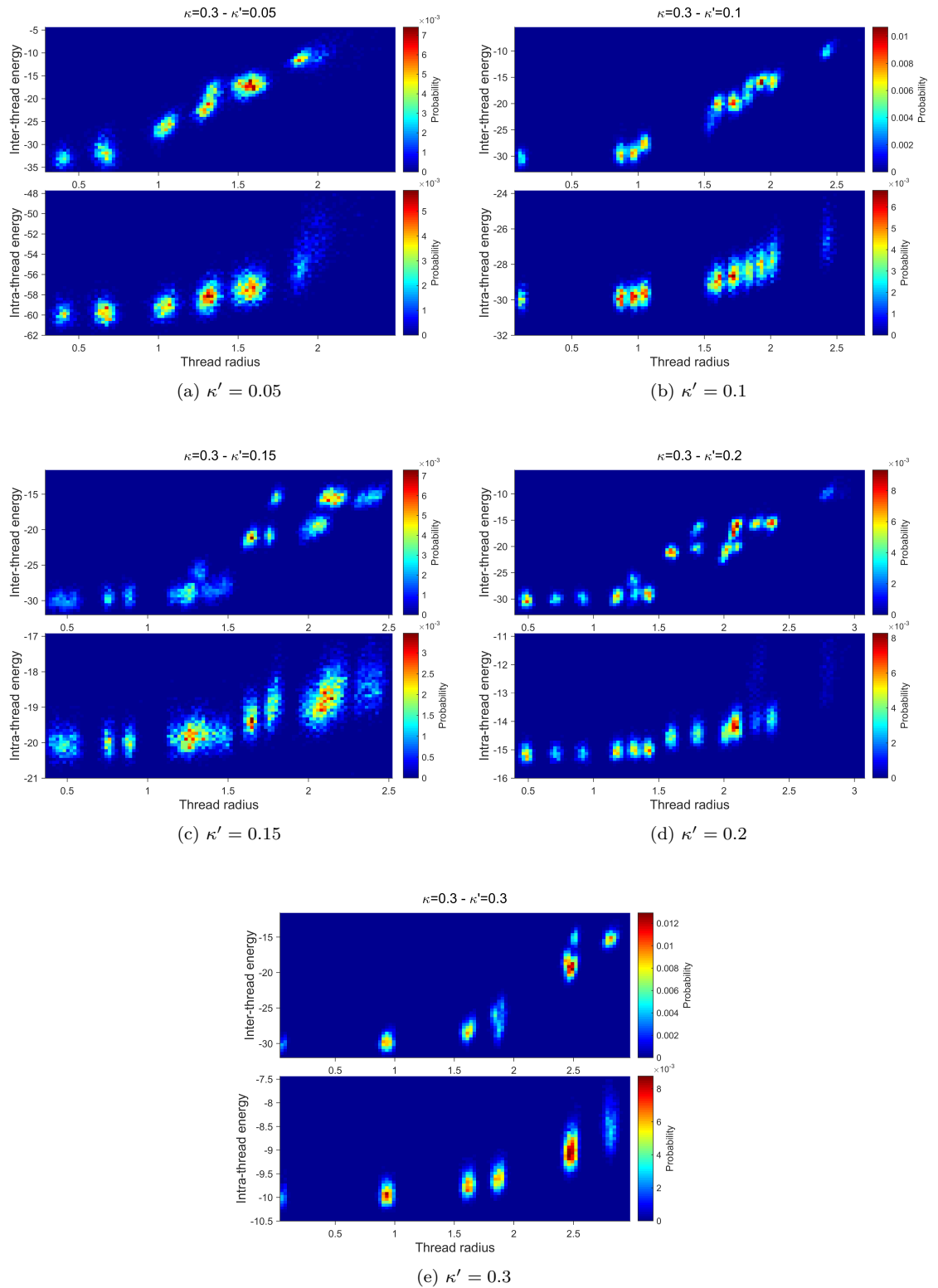


Figure 4.11: Probability of finding threads with a particular Intra- and inter-thread potential energies and radii in the last 1 million steps of the steady-state phases of fibres in different systems with $\kappa = 0.3$. The thread radius is the distance of the thread from the axis passing through the centre of mass of fibre.

4.3 Thermal Hysteresis and Seeding

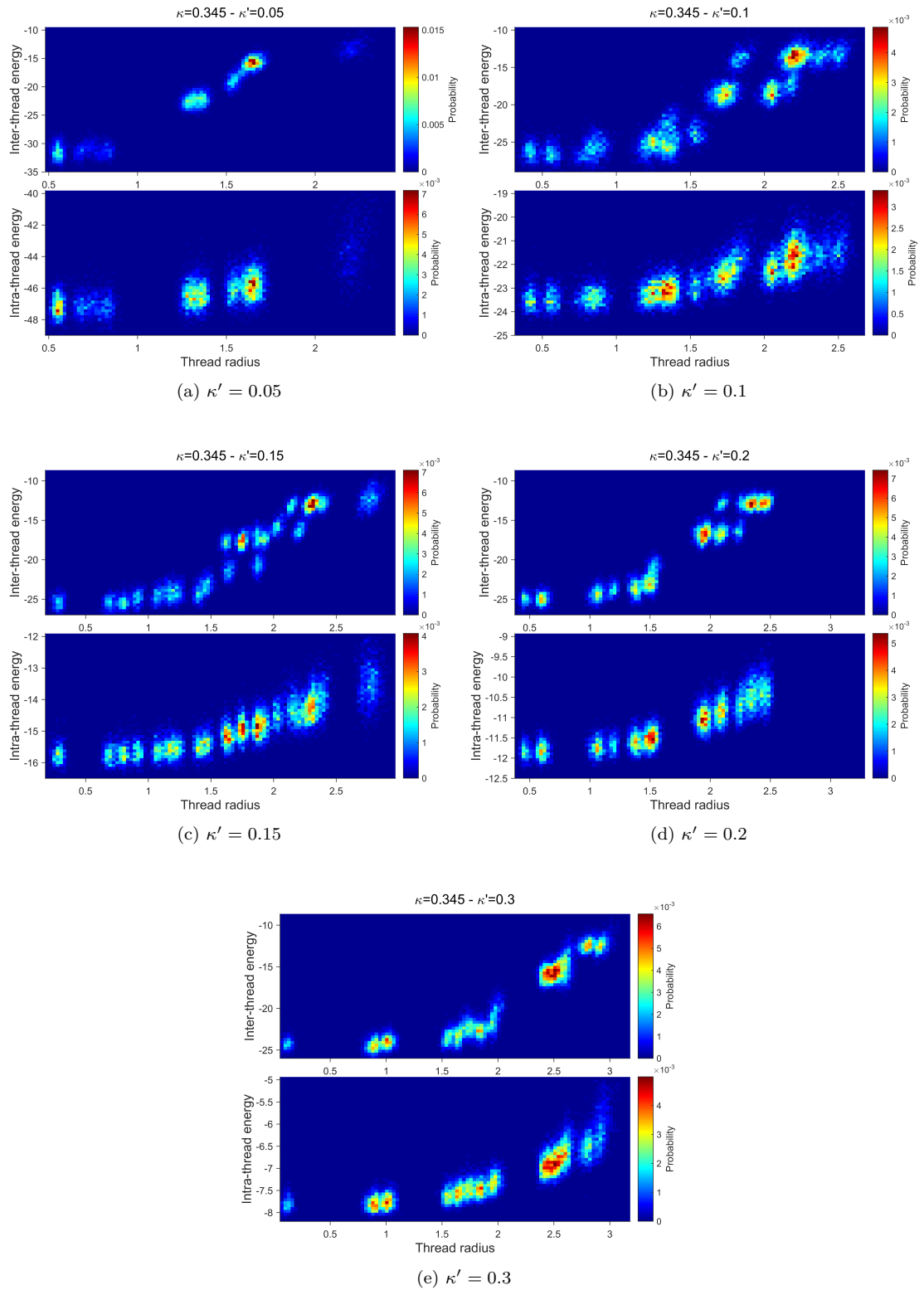


Figure 4.12: Probability plots for different systems with $\kappa = 0.345$ (see caption of Figure 4.11).

4.3 Thermal Hysteresis and Seeding

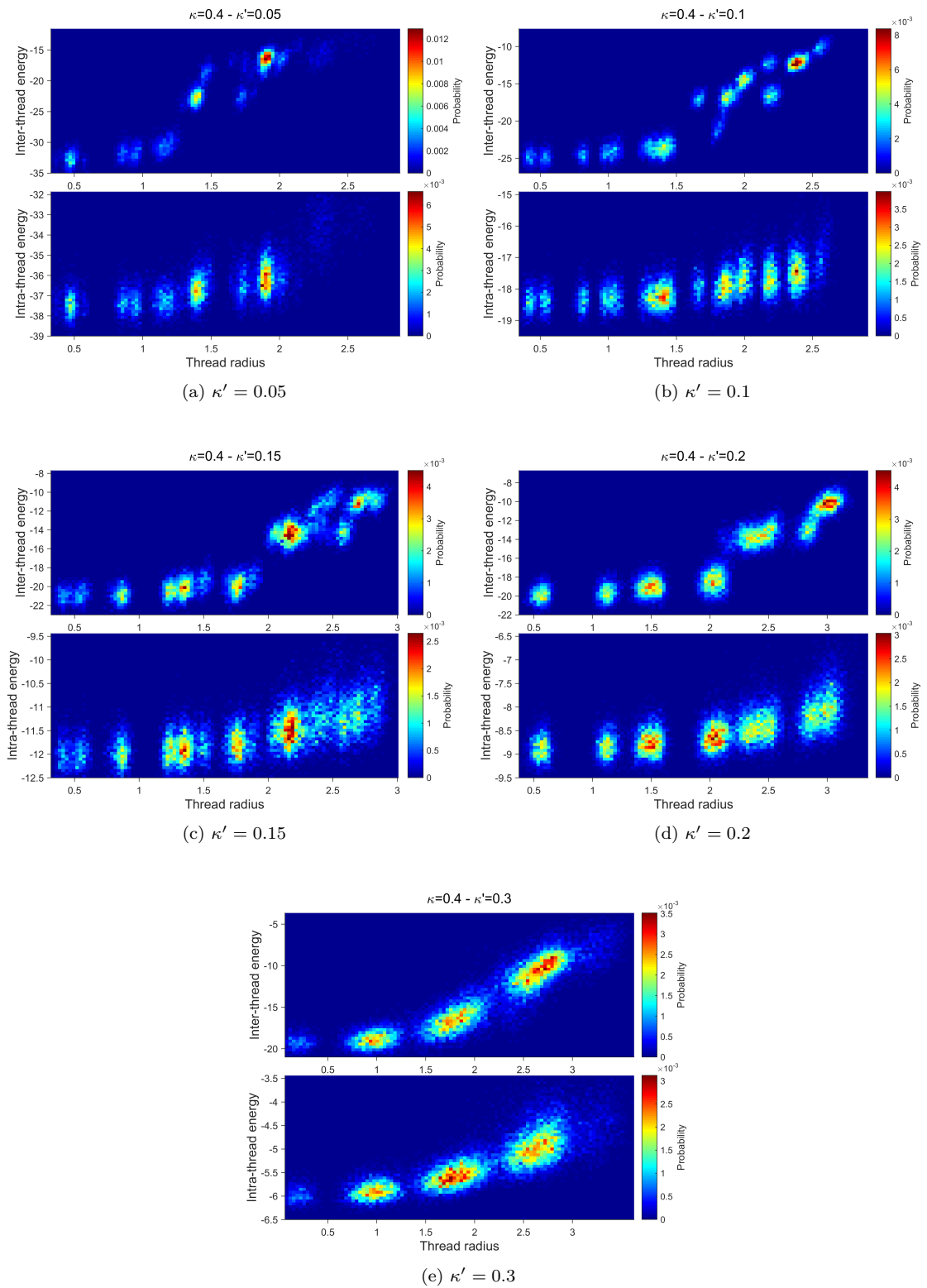


Figure 4.13: Probability plots for different systems with $\kappa = 0.4$ (see caption of Figure 4.11).

4.3 Thermal Hysteresis and Seeding

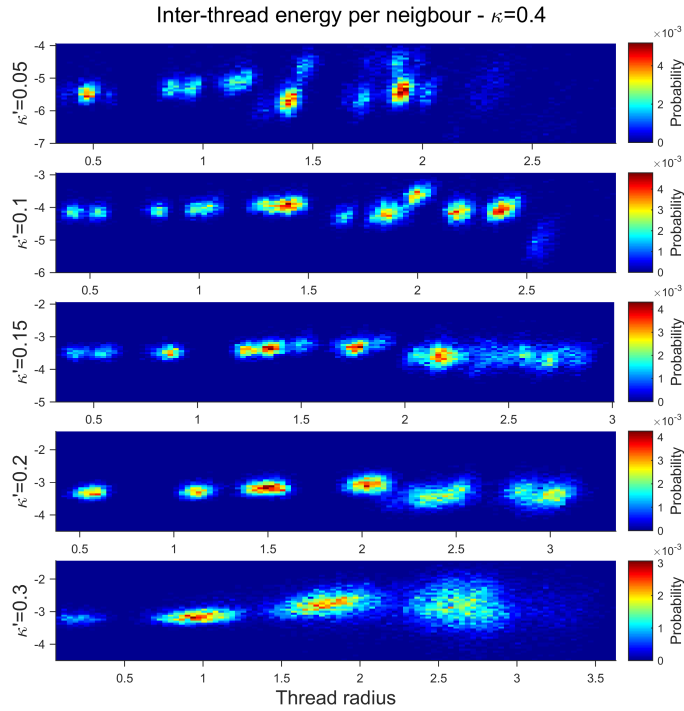


Figure 4.14: Probability plots of inter-thread potential energies normalized by the number of neighbouring threads for systems with $\kappa = 0.4$.

To study the hysteresis, the final fibres formed on cooling were warmed in increments of 0.01 until they fully dissolved. As with gentle cooling simulations, equilibration was gauged at each temperature by the stabilisation of the fibre size and the number of free monomer particles in the supporting fluid. Typical run-lengths here were 3×10^6 MD time-steps.

As discussed in previous section, on gentle cooling simulations, systems remained isotropic and no significant permanent cluster formed until the fibre formation temperature reached. At this point, the growth processes started and a dominant proportion of particles became part of the formed fibre (typically, 90% of the simulated particles). On heating these fibres, particles were shed into solution at every temperature increment, but a steady state was readily achieved at each step. This is depicted on the "Heating up" branch of the overall cluster size graph shown in Figure 4.15 for the $\kappa' = 0.15$ system. Although it progressively reduced in size on heating, as illustrated in the figure, the fibre retained its integrity up to $T=1.72$, that is 13.9% above the temperature at which rapid formation was observed ($T=1.51$).

4.3 Thermal Hysteresis and Seeding

This very large thermal hysteresis is far greater than which would be expected for the biphasic gap in typical soft matter systems - it corresponds to about 40°C for a room temperature process. This, coupled with the fact that when fibre formation did occur on cooling from the isotropic state, it involved aggregation of over 90% of the simulated particles, is strongly suggestive of bistability. In particular, it signals that the cooling branch incurred kinetic trapping in the metastable isotropic state. It is also reminiscent of experimental observations such as the polymerization of perylene bisimide into a long aggregate [141], and the large-scale assembly of the chromonic liquid crystal IR-806 [142].

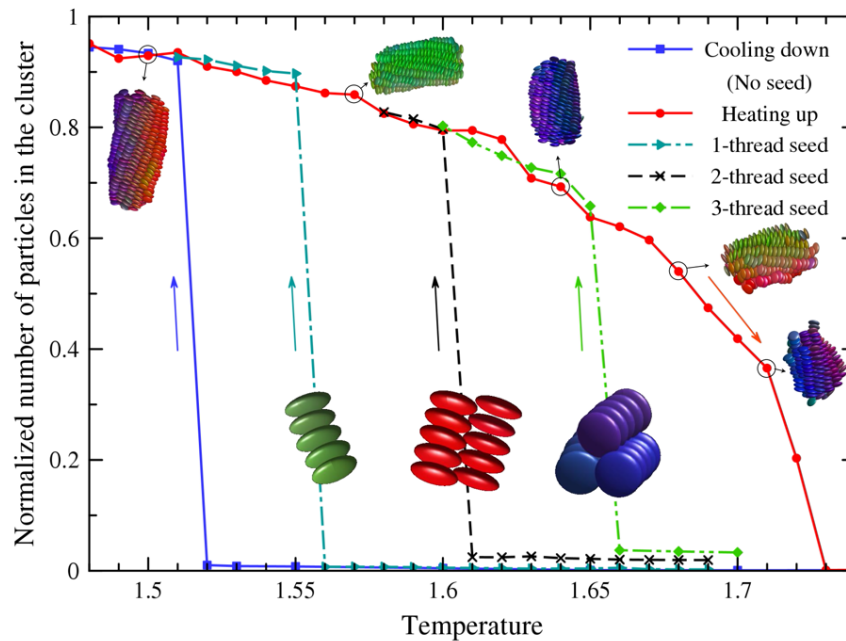


Figure 4.15: Averaged proportion of particles over the production phase (last 1 million steps at each temperature) in the biggest cluster on incrementally cooling and heating various $\kappa = 0.345$, $\kappa' = 0.15$ systems of 600 GB discs. The configuration of discs used to seed certain of the cooling sequences is shown on the corresponding curve. The diminution of the fiber on heating is illustrated by snapshots obtained at different temperatures. Maximum Standard Deviation of data is 3% and occurs at $T=1.72$ on the heating curve.

The structural analysis of the biggest cluster shows very interesting data which is illustrated in Figure 4.16. On heating, fibre pitch length data remained nearly flat up to temperature 1.65 and then slightly dropped to about 92% of its original value. Although particles dissolved from fibre into the solution and the fibre became smaller, the number of threads of the fibre remained nearly constant - suggesting

4.3 Thermal Hysteresis and Seeding

that the fibre shrinkage occurred from its ends, not laterally. This was confirmed by the data for the principal Moments of Inertia and also the aspect ratio of the fibre. Snapshots of the fibre in these simulations, illustrated in Figure 4.15, also show that the length of the fibre decreased, while its diameter remained nearly fixed. The sharp drop in the number of threads and, eventually, the dissolution started at temperature $T=1.71$, at which the number of threads went below 19, and, therefore, the third layer of threads broke down. It should be noted that there is a slight variation between the data (number of particles, number of threads etc.) of fibres studied here and those presented in the previous section, as they were taken from different simulations performed for the same set of input parameters.

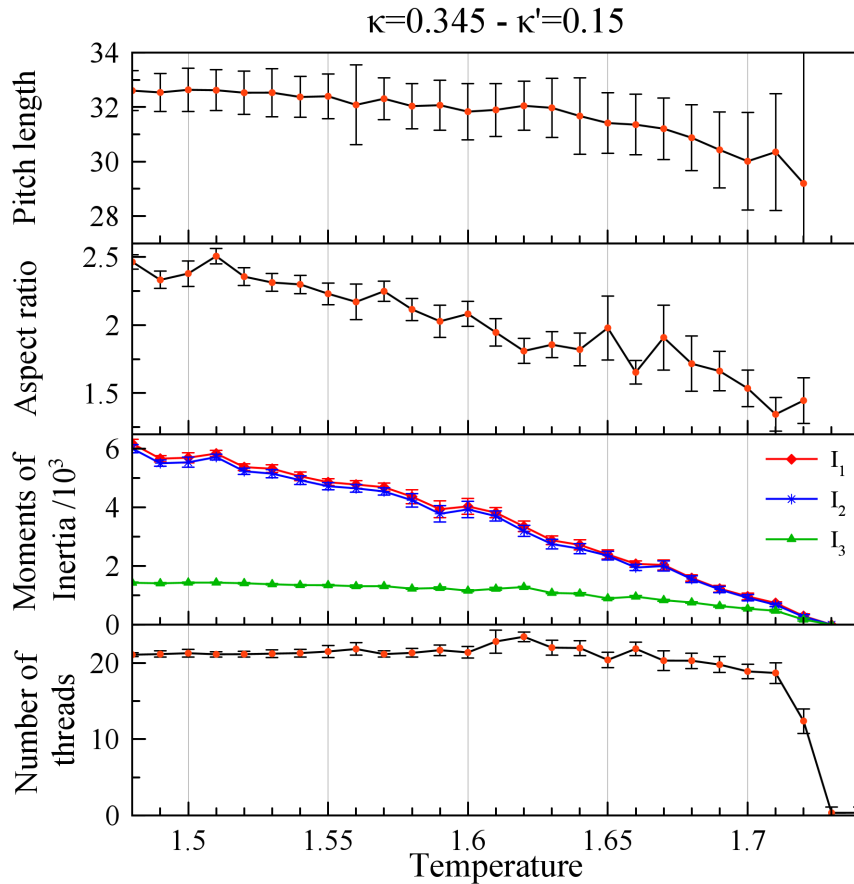


Figure 4.16: Averaged structural properties of the biggest cluster over the production phase in heating simulations of $\kappa = 0.345$, $\kappa' = 0.15$ system. The error bars show \pm Standard Deviation of sampled data.

The responses of other fibres formed with $\kappa = 0.345$ to the heating up simulations are plotted in Figure 4.17. For each system, the graphs were drawn from the formation

4.3 Thermal Hysteresis and Seeding

temperature and, therefore, the temperature persistence window is shown on the horizontal axis. Although the temperature range for which the fibres remained viable was higher for lower κ' values, data of Table 4.2 shows that the persistence range for all cases was about 10-15% above the formation temperatures, with a slight drop as face-face well-depth increased. In all systems except the one with $\kappa' = 0.3$, the number of threads remained nearly constant in heating before it sharply dropped. For $\kappa' = 0.3$, there is one relatively small drop (6 thread) to a plateau of 30 threads (i.e. 5 layers) and then persists until the fibre completely dissolved. This 6 thread drop suggests that, when an outer layer of threads becomes unstable, it disintegrates and all threads of that layer quickly dissolve.

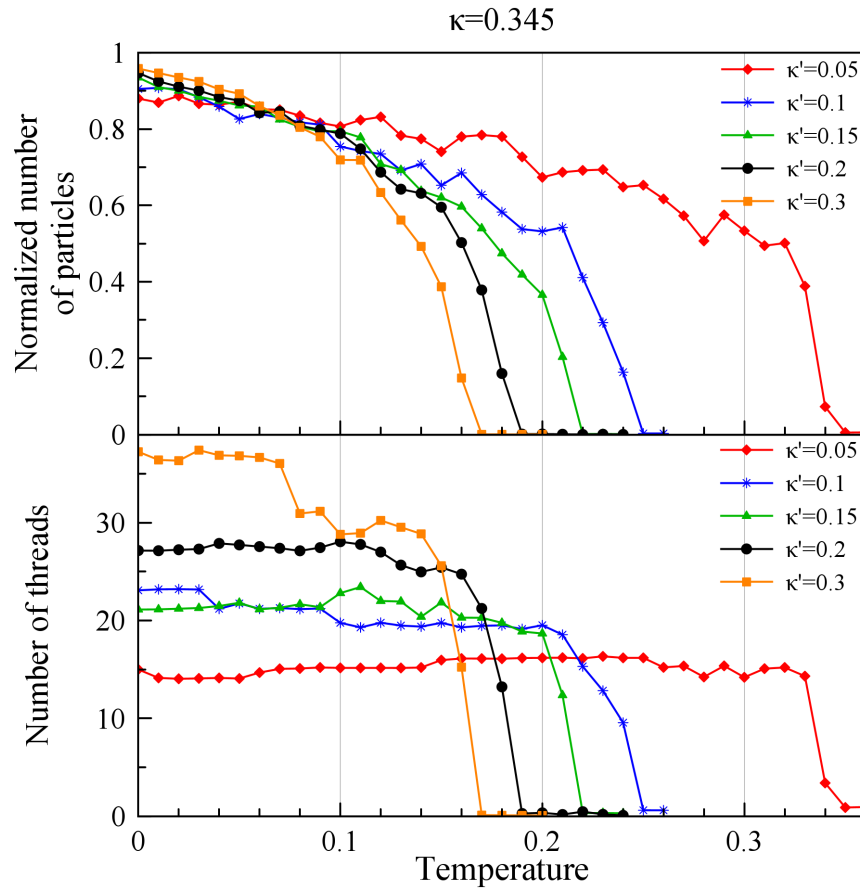


Figure 4.17: Averaged number of particles and threads in the fibres in heating up simulations for systems with $\kappa = 0.345$. The Horizontal axis is the temperature increase from the formation temperature of each system. Maximum Standard Deviation of data for number of particles is 3.8% and for number of threads is 2.1.

4.3 Thermal Hysteresis and Seeding

Table 4.2: Formation, dissolution and persistent range temperatures for the systems with $\kappa = 0.345$ in heating up simulations.

κ'	0.05	0.1	0.15	0.2	0.3
Formation Temperature	3.54	2.03	1.51	1.25	0.99
Dissolution Temperature	3.87	2.27	1.72	1.43	1.15
Persistent range (%)	9.3	11.8	13.9	14.4	16.2

In the previous section, it was shown that, for particular systems, when the number of threads gets sufficiently large, the twisted fibre becomes unstable and a transition to a straight fibre happens. It was our curiosity to understand if the reverse process, transition from a straight fibre to a twisted one, can also occur. The data from heating up simulations for the only straight fibre ($\kappa' = 0.05$) show that it remained straight until it fully dissolved - the P_2 was always above 0.95. This is not surprising because the face-face interaction of discs is very strong for this system, and on the growth phase, it was also always straight. However, the heating up simulations were repeated for this straight fibre with different values of κ' . That is, the configuration of this straight fibre was taken and then equilibrated with κ' values of 0.1 and 0.2 at the temperatures at which the normal twisted fibre with these values formed. Then, the heating up simulations were performed for these straight fibres with less strong face-face interactions in the hope of observing the reverse transition from straight to twisted fibre. Figure 4.18 shows the orientational order parameter for these straight fibres on the heating up simulations. The P_2 remained high until the number of threads in the fibres reached 15 and 19 for κ' values of 0.1 and 0.2, respectively, the transitions to the twisted fibre being initiated by drops in the P_2 values. This observation confirms that the structural transitions observed here, like those illustrated in Figure 4.7, are highly influenced by the size of the object. The persistence temperature ranges for these initially straight fibres were also consistent with those of Table 4.2 for the same value of κ' .

To study seeding, further full cooling sequences were undertaken of systems with $\kappa = 0.345$ and $\kappa' = 0.15$ loaded with a single cluster consisting of, respectively, 1, 2 or 3 threads of 5 particles. The relative positions and orientations of the particles in these seed clusters were taken from the core of the fibre formed in the original

4.3 Thermal Hysteresis and Seeding

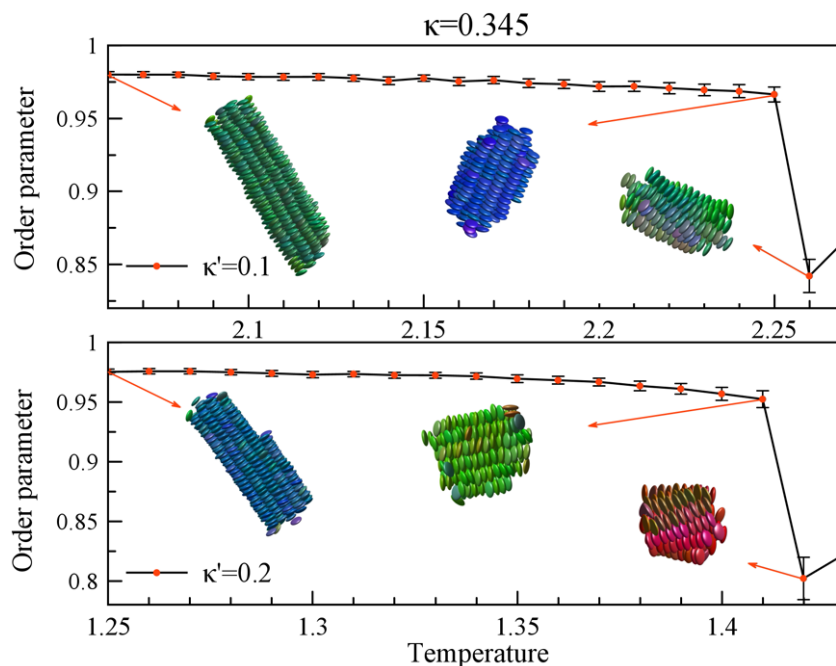


Figure 4.18: Transition of straight fibres to twisted fibres on heating. The graphs show the averaged orientational order parameters for the straight fibres taken from $\kappa' = 0.05$ but simulated with $\kappa' = 0.1$ and $\kappa' = 0.2$. Some snapshots of the fibres at different temperatures are shown. The error bars show \pm Standard Deviation of sampled data.

simulation with these parameters. In these seeded cooling runs, the integrity of the seed clusters was maintained by increasing the mutual well-depths of seed particles by a factor of 10, whereas normal interactions were applied between seed particles and the remainder of the system. Here, the time step was reduced to 5×10^{-4} , and run-lengths were extended to at least 5×10^6 steps.

Figure 4.15 also shows the temperature dependence of the steady-state aggregate size when the $\kappa = 0.345$, $\kappa' = 0.15$ system was cooled in the presence of permanent seed clusters comprising, respectively, one, two or three 5-disc threads. This shows that the presence of each of these seeds had a significant effect on the fibre-formation. In each case, the fibre branch of the thermal hysteresis loop was accessed at a successively higher temperature - the fibre forming temperature being increased by 2.6%, 6% and 9.3% for the one-, two- and three thread seeds, respectively. Equivalent behavior was found in further simulations involving a range of other seeds (not shown), the shift of the fiber-forming temperature generally being proportional to the number of discs in the seed. For seeds which had imprinted twist, the sense of

4.3 Thermal Hysteresis and Seeding

chirality of the final fibre always matched that of the seed used. Interestingly, for the 2-thread seed, the threads lost their chirality very quickly (few thousands time steps), as the straight configuration has the minimum energy for the 2-thread system. This small cluster then had equal chance for being left- or right-handed for the rest of its growth pathway, and it happened to choose a different handedness from the original seed.

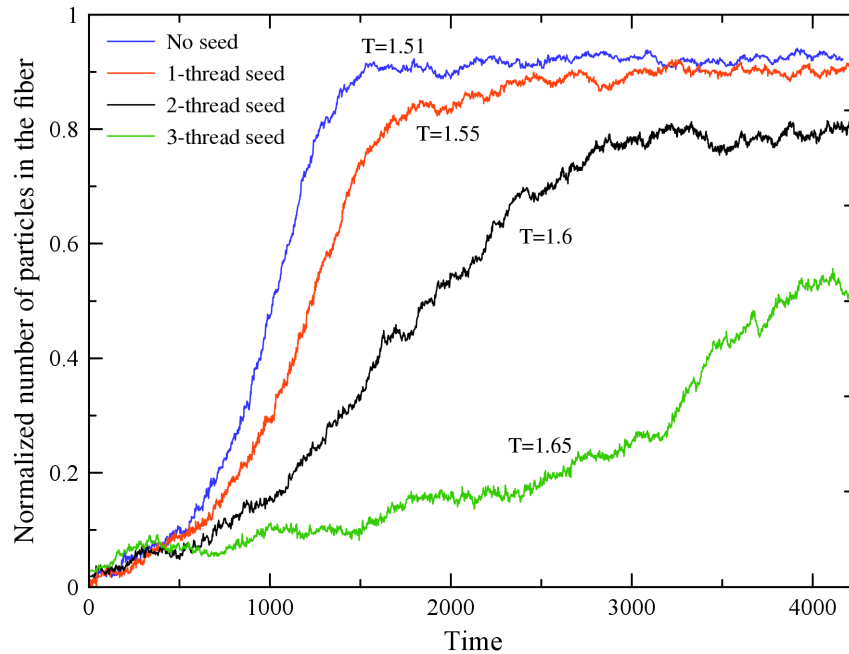


Figure 4.19: Normalized number of particles in the formed fibre in each investigated system versus reduced time ($\kappa = 0.345$, $\kappa' = 0.15$). To aid comparison, all graphs are drawn from the beginning of the fibre growth phase and any latency prior to fibre initiation (few millions MD time-steps) is omitted. The formation temperature for each system is written next to the associated graphs. The system with the 3-thread seed continued to grow beyond the time window shown here.

In each of these examples of seed-enabled fibre formation, it is noteworthy that the resultant assembly achieved essentially the same cluster size as that of the heated fibre at the corresponding temperature. This suggests the existence of a well-defined ‘fibre state’. Time-lines of the respective fibre formation processes (Figure 4.19) indicate that, while the presence of seeds made fibre formation viable at increased temperatures, the timescales associated with the assembly were extended, significantly in the case of the three-thread seed. It is also apparent, from Figure 4.19, that fibre growth was essentially monotonic for all three of the seeded systems shown here and

4.4 Kinetics of Fibre Formation

did *not* suggest coexistence between states with similar free energies. This provides yet more evidence that the fibre branch represents the thermodynamically stable state for much of the thermal hysteresis loop depicted in Figure 4.15, and that kinetic trapping, that is the absence of an accessible kinetic pathway, was central to these systems remaining isotropic down to the temperatures shown in Figure 4.2.

4.4 Kinetics of Fibre Formation

In this section, the kinetics of fibre self-assembly and the pathway from isotropic state to the fibre state are discussed. Particularly, focus is given to the pre-assembly and growth phases of fibre formation. This is achieved by investigating snapshots and videos of the simulated systems and also comparing statistical data of different stages. Here, the particles with the shape parameter of $\kappa = 0.345$ are studied.

On cooling initially isotropic systems of 600 GB discs from high temperature, systematic changes were observed in the averaged proportions of particles identified either as monomers or as being in threads of various lengths. This behavior is exemplified by the data shown in Figure 4.20 for the system $\kappa = 0.345$, $\kappa' = 0.15$, which indicates how the monomer number dropped and the numbers of particles in dimer and trimer stacks increased as temperature was decreased from 1.74 to 1.52. At each of these temperatures, a dynamic equilibrium was achieved in the monomer, dimer and trimer numbers. Within each simulation, this was characterised by continuous making and breaking of highly mobile threads and, occasionally, short-lived, multi-thread objects.

Figure 4.20 shows that, by cooling down of the isotropic system, the number of monomers decreased, which indicates that the aggregation of particles actively occurred and the extent of this aggregation went up as the temperature was dropped. In all simulations at temperatures above the fibre forming temperature and also in the pre-assembly phase at $T=1.51$, which is associated with a lag-time in the initiation of the fibre (first 3.5 million MD steps not shown in Figure 4.3), there were always some short threads and few small clusters in the system, but they failed to form a multi-thread fibre. These small clusters, which were potential initiation sites

4.4 Kinetics of Fibre Formation

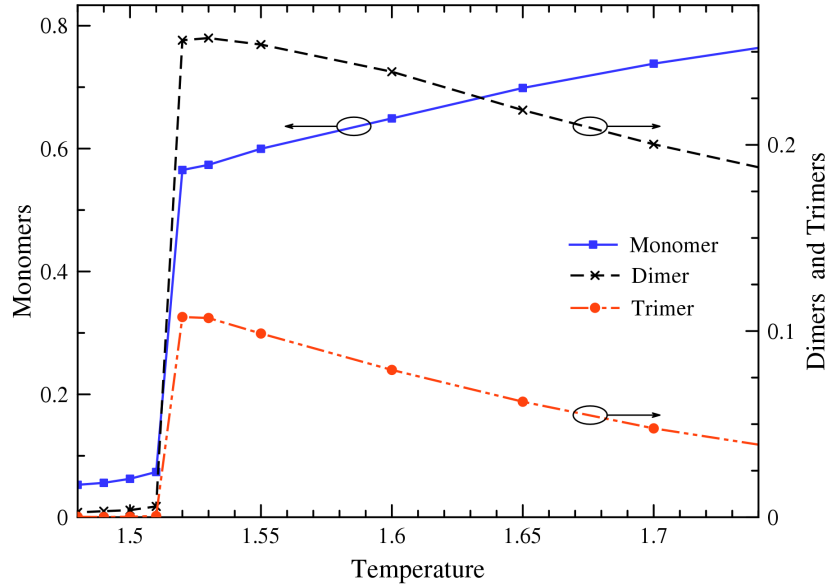


Figure 4.20: Normalized numbers of discs in the form of monomers, dimers and trimers, averaged over the production phases (last 10^6 steps) of a cooling sequence of the $\kappa = 0.345$, $\kappa' = 0.15$ system without seed. Arrows indicate the associated vertical axis for each data set. Maximum Standard Deviation of data is 2.7%, and is not shown for simplicity.

for such a fibre, dissolved into the solution and locked the perseverance needed to interact with other monomers or threads and, so, grow further. In another words, they were not sufficiently long-lived to make a viable initial cluster. However, one may ask why the fibre did eventually form at temperature $T=1.51$ and not at a higher temperature. This can be informed by the so called “mosaic plots”, illustrated in Figure 4.21. In each panel of this figure, all small clusters (not only the biggest one) which formed in the sampled configurations were analysed to determine the probability of finding a cluster with a particular number of threads (N_{Thread}) and particles ($N_{Particle}$) at the investigated temperature. The right panel shows such a probability during the pre-assembly phase (before initiation of the fibre) at the fibre forming temperature of this system. It should be noted that the scale is logarithmic, meaning that there is a 5-6 orders of magnitude variation in the probability data. Here, it was supposed that the shortest thread is dimer and the smallest cluster is a twin with 2 threads and 4 particles. The figure also shows the probability data for lone threads of different length ($N_{Thread}=1$). With decrease in temperature, the chance of having bigger cluster increased - the right top corner of the panels from left

4.4 Kinetics of Fibre Formation

to right changed from dark blue to light blue which is about a 1 order of magnitude increase in probability. For $N_{Thread} = 1$, the distributions are roughly isodesmic [143], with monotonic decay in probability with thread length. For $N_{Thread} > 1$, however, an asymmetrical distribution about a single maximum is seen. For each $N_{Thread} > 1$, the most probable size of cluster shifted up slightly with decrease in temperature - longer threads formed.

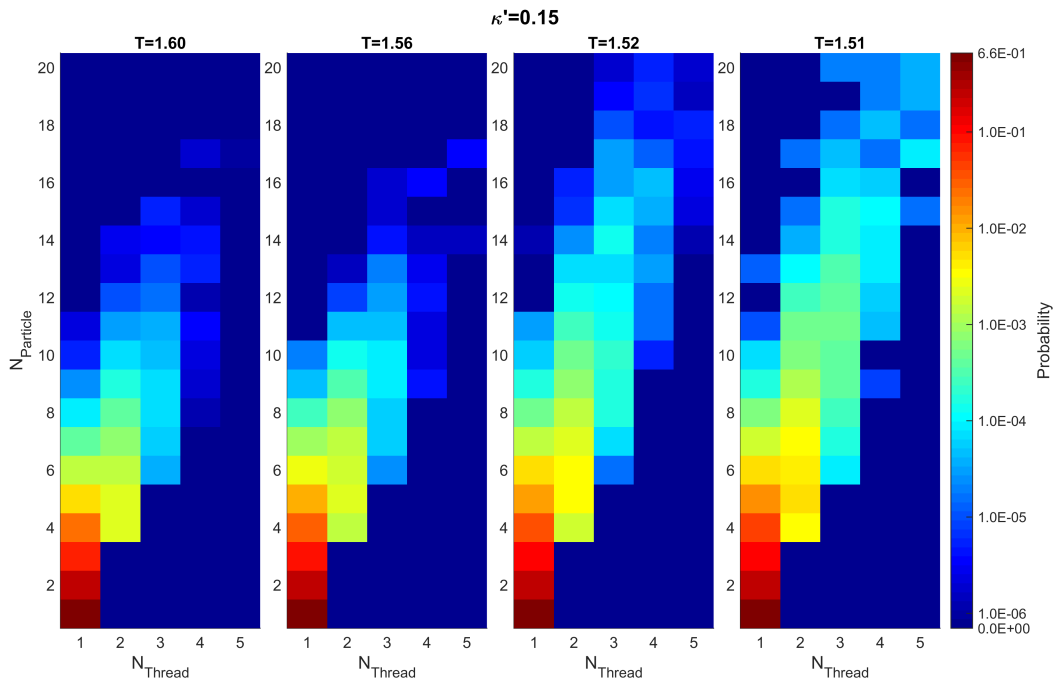


Figure 4.21: Probability of finding a cluster with a particular number of threads (N_{Thread}) and particles ($N_{Particle}$) at different temperatures in cooling down of the system with $\kappa = 0.345$, $\kappa' = 0.15$. The right panel shows the pre-assembly phase at fibre forming temperature. The scale is logarithmic.

We interpret these data in terms of a hierarchy in which a distribution of first generation aggregates (threads) acts as the building material for second (twins) and third (triplets) generation objects. At lower temperature, the chance of dissociation decreases and, so, clusters can persist for longer times. For example, at the fibre forming temperature, the probability of having a 2-thread cluster of 5 particles is about 10 times of that of T=1.60. At that same temperature, however, no aggregates of 5 threads or more were seen, even though it is well inside the thermal hysteresis window shown in Figure 4.15. Thus, the system was kinetically trapped in the

4.4 Kinetics of Fibre Formation

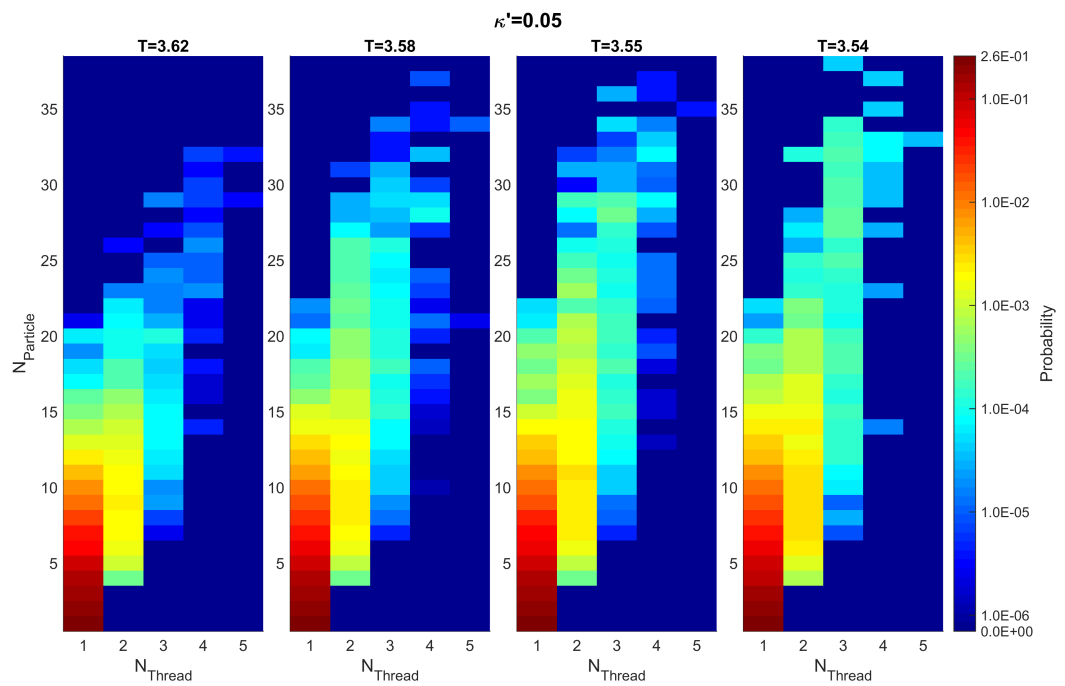
isotropic phase, because it was incapable of achieving the necessary intermediate 5 and 6 thread clusters needed to form a full fibre.

This understanding can be also a complement to the seeding concept studied in the previous section. By seeding, we are, in fact, guaranteeing the presence of a long-lived cluster at temperatures for which the unseeded system had a vanishingly small chance of achieving the same. For example, a 2×5 permanent seed was sufficient to induce fibre growth at $T=1.6$, but an unseeded run at this temperature found such a seed to have probability of 10^{-4} . Therefore, the seeded system could explore the regions of the phase space which were effectively inaccessible without the seeds at that temperature, and consequently, was able to overcome the barrier of nucleation, and eventually form the fibre.

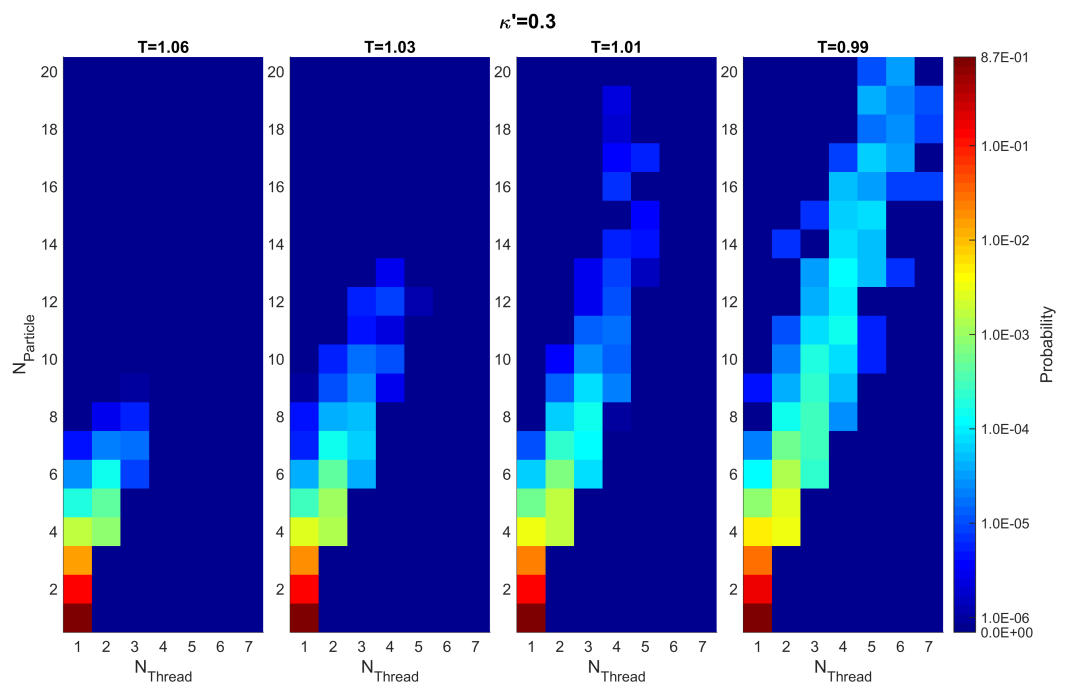
Figure 4.21 also gives some information about the most probable state of formed clusters. For this system with $\kappa' = 0.15$ at the pre-assembly phase of $T=1.51$, for example, it is more likely for a 3-thread cluster to have 11 particles. Definitely, this is a function of the relative strength of face-face interaction of particles, as illustrated in Figure 4.22 showing the same plots for other investigated systems with $\kappa'=0.05$ and 0.3 . For these two κ' values at their pre-assembly phase of fibre forming temperatures, the most likely cluster of 3 threads have 27 and 8 particles, respectively. These three mosaic plots also depict that the systems with different anisotropy parameters explore different regions of the phase space (at least in terms of number of particles and threads in the cluster) to form a fibre. For $\kappa' = 0.3$, only 4% above the fibre formation temperature, the system never had the chance to form a cluster with more than 14 particles, and therefore, a multi-thread fibre was never observed at this temperature.

Now, by having a better picture of the pre-assembly phase, we can study the growth phase of fibre formation to understand the pathway of self-assembly of multi-thread fibres from discotic particles. The results of this work also confirm that the formation of highly elongated stacks of molecules involves a hierarchy of interacting processes [31–33]. In such a hierarchy, the highest-order object is generated via a cascade of lower-order structures which themselves develop through a series of interconnected or cooperative processes. In the growth phase, the building-blocks'

4.4 Kinetics of Fibre Formation



(a) $\kappa' = 0.05$



(b) $\kappa' = 0.3$

Figure 4.22: Mosaic plots for a) $\kappa' = 0.05$ and b) $\kappa' = 0.3$. See caption of Figure 4.21.

4.4 Kinetics of Fibre Formation

interactions lead to formation of small threads. The length of these threads varies with the energy anisotropy of particles interaction (see Figures 4.21 and 4.22). By lateral association of these threads, small clusters of 2 threads (twins), 3 threads (triplets), etc. form. However, these processes are bi-directional - making and breaking scenarios both happen. This is illustrated by the first half of the suggested pathway shown in Figure 4.23. This formation and dissociation happened in the pre-assembly phase of the formation temperature and also at higher temperatures as discussed above. Provided a small cluster persists for a sufficiently long time, however, a 7-thread twisted core can form in the system. Investigation showed that, as soon as a complete layer of threads forms around the central thread, system growth is irreversible and dissociation does not happen. Instead, this twisted core continues to grow in both lateral and longitudinal directions and, eventually, a twisted multi-thread fibre forms (Figure 4.23). For the straight fibres which were initially straight ($\kappa' = 0.05$ of shape parameters $\kappa = 0.345$ and $\kappa = 0.4$), the same pathway in which the initial core is straight can be suggested. A video of the system with $\kappa = 0.345$, $\kappa' = 0.15$, included as Appendix D, shows this hierarchy by visualizing all clusters which form in the course of simulation. From this, many making and breaking events of thread twins are apparent prior to the one that goes on to form the fibre.

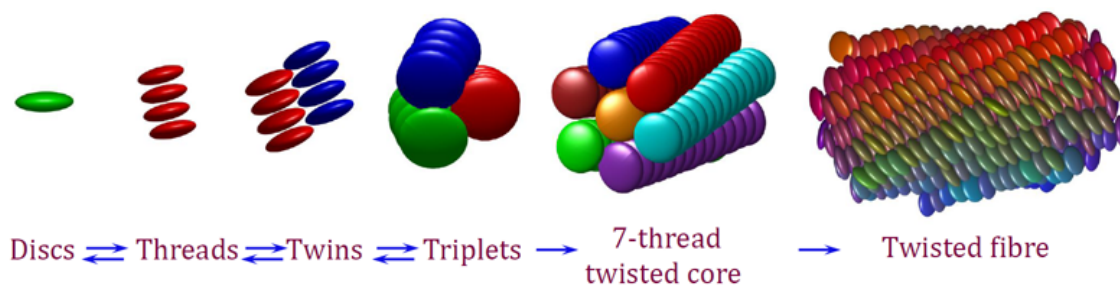


Figure 4.23: A hierarchical pathway for self-assembly of multi-thread twisted fibres from discotic building blocks for the system size studied here.

The probability plot for the entire assembly can give us a better picture of the growth trajectory explored by the system on route from the isotropic state to the final fibre. Such a plot is shown in Figure 4.24a for the system with $\kappa' = 0.2$ at its fibre forming temperature. For the system size investigated here, when the fibre is

4.5 System Size Effects

initiated, it remains the only cluster in the simulation and another cluster rarely forms in the system. Therefore, the pathway, which can be followed in this figure, only gives information about the growing fibre. The vertical lines marked in this figure, illustrate the number of threads associated with the formation of a complete layer of threads (different layers of threads are coloured differently in Figure 4.24b). These correspond approximately to vertical sub-sections in the growth trajectory. This is because, as discussed for the formation of small initial core, when a thread layer completes, it acts like a one-way valve - the cluster rarely goes back through it, instead continues to grow and have its number of threads increase.

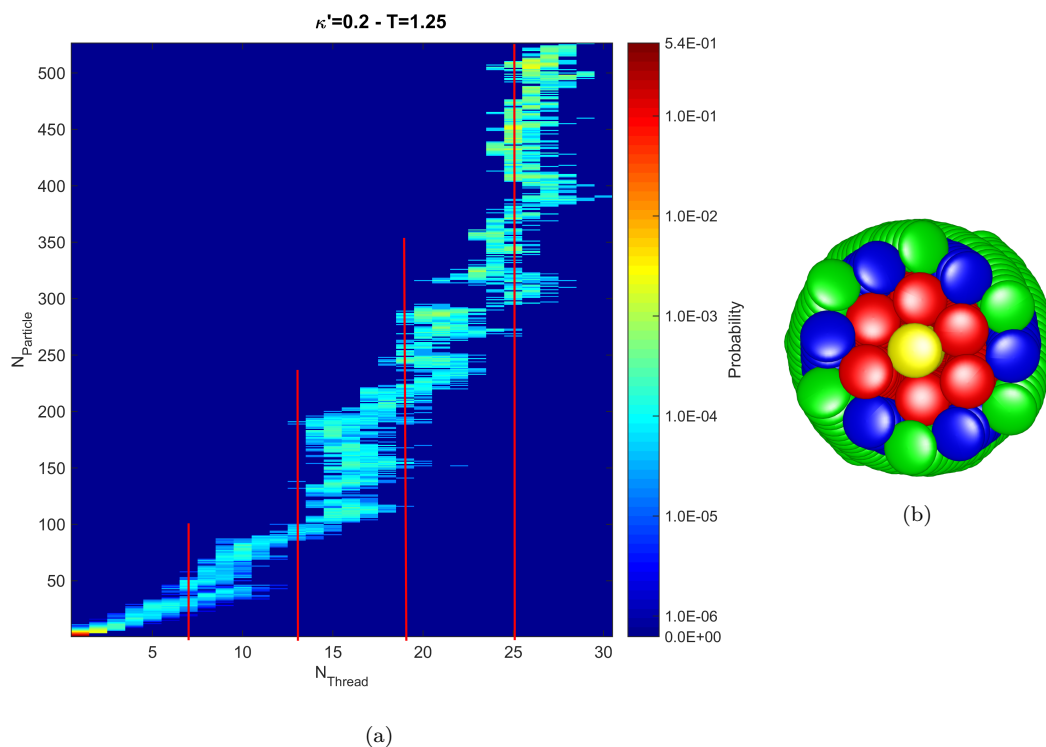


Figure 4.24: a) The mosaic plot for all three phases; pre-assembly, growth and steady-state, of the system with $\kappa = 0.345$, $\kappa' = 0.2$, at its fibre forming temperature, $T=1.25$. b) A perfect twisted fibre with distinct layers of threads.

4.5 System Size Effects

In previous sections, using a relatively small size of simulation, we have shown that many interesting phenomena occur in the self-assembly of fibres formed by

4.5 System Size Effects

discotic building-blocks. We observed that, even in this small size, some features of the growing fibre such as its pitch length and order parameter can change during the growth. On the other hand, it has been argued that in a bundle of twisted filaments (a continuum representation of threads in a twisted fibre), filaments with larger radius have increased curvature with a bending energy cost that scales as r^4 [137]. This size-dependent cost can act as a self-limiting factor which controls the lateral size of the object - twisted bundles have to have finite radii. These together provide motivations for studying the same procedure of fibre self-assembly but in a substantially bigger system. Here, therefore, we perform simulations for 20,000 discs with $\kappa = 0.345$ and a range of κ' values. The same number density is used as for the previous sections, $\rho = 0.075$, which means that the cubic box length was 64.36 disc diameters. Direct cooling from isotropic configurations at high temperatures was used to identify the fibre forming temperature for each system.

Investigations showed that the fibre forming temperatures for the significantly bigger systems were slightly higher than those for the simulations with 600 discs plotted in Figure 4.2. This 2.5-4% increase in the formation temperature (compared in Figure 4.25) can be due to the fact that, by an increase in the number of building blocks in the system, the probability of formation of intermediate clusters (first half of the pathway illustrated in Figure 4.23) was boosted, and therefore, there was more chance to have a sufficiently long-lived small cluster which could act as the core site of the growth.

Similar to the previous sections, the initial 7-thread core for the strongest face-face interaction ($\kappa' = 0.05$) of the disc thickness of $\kappa = 0.345$ was straight and it grew without observation of chirality. On the other hand, the systems with other investigated energy anisotropy parameters were initially twisted, and then, during the growth, underwent various untwisting scenarios which were not observed for smaller systems with the same inputs. To be able to compare with the data for the system with 600 discs presented in Figure 4.3, we focus on the system with $\kappa' = 0.15$. The time lines of data for the growth phase of this system at formation temperature of $T=1.57$ are illustrated in Figure 4.26.

4.5 System Size Effects

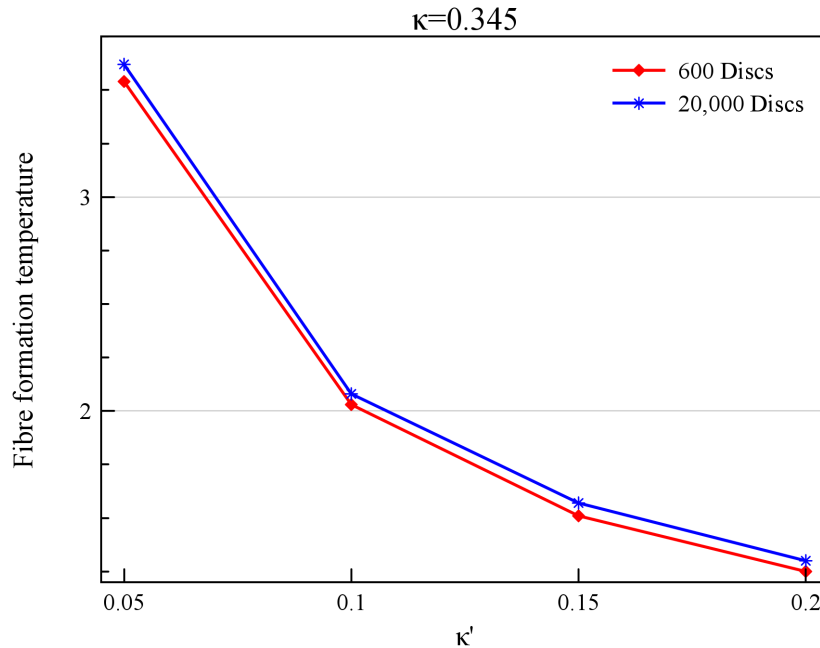


Figure 4.25: Fibre forming temperature for two system sizes studied in this work for discs with $\kappa = 0.345$.

It was observed that, for the bigger systems also, when the growth was initiated, it continued until almost all the particles in the simulation became a part of the fibre - percentage of particles in the fibre reached 90%. The curves for the number of particles and threads are monotonic which means that the object grew in both lateral and longitudinal directions. This is also shown in Figure 4.27 from plots of the time lines of the radius and length of the fibre. Both the fibre length and radius increased almost linearly with time, while the rate of longitudinal growth was about 6 times the radial one. By careful examination of the radius curve, one may capture a slight (maybe negligible) amount of downward concavity, particularly at the first few million steps, which means that, as the fibre grew, the tendency to grow laterally slightly dropped. The unmatched rates of growth in the two directions caused the aspect ratio of the fibre to increase in time. This behaviour which was not noticed in the smaller system size (possibly due to small variation of data) can be also seen in the graphs of normalized Moments of Inertia, labelled by N-MoI in Figure 4.26. The difference between the largest and smallest MoIs of the fibre increased with time, which depicts that the fibre became elongated as it grew.

4.5 System Size Effects

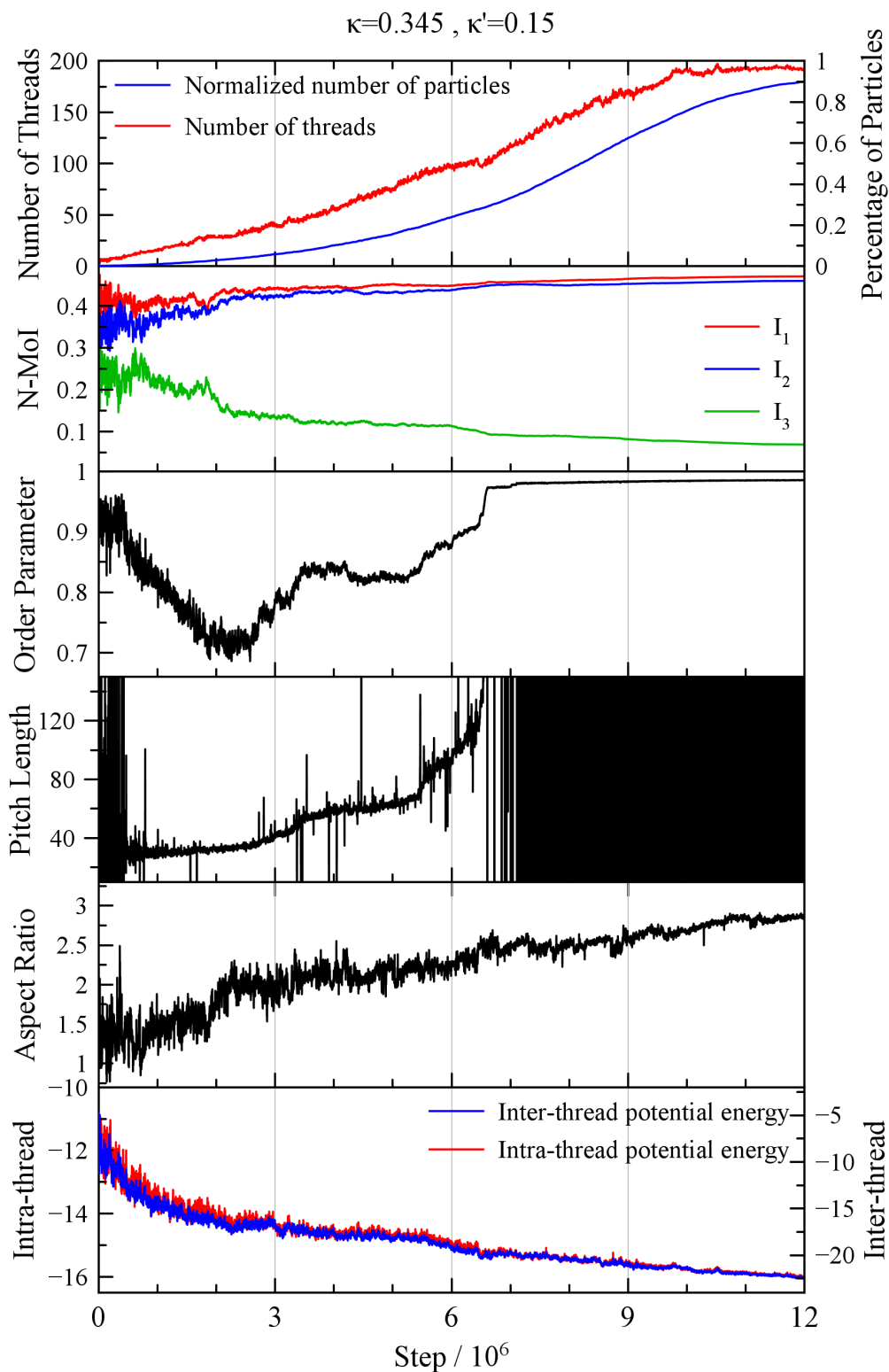


Figure 4.26: Time lines of different parameters measured at the growth phase for the big system ($N_{Particle} = 20,000$) with $\kappa = 0.345$ and $\kappa' = 0.15$ at fibre forming temperature $T=1.57$. The time-lag for the initiation of the fibre (first 3.91 million steps) was omitted and the curves shifted to the beginning of fibre growth.

4.5 System Size Effects

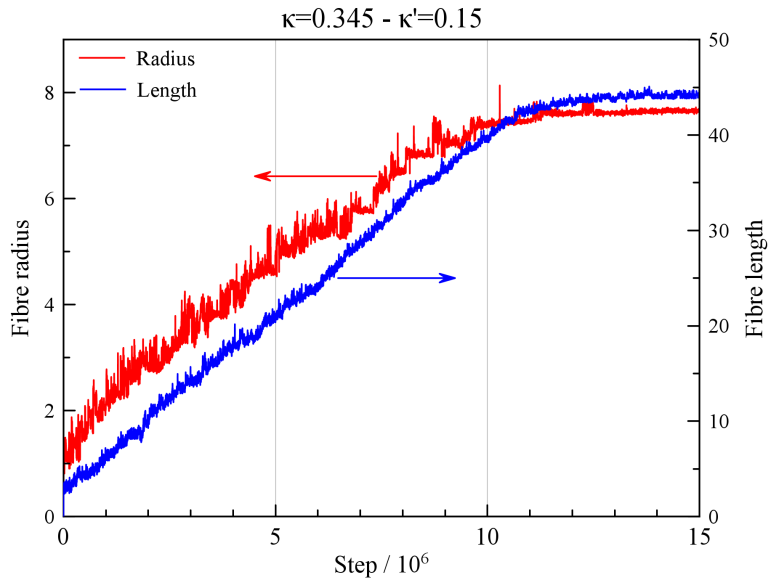


Figure 4.27: Time lines of of fibre radius and length for the big system ($N_{Particle} = 20,000$) with $\kappa = 0.345$ and $\kappa' = 0.15$ at fibre forming temperature $T=1.57$. The arrows point at the associated vertical axis of each curve.

The most interesting behaviour observed in the systems with bigger sizes was the untwisting of the twisted fibres. Similar to smaller systems, the discs with κ' values larger than 0.05 initially formed twisted fibres. Change of handedness was the feature of the initial small cluster (note the large variation of pitch length at the very beginning of the growth), but it was locked in place when the object became larger than 7 threads and the pitch length was stabilized at 30 disc diameter. From this point, the lateral growth of the object led to a drop in orientational order parameter and also a slight increase in the pitch length. These features were also seen in the smaller system size, but what is new for this κ value occurred from about 2 million steps after the initiation of the fibre. The decaying order parameter was arrested at about 0.7 and then reversed toward a temporary plateau at 0.83. This period was associated with an increase in the pitch length of the fibre at a higher rate than that observed previously. At the end of this levelling-off, the pitch length had almost doubled and reached a value of 65 disc diameters. From MD step of 5.2 million, the fibre underwent a second untwisting scenario as indicated by rapid changes in both order parameter and pitch length. This is where the fibre became totally untwisted into a perfect straight fibre with infinite pitch length and high order parameter. A

4.5 System Size Effects

video of this system available in Appendix D can shed some light on the process of untwisting.

Some snapshots from different stages of this transition are shown in Figure 4.28. The twist is apparent (note the slight change of colour along the threads) from the snapshots of the fibre until the final jump in the order parameter and pitch length happened and it became a straight fibre. By following the individual threads during the untwisting, it is clear that they did not break as the fibre straightened - the morphological change was an en masse untwisting with the threads maintaining their integrity. The overall shape of the fibre is a function of its local packing, for hexagonal packing in twisted fibre, the cross-section is circular, while the final straight fibre surface is faceted with an uneven hexagonal shape. That is, the micro-structure features are inherited to the supramolecular length-scales.

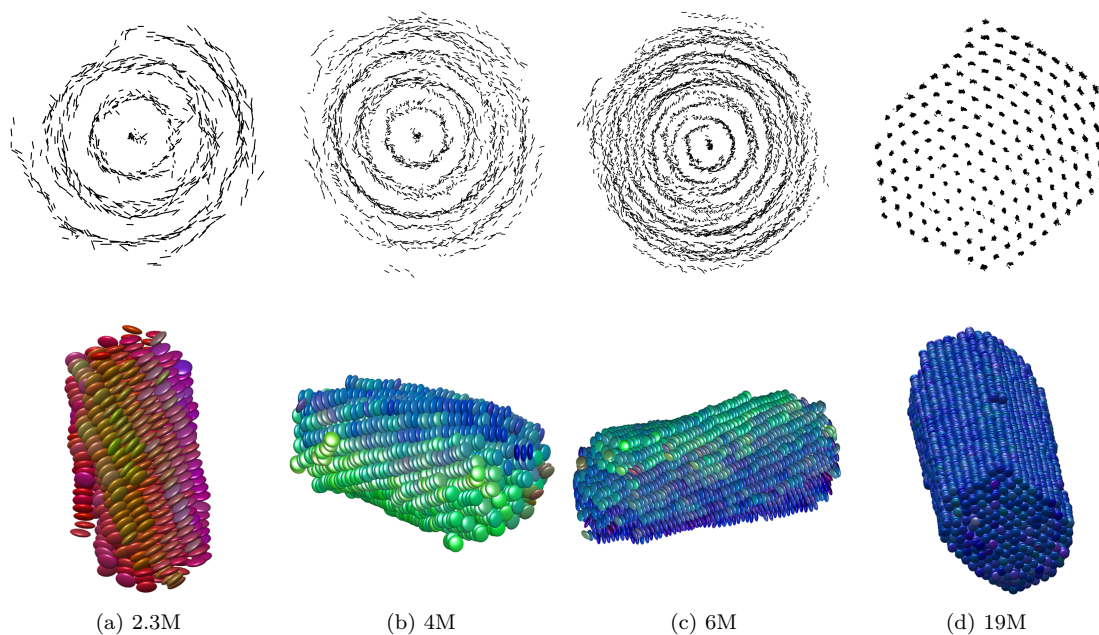


Figure 4.28: Top panel: The short axes of the discs in the fibre formed in $\kappa = 0.345$, $\kappa' = 0.15$ system, viewed along the director. Bottom panel: The snapshots of the associated fibres. The time step at which the configurations are taken are written below each column and are consistent with those presented in Figure 4.26. The right column is the final steady-state configuration of the fibre. The letter M stands for million.

The bottom window of Figure 4.26 shows intra- and inter-thread energies per particle averaged over all threads of the fibre. Both energy plots follow the same trend and drop as the fibre grows. As the motivation for the twisted fibre to undergo

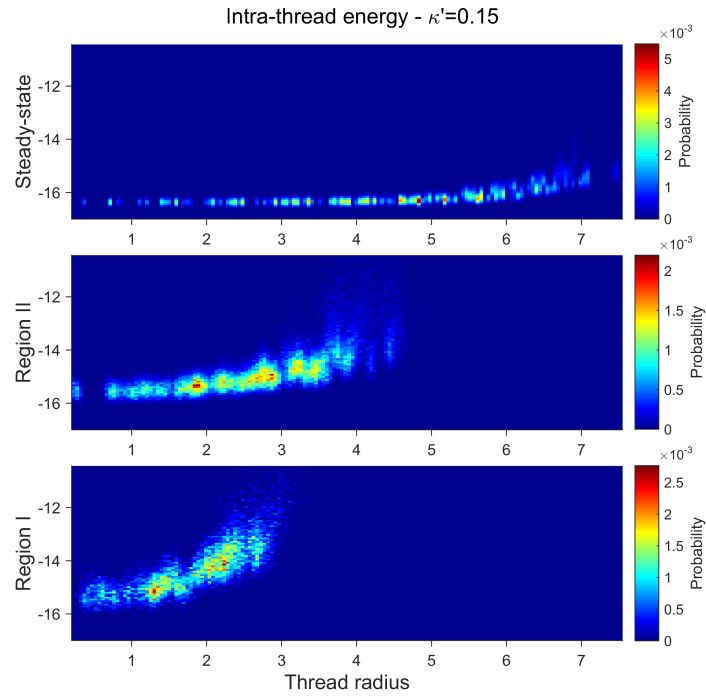
4.5 System Size Effects

the discussed transition and become straight is energy gain, we expected to see more distinct features in these plots. In order not to miss any feature due to averaging, we investigated the energy of each thread in the fibre. Figure 4.29 shows the probability plots for finding a thread with particular intra- or inter-thread potential energies at a radial distance from the centre of mass of fibre (similar to Figure 4.13). In this figure, the plots labelled regions I and II were sampled over subsections of the aggregation corresponding to the constant P_2 windows before the partial and complete untwisting, respectively. These sampling windows are marked in Figure 4.30 by R_I and R_{II} .

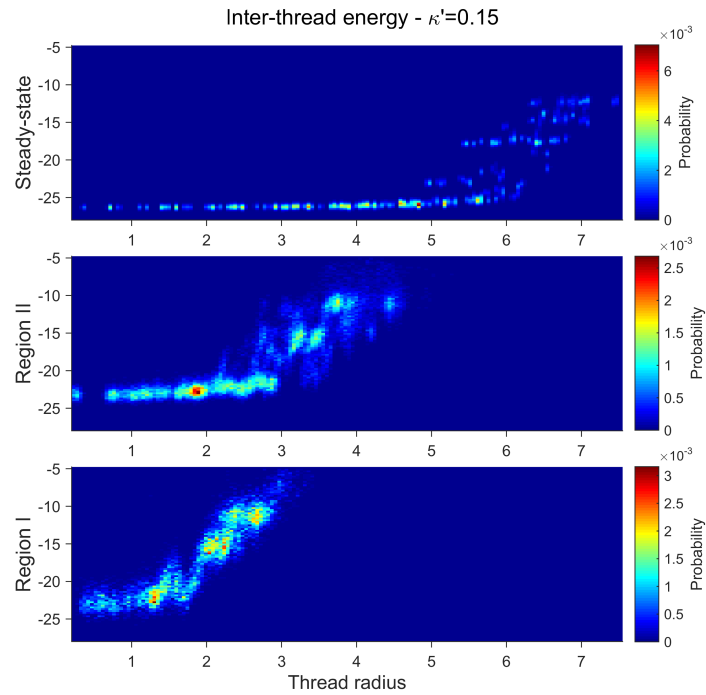
The intra-thread energy plots of Figure 4.29 show that the lowest energy level occurs at the central threads with the smallest radii. Although we expected that by an increase in the radius of the object, the central threads experience compression and, therefore, they might be shifted away from the minimum of the face-face energy curve (Figure 3.2), this is not apparent from these data - the central threads always had the lowest intra-thread energy. In twisted fibres (Regions I and II), the intra-thread energy was a function of location of thread in the fibre - the surface threads had weaker face-face interactions (about 15%). This is possibly due to the increased tilt angle of particles in the outer layers. The fibre were able to counter this by gradually increasing their pitch length between Regions I and II. Therefore, for example, the threads at radius of 2 disc diameters in Region II, with higher pitch value and less tilt angle of particles, had lower intra-thread energy than their counterparts in Region I. In the straight fibre, however, all the threads were equivalent, and had approximately the same value of intra-thread energy - surface thread energies show a slight deviation of about 5%. In addition to less variation, the fibre also benefited from being straight in the sense that the intra-thread energy dropped to lower values, from roughly -15.4 in central threads of Region I to -16.3 in the steady-state phase.

The locations of threads in the fibre are more crucial for the energy gained by interacting with neighbouring threads, as illustrated in the inter-thread energy plots of Figure 4.29b. For twisted fibres, there are at least two factors which affect this energy. One is the number of neighbouring threads - surface threads have fewer neighbours, and consequently, less energy gain of lateral interaction. The other factor is the variation of inter-thread distance with the radius of the threads.

4.5 System Size Effects



(a) Intra-thread energy per particle.



(b) Inter-thread energy per particle.

Figure 4.29: Probability plots of intra- and inter-thread potential energies per particle for the system with $\kappa = 0.345$ and $\kappa' = 0.15$. The range of radii and energies in horizontal and vertical axes of each part is set the same to aid comparison. Regions I and II are defined in Figure 4.30. The steady-state plots were sampled from the last 2 million steps of the simulation (1000 configurations).

4.5 System Size Effects

Hall *et al.* discussed that in a bundle of twisted filament, the transverse distance between filaments increases from the centre of the bundle to its surface [144]. This increased strain causes the threads to have smaller interdigitation, and therefore, the inter-thread energy goes to larger negative values at larger radius. This latter issue, however, is solved in the straight fibre and all the threads, which are not at fibre surface, have the same inter-thread energy level. Hence, the whole fibre has a lower level of energy. These together provide an understanding for the motivation to exhibit an untwisting transition: an increase in the lateral size of the growing fibre is associated with the energetic cost due to the bending (intra-thread) energy and increased lateral distance of the threads (inter-thread energy). Depending on the stiffness of the threads and their lateral cohesion with other threads, at a particular size of the growing object, the energy gains of forming a bigger object do not balance the energy costs. Therefore, the object has to either stop lateral growth or find an alternative solution. Here, we showed that the cluster found this alternative solution by morphing into a straight fibre. This straight structure, then, could sustain lateral growth and so accumulate more than 90% of the material in the simulation box.

The behaviours of other investigated bigger systems with different κ' values are compared in Figure 4.30 by plotting their orientational order parameter time lines. Apart from $\kappa' = 0.05$ system, in which the fibre was straight from the beginning of the growth phase, similar untwisting phenomena were observed for all systems. By an increase in κ' parameter, the time window, in which the transition to straight fibre occurred, increased. Table 4.3 compares some properties of the investigated systems at different stages of the growth marked in Figure 4.30. The steady-state data were averaged over the last 1-2 million MD steps of the simulations, where, in all cases, the order parameter of the fibre was quite high (above 0.97). It should be noted that, since the fibres in Regions I and II were growing objects, the variation of data (Standard Deviation) is higher than that in the steady-state phase. At the beginning of the partial untwisting, just after region I, the sizes of the fibres were larger than the smaller systems with 600 particles that were investigated in the previous sections. This indicates that system size does have an effect on the characteristics which we observe in a simulation. The threshold size of the object for triggering both partial

4.5 System Size Effects

(region I) and complete (region II) transitions were generally dependent on the κ' value, increasing with a weakening of the face-face interaction.

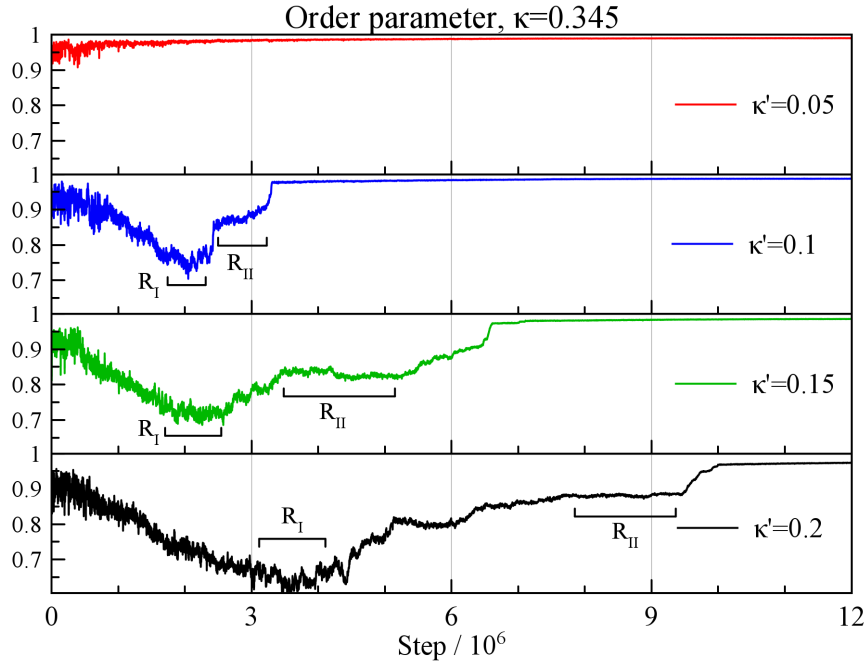


Figure 4.30: Time lines of the orientational order parameter for different investigated κ' values in systems with $\kappa = 0.345$ and $N_{particle} = 20,000$. Regions I and II, being the levelling-off parts before respectively, partial and complete untwisting, are marked in each system. The time-lag in the initiation of the fibre is omitted and the graphs are plotted from the beginning of the growth phase.

In the weakest face-face interaction case, $\kappa' = 0.2$, although the steady-state order parameter of the final fibre was 0.977, which can be an indication of it being straight, the final pitch length for this system was found to be finite but significantly large (about 660 disc diameter). The steady-state length of this fibre was 39.4 ± 0.2 disc diameters which means that only 6% of the full pitch was observable in the fibre. This large pitch length can only be visualized if we look at the object along the threads - Figure 4.31 shows the snapshots of the fibres at different systems. However, the data for the normal distributional functions, plotted in Figure 4.32, show that the the first peak splitting characteristic of the straight fibres (see Figure 4.8) can be also seen in the $g_{\perp}(r)$ data at the steady state phase of $\kappa' = 0.2$ system. The figure also shows that, after the initial partial unwinding, the local hexagonal packing of the particles was slightly distorted and the first symmetric peak began

4.5 System Size Effects

Table 4.3: Averaged properties of systems with 20,000 particles and $\kappa = 0.345$ at different regions in their fibre forming temperatures. Regions I and II were marked in Figure 4.30 and the Steady-state data were sampled over the last 1-2 million MD steps of the simulations. N_P , N_T , P and AR stand for number of particles, number of threads, pitch length and aspect ratio of the fibre, respectively. The figures after \pm signs are the Standard Deviation of data.

	κ'	N_P	N_T	P	AR
Region I	0.1	777 ± 136	33.8 ± 5.7	34.7 ± 3.1	1.72 ± 0.15
	0.15	664 ± 123	29.7 ± 2.3	32.9 ± 1.4	1.84 ± 0.22
	0.2	957 ± 132	41.9 ± 3	34.2 ± 1.4	1.65 ± 0.13
Region II	0.1	1456 ± 219	51 ± 4.4	63.8 ± 9.6	1.68 ± 0.09
	0.15	2394 ± 545	63.1 ± 10.4	59.6 ± 13	2.13 ± 0.1
	0.2	6178 ± 770	115.7 ± 9.2	99.3 ± 5.9	2.2 ± 0.1
Steady-state	0.05	18310 ± 39	157.1 ± 0.3	∞	4.18 ± 0.03
	0.1	18765 ± 39	206 ± 0.3	∞	2.56 ± 0.01
	0.15	18943 ± 34	191.8 ± 0.7	∞	2.95 ± 0.02
	0.2	19081 ± 18	211.9 ± 1.9	661.4 ± 57	2.54 ± 0.02

to maintain a shoulder at larger r_{\perp} , as the object prepared itself for morphing into the final structure. The location of the first peak in $g_{\perp}(r)$ data was slightly shifted to the smaller r_{\perp} values as the growth progressed (about 4% from Region I to the steady state). This suggests that the interdigitation of the particles was enhanced, which may explain the reasons for the increase in the inter-thread energy observed in Figure 4.29b. As discussed before, the change of packing approach of particles caused the overall morphology of the fibre to change from a circular to a faceted object, as illustrated in Figures 4.28 and 4.31.

Incorporating the effects of system size into the fibre self-assembly pathway suggested in the previous section, we can modify the pathway based on the energy anisotropy parameter and also the system size, as illustrated in Figure 4.33. For systems with $\kappa = 0.345$, the bidirectional processes at the early stages of the hierarchy and also the faceted final object are conceptually the same, but the middle stages are a function of the energy anisotropy parameter. For relatively weaker face-face interaction, a transition from the twisted fibre to the straight one occurred in a multi-step fashion, which mainly depends on the lateral size of the object. In the

4.5 System Size Effects

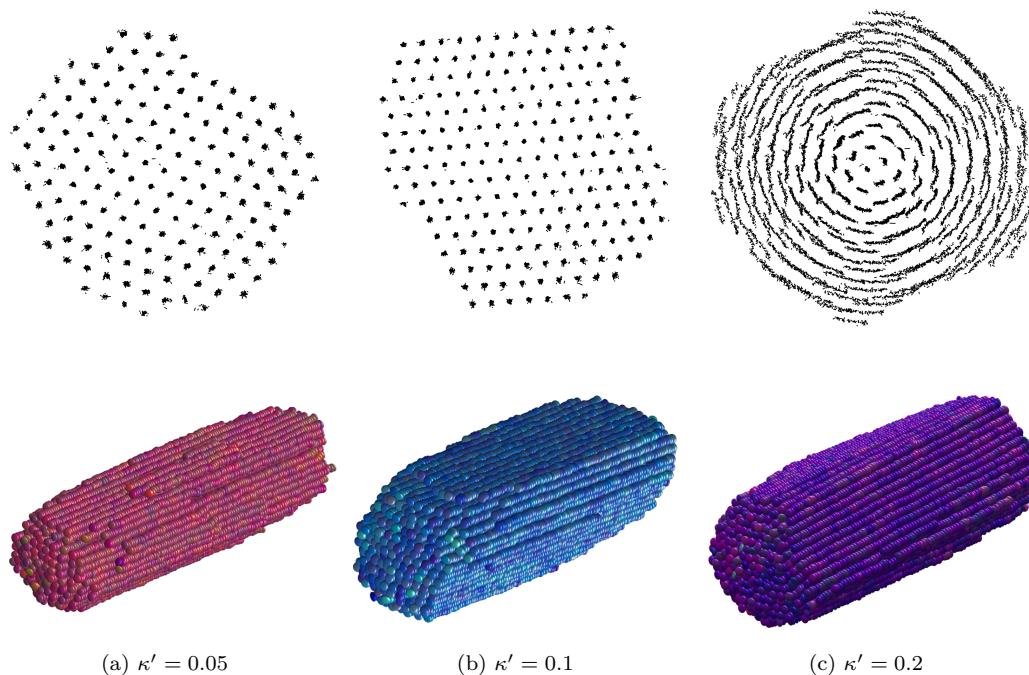


Figure 4.31: Top panel: The short axes of the discs in the final fibre formed in $\kappa = 0.345$ systems with different κ' values, viewed along the director. Bottom panel: The snapshots of the associated fibres.

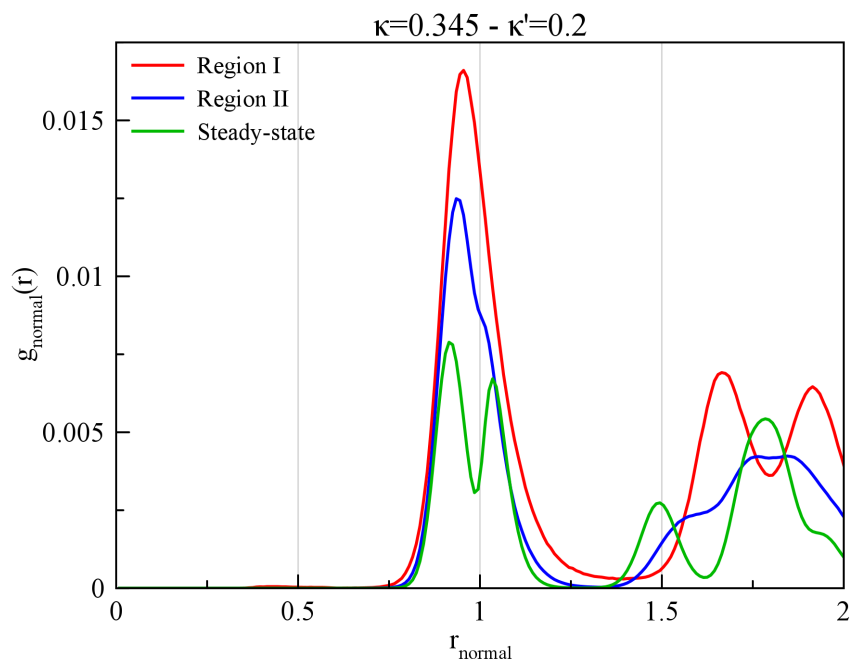


Figure 4.32: Normal distribution function, $g_{\perp}(r)$, at different stages of the growth for the fibre formed in system with $\kappa' = 0.2$. Each set of data is normalized in such a way that the total area be one.

4.5 System Size Effects

$\kappa' = 0.05$ system, however, due to the stiffness of the threads, the initial 7-thread core was straight and the growing object always remained straight.

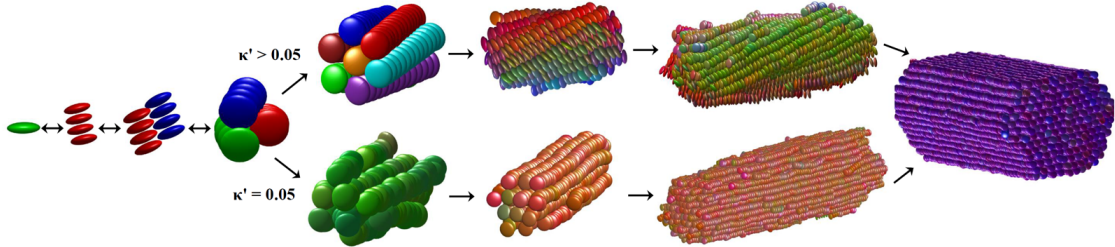


Figure 4.33: A suggested pathway for the formation of faceted big fibres in systems with $\kappa = 0.345$.

Here, thermal hysteresis was also investigated by heating up the straight fibre formed in the system with $\kappa = 0.345$ and $\kappa' = 0.15$. The temperature increment of 0.01 was applied from the formation temperature of $T=1.57$. At each temperature, a simulation of 4 million MD steps was performed. As previously seen for 600 particle systems, the fibre remained intact for a significantly large temperature window - 22.9% above the formation temperature. This again confirms the existence of the thermal hysteresis in the formation of fibres, even in this large system with more scope to explore different regions of the phase space. Figure 4.34 illustrates some data from the heating-up simulations of the investigated system. The particles were shed constantly into the solution - the number of particles monotonically decreased. The number of threads, however, showed a very interesting trend. It remained nearly unchanged up to temperature 1.85 at which point the size of the object had reduced to 1/3 of the initial one. This means that fibre shrinkage occurred entirely by diminishing its length, as confirmed by the data of Moments of Inertia in which the third MoI remained nearly constant, but the other two decreased with temperature. The fibre was straight in almost all temperatures, except when it became very small, having just 19 threads at temperature 1.93. As the data of P_2 shows, at this temperature a drop in order parameter happened and fibre re-twisted. Two small windows in Figure 4.34 show the time lines of number of threads and P_2 at this temperature. The fibre lost its threads in a step-wise fashion (layer by layer). The fibre with just 3 layers of threads managed to re-establish chirality and become

4.5 System Size Effects

twisted. This re-twisting phenomenon can be seen from the sharp drop in the order parameter data at $T=1.93$.

These results indicate, therefore, a further thermal hysteresis which goes beyond that found in section 4.3 for 600 particle systems. Specifically, there is an untwisted fibre state as well as the twisted fibre and isotropic. This explains why the thermal hysteresis observed here is significantly larger than that seen in Figure 4.15. We can also speculate that incorporating direct chiral interaction into the system would offer a route to controlling the relative stability of these states.

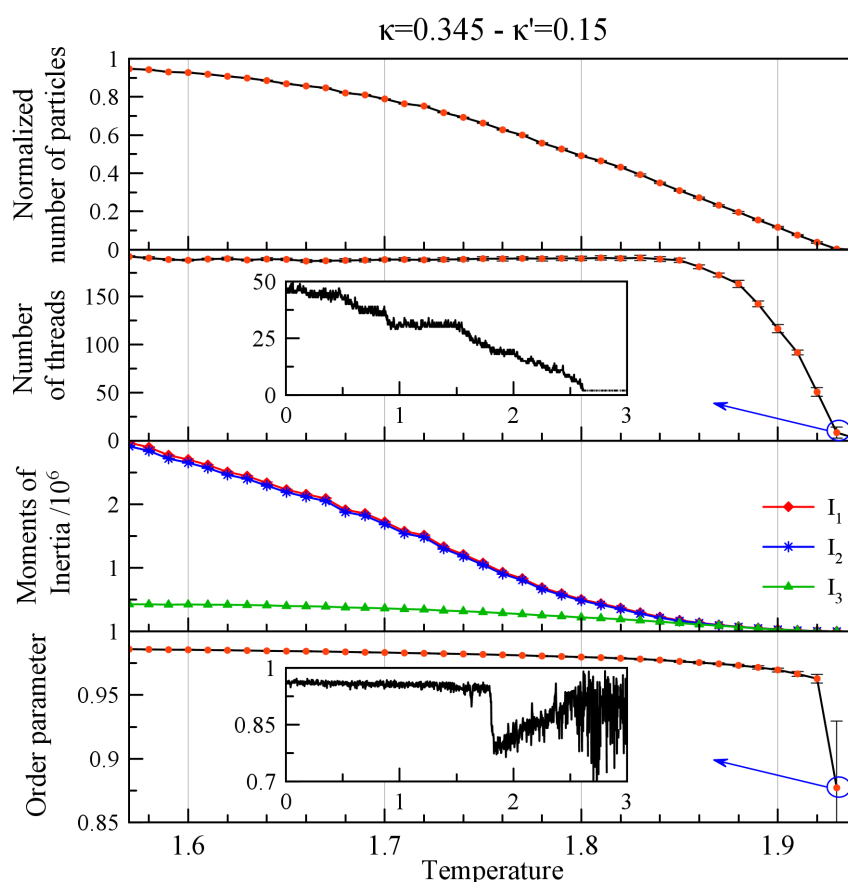


Figure 4.34: Averaged structural properties of the biggest cluster over the production phase in heating simulations of $\kappa = 0.345$, $\kappa' = 0.15$ system with 20,000 particles. The error bars show \pm Standard Deviation of sampled data. Two small windows show the time lines of number of threads and order parameter for the temperature at which the re-twisting of the fibre happens ($T=1.93$). The horizontal axes are the MD time steps in million.

4.6 Conclusions

In this chapter, we have investigated the self-assembly of fibres formed from discotic building-blocks interacting with the Gay-Berne potential. The results show that this fibre formation is fully reproducible and applies over a significant range of particle shapes and interaction strengths. The characteristics of the final objects, including their morphology, chirality, size, etc. were dependent on the κ and κ' values, although they generally showed the same growth pathway. For some systems, untwisting of growing fibres has been observed, an apparent manifestation of the size-dependent morphological changes expected more generally in assemblies comprising chiral filaments [144]. Further, the observation here of spontaneous structural chirality, achieved through self-assembly of achiral objects, feeds into the ongoing debate on complex continua in which it is argued that the character and properties of any dense-phase material comprising such structures are highly sensitive to the interplay of intrinsic stresses and the packing efficiency of different hierarchical components [137].

The fibre-formation process observed here is subject to kinetic trapping, the isotropic phase remaining indefinitely long-lived well below its window of thermodynamic stability. From the range of simulations performed here, it is apparent that the fibre formation curves depicted in Figures 4.2 and 4.25 correspond to the temperatures at which the monomer number fails to achieve steady state until fibre growth is complete. As such, they represent the limit at which the cooled isotropic phase becomes absolutely unstable with respect to aggregate formation. Fibre formation has also been observed at higher temperatures, either through extending simulation times and sizes or introducing seed clusters. Whilst extending run times and sizes only achieved a modest rise in viable fibre-formation temperatures, seeding with permanent clusters yielded irreversible fibre-growth at significantly higher temperatures. Making and breaking of aggregates is a key feature of early stages of fibre growth. The seeds biased this formation and dissociation part of the growth hierarchy and, thereby, provided the systems with a pathway to explore the regions of the phase

4.6 Conclusions

space which were inaccessible without seeds. Therefore, fibres formed at noticeably higher temperatures.

We also showed that the size of the investigated system may play a role in the observable features of the self-assembly. Increased radius of the growing fibre and, consequently, amplified energy costs of bending of the threads due to larger tilt angles could, in principle, stop the growth process. However, instead, the fibre intelligently found an alternative solution by unwinding itself. The step-wise untwisting of the fibre and morphing into a straight object with equivalent threads provided an opportunity for the cluster to consume almost all the material in the simulation and make a very big faceted fibre.

In the next chapters of this thesis, we will study the self-assembly of various supramolecular structures in amphiphilic chromonic systems by simulating mixtures of discs and spheres. By considering the introduced Tanh potential for the disc-sphere interaction, the amphiphilic behaviour will be modelled. We will show how the second species can incorporate into spontaneous formation of chiral structures such as twisted ribbons, tubes and double-helices.

Chapter 5

Twisted Ribbon Self-assembly

The literature shows that self-assembly of twisted ribbons is a remarkably interesting topic which has gained the attention of many researchers [34, 77, 78, 144–147]. Nature also sees the twisted sheet as an interesting morphology when, for example, the flat valves of a type of seed pod morph into twisted objects with different handedness in a humidity-driven process which leads to the opening of the pod [148, 149]. As set out in Chapter 2 twisted ribbons have also been determined to be a potential precursor for tube formation by morphing into helical ribbons in a chiral self-assembly pathway in which the pitch value and also the width to pitch ratio were found to be the keys [77, 78].

Multi-layer twisted bundles, which were observed experimentally [34, 150], are the other member of the broad family of elongated twisted objects. Obviously, having several twisted layers and their incorporation into the stability of the object adds significantly to the complexity of the formation process and make its investigation even more difficult than that of twisted bilayers. Integrity of layers and the requirement to maintain a consistent amount of twist (pitch) in each layer are significant factors in this complexity.

Self-assembly of these twisted objects, which is complex, hierarchical and subject to trapping in metastable states, can be simulated with computational techniques in order to gain more insight on every level of the process. The literature in this area, which was reviewed in Chapter 2, reveals that, breaking the symmetry either

5.1 Introduction

by using chiral building-blocks or through spontaneous emergence of chirality is necessary in such systems. Therefore, the simple one-component system used for simulation of fibre self-assembly in Chapter 4 cannot be appropriate for investigation of twisted ribbon formation. Investigations of Prybytak [5] showed that the coarse-grain simulation of a bipartite system consisting of amphiphilic discs for which the rims are partially attracted to the spheres can, though, lead to the self-assembly of twisted bilayers for particular parameters of the system.

In this chapter, we employ and extend Prybytak's work [5] on breaking the symmetry in disc-sphere systems to study the self-assembly of twisted bilayers formed by amphiphilic chromonics. The effects of the extent of solvophilicity on the properties of the twisted bilayers will be investigated. We will also shed some light on the details of spontaneous symmetry breaking observed in such systems. Self-assembly of a multi-layer twisted bundle will also be presented by employing the multi hot-spot version of Tanh potential introduced in Chapter 3. Finally, the morphological transition of a chiral cylindrical object into a twisted ribbon structure due to geometrical frustration, which has been experimentally observed and theoretically predicted [144], will be reported.

5.1 Introduction

The aims of this chapter are to shed more light on the different stages of twisted bilayer self-assembly by amphiphilic chromonics, initially performed by Prybytak [5], and then to determine the effects of system parameters, particularly the extent of the solvophilicity of discs, on the self-assembled objects and their structural properties. Investigation of geometrical frustration in such systems and, also, spontaneous formation of multilayer twisted bundles are the other objectives of this part of the current thesis. In the following, some general details of the simulations performed will be presented. The differences of systems studied in each part of this chapter will be highlighted later, when we discuss each particular system.

Here, we used MD simulations of mixtures of amphiphilic discotic building-blocks and simple Lennard-Jones spherical particles. The interaction of discs was governed

5.1 Introduction

by the conventional GB potential discussed in the previous chapters. The Tanh potential introduced in Chapter 3 was used to break the symmetry of the disc-sphere interaction and achieve the amphiphilic properties of the discs. However, there are still no chiral terms in the potential and, therefore, the particles are achiral. For each investigated system, the initial configuration was isotropic with random translational and rotational distributions of particles, equilibrated at high temperatures ($T=4.5-5$). By a trial-and-error procedure, the direct cooling approach (see Chapter 4) was performed to find the highest temperature at which only one aggregate formed in the system. Constant-NVT ensembles were simulated by applying the Nosé-Hoover thermostat on mixtures of discs and spheres at total number density of 0.22. Two different system sizes with 3000 and 6000 discs and 10,000 and 20,000 spheres, respectively, were simulated here, but for both, the number densities of discs and spheres were set to be 0.051 and 0.169, respectively. That is, the side of cubic periodic box was 38.95 and 49.07 disc diameters for each system size. A time-step of 10^{-3} time unit was used for all systems investigated in this chapter.

Here, the shape parameter of $\kappa = 0.345$ was used for the discs. The diameter of spheres was fixed to be the same as the thickness of the discs and, thus, $d_{sphere} = 0.345$. Therefore, the LJ potential parameters introduced in equation (3.34) for spherical particles were $\epsilon_0 = 1$ and $\sigma_0 = 0.345$. The usual unity values for the same parameters were used in the interaction of discs, while the σ_f parameter was the same as the thickness of the disc, $\sigma_f = 0.345$. The energy constants of μ and ν in the GB potential were, as before, 1 and 2, respectively. For these parameters, the value of disc-disc potential well-depth at edge-edge configuration is 2.63 (see Table 5.1). The energy anisotropy parameter for the discs in each system was varied and will be discussed below.

For the GB part of disc-sphere interaction, the ϵ_0 parameter (potential well-depth of edge-sphere configuration) was chosen to be 2, slightly smaller than the disc-disc potential well-depth at edge-edge configuration. The size parameter, σ_0 , can be also determined from equation (3.39), being 0.748 for the particles simulated in this chapter (see Table 5.1). The disc-sphere energy anisotropy parameter was set to be $\frac{\epsilon_{fs}}{\epsilon_{es}} = 0.2$, that is, the spheres were more attracted to the edge of the discs. The

5.2 Twisted Bilayers

Table 5.1: Disc-disc potential well-depths at edge-edge configuration and the zero-repulsion distances (σ_0) for disc-sphere systems for some shape parameters of the discs, κ , studied in this work. In disc-sphere interaction, it was supposed that the diameter of the spheres is the same as the thickness of the discs.

κ	0.25	0.3	0.345	0.4	0.45
well-depth	4.516	3.3	2.63	2.103	1.785
σ_0	0.7289	0.7382	0.748	0.7616	0.7754

modification parameter of $\beta = 1$ was used. Single- and double hot-spot versions of the Tanh potential were applied to model the amphiphilic behaviour of discotic building-blocks - the double hot-spot potential was used to simulate multi-layer bundle self-assembly. The ϵ_{max} and ϵ_{min} parameters of this potential were set at 5 and 0.2, that is, the strength of disc-sphere interaction in the hot-spot zone was 5 times stronger than its normal value. This caused the parameters a and b to be 2.6 and 2.4, respectively. The cross-over parameter l was set to be 0.1. The extent of the solvophilicity of the discs was controlled with the H parameter in the Tanh potential. The H parameter is a measure of the percentage of the rim which is strongly attracted to the spheres. Disc-sphere potential contours for the systems studied in this chapter have been plotted in Figures 3.8 and 3.9. In all simulations, the variable cut-off radius approach, introduced in section 3.4.3, with $\sigma_{cut} = 0.65$ was used.

5.2 Twisted Bilayers

Following the work of Prybytak [5], in this section, disc-sphere mixtures with a single hot-spot model were simulated. The investigations showed that, for a range of H parameter from H=20 to H=50, a twisted bilayer is self-assembled by the system. As the formation pathway for these systems is more or less uniform, similar to the approach of Chapter 4, we will present one of the systems in detail and discuss its formation pathway and the emergence of twist, before averaged properties of other systems with different H values are compared. The significant differences of these systems will be highlighted where necessary.

5.2 Twisted Bilayers

5.2.1 Bilayer formation

Twisted bilayer self-assembly in a system with 3000 discs, having κ' parameter of 0.075 and H parameter of 20, and 10,000 spheres was studied. By a direct cooling procedure, the temperature of $T=2.77$ was found to be the optimum temperature leading to formation of a single cluster in the system. The formation and dissociation of small clusters, observed in the early stages of fibre self-assembly in the previous chapter, was also a feature of the amphiphilic system studied here. The small clusters formed in the early stages consisted of few threads of discs, the integrity of which was stabilized through their interaction with a flexible bunch of spheres in the middle. Figure 5.1 shows snapshots of the biggest clusters formed in the system before the initiation of a permanent object. The spheres in the cluster formed a layer structure and the discs were located at each side of this sphere layer. The orientations of the hot-spot regions were mostly toward the spheres, showing that the sphere-disc interaction was a significant factor for formation of the cluster, although a few discs were also observed whose incorporation into the object were dominated by their interactions with others discs in their threads (see Figure 5.1b for some examples of this situation). For these small clusters, as the change of disc colour suggests, the relative orientations of the threads were not fixed in the cluster - in some cases, the threads in each leaflet even made a 90° angle with each other (Figure 5.1b). However, as the formed object became larger, the tendency of threads at each leaflet to be in a near-parallel configuration increased.

After about 5.5 million MD steps, one of the small formed objects in the system remained viable and never dissolved. This cluster went on grow and become the main and only large aggregate in the system at temperature $T=2.77$ (see the number of particles plots in Figure 5.2). Visualization showed that the formed object was a bilayer with two leaflets of nearly parallel discs sandwiching a layer of spheres (Figure 5.3). This bilayer grew in two directions, sideways and also along the threads. Addition of new small threads to the side of the sheet mostly happened through interaction of hot-spots of those discs and the spheres at the edge and, therefore, on many occasions the side threads sat in the middle of the bilayer, only joining a

5.2 Twisted Bilayers

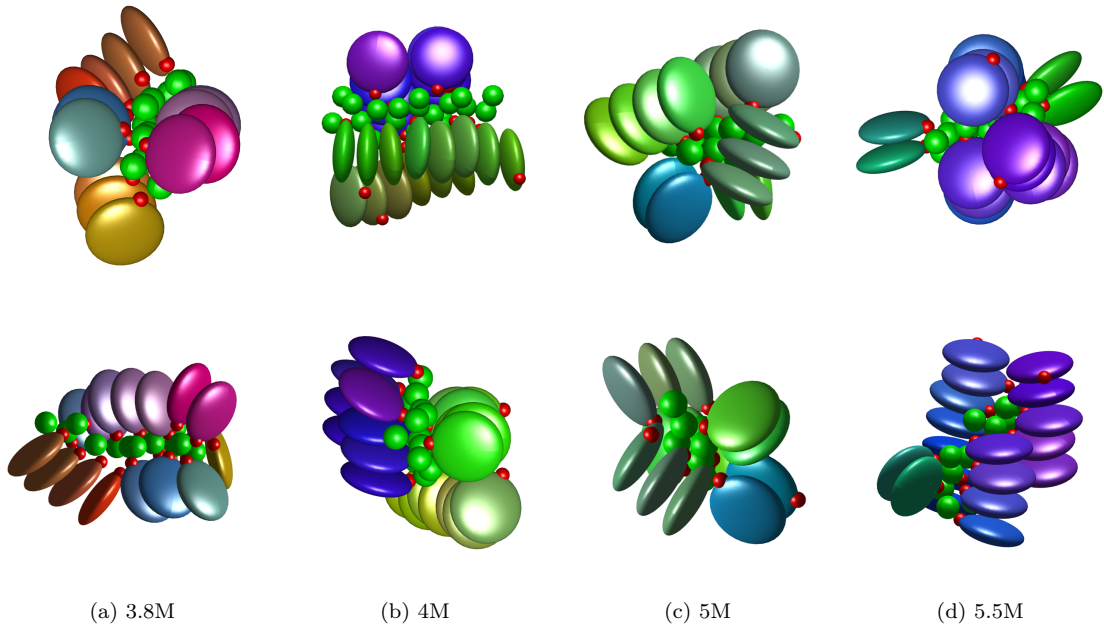


Figure 5.1: Snapshots of the biggest cluster formed in the system with $H=20$, before the initiation of the permanent cluster. Each column shows the snapshots of the same system from different angles. Discs are coloured based on their orientations and the spheres are green. Little red spheres only show the core of the hot-spot region for each disc and are used as a guide of the eyes. The MD step at which the snapshots were taken is written for each column. The letter M stands for million.

specific leaflet at a later stage (one example is shown in Figure 5.3d). The growing twisted bilayer reached its steady properties after about 15-20 million MD step. However, the simulations were run on upto 40 million steps to be sure that the object remained stable and its properties did not change. Figure 5.4 shows the formed twisted bilayer at the end of simulations from 3 different orthogonal views. The short axes of the discs comprising the threads in both leaflets are also illustrated in this figure.

As the snapshots of the formed bilayer in Figures 5.3 and 5.4 show, the threads in each leaflet had a near identical preferred direction, as the high order parameter at the early stages of the growth in Figure 5.2 suggests. However, the threads in each layer had a small angle with the other layer (10-15 degrees) which provided an anisotropy for the structure (see Figure 5.4d). This asymmetry in the layers introduced a twist in the bilayer and both the disc leaflets and the sphere layer became twisted. At the early stages, when the object was still small (5-7 threads), the handedness of this twisted bilayer was not fixed and both left- and right handed

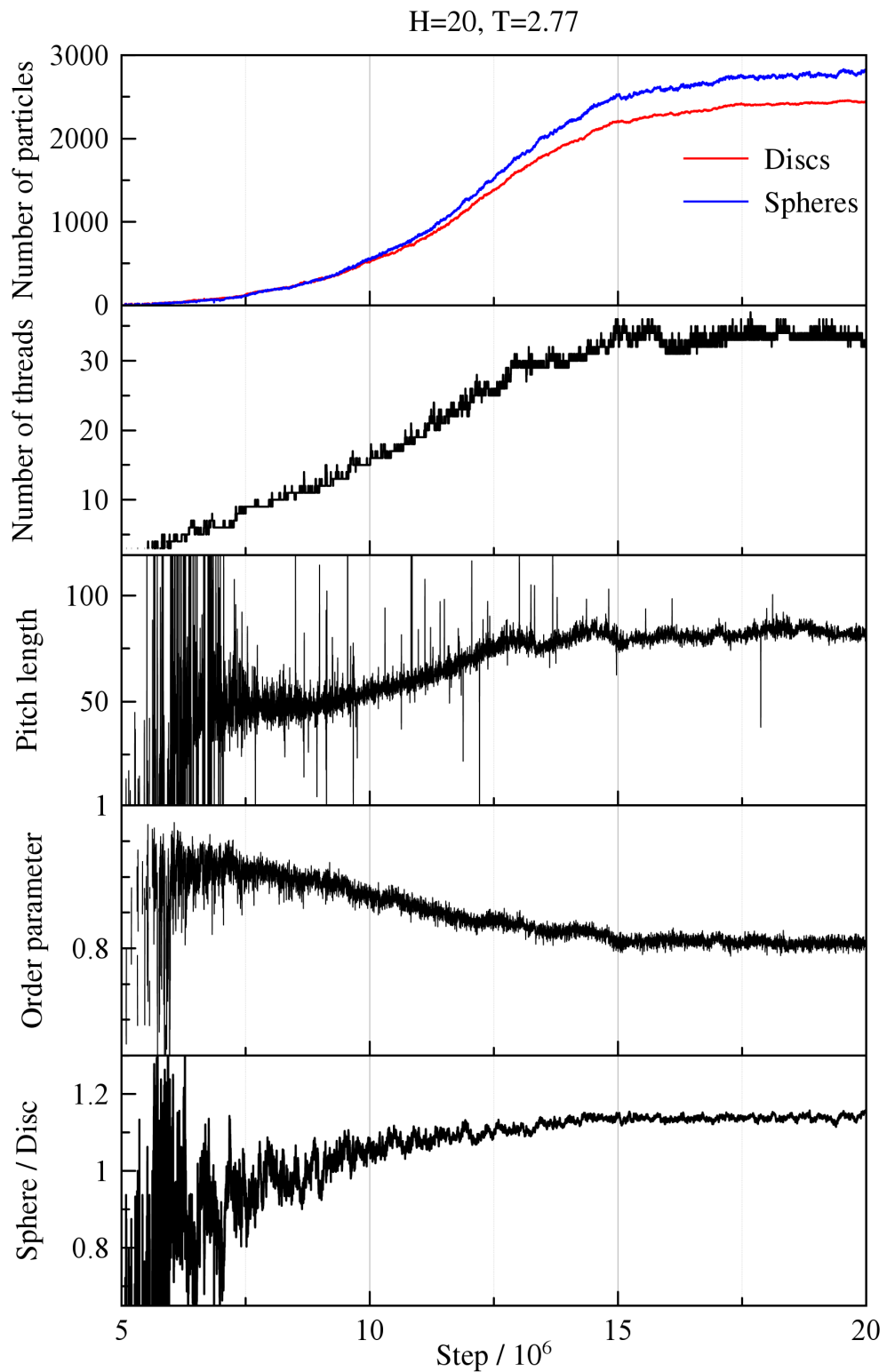


Figure 5.2: Time lines of different structural parameters measured for the system with $H=20$ at temperature $T=2.77$.

5.2 Twisted Bilayers

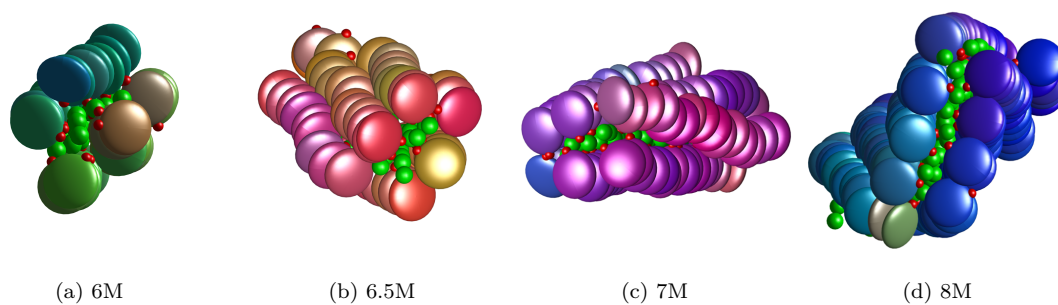


Figure 5.3: Snapshots of the twisted bilayer formed in the system with $H=20$. See the caption of Figure 5.1 for more information.

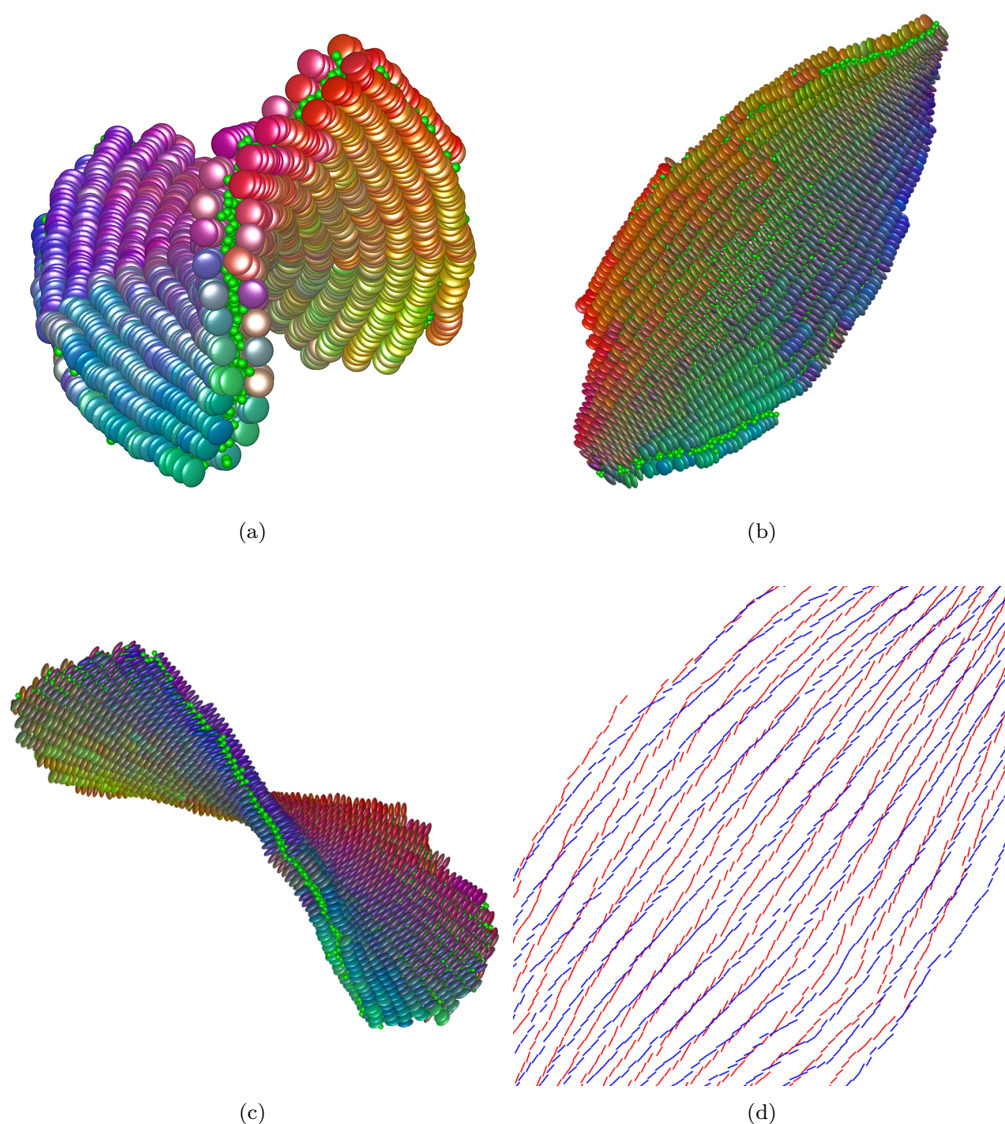


Figure 5.4: Snapshots of the final twisted bilayer formed in the system with $H=20$ after 40 million steps. In parts a, b and c the object was shown from three different orthogonal directions (the scales are not the same). See the caption of Figure 5.1 for more information. In part d, the short axes of the discs in two leaflets were coloured differently to show the small angle between the threads.

5.2 Twisted Bilayers

structures were observed (see the video for this system in Appendix D). The variation of pitch length data at the early stages of the growth shown in Figure 5.2 depicts the change of handedness. Since there is no predefined chirality in the system and it is totally emergent, both left- and right handed structures had the same energy level with, presumably, an energy barrier in between [100]. However, as the object grew, this energy barrier became higher and, therefore, the bilayer was locked into one of the handedness states. For this $H=20$ system, the cluster ceased to chose the change of handedness at 7 threads, and beyond this, the bilayer remained right handed. After about 7 million MD steps, the initial pitch length of the cluster was about 50 disc diameter. In the calculation of the pitch value, it was supposed that the axis of helix was the director of the structure. This is the same as the direction along which Figure 5.4a is viewed.

By an increase in the size of the growing object and also its number of threads, the order parameter of the object dropped because the threads at larger radius had to tilt more to maintain the same pitch value as their counterparts with smaller radii. This is due to the interdigitation of neighbouring threads which was discussed in the previous chapter in relation to fibres. Increase in the bilayer radius was also associated with gradual growth of the the pitch length of the object - the bilayer became less twisted, in response to the energetic costs associated with the bend energy of threads with larger radii. Another reaction of the system to the high stress outer threads was the development of defect lines in the structure. These allowed threads to localize all bend energy in defects rather than distribute it along threads. Through this, the threads with larger radius divided themselves into short straight sections with bend defects at the joint points. The defects were mostly in the form of a mismatch in the orientations of particles. For $H=20$, defect lines were not so apparent, although one may identify one in Figure 5.4a from a sharp colour change. For systems with higher H values, this behaviour was much more noticeable as will be discussed later. Another interesting feature of the formed bilayer is that, if one looks at the bilayer perpendicular to the director, along the eigenvector associated with the smallest eigenvalue of the Q tensor given by equation (3.26), another mechanism of twist with a different handedness can be observed (Figure 5.4c). This can be

5.2 Twisted Bilayers

quantified by a pitch length measurement performed on the sphere layer - we will compare this with other systems later.

The interaction of spheres and discs as the mechanism through which the structure develops these features is very important, and a symmetry breaking was also observed for this interaction. Figure 5.5 illustrates this symmetry breaking by showing the relative configurations of discs and sphere in the formed bilayer. In this figure, all discs and the spheres, which their interaction strength was at least 10% of the hot-spot well-depth, were taken into account. Then, the relative positions of the spheres with respect to the interacting discs were sampled and plotted in this figure. As shown, in the twisted bilayer, the spheres did not sit in the horizontal symmetry plane of interacting discs, but they shifted a little to each side of that plane for reasons of efficient packing. More interestingly, the distribution was not symmetric. Consistent with the twist of the object, for a left handed bilayer, one may observe the mirror image of this distribution plot with respect to the symmetry plane of the disc. By mapping the relative positions of the particles to a cylindrical coordinate system with x-axis along the hot-spot core, the probability plot for finding an interacting disc and sphere couple with particular z - and θ coordinates was drawn in Figure 5.5. This plot shows that, at positive values of angle θ , the spheres tended to slightly shift down, while for negative angles they shifted up.

Considering the product of the z - and θ coordinates as a single characterising parameter, we can study the emergence of this broken symmetry in the bilayer. Figure 5.6 (top panel) shows a probability distribution for the product of the z - and θ coordinates for different time windows along the growth pathway of the twisted bilayer. This shows that the distribution was almost symmetric in the early stages of the growth (between 6 and 7 million steps), but that as the object grew, it became asymmetric, suggesting the appearance of coherent twist and, so, confirming the observation of Figure 5.5. The distribution skewness [151] of the $z\theta$ parameter for the growing bilayer with a particular number of threads was also plotted in Figure 5.6. For smaller objects with a low number of threads, the skewness was close to zero, indicating a symmetric distribution. However, with increase in the number of threads, the skewness grew to increasingly negative values - the left tail of the distribution

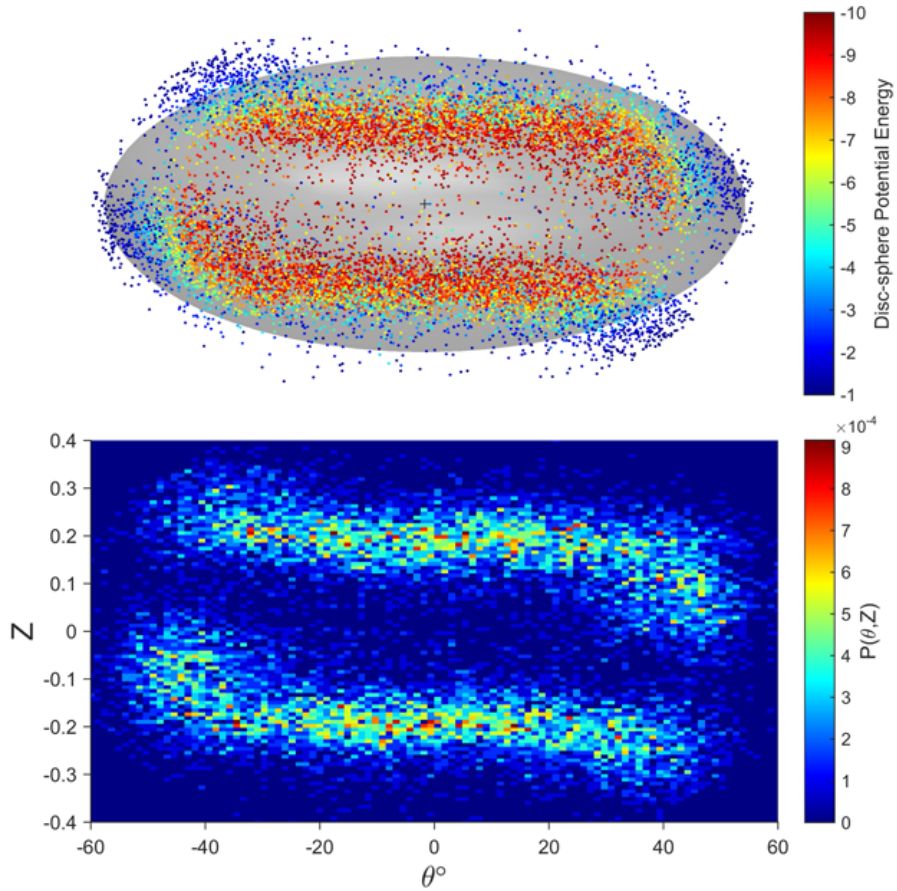


Figure 5.5: Top: Relative positions of spheres (centre of mass) with respect to the interacting discs coloured based on the strength of their interaction. The grey ellipsoid is the zero repulsion surface for disc-sphere interaction. Bottom: The probability plot of finding the relative position of interacting disc and sphere at particular cylindrical coordinates of z and θ . Both figures were sampled for $H=20$ system at the step of 15 million.

became longer (for aggregates with left-handed chirality, this was reversed and the skewness became positive in the steady-state phase). The sharp drop observed from 7 to 8 threads is consistent with the above discussion about change of handedness of the object at early stages. The skewness of $z\theta$ distribution reached a steady value when the cluster became larger than roughly 25 threads which happened after about 12.5 million steps (Figure 5.2). This was almost the point that the pitch length of the twisted cluster also became steady, after a gradual increase.

It was found that for the amphiphilic systems studied in this work, the sphere/disc ratio in the structure, being a characteristic of each system, is an important observable because, for the growing object, it is energetically favourable to increase the number

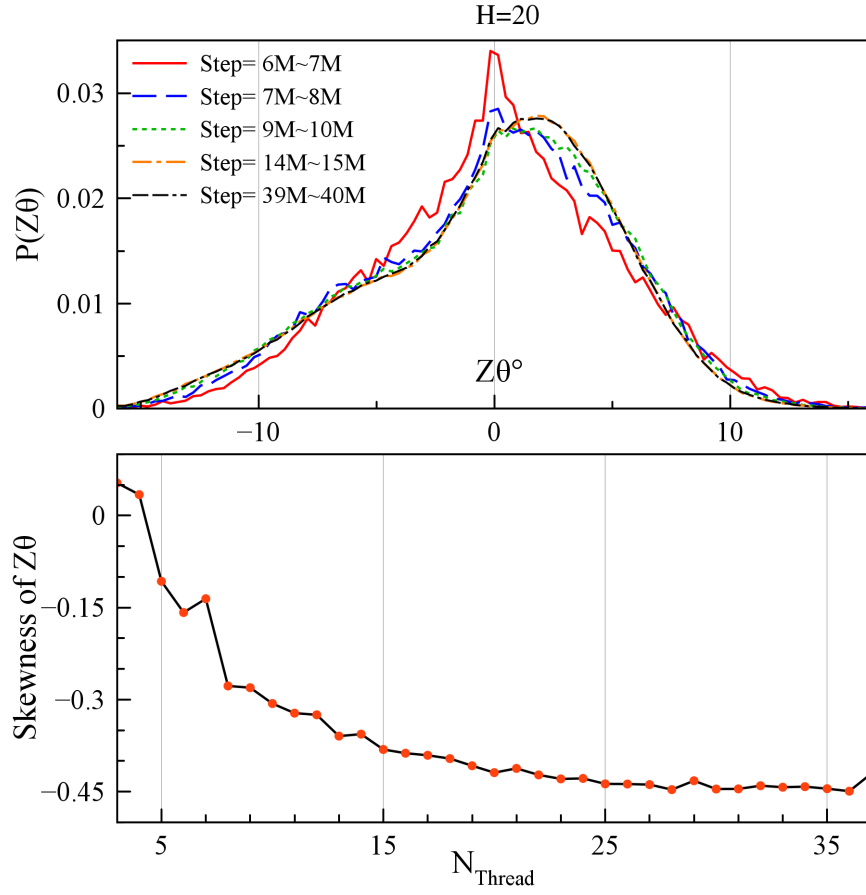


Figure 5.6: Top: Probability distribution of $z\theta$ component in disc-sphere relative positions sampled for the bilayer formed in the system with $H=20$ over the time window shown in the figure. Bottom: The skewness of distribution of $z\theta$ based on the number of threads in the cluster. Smaller number of threads belongs to the early stages.

of disc-sphere interactions. This tendency is illustrated by the sphere/disc ratio plot in Figure 5.2. For $H=20$ system, the sphere/disc ratio in the early stages was roughly 0.9, but with increase in the size of the object it went up to a steady value of 1.14.

Figure 5.7a illustrates the variation of the averaged energies of the growing cluster. The disc-disc inter- and intra-thread energies, first, were normalized with the number of discs in each thread and, then, the thread energies were averaged over the cluster. This approach of normalization caused the disc-disc total energy to be slightly smaller than the sum of the intra- and inter-thread energies shown in the figure. The disc-sphere potential energy was also normalized with the number of discs in the cluster. As seen, by an increase in the size of the object, the energies of the system went to more negative values, a more favourable condition for the

5.2 Twisted Bilayers

structure. They reached steady state values roughly at the same time at which the curves of Figure 5.2 levelled-off. The magnitude of the negative disc-sphere energy per disc was greater than that of the total disc-disc interaction, indicative that the ratio of the two species is fundamental in building the structure. Figure 5.7b gives a better picture of the distribution of energies in the bilayer, showing the probability contours of each type of energy based on the radial location of the associated thread in the bilayer (the radial distance was measured from the centre of mass of the bilayer, perpendicular to the director vector of the cluster). For measuring the disc-sphere energy of each thread, the same approach as that of disc-disc inter-thread energy was used. As the figure shows, the central threads had very negative energies but, at increased radii, less negative values were seen due to their less favourable situation. These measurements, in fact, quantify previous discussions relating to the energetic costs associated with the sideways growth of the object. The edge threads had significantly smaller energies compared to the inner ones, similar to what was observed for fibres in the previous chapter.

Investigations of the structure showed that, although the sphere layer was a helicoidal surface with the same pitch length as the whole bilayer, it was also locally corrugated. The threads of discs in each leaflet effectively located themselves in the groove spaces of the threads in the opposite leaflet (see Figure 5.4a). In order to be efficiently packed, the spheres also followed the same trend and became corrugated along the threads. This is shown in Figure 5.8, where the local Mean curvature was illustrated for a triangulated surface fitted on the sphere layer of the structure. The triangulation was performed with up-sampling ratio of 15 and 2-pass smoothing (see Chapter 3). The corrugation is apparent by the periodic change of sign of Mean curvature in Figure 5.8.

Having gained insight into the self-assembly pathway and structural characteristics of a twisted bilayer in an amphiphilic chromonic system, in the next subsection, we will study the effects of changing the size of the hot-spot region. In this, we will concentrate on the properties of the final formed twisted bilayers, but any possible differences in the formation pathway will be noted where appropriate.

5.2 Twisted Bilayers

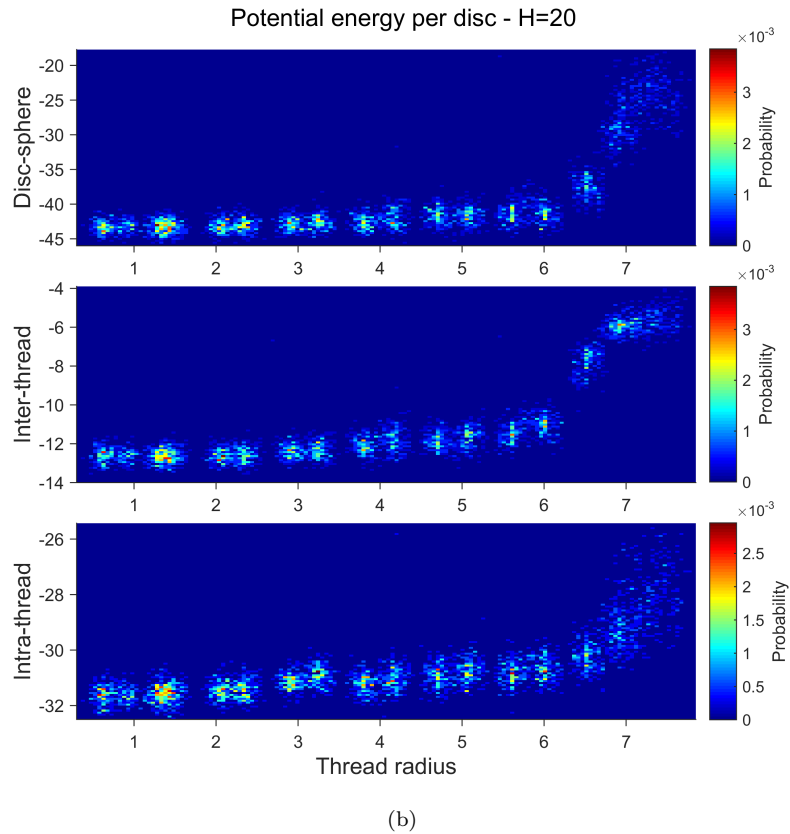
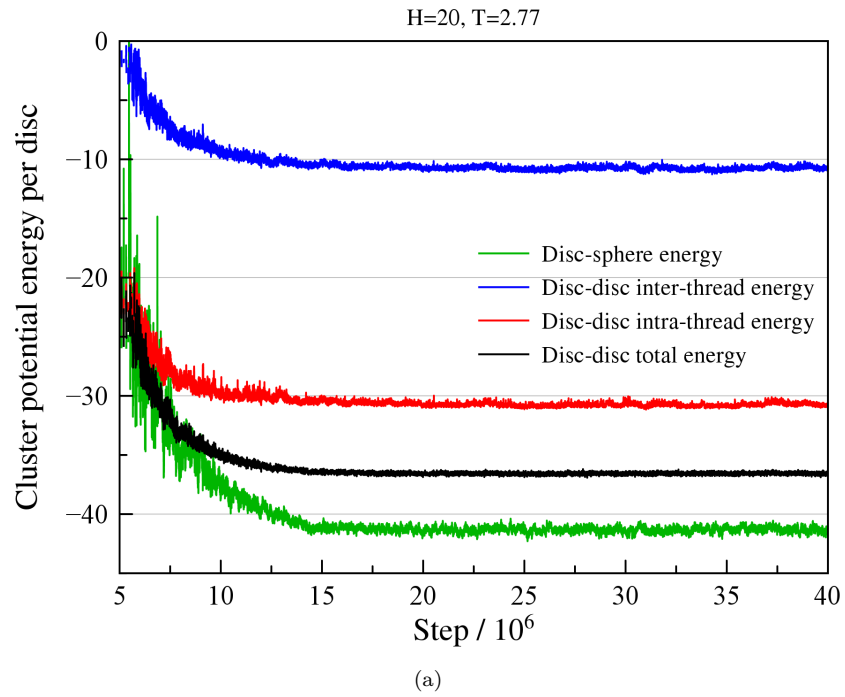


Figure 5.7: Potential energies of the bilayer formed in the H=20 system. a) Times lines of the averaged energies normalized by the number of discs. b) The probability plots of different energies of the bilayer based on the radial distance of the thread from the centre of mass of the bilayer, sampled over the last 1 million steps of the simulation.

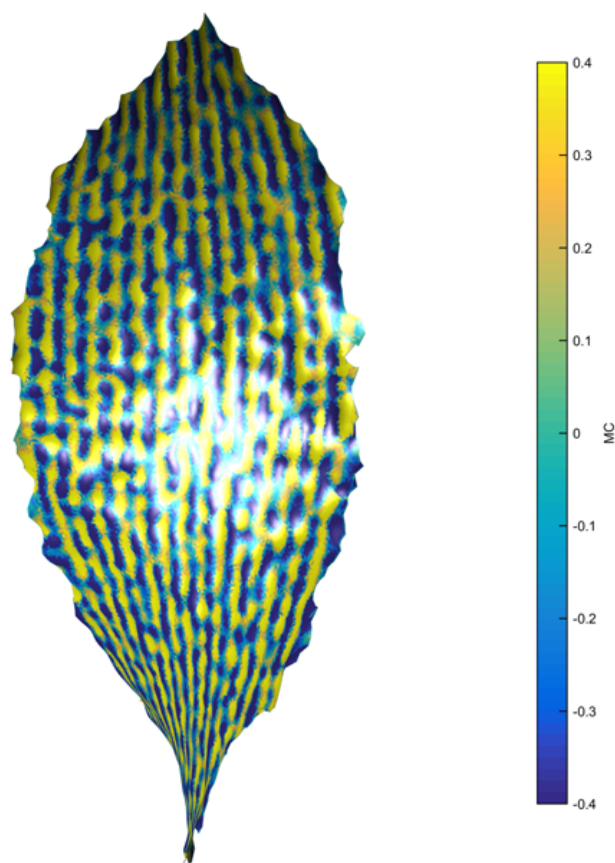


Figure 5.8: Mean curvature for the triangulated surface fitted on the sphere layer of the twisted bilayer formed in the $H=20$ system at step of 40 millions.

5.2.2 Extent of solvophilicity effects

In this subsection, the effects of the size of the disc hot-spot, the extent of solvophilicity, on the characteristics of twisted bilayers self-assembled by amphiphilic chromonic systems are investigated. This was achieved by investigating the effects of the H parameter on assemblies formed by mixtures of 3000 discs and 10,000 spheres. The simulation settings were exactly the same as those used for investigation of the $H=20$ system in the previous subsection, but with 10 new H values, ranging from $H=22$ to $H=50$.

All of these simulations led to formation of a twisted bilayer structure, albeit with slight differences being apparent between them and that which was formed in the $H=20$ system. Figure 5.9 shows snapshots of the final structures formed in some of the investigated systems. As seen, the handedness of the formed twisted bilayer

5.2 Twisted Bilayers

is completely random, and both left- and right handed structures were obtained. The formation pathway of the bilayers generally followed the same as that suggested previously. We therefore do not discuss it again. However, the averaged properties of the formed bilayers after equilibration to the steady state is the focus of this section. For each system, a simulation of 30-40 million MD steps was performed, the data being reported here being averaged over the last 5 million steps of each simulation.

By direct cooling of each system to find the formation temperature of each bilayer, an almost linear rise in that temperature was observed with increase in hot-spot size (Figure 5.10). That is, having a larger region around the discs which interacts more strongly with the spheres, increased the chance of initiation of the cluster at higher temperatures.

Figure 5.11 compares some of the averaged properties of the formed bilayers in each system. As shown in part (a) of this figure, on increasing the H parameter, the number of particles in the cluster first remained nearly unchanged and then dropped. The number of particles in the structure formed by the H=50 system was about 65% of that achieved by the system with H=20. This may be due to the effect of higher aggregation temperature of the former system. Other energy-related factors may also have an impact, as will be discussed later. Although it seems that the numbers of both discs and spheres in Figure 5.11a followed the same trend, their ratio, illustrated in Figure 5.11c, shows a different pattern. The sphere/disc ratio increased upto H=30 (by about 5%) and then experienced a plateau. Larger hot-spot regions provided greater volume for spheres to be packed in the middle of leaflets. However, this saturated at about H=30. The second increase in the disc/sphere ratio is due to another effect which is apparent, for example, in Figure 5.9d. For bilayers with larger H value, the interdigitation of threads decreased and reached a point in which longitudinal splits developed between threads, so allowing spheres to deviate from the monolayer sphere sheet and reside between threads (one of these is marked in the figure). This provided extra space for spheres in the solution to join the sphere-saturated structure in the systems with larger H, and caused the sphere/disc ratio to increase.

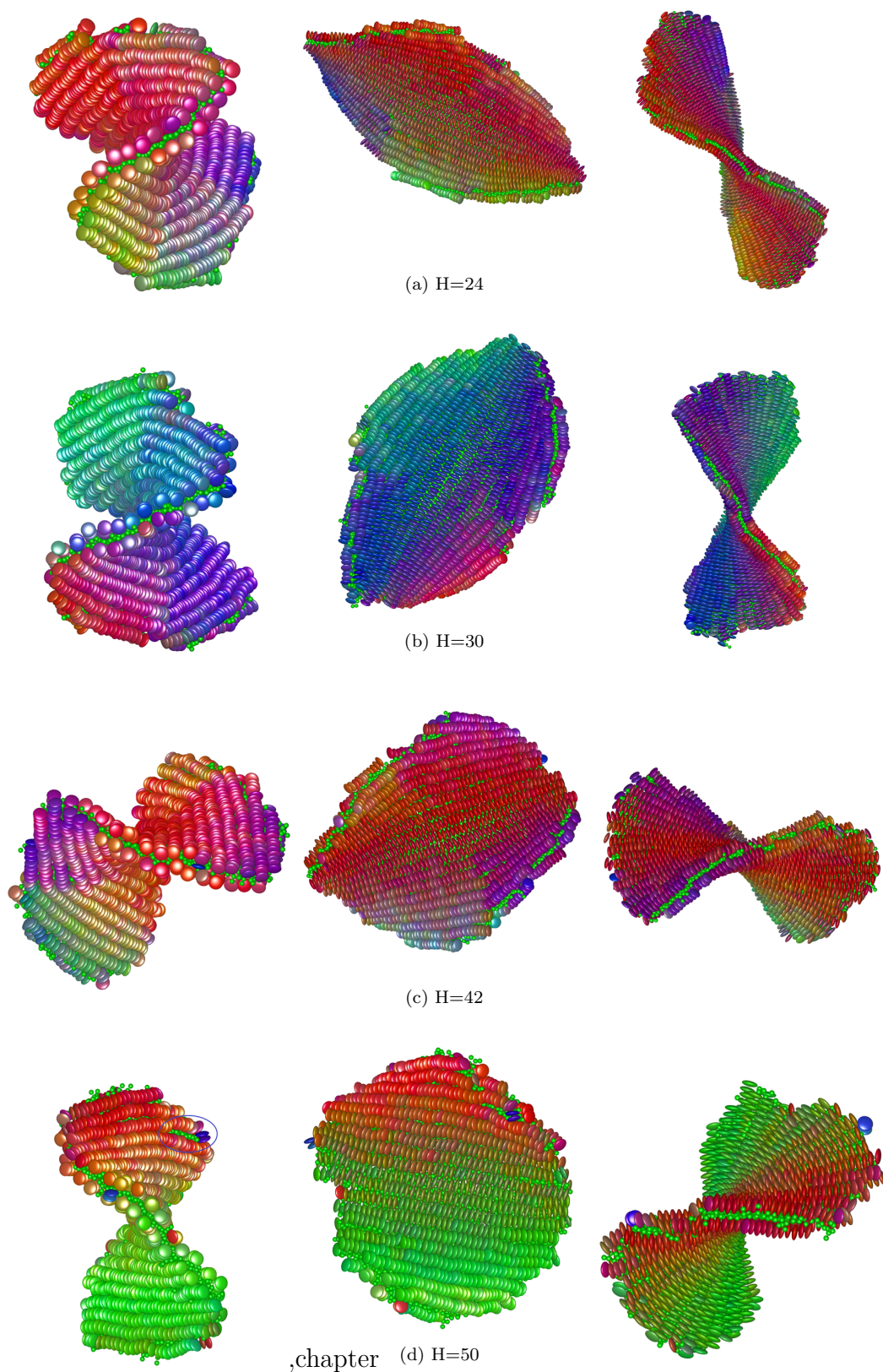


Figure 5.9: Snapshots of the final twisted bilayers formed in systems with different H values. The same object are shown from three different orthogonal views in each horizontal panel. See caption of Figure 5.1 for more information about the colouring approach.

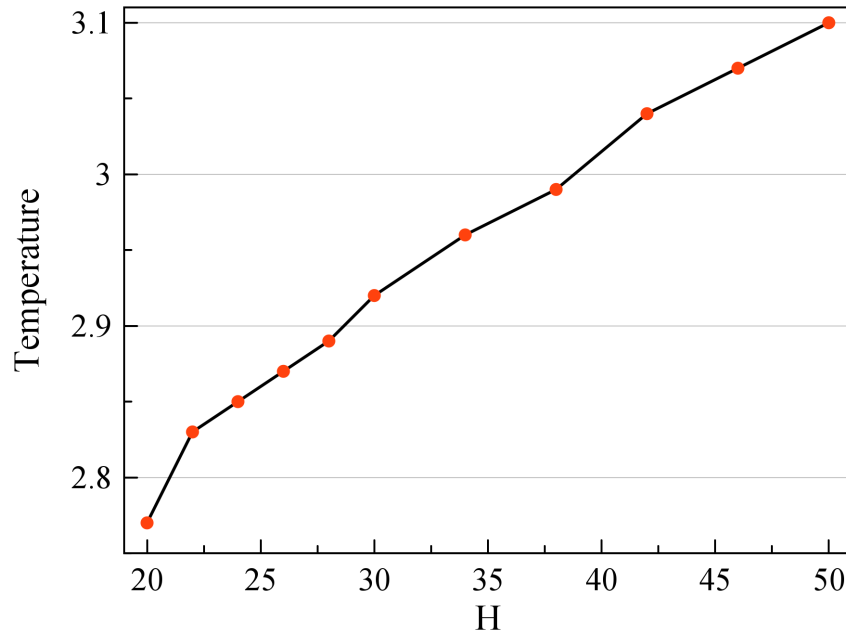


Figure 5.10: Formation temperature for the bilayers studied here.

Although the bilayers formed in systems with higher H values had smaller total numbers of particles, Figure 5.11b shows that the number of threads involved was generally larger in such systems. This can also be observed in the snapshots of the bilayers illustrated in Figure 5.9. Having fewer particles and larger numbers of threads meant that each thread was, on average, shorter. This can be also concluded from the normalized moments of inertia data shown in Figure 5.11d. The largest moment of inertia remained nearly unchanged for all systems, indicating that the formed objects had a sheet-like structure. The second moment of inertia dropped from high to intermediate values with increase in H , while the third one showed a compensation increase. This suggests that the lower H systems had long and thin shapes, while for higher H parameters, the object became shorter and fatter. Figure 5.12 also gives information on the size of the final objects formed in each system. This shows the length of the longest thread (the central one) along the director of the system, and the radius taken as the average distance of the particles in the outermost thread from the central axis of the object. The length measure dropped from about 34 disc diameters, for $H=20$, to 19 in the system with $H=50$. But, correspondingly, the radius experienced an increase from about 7 to nearly 10

5.2 Twisted Bilayers

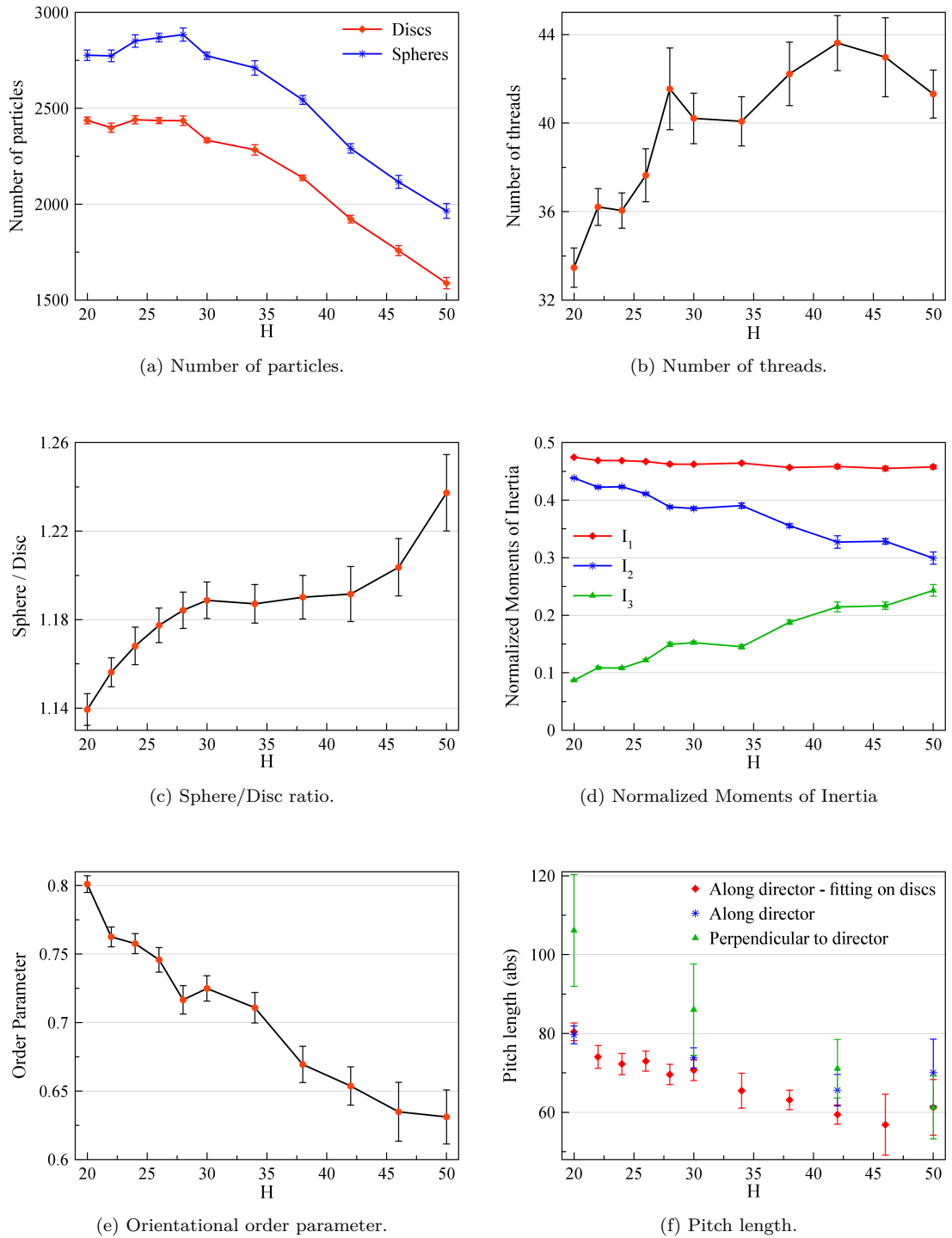


Figure 5.11: Averaged values of different parameters for the investigated systems at their formation temperatures. The sampling was performed over the last 5 million steps (2500 configurations) in the steady-state phase. The error bars show \pm Standard Deviation of data.

5.2 Twisted Bilayers

disc diameters. It should be noted that, since the size of simulation box was 38.95 disc diameters, none of the structures were affected by their own periodic images. As a result of these dimension changes, the aspect ratio of the structure (length to diameter ratios shown in Figure 5.12b) dropped from about 2.3 to 0.95 across the H range considered. Given that the disc-disc interaction was the same in all these systems and that the size of disc-sphere hot-spot was the sole variable, the degree of control over the assembled structure is noteworthy.

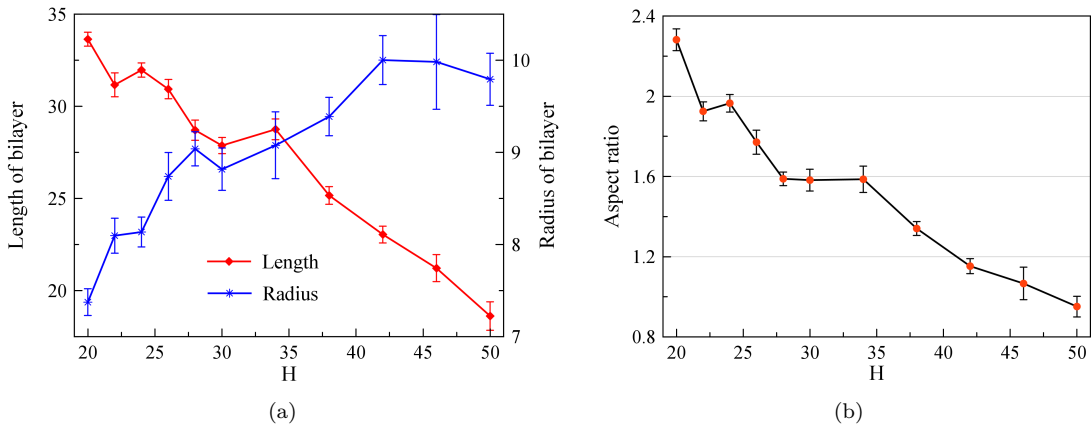


Figure 5.12: a) Averaged values of length and radius of the formed bilayers in different systems. b) Aspect ratio (length/diameter) of the self-assembled structures. The error bars show \pm Standard Deviation of data.

As discussed for the H=20 system, both the order parameter and the pitch length of the formed objects changed during their growth, the P_2 dropping while the pitch length increased. This effect is associated with lateral growth. The percentage of the drop in the order parameter during the growth was higher for the systems with larger H parameter, while the untwisting of the object (increase in pitch length) was more marked for the systems with lower H. The steady state values for these observables are given in Figures 5.11e-f. The orientational order parameter of the bilayers dropped with increase in the extent of solvophilicity, while the smaller objects were more twisted and had shorter pitch lengths. In Figure 5.11f, three different pitch length values are shown for four systems. One (red diamonds) is the usual longitudinal pitch length reported so far and measured by fitting a director-aligned helix on each disc thread, similar to the analysis performed for fibres. The other two pitch values were measured by fitting a helicoid surface on the sphere layer and

5.2 Twisted Bilayers

measuring the pitch of that helicoid. The blue stars in Figure 5.11f represent the sphere layer pitch along the director, whereas the green triangles give that along a perpendicular axis to the director. This second axis is, in fact, the eigenvector associated with the smallest eigenvalue of the Q tensor for the discs in the bilayer. This approach gives us a means by which to quantify the second observable twist in the structure, the one which is apparent in the right column of the snapshots shown in Figure 5.9. Figure 5.11f shows the absolute values of pitch lengths, but it should be noted that, in each structure, the first and second twist necessarily had opposing handedness. For smaller H values the pitches along the director measured from the disc thread and the sphere sheet matched perfectly, but they gradually diverged with increase in H . The height of the error bars also increased when the size of the hot-spot went up. This can be explained by noting the defect lines which developed in the structures (see Figure 5.9). Thus, for higher H values, instead of following a smooth helix, the threads morphed into linked linear sections. This introduced inaccuracy into both the thread-based and the sphere-based calculations of longitudinal pitch at larger H . The pitch length associated with the second twist also decreased by an increase in H , but was significantly larger than those in the longitudinal twist for $H=20$.

It is also noteworthy to study the handedness adjustment at the early stages of the bilayer growth. This is characterized by the plots in Figure 5.13 which shows the Standard Deviation of longitudinal pitch as a function of the number of threads in growing bilayers. In this figure, only the objects with the same handedness of the final structure were sampled. For each H value, the Standard Deviation of pitch length data reached a low value at a particular number of threads. For the systems with $H=20, 30, 42$ and 50 , this happened at $N_{thread}=8, 10, 12$ and 15 , respectively. In the bilayers with smaller numbers of threads than these figures, the chirality was not fixed and, therefore, large variations in the pitch length were observed. Generally, these data show that, systems with larger H values were more flexible and could change their handedness at larger bilayer width.

The potential energies of the self-assembled twisted bilayers with different H are compared in Figure 5.14. As shown, the disc-disc potential energies of the

5.2 Twisted Bilayers

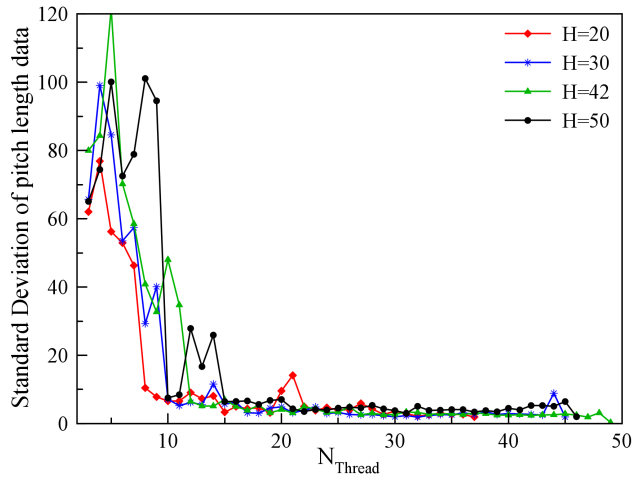


Figure 5.13: Standard Deviation of pitch lengths of the bilayers formed in different systems versus the number of threads of the object. The clusters with the same handedness as the final bilayer were only sampled. After reaching the steady values, no change of handedness was observed for each system.

structures became less negative with increase in the extent of solvophilicity. From $H=20$ to $H=50$, the drop in inter- and intra-thread energies was 26.8% and 6.1%, respectively. The magnitude of the total disc-disc energy therefore experienced a 8.9% decrease. The disc-sphere energy, however, followed the same trend as the sphere/disc ratio shown in Figure 5.9c, and became more negative before levelling-off. The trends of the disc-disc and disc-sphere potential energies caused the overall potential energy of the bilayers to have a minimum at $H=28$. Figure 5.15 illustrates the energy distribution across the cluster for systems with $H=30$ and $H=50$. These can be compared with that of the $H=20$ system shown in Figure 5.7. The energy distribution in the threads for these different systems has roughly the same trend, but the variation of energy level at a fixed thread radius is more marked for systems with higher H values. Interestingly, in the $H=50$ system, there is a possibility of finding some edge threads with inter-thread energy of nearly zero. For these, the disc-sphere interaction provided the driving force to keep those threads in the cluster. In this system with reasonably continuous threads and no defect lines, the radius-dependent variation of the energies is not so apparent, except for the weaker inter-thread energy of the edge threads.

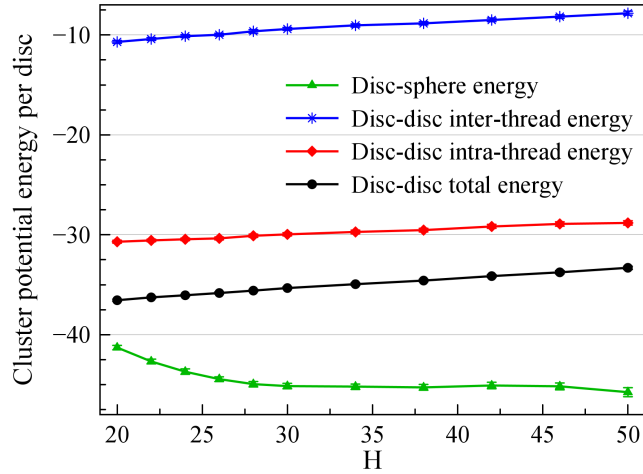


Figure 5.14: Averaged values of potential energies for the self-assembled structures in different systems. The normalization of each was performed similarly to that explained for Figure 5.7. The error bars (with nearly the same height as the symbols) show \pm Standard Deviation of data.

5.2.3 A bilayer with tears

Simulations of bigger systems with the same input parameters as those used in the previous subsection generally led to the observation of similar bilayer aggregates. However, the dimensions of the formed objects became close to the simulation box size and, therefore, the periodic boundary effects were more significant. From the investigations of fibre self-assembly, we learnt that lateral growth of the objects can be influenced by the energy anisotropy of the discs. Therefore, in order to encourage the lateral growth of the bilayer, we simulated a mixture of 6000 discs with slightly weaker face-face interaction, $\kappa' = 0.1$, and 20,000 spheres. The structure observed in the $H=25$ version of this system is explored in this part of the work.

By a direct cooling procedure, it was found that at temperature $T=2.65$, a single stable bilayer formed in this system. As the face-face interaction strength was slightly weaker than that of previously studied systems, the cluster formation occurred at a lower temperature than that illustrated in Figure 5.10. The self-assembly pathway, however, was generally the same as that discussed previously. We, therefore, focus on the characteristics of the final object, which is shown in Figure 5.16.

5.2 Twisted Bilayers

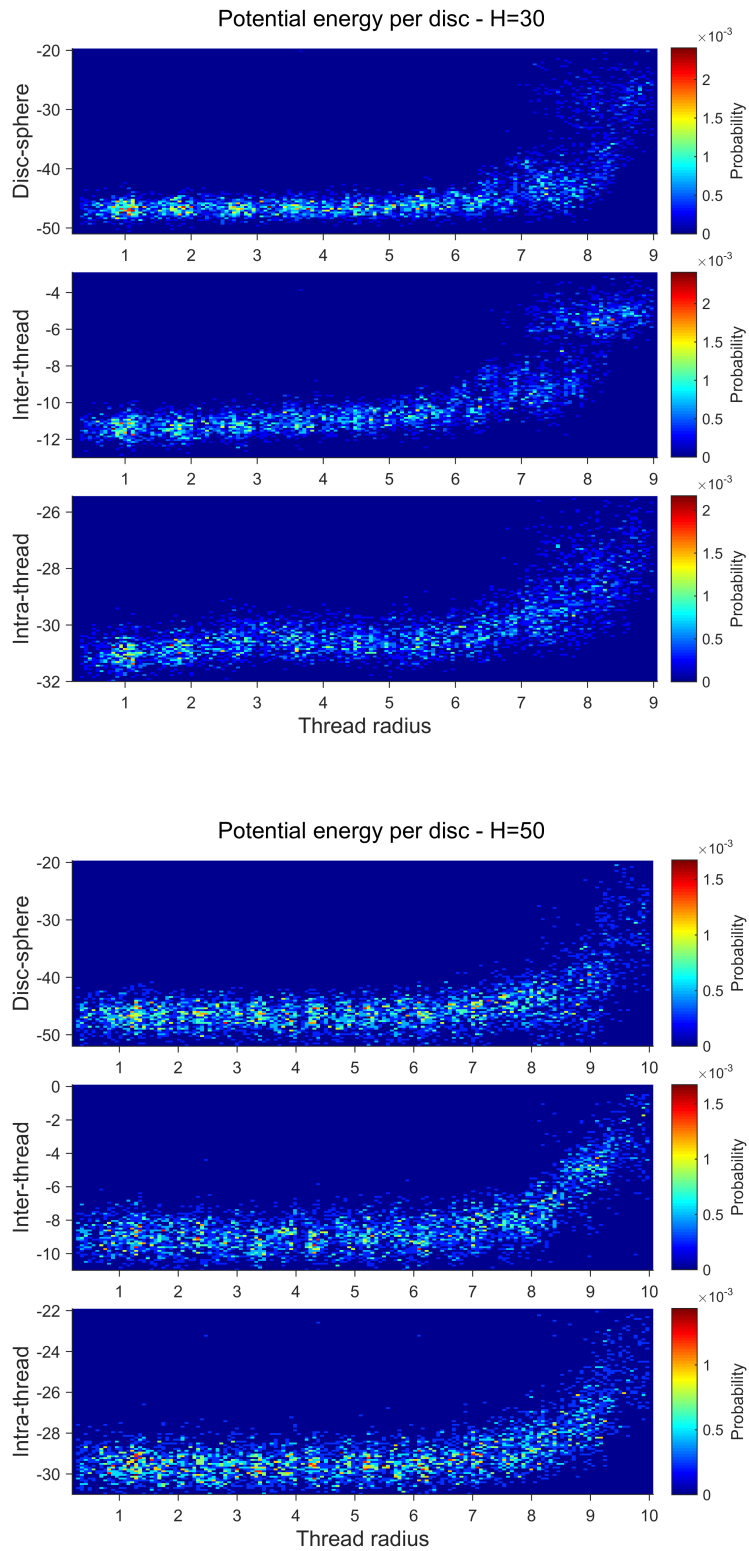


Figure 5.15: The probability plots of different energies of the bilayer based on the radial distance of the thread from the centre of mass of the bilayer for two systems with $H=30$ (top) and $H=50$ (bottom), sampled over the last 1 million steps of the simulations.

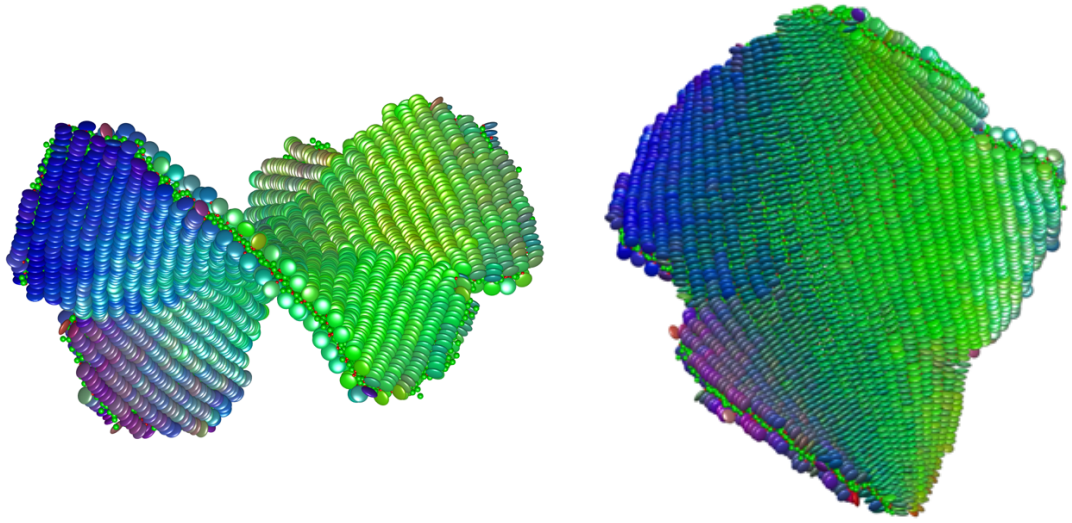


Figure 5.16: Two views of the twisted bilayer formed in a system with $\kappa' = 0.1$, $H=25$, 6000 discs and 20,000 spheres after 61.2 million MD steps.

Table 5.2 gives some information about the properties of the self-assembled twisted bilayer in this system. Nearly 71% of the simulated discs formed the final structure which is slightly less than was the case for the $H=25$ in a system with $\kappa' = 0.075$ (see Figure 5.11). The sphere/disc ratio, however, was larger than that in the previously studied bilayers. As the values of this ratio in the entire simulation (not shown here) was always larger than that of the bilayers with $\kappa' = 0.075$, it can be concluded that the disc-disc interaction strength, rather than the system size, was the main cause. As expected, the weaker face-face interaction encouraged the lateral growth of the bilayer and the aspect ratio of the object dropped to about 1.14 (for this H value and stronger face-face strength, it is around 1.8). The disc-disc potential energies per disc were smaller than those in systems with $\kappa' = 0.075$, but the disc-sphere energy of this bilayer (normalized with the number of discs) was greater, presumably because the sphere/disc ratio was larger.

The threads in this bilayer were less stiff than those of previous systems and, therefore, the object could accommodate more lateral growth: more than 70 threads were formed with nearly the same pitch length value as before. However, a number of defect lines were formed by this system to localise the bend energy of the threads. In Figure 5.16, two defect lines in the right side of the object and one in the left side are apparent. The mismatch in the orientation of particles along these defect lines

5.3 Multilayer Twisted Bundle

Table 5.2: Averaged properties of the bilayer self-assembled in a system with $\kappa' = 0.1$, $H=25$ and 6000 discs. The data are sampled over the last 5 million steps (500 configurations). The figures after the \pm sign are the Standard Deviation of data.

Number of discs	4234 ± 18	Number of spheres	5420 ± 26
Sphere/disc	1.28 ± 0.01	Number of threads	74 ± 2
Order parameter	0.59 ± 0.01	Pitch length	76.5 ± 2.7
Length of bilayer	33.3 ± 0.4	Aspect ratio	1.14 ± 0.03
Inter-thread energy	-9.0 ± 0.1	Intra-thread energy	-22.0 ± 0.1
Total disc-disc energy	-27.1 ± 0.1	Disc-sphere energy	-47.9 ± 0.2

enables the structure to develop straight threads with lower elastic stress and, at the same time, allowed it to maintain its twist. The required mismatch in particle orientation at such a defect increases with distance from the central axis. This increase, eventually, affected the integrity of the threads and ‘tears’ appeared on the sides of the structure at the ends of the defect lines (see Figure 5.16).

5.3 Multilayer Twisted Bundle

In this section, the self-assembly of a multilayer twisted bundle in an amphiphilic chromonic system is investigated. As shown in the previous section, the single hot-spot model of coarse-grained discs, is capable of spontaneous formation of twisted bilayers. The aim here, therefore, was to investigate whether the double hot-spot version of this potential could also achieve a self-assembled object with both coherent chirality and additional direction of growth.

Several test systems with double hot-spots and moderate numbers of particles were studied in this venture, but, here, we only report the outcome of one of these: a mixture of 6000 discs and 20,000 spheres. Recalling equation (3.49) for the Tanh potential, we considered the double hot-spot version with two opposite hot-spots on the rim of the discs ($\hat{\mathbf{u}}^{hs}_1 = -\hat{\mathbf{u}}^{hs}_2$). The simulation input parameters were exactly the same as those used for the bilayer systems in the previous section, but here, with a slightly weaker choice of face-face interaction ($\kappa' = 0.1$) for the disc-disc potential. The size of the hot-spots on each side of the discs was $H_1 = H_2 = 25$.

5.3 Multilayer Twisted Bundle

In a direct cooling, it was found that, at temperature $T=3$, one of the small clusters formed in the system could grow and become a dominant aggregate. Figure 5.17 shows a sequence of snapshots of this developing system. In all of these, the structure is viewed along the director vector. Similar to the bilayer self-assembly, the cooperation between the two types of interaction, disc-disc and disc-sphere, was key to the initiation and growth of the object locally. Spheres formed layers which were sandwiched between sheets of parallel disc threads. While most discs had a preferred direction, some threads in the outermost layers were aligned at an angle compared with the others. The object formed here, similar to the bilayer, grew both sideways, by addition of new threads, and longitudinally along the threads. In addition, having identical solvophilic regions on both sides of the discs, the structure also had a third direction of growth perpendicular to the sphere layers. As a result, a multilayer structure developed. The snapshots illustrate that the threads in each layer of this were slightly twisted with respect to one another - this is apparent from the gradual change of colour of the particles in successive layers. That is, two neighbouring disc leaflets could slide over the sphere layer and maintain an angle with each other. Strikingly, the angles of successive layers were consistent, all of the same handedness, so causing the full assembly to be twisted.

Figure 5.18 reveals more information about this growing structure via the time lines of various properties. As the number of particle curves show, the small cluster, which was initiated after about 1.5 million MD steps, grew monotonically and, eventually, more than 92% of the discs in the simulation box became a part of the aggregate. The sphere/disc ratio of the whole cluster also went up during the growth and reached the steady value of 2.08, significantly higher than that of bilayers. This is due to the increase in the ratio of the number of layers (sphere to disc) from 1:2 for bilayers to 13:14 for the final configuration of the multilayer structure formed here (see Figure 5.19).

The normalized moments of inertia of the cluster give very interesting information about the growth of the multilayer bundle. Initially, the growth perpendicular to the layers was dominant and, for example, from 1.7 million to 4 million steps, the number of disc layers increased from 4 to 10, while the number of threads in the

5.3 Multilayer Twisted Bundle

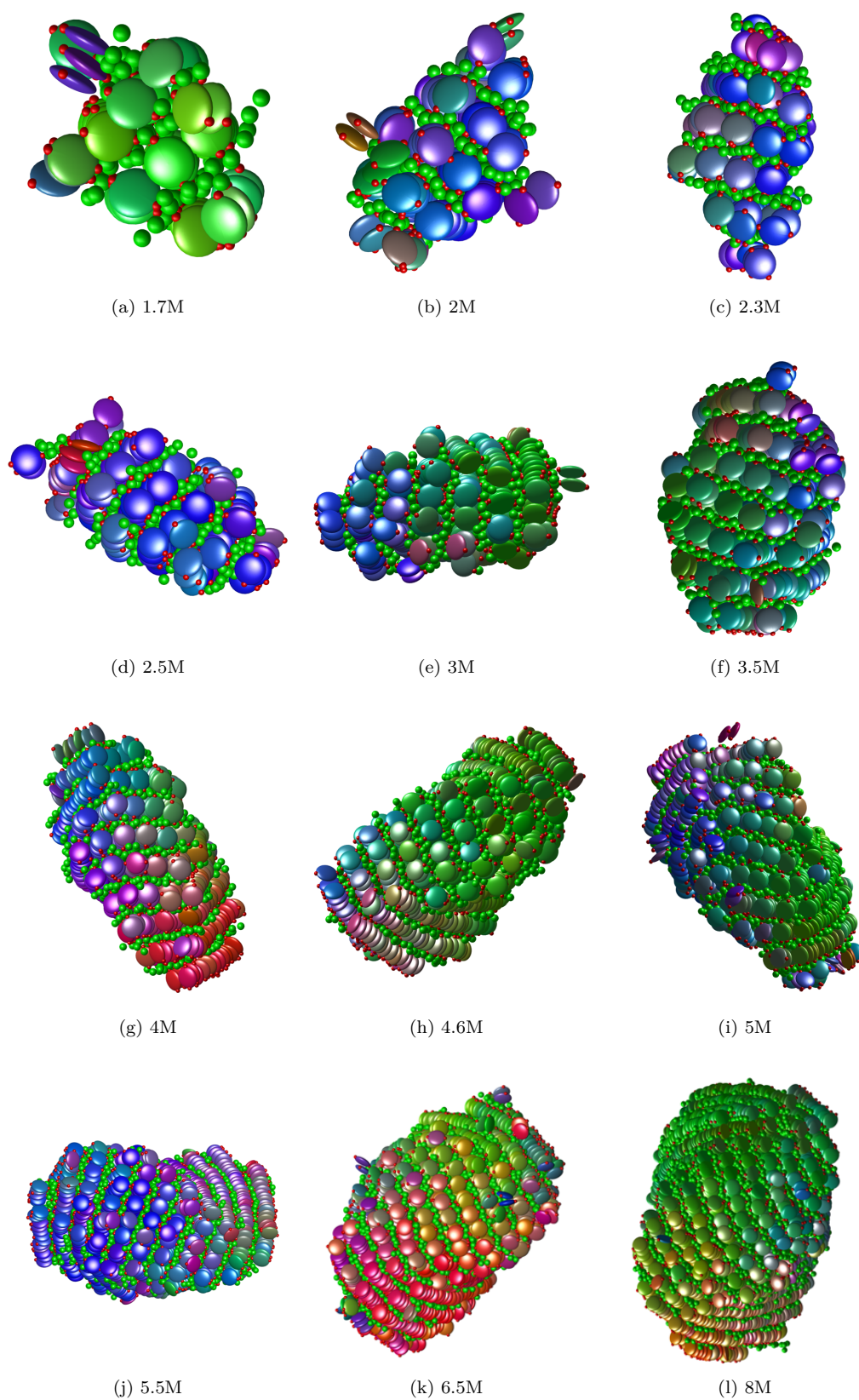


Figure 5.17: The snapshots of the multilayer twisted bundle formed in a system with $H_1 = H_2 = 25$ at different time steps written at the bottom of each part, where the object is viewed along the director. See the caption of Figure 5.1 for more information on colouring approach.

5.3 Multilayer Twisted Bundle

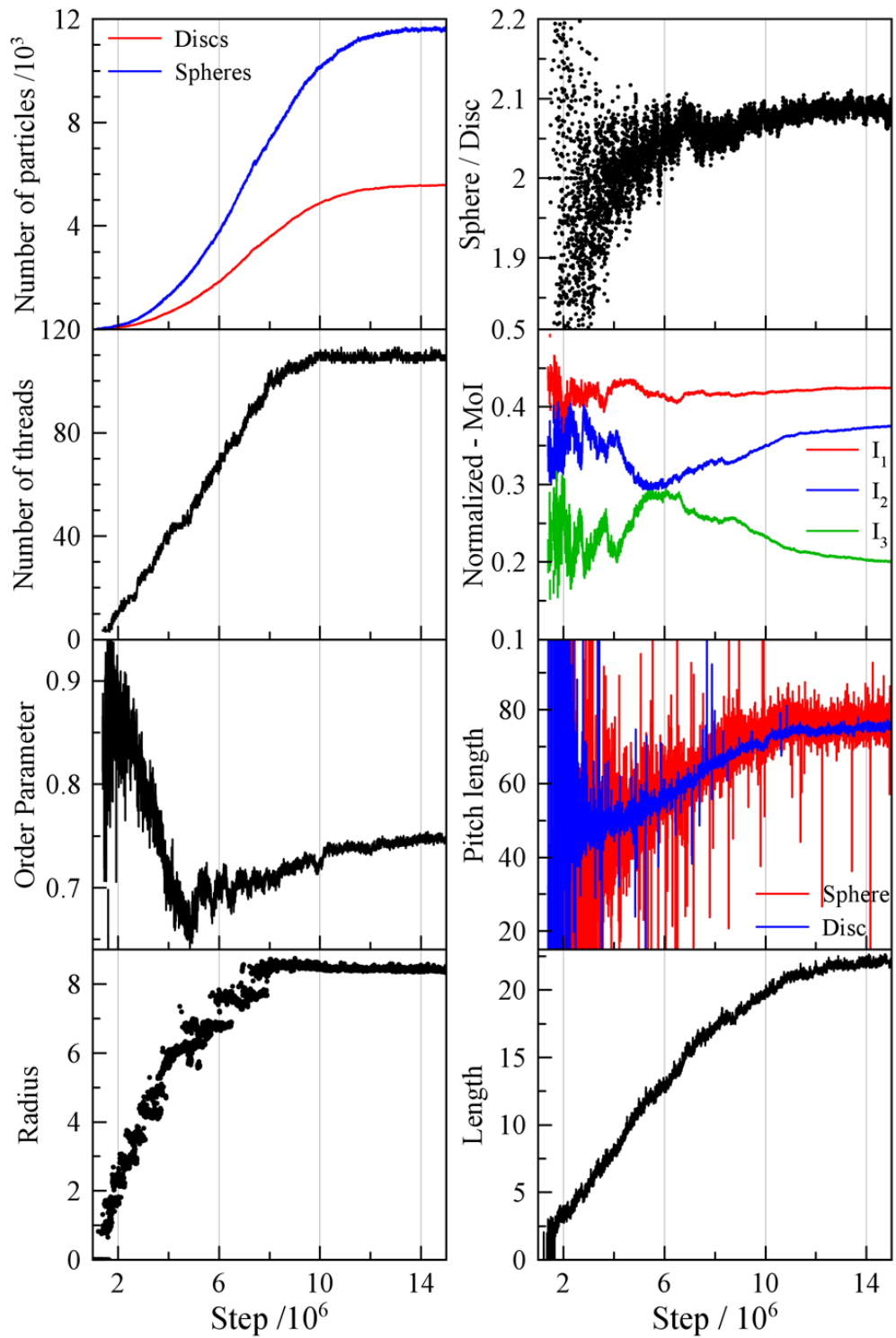


Figure 5.18: Time lines of different structural parameters measured for the system with $H_1 = H_2 = 25$ at temperature $T=3$.

5.3 Multilayer Twisted Bundle

widest sheet went from 4 to 6 (see Figure 5.17). The zigzag trend of the moments of inertia curves is due to addition of new layers to the cluster. Between time steps of 4.1 and 4.9 millions, the number of threads remained constant, but the length of the cluster increased. Longitudinal growth showed a monotonic trend (see the length of longest thread curve) and, in this window, was the only mechanism by which the new particles joined the growing object. This caused the second and third components of the normalized moments of inertia to approach each other, while the largest one remained steady. As the size of the bundle increased, the order parameter of the object dropped and the pitch length increased, similar to the behaviour of other systems investigated in this work. It should be noted that the pitch length of the cluster along the director axis was measured by two methods; one by fitting helices to all disc threads and the other by fitting a helicoidal surface on the biggest sphere leaflet in the centre of the object. Although, fluctuations were larger for the sphere-based approach, both methods gave the same average values for the pitch length of the bundle. The increase in the pitch length (untwisting) due to the growth was almost monotonic, until the object reached a steady size. However, the orientational order parameter showed an unexpected behaviour.

After 4.9 million MD steps, layer widening became the dominant mechanism of growth. Since the aggregating particles joined the existing (mostly the central) layers and formed new threads with radii smaller than the outermost layers, they had less tilt angle. Thus, the number of particles with low deviation from the preferred direction increased and, consequently, the orientational order parameter went up. The up and down behaviour of P_2 curve after this point was due to the combined effect of addition of threads to the existing layers and the development of a few new disc layers - this was ceased at 8 million steps, at which point the number of layers (radius of the outermost thread) reached a steady value.

Different rates of growth in the three different directions, each of which was also time dependent, caused the investigated structural properties to have a time lag in reaching the steady state values. While the number of layers and the largest radius of the threads both became steady at about 8 million steps, the number of threads increased until 10 million steps and other parameters varied until about

5.3 Multilayer Twisted Bundle

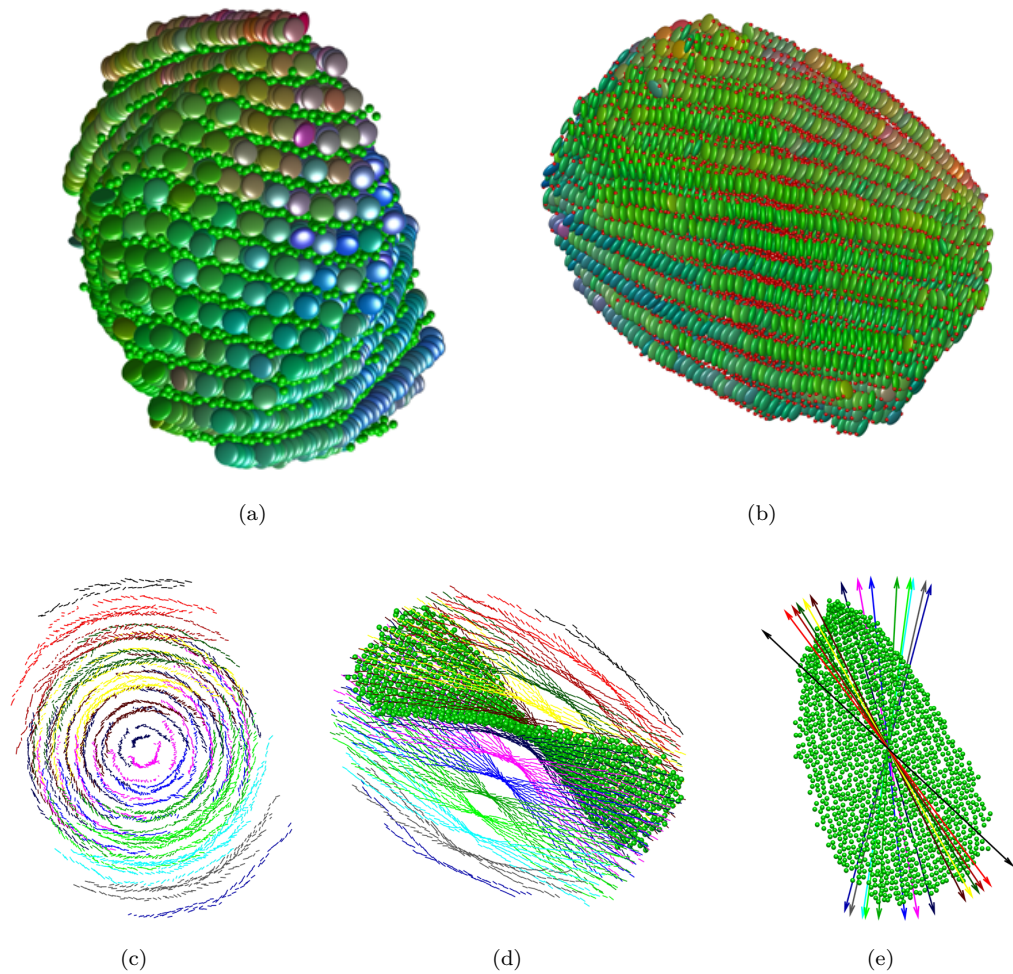


Figure 5.19: Snapshots of the final multilayer twisted bundle formed in the system with $H_1 = H_2 = 25$ after 17 million steps. In parts c and d the short axes of discs are shown. The discs in different layers are coloured distinctly. In part e, the director vector of each disc layer was drawn with the same colour that the associated discs were shown in parts c and d, and the object was viewed perpendicular to these vectors. The same sphere layer was shown in parts d and e.

14-15 million steps. The simulation was run on beyond this, to be sure that the system was equilibrated. Figure 5.19 shows some snapshots of the final multilayer twisted bundle spontaneously formed in this system. Similar to the bilayers, here, two different approaches for the twist with different pitch length were observable (see snapshots of Figure 5.17 for the one along the director, and Figure 5.19d, for the one perpendicular to the director). One may also capture a third manifestation of twist in this multilayer object by considering the discussed angles between the threads in neighbouring layers. Moving in a direction perpendicular to the layers

5.4 Geometric Frustration

(along the eigenvector associated with the smallest eigenvalue of the Q tensor for the whole bundle), the director vector of each layer rotates and a twist across the bundle is apparent (see Figure 5.19e). In a very rough measurement, this twist had a pitch length of about 100 disc diameters. Here, the twist along the main director had a left handed chirality, while those along the two orthogonal axes were right handed. The three different twist modes in this multilayer bundle are illustrated in Figure 5.19c-e.

5.4 Geometric Frustration

An alternative title for this section could be “Self-assembly of rope structures”. However to emphasize on the geometric frustration phenomenon which led to the formation of a twisted ribbon (the focus of this chapter), the current title was chosen.

Although the term ‘geometric frustration’ is mostly used in solid state physics, in soft matter it is employed to describe situations in which a preferred pattern of local ordering cannot be propagated globally [137]. Therefore, two or more distinct patterns of order are preferred by the interaction and structure of the building blocks. In comparison to rigid systems, in which this situation restrains the assembly, in soft systems, imperfect order over some finite range can be allowed - similar to the defect lines we observed in the bilayers. In unfrustrated systems, the assembly is thermodynamically governed, with the negative bulk free energy gain of order of $-L^D$ (L and D are size and dimensionality of the system, respectively) and positive surface energy cost at boundary of order of L^{D-1} . In frustrated systems, however, another energy cost of frustration is also added to this trade-off. This energy cost is an increasing function of L and can sometimes dominate the bulk energy gain and lead to structural and thermodynamic behaviours different from those seen in unfrustrated assemblies [137]. An example of this was given in the previous chapter, when the energy cost of growing twisted threads with larger radii caused the twisted fibre structures to undergo an untwisting event and become a straight object, in which all threads had identical stress. Here, another fascinating transition due to geometric frustration in a spontaneously formed, chiral structure is explored.

5.4 Geometric Frustration

In the bilayer and multilayer aggregates investigated thus far in this chapter, the size of the hot-spot zones around the rim of the discs was sufficiently large to overlap with that of the disc in the neighbouring threads. Consequently, the opposite threads provided a sheet-like space for the spheres, leading to the observation of twisted ribbons in the disc-sphere systems. Here, we investigate the limiting size of hot-spot in this pathway and, thus study the assemblies found for other hot-spot sizes. For this, simulations were performed on mixtures of single hot-spot discs and spheres with exactly the same input parameters as those considered for studying bilayers in section 5.2. The same face-face strength of disc-disc interaction ($\kappa' = 0.075$) and also a slightly weaker one ($\kappa' = 0.1$) were used. A range of hot-spot sizes (H parameter), smaller than those used for bilayer investigation, was employed in this section.

For the investigated range of hot-spot sizes ($10 \leq H < 20$), a new class of twisted structure self-assembled in these systems. The basic unit of these structures consisted of 5 helical threads wrapped around a central long core of spheres. An example of this so-called “rope” structure is illustrated, for $H=17$, in Figure 5.20. The small size of the hot-spot prevented the structure from having sideways growth sites and, therefore, the only mechanism of growth through disc-sphere interaction was along the axis of this 1D structure. The discs oriented themselves in such a way that the hot-spots were pointed towards the centre, so, providing a tape like space for the spheres. The cross section of the core space had about 1 sphere thickness and 3-4 sphere width (see part c of Figure 5.20). Twist is apparent for the disc threads, with a significantly shorter pitch length than those of the other twisted structures studied so far - this is the first time a complete pitch length has been observed in the self-assembled structures of this work (Figure 5.20a). Interestingly, the sphere tape was also twisted, although there might be some defects in the structure (Figure 5.20c).

In the simulations of these systems, both left- and right handed twisted structures were observed with equal likelihood. Thus, where two or more ropes with the same or different handedness self-assembled, the lateral interaction of these ropes led to interesting observations. Some of these are as exemplified in Figure 5.21. For that shown in panel a, two left-handed ropes, one longer and one smaller, formed in the

5.4 Geometric Frustration

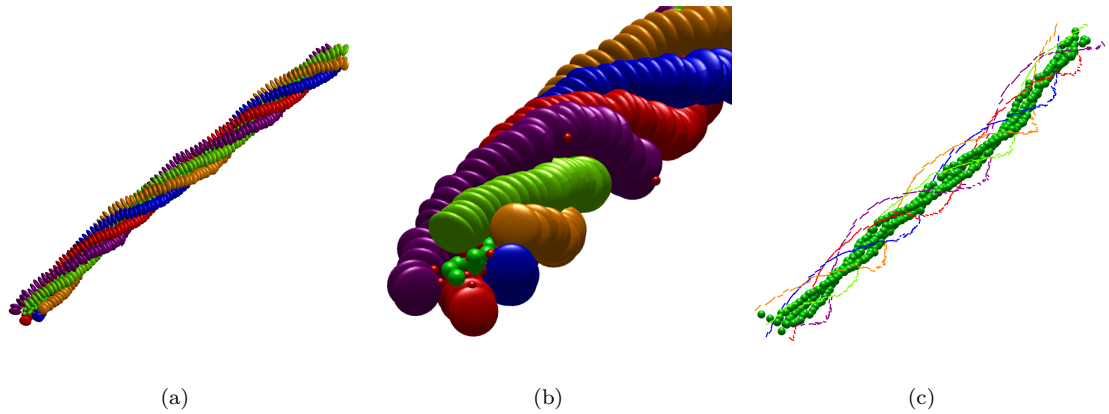


Figure 5.20: Snapshots of the rope structure formed in the system with $\kappa = 0.075$ and $H=17$. All three parts show the same configuration. The discs were coloured based on their threads. In part c, the short axes of discs were drawn with the same colours as those in the other parts. The twist in the sphere cluster is apparent in part c.

system and, after a while, they coalesced and made a double-rope structure. The match in the handedness of these ropes provided them with the opportunity to wrap around each other and, thus, a second mechanism for twist appeared (see the twist of sphere clusters around each other). As can be seen, the pitch length of this secondary twist was longer than that of the threads within each rope. In an alternative scenario, two ropes with different handedness interacted laterally and made an object with two parallel sphere clusters, each in the centre of a 5-thread rope (Figure 5.21b).

Lateral interaction of formed ropes was not the only mechanism of formation of multi-rope structures. In some systems, a formed rope acted as a template for the deposition of more discs on its outer surface. These discs, then, formed the next ropes attached to the template through interaction with other particles. In this way, the handedness of the initial structure was imprinted into the formed 5-thread ropes, leading to a consistent chirality for the whole object. Figure 5.22 shows the snapshots of a multi-rope structure which formed in a system with a very small hot-spot size, $H=10$. The surface threads (with hot-spots oriented outward) formed due to disc-disc interactions and have not used their disc-sphere capability yet to form a new rope. Here, the pitch length is significantly longer than that for the ropes with higher H values and, therefore, the threads could tolerate the energy costs associated with the lateral growth.

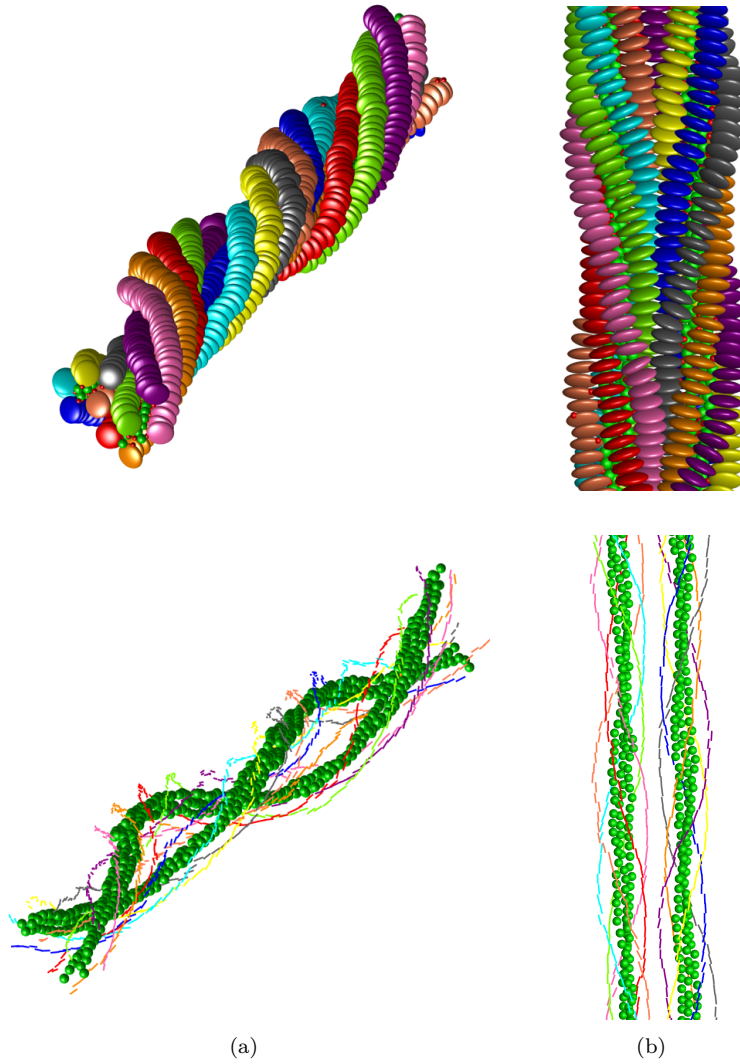


Figure 5.21: Snapshots of the double-rope structures formed in two systems, a) $\kappa' = 0.1$, H=13 and T=2.38; b) $\kappa' = 0.075$, H=17 and T=2.71. The bottom panel shows the same configurations as the top ones, but the short axes of the discs were drawn.

As the main mechanism of the growth for the ropes was along the axis, the very long structures formed by these systems were prone to interacting with their own images through periodic boundary condition. This might have had an impact on the properties of the systems we studied. Therefore, only qualitative report of these observations has been given thus far in this section, so as to prevent any possible misunderstanding in the interpretation of data. However, in some cases, the lengths of the self-assembled objects were shorter than the simulation box side and this issue did not arise. Here, we explore one such system by providing some quantitative analysis.

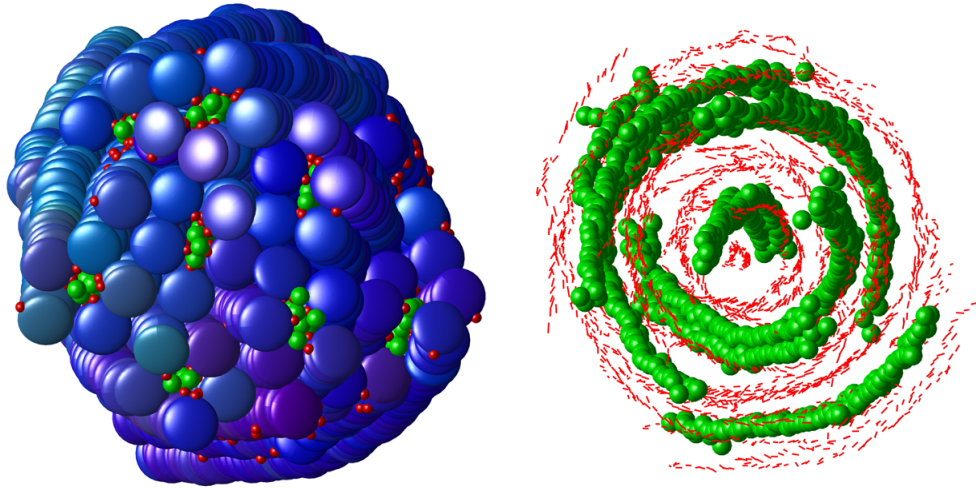


Figure 5.22: Snapshots of a multi-rope structure formed in the system with $\kappa' = 0.075$, $H=10$ at temperature $T=2.5$. In the left figure, the discs were coloured based on their orientations. The right hand image shows the same configuration in which the short axes of the discs were drawn.

In the simulation of a mixture of 3000 discs, having $\kappa' = 0.1$ and $H=15$, and 10,000 spheres at temperature $T=2.42$, after about 3 million MD steps, a structure of a few (3-4) parallel threads formed and persisted (Figure 5.23a). Addition and dissociation of new threads continued and the formed 5-thread structure provided a closed space for spheres between threads (Figure 5.23b). When the fifth thread became sufficiently long and its incorporation into the structure was established, the object became twisted (Figure 5.23c). The pitch length for this small rope was about 18 disc diameters, as shown in Figure 5.25. Formation of individual threads on the surface of this small object then took place through disc-disc interaction, although these subsequently dissolved. An example of one of these threads formed on the main rope is shown in Figure 5.23c.

The self-assembled rope structure grew longitudinally by addition of discs and spheres at the available growth sites at the ends of the object. After about 7.6 million MD steps, another rope, which had formed independently with similar handedness, joined the initial one (Figure 5.23e). These two structures, were initially at an angle to one another, but they rearranged into a structure with a common axis (Figure 5.23f). While the longitudinal growth of this double-rope structure continued, a very small cluster of three threads formed in one of its main grooves (Figure

5.4 Geometric Frustration

5.23g). This small cluster developed into a 4-thread (Figure 5.23h) and, eventually, a 5-thread (Figure 5.23i) object, attached to the initial double-rope structure. The mechanism of the second rope addition to the cluster was different from that of the third one. The former involved a cluster-cluster interaction, while for the latter, the initiation and growth occurred on the existing structure and, therefore, the handedness was imprinted in the newly formed object. This difference is apparent from the number of particle curves shown in Figure 5.25, in which a jump is associated with the coalescence event, but the initiation and growth of the third rope is not readily distinguishable. The sphere/disc ratio for this rope structure (Figure 5.25) was significantly lower than that of other structures studied in this chapter. The coalescing of the first two ropes and the growth of the third did not also affect this ratio, and it remained about 0.65.

The twist of ropes around each other (similar to that illustrated in Figure 5.21a) is indicated by the red curve of pitch length data in Figure 5.25. This pitch length was measured by fitting a helix to each sphere cluster, whilst assuming the axis of the helices to be the director of the disc cluster. The pitch lengths presented in blue and black are the average of the helical pitches fitted to each disc thread in the cluster. In the blue region, two distinct different pitch lengths were apparent, and these are aggregated into a low confidence-value average. As discussed, the pitch length of the ropes is larger than that within each rope, as is also apparent from Figure 5.25, where there is a difference of about 20%.

The secondary pitch of the multi-rope object caused the elongated structure to have a circular cross section, as is apparent in Figures 5.23i-j. Figure 5.24a shows the side view of that presented in the Figures 5.23j at 11.5 million steps. The short pitch length of the structure (being highly twisted) caused significant stress in the outer threads and led to formation of thread defects, as marked in the figure. This can be interpreted in terms of the distortion energies in the outer threads exceeding some threshold and, thus, destabilising the structure. Any further addition of threads to this structure, whilst contributing negative interaction energy, would also necessarily add further to this distortion stress. In this trade-off, the object had to either stop its lateral growth or find another solution. The alternative solution of the system for

5.4 Geometric Frustration

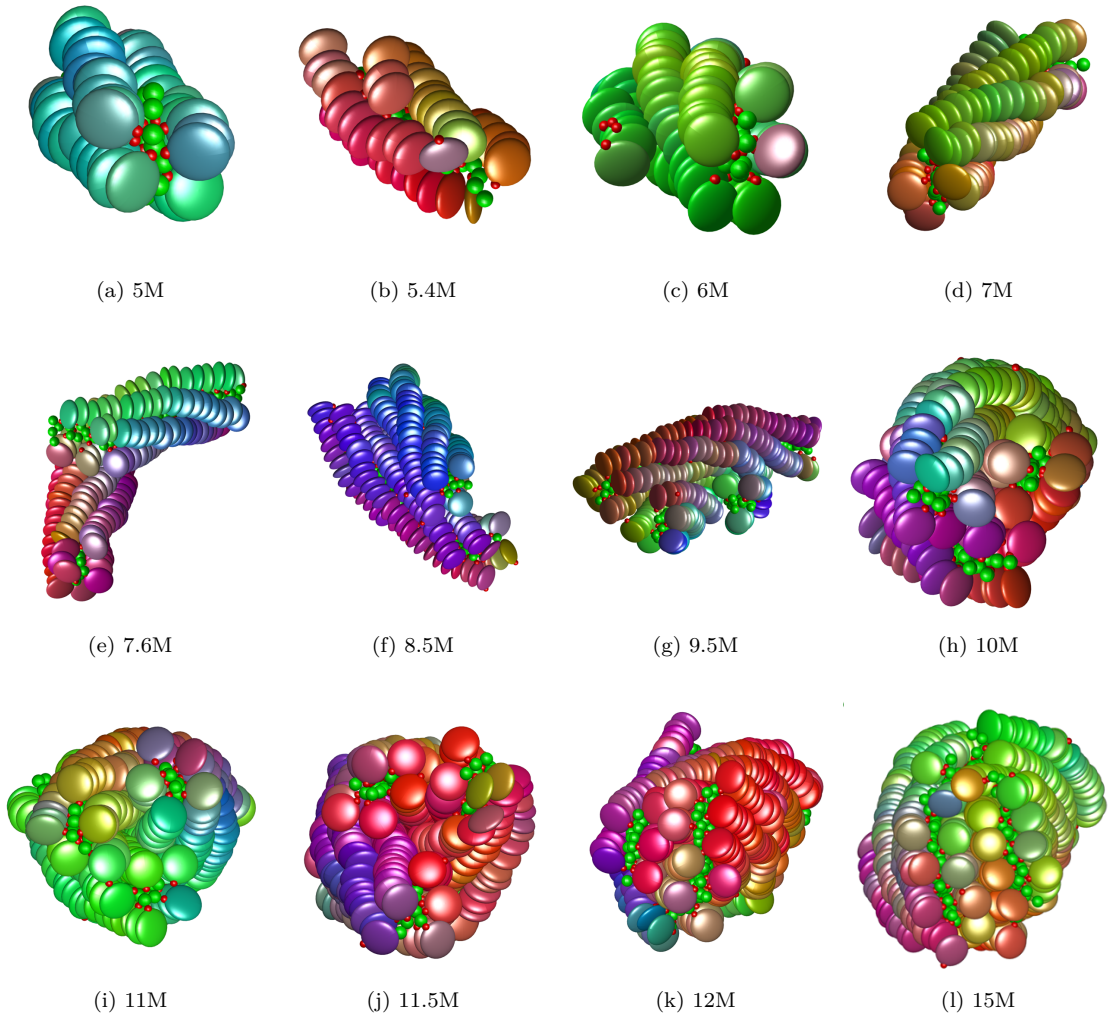


Figure 5.23: The snapshots of self-assembly of 3-rope structure and then its transition to the multi-bilayer structure in a system with $\kappa' = 0.1$, $H=15$ at temperature $T=2.42$. The discs are colour-coded based on their orientations.

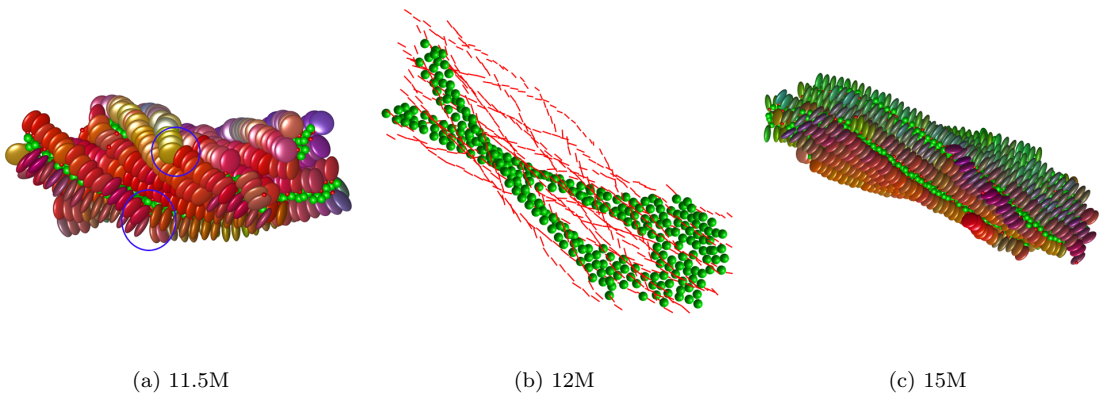


Figure 5.24: Snapshots of the system presented in Figure 5.23 from different views. In part a, the defected threads were marked with blue circles. In part b, the short axes of disc were drawn and one of the sphere cluster was not shown for clarity. In part c, the side view of the twisted double-bilayer was illustrated.

5.4 Geometric Frustration

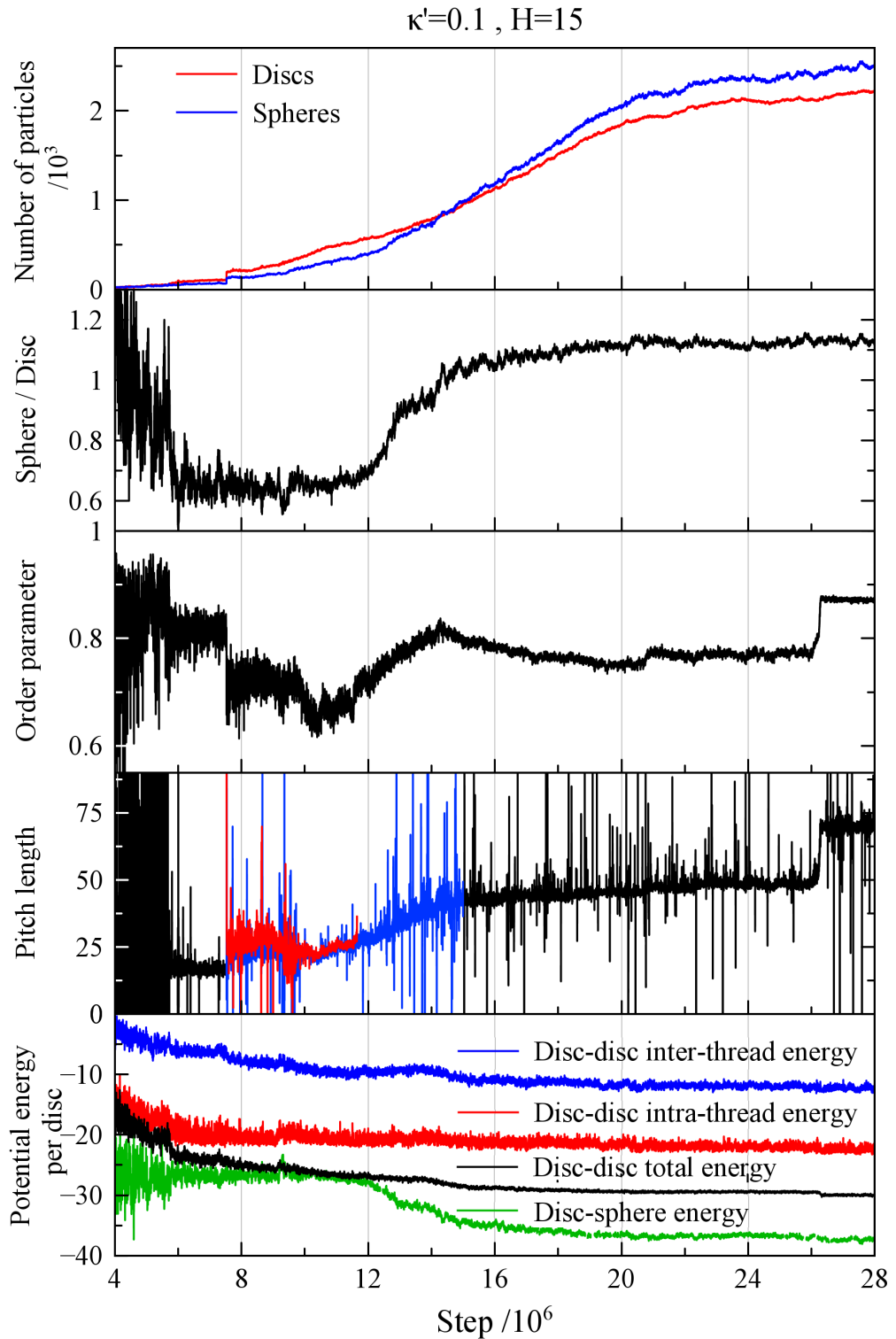


Figure 5.25: Time lines of different properties of the rope system with $\kappa' = 0.1$, $H=15$ at temperature $T=2.42$ which morphed into a double-bilayer structure. In pitch length data, the blue part is for the multi-rope structure in which there are two different pitch lengths, and the red curve is the pitch length of ropes wrapped around each other before the start of transition.

5.4 Geometric Frustration

this frustrated situation was a discontinuous morphological change into a completely different structure. As shown in Figures 5.23k and 5.24b, two of the ropes opened their sphere spaces to one another and laterally merged. This merging of sphere clusters started at one end of the aggregate and propagated along full length of the object. As a result, the two ropes transformed into a bilayer structure. The sheet-like character of the bilayer then influenced the third rope, inducing it to also morph by opening up a lateral space for more spheres to join from the solution. Eventually, a double-bilayer formed (Figures 5.23l and 5.24c).

In undergoing this geometrical transition, the disc-disc potential energy of the cluster was only slightly affected, but the system benefited from a considerable strengthening of the disc-sphere energy, as shown in Figure 5.25. This was due to the significant increase in the sphere/disc ratio of the object. Within the transition, from 11.7 million to 15 million steps, the ratio increased by about 70% and reached a steady value of 1.14. The orientational order parameter, shown in Figure 5.25, was another interesting observable for this system. The order parameter of the single rope, being around 0.8, dropped on the attachment of the second one and dropped even further through the growth of the third. With the start of the transition, the order parameter went up until the double-bilayer was fully formed. In addition to the huge geometrical transition, this interesting system, similar to the other thread-based systems, untwisted itself to longer pitch lengths as it grew. A partial unwinding is apparent in the P_2 curve at about 21 million time steps and a second, more significant one, at about 26 million MD steps. Both of these were associated with an increase in the pitch length of the twisted structure which, finally reached a steady value of about 70 disc diameters. This two-step unwinding was similar to that observed for big fibres, as illustrated in Figure 4.30. Figure 5.26 shows two views of the final structure in this system.

This double-bilayer structure had two benefits over the multi-rope one. First, the growth of the object was less restricted and the number of threads in the structure increased from 15 (before the transition) to over 32 in the final object. The second advantage of the multi-bilayer structure was that it could freely untwist relatively easily to ease elastic stress. Morphological variation between an elongated

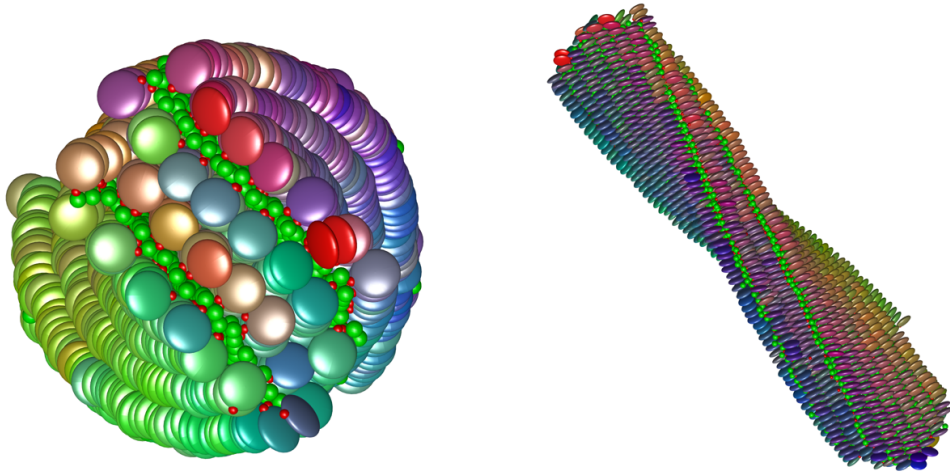


Figure 5.26: Two views of the final double-bilayer structure morphed from a cylindrical object with rope base unit, formed in the system with $\kappa' = 0.1$, $H=15$ after 33 million MD steps.

twisted amyloid fibre with circular cross section and a twisted ribbon has also been experimentally observed [152] (see Figure 5.27). Later, Grason and co-workers [137, 144], theoretically and through simulation of a continuum model, showed that such changes were driven by geometric frustration of twist. The bending energy of the filaments in a twisted bundle has been argued to vary as $r^4 P^{-4}$, where r is the radius of the filament in the bundle and P is the pitch length. This size dependent energy can lead to self-limiting radii in chiral fibres - just as the frustrated multi-rope structure could not grow larger than 15 threads. It has also been shown that the circular cross section shape is unstable in geometrically frustrated twisted bundles [144]. The cross section transition can occur when the ratio of inter-thread strain energy to intra-thread bending energy exceeds a critical value. Both of these behaviours were observed in the simulations of this section, which strongly suggests that the multi-rope bundle was a geometrically frustrated structure.

The simulations of bilayer and rope structures presented in this chapter illustrate two regimes for the self-assembly of the amphiphilic chromonic systems studied here. For smaller hot-spot sizes, i.e. lower H values, twisted multi-rope bundles were formed, while for larger hot-spot sizes, a twisted bilayer (a sandwich of discs with a jam layer of spheres in between) self-assembled. A transition from the rope-based

5.5 Conclusions

to the bilayer-based structures can happen due to geometrical frustration. For the system with $\kappa' = 0.1$, this transition happened at $H=15$, while for slightly stronger face-face interaction, $\kappa' = 0.075$, the transition was triggered at $H=17$. For the latter, a similar pathway was observed for this morphology change, but, as the structure was influenced by the periodic boundary condition effects, the results have not been presented here.

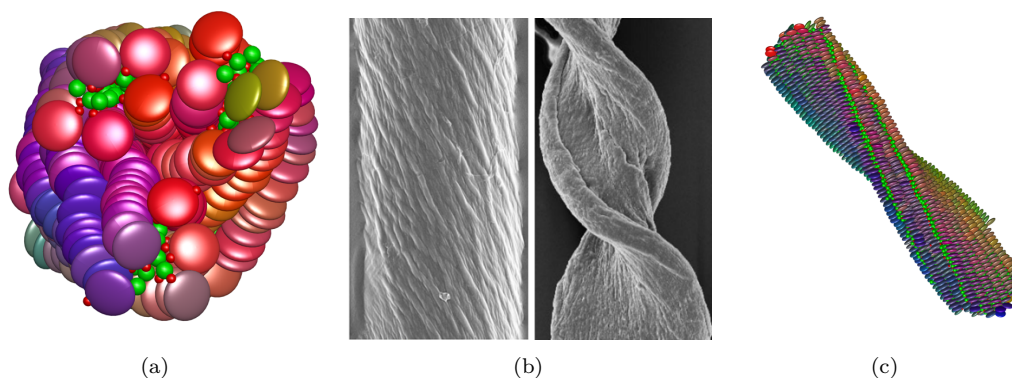


Figure 5.27: Morphology selection between a twisted fibre with circular cross section (part a and part b-left) and a twisted tape (part c and part b-right) due to geometrical frustration. Parts a and c are the results of the present work (see the text). Part b was observed in the experimental work of Ridgley *et al.* [152]. The picture was taken from reference [137].

5.5 Conclusions

In this chapter, the self-assembly of twisted bundles in amphiphilic chromonic systems was studied through MD simulations. The building-blocks were Gay-Berne discs having one or two hot-spot zones around their rims which were attracted to the second species in the simulations, Lennard-Jones spheres. For a single hot-spot model, with H parameters ranging between 20 and 50, a twisted bilayer structure, consisting of two layers of discs and a layer of spheres in between, self-assembled. Threads of discs were also an important feature of this supramolecular structure, a small angle developing between the thread axes in the two leaflets. This angle, together with the efficient packing of spheres, caused the structure to become twisted and, consequently, an emergent pitch length to develop despite the achirality of the building-blocks. The

5.5 Conclusions

simulations also showed that the structural properties of the self-assembled bilayers were influenced by the the extent of solvophilicity of the discs, a parameter which may be used as a tool for the design of such structures with different characteristics. The intelligent response of the systems to the increasing elastic costs of lateral growth of the twisted object was the development of some radial defect lines to localise bend via a concerted mismatch in the particle orientations. In a larger system, the width of the object was so big that the orientational mismatch altered the integrity of the threads and tears developed on the sides of the twisted bilayer.

For smaller hot-spot sizes, interesting twisted structures formed based on ropes of 5 threads of discs wrapped around an elongated cluster of spheres. Significantly shorter pitch lengths were observed in this class of structure compared to other supramolecular structures investigated here. The lateral growth of the basic unit was either through rope-rope interaction or by the growth of a new rope on an existing cluster. This could introduce another emergent twist with larger pitch length than that within the ropes. Due to being highly twisted, the extended lateral growth was also elastically costly for this class of self-assembling structure. This could lead to geometrical frustration in the growing object. However, for a critical size of hot-spot, the system found an alternative solution for the frustrated object by morphing into a multi-bilayer structure - 2 bilayers formed on top of each other. The ability to undergo further lateral growth and to unwind were the advantages of the double-bilayer over the multi-rope.

Simulations of a double hot-spot version of the developed Tanh potential for modelling the amphiphilic behaviour of the discs led to formation of a multi-layer twisted bundle. This structure consisted of layers of discs interacting with spheres on both sides. Three different directions of growth and also three modes of twist were observed for this fascinating structure. Similar to the bilayers, each layer of discs had two pitch lengths associated with two modes of twist (along the threads and perpendicular to them) with different handedness. The sphere layers in the structure acted as lubricant surfaces and caused a consistent angle between the threads of successive layers. This, which can be quantified by the rotation of layer directors

5.5 Conclusions

along the perpendicular axis to the layers, was the third mechanism of the twist in this multi-layer bundle structure.

In the next chapter, self-assembly of tubes in mixtures of amphiphilic discs and spheres is investigated.

Chapter 6

Tube Self-assembly

As discussed in Chapter 2, there are several pathways for self-assembly of tubes from amphiphilic molecules, the literature of two of which were described in detail. Bilayer structures are an important intermediate in most of these routes. Regardless of the pathway, chiral tube formation or rolling-up, a transition from a state involving two identical layers to another one in which the leaflets have different characteristics is necessary. For bilayers, this transition is costly (or at least, associated with a significant energy barrier) because the symmetry of the layers has to be broken to achieve a structure which has inner and outer layers with different radii, i.e. different mean curvatures. This is particularly challenging when the building-blocks are flat core molecules with little flexibility. As with the hierarchical processes discussed so far, for every energy barrier between different hierarchies, there is a chance that systems may become trapped in a metastable state or have their growth diverted along a non-optimal pathway. This may, indeed, be an interpretation of what we observed for the twisted bilayers studied in Chapter 5, where attempts were made to obtain wide structures which undergo a transition from a twisted bilayer to a helical ribbon, a known step for chiral formation of tubes (recall Chapter 2). Instead, when wide twisted bilayers were achieved, they developed defect lines to relieve bend stress rather than exhibiting the tube formation pathway suggested in Figure 2.13. For the observed twisted bilayers of similar leaflets with nearly parallel thread directions, therefore, the twist to helix morphological change did not appear achievable for

6.1 Introduction

the system sizes and simulation time-scales accessible here. However, for a bilayer structure in which the leaflets are not identical, observation of a transition to a tube may become feasible. The rolling up pathway would then be the underlying mechanism for the tube formation.

In this chapter, we investigate the possibility of observing the self-assembly of tubes via a new rolling-up pathway, something which has not previously been reported. For this, the same bipartite amphiphilic chromonic system, described in the previous chapter is used, but with different particle sizes and, therefore, interaction parameters. We first probe the different stages of tube formation hierarchy in this pathway by studying one system in detail. Then, we investigate how the diameter of the self-assembled tubes can be controlled by changing the system parameters.

6.1 Introduction

The aims of this chapter are to determine if the self-assembly of tubes, a complex and very slow process [79, 89], is accessible to the simple coarse-grained models we have developed and used in this work and, if so, gain insight into the pathway of this spontaneous formation and the influence key parameters have on the final object.

As previously, MD simulations have been performed on a mixture of amphiphilic discotic building-blocks and simple Lennard-Jones spherical particles. The general settings of the systems investigated in this chapter are the same as those described in the Introduction section of chapter 5. However, the key difference is the interaction strength of the building-blocks due to their different sizes. Here, thinner discs with $\kappa = 0.3$ were used. The sphere diameters were again fixed to be the same as the disc thickness and, thus, $d_{sphere} = 0.3$. Therefore, the LJ potential parameters, introduced in equation (3.34) for spherical particles, were $\epsilon_0 = 1$ and $\sigma_0 = 0.3$. The usual unity values for the equivalent parameters were used in the disc-disc interactions, while the σ_f parameter was the same as the thickness of the disc, $\sigma_f = 0.3$. The energy anisotropy parameter for the discs was $\kappa' = 0.075$. For the GB part of disc-sphere interaction, the ϵ_0 parameter (potential well-depth of edge-sphere configuration) was chosen to be the same as the edge-edge well-depth between two discs. The

6.2 Tube Formation Pathway

size parameter, σ_0 , was determined from equation (3.39). These gave $\epsilon_0 = 3.3$ and $\sigma_0 = 0.7382$, respectively (see Table 5.1). The ϵ_{max} and ϵ_{min} parameters of the Tanh potential were set to be 5 and 0.2, as previously. In all simulations, the variable cut-off radius approach with $\sigma_{cut} = 0.65$ was used. The extent of solvophilicity of the discs was controlled with the H parameter in the Tanh potential.

6.2 Tube Formation Pathway

In the simulations of the system with 3000 discs, 10,000 spheres and $H=40$ at temperature $T=4.5$, after about 9 million MD time steps (the step size of 5×10^{-4} time unit was used for this system), it was observed that a single cluster formed and did not dissolve - in contrast with its predecessors which self-assembled at earlier times and then melted back into solution (see the number of particle curves in Figure 6.1). Similar to the amphiphilic chromonic systems investigated in the previous chapter, the cooperation of disc-disc interactions, mostly in the form of small stacks, and the interplay of these discs and an aggregate of spheres was key to the initiation of this cluster (Figure 6.2a). Then, a double-helix structure was observed at 10 million MD steps (Figure 6.2b). This is similar to what was predicted by Fejer *et al.* [99, 103] for a small cluster of discotic particles with edge-edge preference (see Figure 2.20). As illustrated, the cores of hot-spot areas of the discs, shown by small red dots, are generally pointed towards the sphere cluster in the centre of the object. The main difference of this formed bilayer-like structure with the early stages of twisted bilayer formation observed in Chapter 5 (e.g. Figure 5.3) is the orthogonality of threads in opposite leaflets. That is, the curved threads at each side are similar to lobes of a ‘tennis ball’ which hold the sphere aggregate.

The next step of the growth was the addition of a new thread to this double-helix, that is, two adjacent threads on one side of the sphere cluster and a single long curved thread on the other (Figure 6.2c). As can be seen, the threads on the opposing sides remained orthogonal to one another. Addition and dissociation of monomers and threads then determined the growth characteristics of the object until about 19 million MD steps (Figure 6.2d-e). The data of normalized Moments of Inertia in

6.2 Tube Formation Pathway

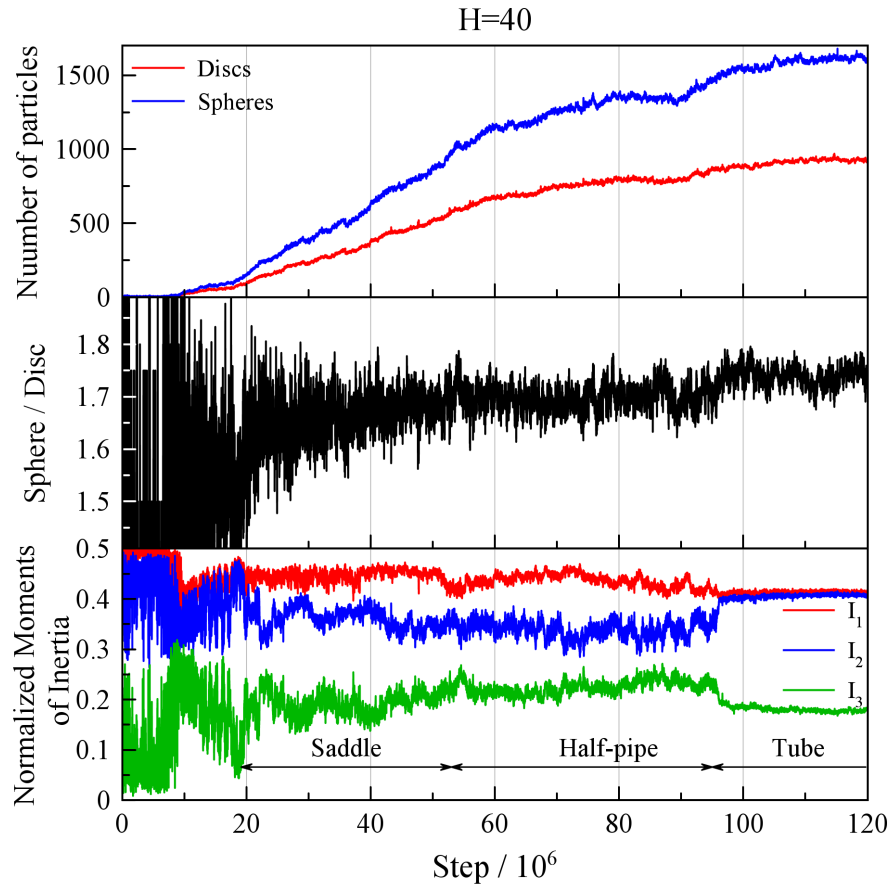


Figure 6.1: Time lines of the parameters of the system with $H=40$ at $T=4.5$. Two leaflets of discs are considered as a single cluster.

Figure 6.1 also shows that, the object became increasingly elongated over this growth phase (2 large components and a small one). This then changed, indicating cross over to another growth approach. One possible motivation for this switch was the low sphere/disc ratio of this elongated cluster. As discussed in the previous chapter, growing aggregates favour structures which increase this ratio, so as to be benefited from having larger numbers of hot-spot interactions with spheres. Therefore, a decrease in this ratio is energetically unfavourable for a system. The change in growth mode at 19 million MD steps was associated with this ratio recovering to a value of about 1.65. Configuration snapshots show that, from this point, a bilayer structure with two orthogonally aligned leaflets of discs and a layer of spheres in between was apparent (Figure 6.2f). Now, there are 4 zones at the edges of the

6.2 Tube Formation Pathway

bilayer for addition of spheres and, therefore, the number of spheres was able to grow at a higher rate (see number of particle curves in Figure 6.1).

As said, a significant difference between the bilayers explored in this chapter with $\kappa = 0.3$ and those of the previous chapter with $\kappa = 0.345$ is that, here, the threads in opposing leaflets were in an orthogonal arrangement with respect to each other. This orthogonal arrangement was also observed in the experimental work of Maliszewskyi *et al.* [153], where bilayer Langmuir-Blodgett films of triphenylene-based discotic molecules were studied. In some cases, they observed an unexpected square-fold symmetry, instead of the usual hexagonal columnar structure. It was argued that this observation is a consequence of having two layers with orthogonal columns, similar to the bilayers of this chapter. The authors further speculated that there may be two minima in the orientational potential energy; one associated with parallel stacks and another for configurations in which the threads in different leaflets have a roughly 90° angle with each other. In addition, here, although each layer of discs covered the same area of spheres, they had an important structural difference. One layer persistently consisted of a smaller number of long threads, while the other one had a larger number of shorter threads. This resulted in the two layers having different mechanical properties, therefore, the emergent broken symmetry required for eventual tubule formation. Having curved threads with about 90° angle with respect to each other caused the sphere layer to adopt a saddle shape [148], as is apparent in Figures 6.2g-h and 6.3a.

The monotonic graphs of number of particles for both spheres and discs depict that the saddle structure continually grew. This caused the threads near four growth zones to be less interdigitated, which is not energetically favourable. In some cases, a few short threads formed at the sphere-rich edges of the leaflet to compensate the increased area and cover the exposed spheres - one example of this can be seen at the right edge of the top panel of Figure 6.3a. This resulted in disc-disc energy only dropping slowly to lower negative values, as shown in Figure 6.4. This figure also shows the time lines of key observables for the two leaflets of discs. To be able to identify each leaflet as a separate cluster, additional constraints were applied to the cluster analysis code. The thresholds for disc-disc distance within threads and the

6.2 Tube Formation Pathway

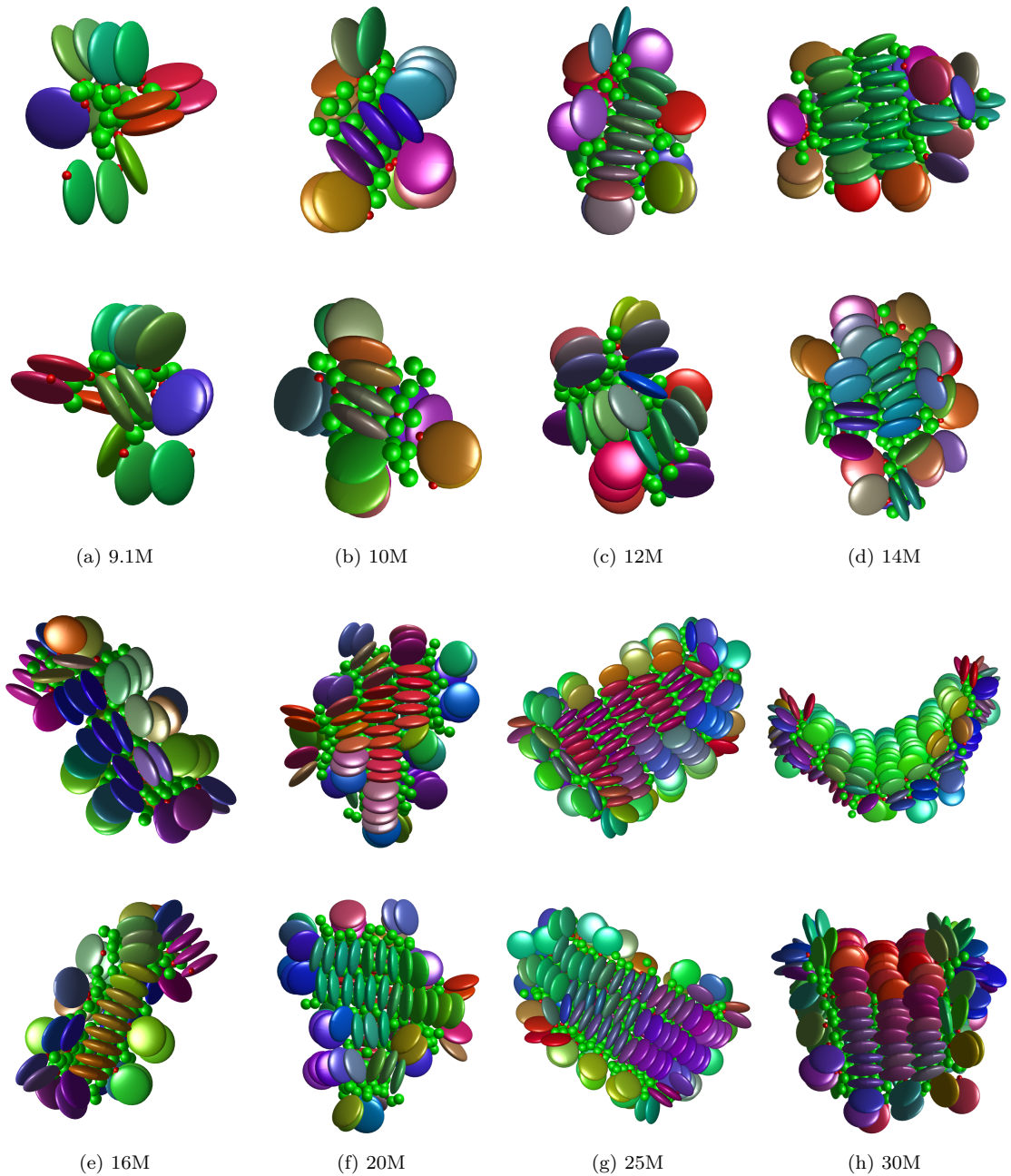


Figure 6.2: The snapshots from the system with $H=40$ at different time steps written at the bottom of each part. Two views of the same configuration are shown at the top and bottom panels. The discs are colour-coded based on their orientation and the spheres are in green. The small red dots at the rim of each disc show the core of hotspot region as a guide to the eyes. The letter M stands for million.

6.2 Tube Formation Pathway

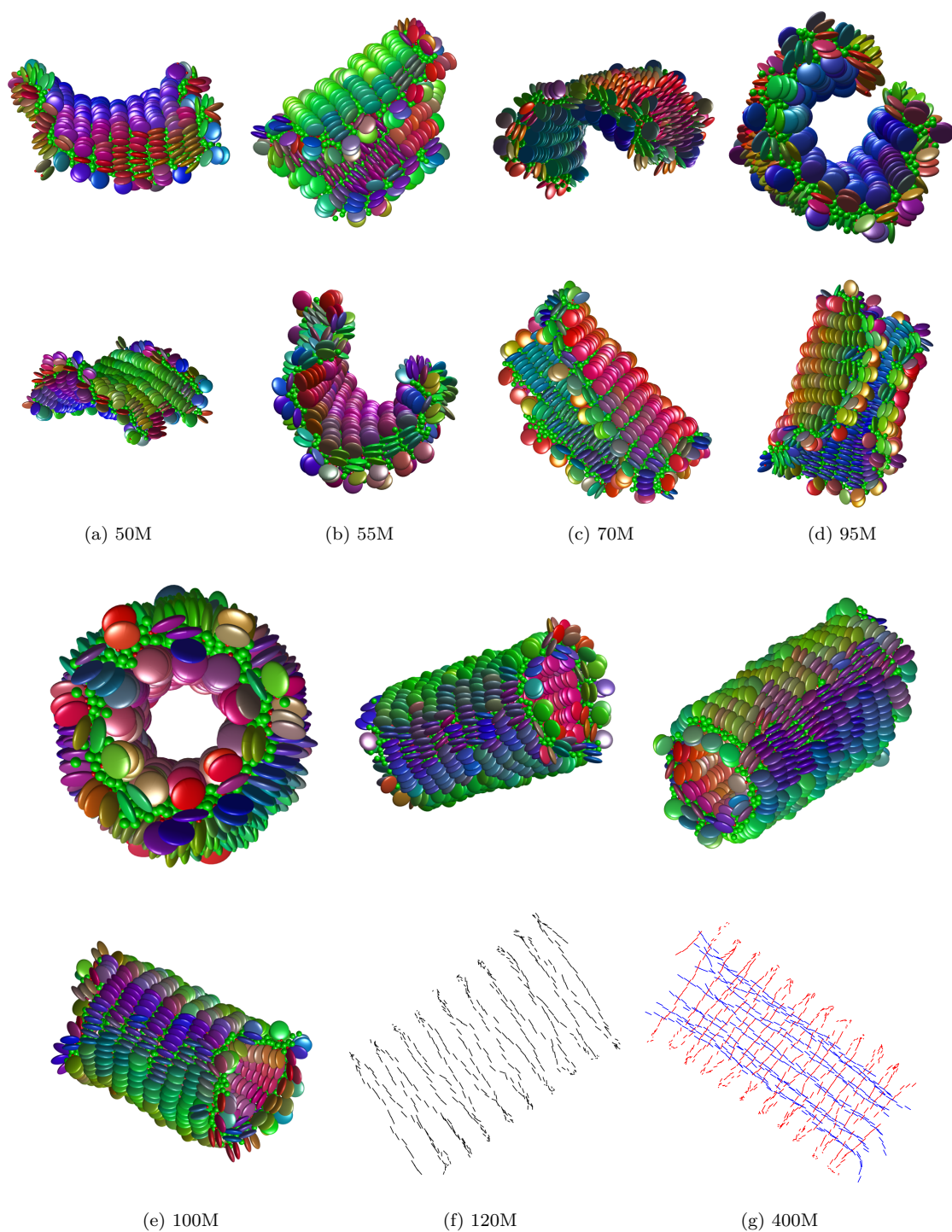


Figure 6.3: See caption of Figure 6.2. The bottom panels of parts f and g show the short axes of particles in the same configuration as the top panels.

6.2 Tube Formation Pathway

thread-thread distance in the cluster were reduced from 0.7 and 1.5, which were used for extracting the data of Figure 6.1, to 0.47 and 1.1 disc diameters, respectively. The maximum angle between the short axes of particles in the neighbouring threads was also reduced from 90° to 30° . These changes made it possible for the two layers of discs to be consistently identifiable. Because of these restrictions, the particles at the edges of the cluster, which were not sufficiently aligned with the threads in either leaflets, were excluded from these time lines and, therefore, the sum of the number of particles in each layer in Figure 6.4 sometimes drops below that of Figure 6.1.

At about 51 million MD steps, another morphological change was observable, the saddle shape being abandoned in favor of “half-pipe” structure. This structural transition is apparent in almost all of the graphs in Figure 6.4. The half-pipe shape of the cluster can also readily be seen in Figure 6.3b, and the terms ‘inner’ and ‘outer’ layers used in Figure 6.4 are straightforwardly identifiable. In the inner layer, the threads were almost parallel with high order parameter (see Figure 6.4). However, they were also slightly curved only at their ends. The threads in the outer layer became equivalent and their local curvature was almost constant along the thread. A similar pattern of parallel stacks and arced threads was predicted by Fejer *et al.* [99] by minimization of global energy of 36 discotic particles with edge-edge preference (the same system with 10 particles formed a double-helix structure). The transition from saddle shape to half-pipe structure is consistent with what was found in previous chapters where the size of the object had an effect on its large-scale morphology.

By fitting a triangulated surface on the sphere layer of the cluster (the triangulation was performed with up-sampling ratio of 8 and 2-pass smoothing - see Chapter 3), the averaged Mean curvature of the layer, illustrated in Figure 6.5a, was measured. As indicated by the jump in data at about 51 million MD steps, on morphing into the half-pipe structure, the cluster significantly increased its Mean curvature. Although the disc-disc and disc-sphere energies of the outer layer remained roughly constant through this transition, those for the inner layer experienced a significant strengthening - see two bottom windows of Figure 6.4. As the cluster grew, the curvature of outer threads increased and the edges were pushed towards each other

6.2 Tube Formation Pathway

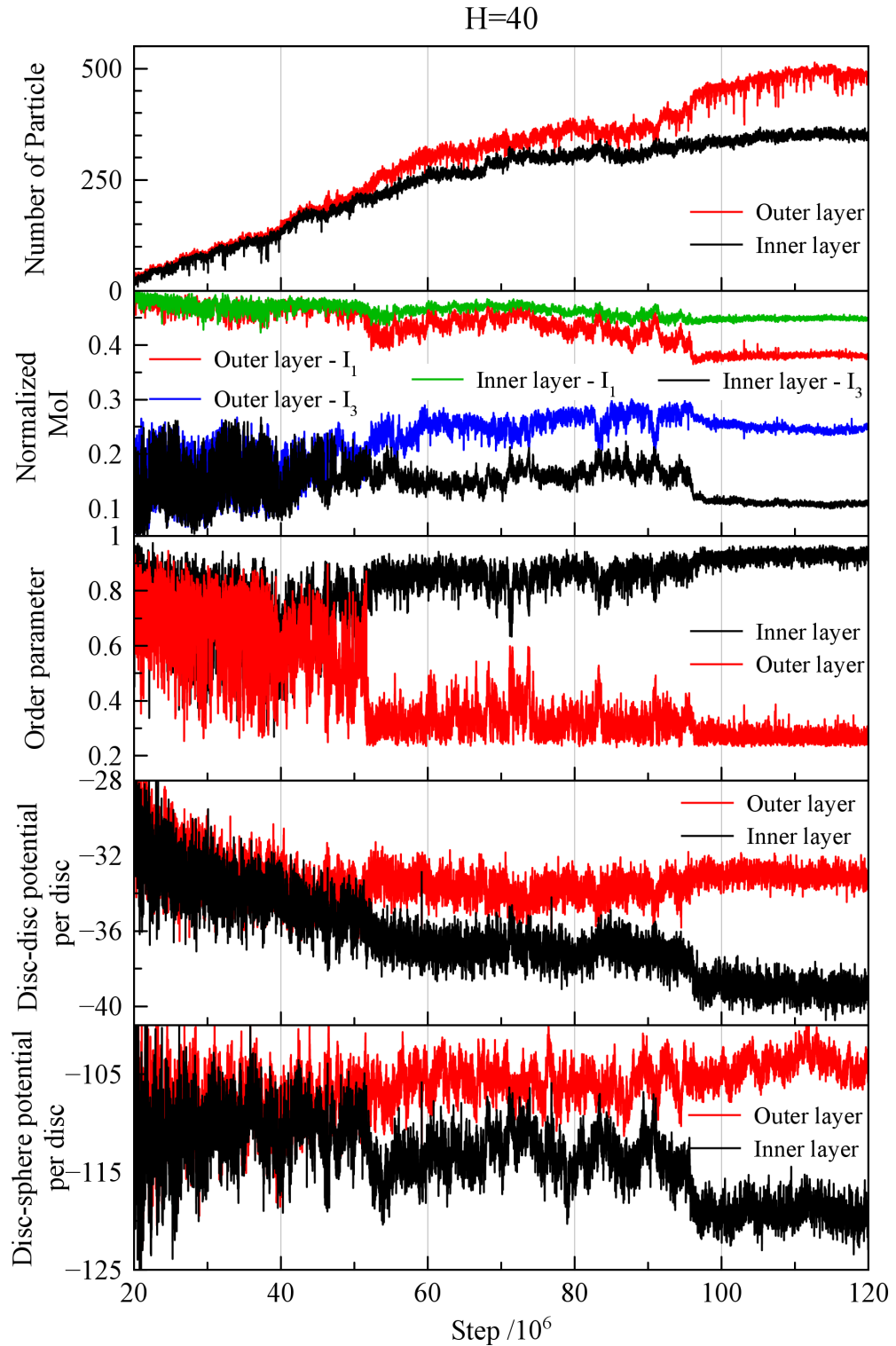


Figure 6.4: Time lines of data for two layers of discs identified by applying more constrains on the cluster analysis code. Before the transition to the half-pipe, the inner and outer layers are meaningless concepts and this classification is just based on the number of particles in each layer. There is a high likelihood that, in this zone, the layers swap their names.

6.2 Tube Formation Pathway

as the half-pipe rolled on itself (Figures 6.3b-d). This continued upto 96 million steps, at which point, the edges touched and rapidly unified. The second sharp jump in the Mean curvature data (Figure 6.5a) at 96 million steps is a consequence of the associated reduction in the radius of the object. At this point, a full tube with distinct inner and outer layers was apparent (Figure 6.3e). Eleven threads formed the inner layer - the inner diameter of the tube was fixed at roughly 2.4 disc diameters. The tube completion also led to an increase in the sphere/disc ratio as indicated by Figure 6.1. This increase was more significant for the inner layer and caused the disc-sphere potential to go to more negative energy values. This also strengthened the disc-disc interaction of the inner layer, although the increased curvature of the outer layer had a slight weakening of its interaction strength. The closing of the tube had also an effect on the normalized Moments of Inertia data of the object, as shown in Figure 6.1. In this figure, different stages of growth (saddle, half-pipe and tube) are also labelled.

For the twisted bilayers with nearly parallel threads, it was seen that the sphere layer was corrugated (see Figure 5.8). Here, the orthogonal arrangement of threads caused the sphere layer to be undulated. This is illustrated in Figure 6.5b by showing the Mean curvature contour of the sphere layer for one of the configurations. This undulation feature provided the spheres with the opportunity to be effectively packed in the grooves of the disc threads of both leaflets. The two parts of Figure 6.5 together show that, although the sphere surface was undulated, the averaged Mean curvature could capture the morphological transitions of the structure.

Interestingly, the closing process of the tube led to the formation of a helical pattern in the outer layer, with a very short pitch length of one disc diameter. This is illustrated by showing the short axes of the particles in the outer layer in the bottom panel of Figure 6.3f. The simulations of other systems which will be discussed later showed that this helical pattern was not absolutely reproducible. It occurred in some tubes, whilst the alternative, formation of separate rings of discs in the outer layer, occurred in others. Careful examination of the inner layer in this system with the helical outer layer revealed that the threads were slightly twisted (see top panel of Figure 6.3e). Although a large variation in the pitch of these twisted threads was

6.2 Tube Formation Pathway

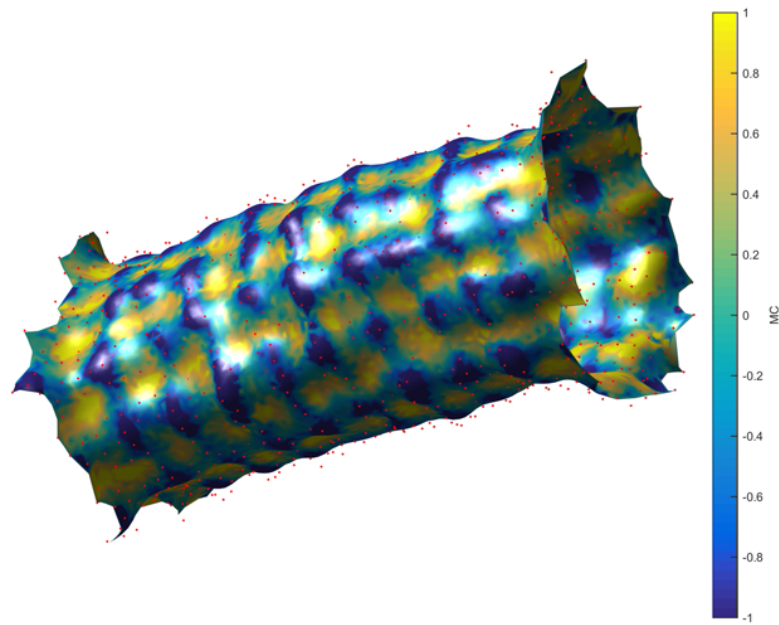
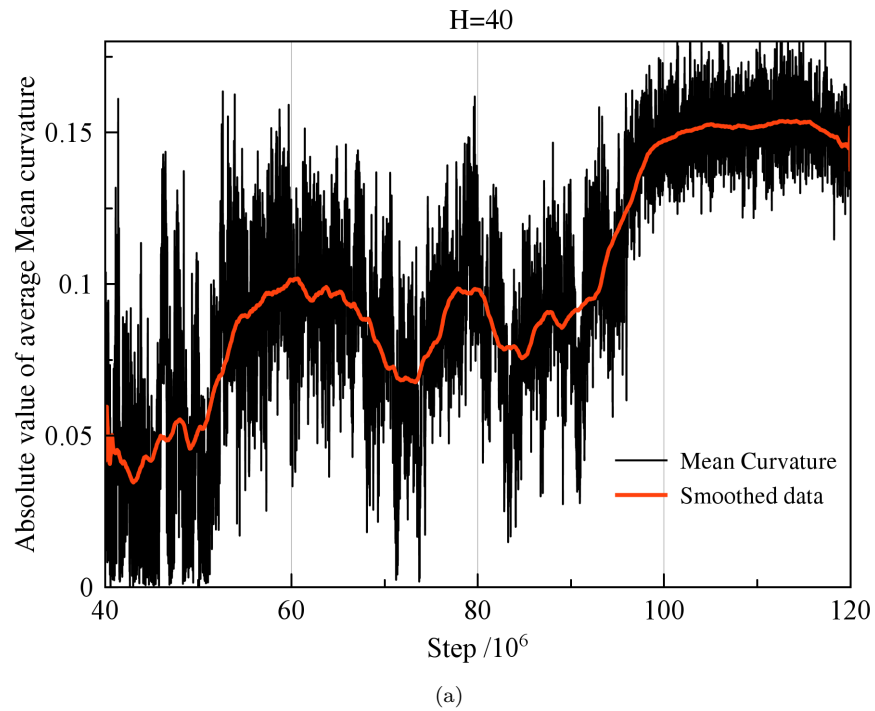


Figure 6.5: Mean curvature measurement on the triangulated surface fitted on the sphere layer. a) Absolute of averaged values of local Mean curvature in the system with $H=40$. The smoothed curve is the result of moving-average smoothing in a neighbourhood of 500 data points. b) The Mean curvature plot for the tube formed at the system with $H=40$ in the step of 120 million. The small red dots show the positions of centre of spheres.

6.2 Tube Formation Pathway

observed, on average, the pitch length was in the range of 150-300 disc diameters. It is noteworthy that the inner layer maintained a different handedness from the outer layer and that this caused the angle between the threads of the two leaflets to be close to normal. The discussed pathway for self-assembly of tube in this system can also be observed in full in a video presented in Appendix D. As is apparent from the video, the discs in the outer layer of the tube were continually being exchanged with those in the surrounding solution. This mobility was also observed for the sphere layer. On the other hand, the discs in the inner threads rarely changed their positions in the structure, except those which were very close to the edges of the tube.

This simulation was run on for a very long time to see whether the formed tube was a final stable structure. The results showed that the tube slightly continued to grow in length, as illustrated by the number of particles and moments of inertia curves (Figure 6.6). No significant change was observed in the tube structure though, and after 400 million MD steps, it still had the same features as described above (see Figure 6.3g). Thus, the number of discs in the object reached a steady state value of about 1/3 of the size of the simulated system, meaning there was still considerable material for further growth. The steady-state inner diameter and length of the tube were 2.39 ± 0.02 and 13.13 ± 0.5 disc diameters, respectively. Therefore, the aspect ratio based on the inner diameter was 5.5.

Reproducibility

In order to investigate the reproducibility of the observed pathway for the self-assembly of tubes, the simulation just described was repeated in a bigger system with 6000 discs and 20,000 particles (double the original size) with the same overall density of 0.22, $H=40$ and slightly higher time step of 6×10^{-4} . The simulation of this bigger system in temperature $T=4.5$ (the same temperature as the smaller system) led to formation of several clusters which then coalesced to form a defected structure. By performing the simulation at the slightly higher temperature of $T=4.54$, however, one dominant cluster was observed with a few small clusters also occasionally forming.

6.2 Tube Formation Pathway

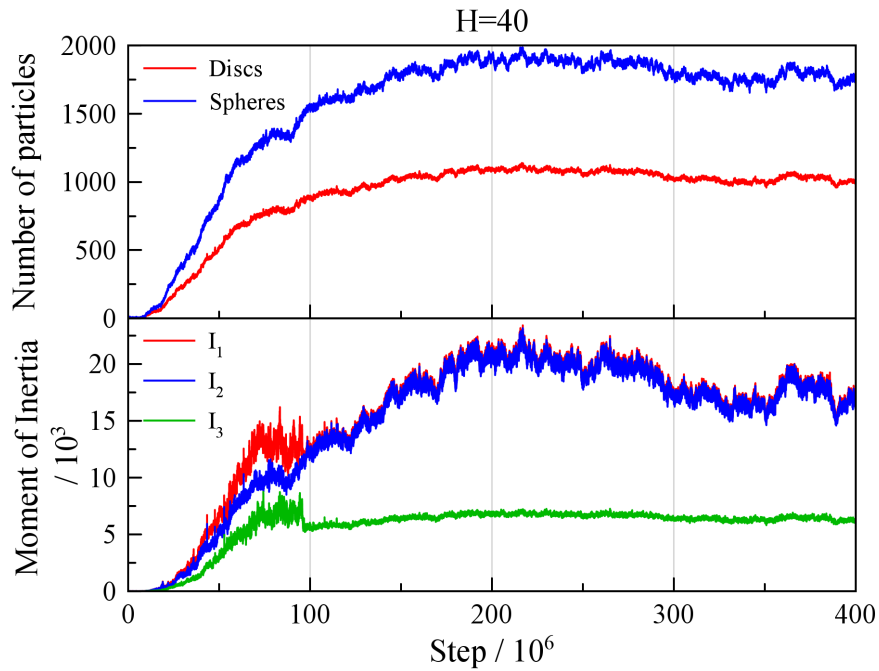


Figure 6.6: Time lines of the number of particles and also the Moments of Inertia of the discotic cluster for system with $H=40$ at $T=4.5$.

This is similar to what we observed for fibre formation (Chapter 4), where an increase in system size was associated with systems forming assemblies at slightly higher temperature (see Figure 4.25).

Results showed that this bigger system followed the same sequence of stages as described above to self-assemble the tube, although there were some slight differences. In this higher temperature simulation, the system remained in the early stages of growth for a long time, e.g. the leaflets in the biggest cluster at step of 80 millions had only 2 and 3 threads. The large variations of Moments of Inertia and sphere/disc ratio, shown in Figure 6.7 upto this time step, are, thus, similar to what we observed in the smaller system of Figure 6.1 below time step of 20 millions. It seems that, this is the consequence of the higher temperature of this system, which will have made the process of adding material to the cluster more difficult. The jump in the number of particles curves at 94 million steps is due to the coalescing of a small cluster and the main object. As the general morphology of the main object was soon recovered, the simulation was left to run on. The important transition from saddle structure to a half-pipe morphology was also observed in this system, indicated by

6.2 Tube Formation Pathway

the sharp change of the normalized Moments of Inertia (particularly the biggest one) at about 123 million steps. The tube structure eventually formed with the merging of the edges of the half-pipe, at 151 million steps. This led to an increase in the sphere/disc ratio of the cluster to an average value of 1.73, very close to that of the smaller system, 1.74.

Here, the merging process and the formation of the tube was comparatively slow, starting from the central threads of the outer layer and, then, incorporating more and more of the structure as the edge threads curved round to complete the tube. Initially, the completed part of the outer layer formed a helical pattern, like that obtained for the smaller simulation system. However, as more and more outer threads become incorporated, this changed into several separate rings alternative and the short pitch helical structure was lost (see Figure 6.8). This was the only noticeable difference of these two recent systems.

The disc-disc and disc-sphere potential energies of each layers of discs, plotted in Figure 6.9, also show effectively the same behaviour as was observed in the smaller system. The transition into the half-pipe morphology can be identified by the initial divergence in the energies of two layers, although in this figure the difference is less apparent than it is in Figure 6.4. The merging of the outer threads, however, is associated with a significant difference in the energies of the layers. As shown in the figure, shortly before the big change at about 151 million steps, the energy difference between the two layers was significantly reduced. This was likely due to the detail of the merging process exhibited by this system, which started from the center and imposed local saddle deformation, in which the two layers were more or less equivalent. This local saddle structure is apparent, i.e. in the top edge of Figure 6.8a, even after the start of merging.

The tube formed by the 6000 disc system had slightly fewer particles (only 6%) than that of the 3000 disc system. In both cases, the inner layer consisted of 11 threads, with average inner diameters of 2.54 (6000 discs) and 2.39 (3000 discs). This indicates that, the size of the self-assembled tube and, in particular its diameter, were dictated by the interaction parameters rather than the system size. This contrasts with the results obtained for self-assembling fibres and twisted ribbons, in

6.2 Tube Formation Pathway

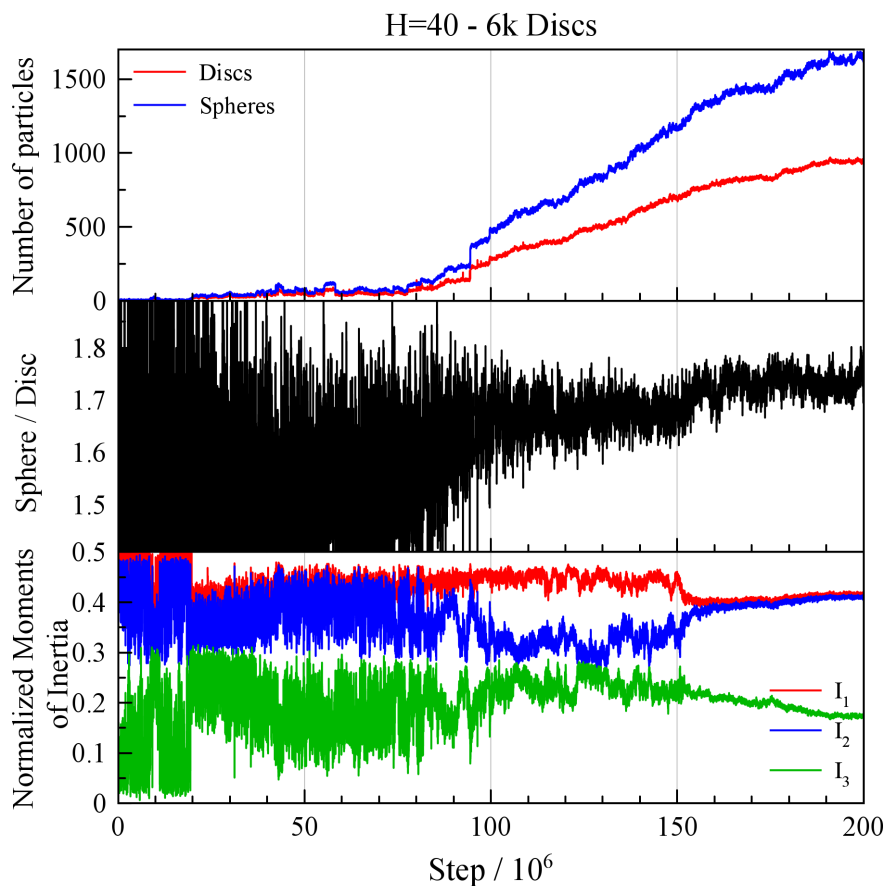


Figure 6.7: Time lines of the parameters of the bigger system with 6000 discs and $H=40$ at $T=4.54$. Two leaflets of discs are considered as a single cluster.

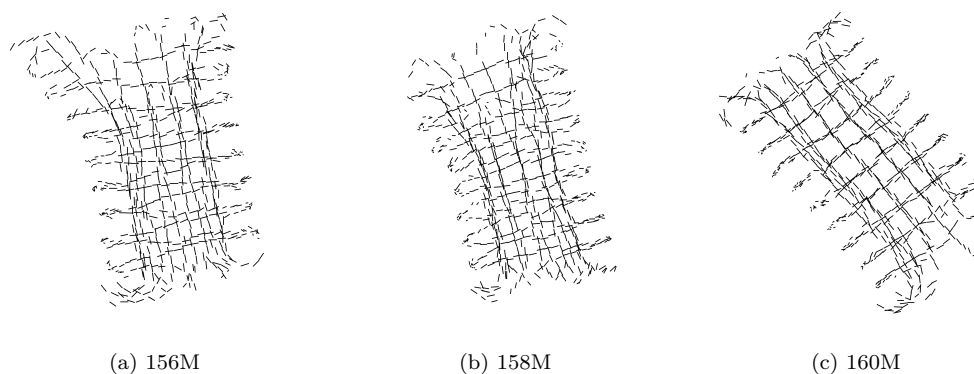


Figure 6.8: Short axes of the discs in the tube structure formed in the system with 6000 discs and $H=40$ at different MD time steps. In parts a and b, the outer layer has a helical pattern, while in part c, it morphed into several separate rings.

6.3 Controlling Tube Size

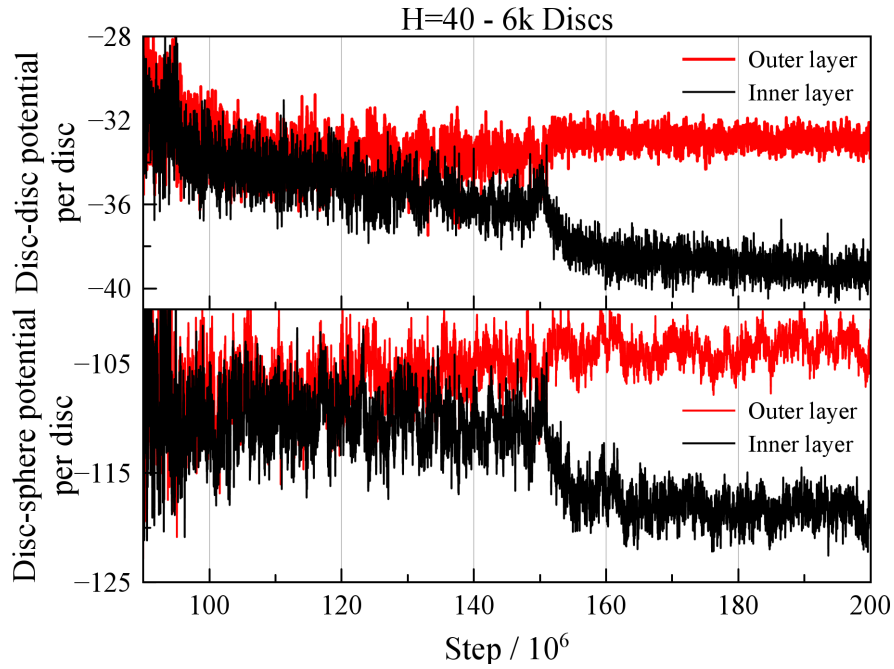


Figure 6.9: Time lines of disc-disc and disc-sphere potential energies per disc for the two leaflets in the system with 6000 discs and $H=40$.

which, change of the simulation size changed features of the self-assembled objects. Therefore, in the following section, we investigate the effect of interaction parameters on tube size.

6.3 Controlling Tube Size

The aim of this section is to assess the generality of the self-assembly pathway just described and, so determine whether this tube formation mechanism is limited to a very specific set of input variables or holds true widely. To this end, equivalent simulations were performed for systems with hot-spot sizes ranging between $H=30$ and $H=50$. In the previous chapter on twisted ribbon self-assembly, it was found that the size of the hot-spot can have an effect on the flexibility of the object and, consequently, its character. Here, we might expect to see a similar impact on the rigidity of the threads and, therefore, their capability to maintain the curvatures needed to form a tube.

6.3 Controlling Tube Size

In all simulations presented here, mixtures of 3000 discs with $\kappa = 0.3$ and 10,000 spheres with $d_{sphere} = 0.3$ were simulated at a total number density of 0.22. All other input parameters were the same as those set out in the introduction section of this chapter. Four sizes of hot-spot, H=30, 35, 45 and 50, were employed to investigate the effects of this parameter on the spontaneous formation of tubes. A time step of 7.5×10^{-4} unit (slightly larger than the previous system to speed up the assembly) was employed for all of the systems except for H=50, for which it was set to be 5×10^{-4} .

The systems with H=30 and H=35 followed the pathway for tube formation, but they did not manage to pass through the last stages of the previously observed system because the number of particles available was not sufficient for them. In order to enable the objects to achieve fully formed tubes in these two systems, a combination of modifications were implemented. After the steady state had been established in the initial systems with 3000 discs, more materials (discs and spheres) were provided to the system, whilst maintaining the overall temperature and density. Individually, the systems were enlarged to 6000 discs and 20,000 spheres, the new particles being randomly distributed in the final configuration of the smaller system. For both systems, the aggregate grew but neither achieved full tube formation. For the H=30 system, after a steady object size had been achieved, the system was gently cooled from the formation temperature of $T=4.37$. Temperature decrements ranging from 0.01 to 0.04 were used, with 15-20 million MD steps being performed at each temperature. For the H=35 system, a second round of material addition (at constant overall density) was attempted, resulting in a system with 9000 discs and 30,000 spheres. After reaching a steady state size at the initially simulated temperature, a gentle cooling sequence was implemented with temperature decrement of 0.05 and 20 million MD steps at each temperature. Through this approach, a full tube eventually self-assembled. It should be noted that, in order to maintain density at each material addition step, the simulation box size were increased to 49.07 and 56.18 disc diameters for systems with 6000 and 9000 discs, respectively. Investigations showed that both material addition and gentle cooling, led to further growth of the formed objects (see the number of particle curves in Figures 6.10).

6.3 Controlling Tube Size

That is, the existing cluster acted as a template for the growth, similar to what was observed in the seeding of fibre-forming systems in Chapter 4. Without these modifications, it would not have been possible to observe the tube formation for these two H parameters because of the limits of computational resources available. For example, even by applying these modifications, in the $H=30$ system, the parallel simulation of 685 million MD steps toward the full tube assembly lasted about 8 months on 12 cores.

Figure 6.10 shows time lines of some structural properties of the growing aggregates in the systems with $H=30$ and $H=35$. The beginning of the described modifications were marked for each system. As can be seen, these modifications did not have a significant effect on the normalized Moments of Inertia of the growing cluster. Similar features as those described in the $H=40$ system can be identified for these two systems - different stages of the tube formation pathway are labelled.

The results show that, for all of the H values investigated, systems initially formed a saddle structure, the curvature of which increased with increase in H . This is why the aggregates with smaller hot-spot size required additional source material to be able to morph into the half-pipe structure. The change from saddle to half-pipe for the $H=30$ and $H=35$ systems is illustrated in Figure 6.11 by two snapshots for each system before and after the structural change. As seen, in the $H=35$ system, the flexibility of the inner threads was still sufficient for negative Gaussian curvature to be retained at the edges of the structure even after the transition. For the systems with higher H parameters ($H=45, 50$), the sizes of the cluster and, therefore, the numbers of threads involved were significantly smaller, such that the curvature and structural changes were less clear-cut. For example, in the $H=50$ system, at the point which the tube formed, the outer layer had only 2 complete and one partial rings. Figure 6.12 illustrates the growth of the tube in this system with $H=50$ by showing time lines of some properties of the biggest aggregate. Due to the small size of cluster, the formation stages before tube closing were not labelled separately in this figure.

After very long simulations (65, 60, 475 and 680 million steps for the systems with $H=50, 45, 35$ and 30 , respectively), a tube structure self-assembled in each

6.3 Controlling Tube Size

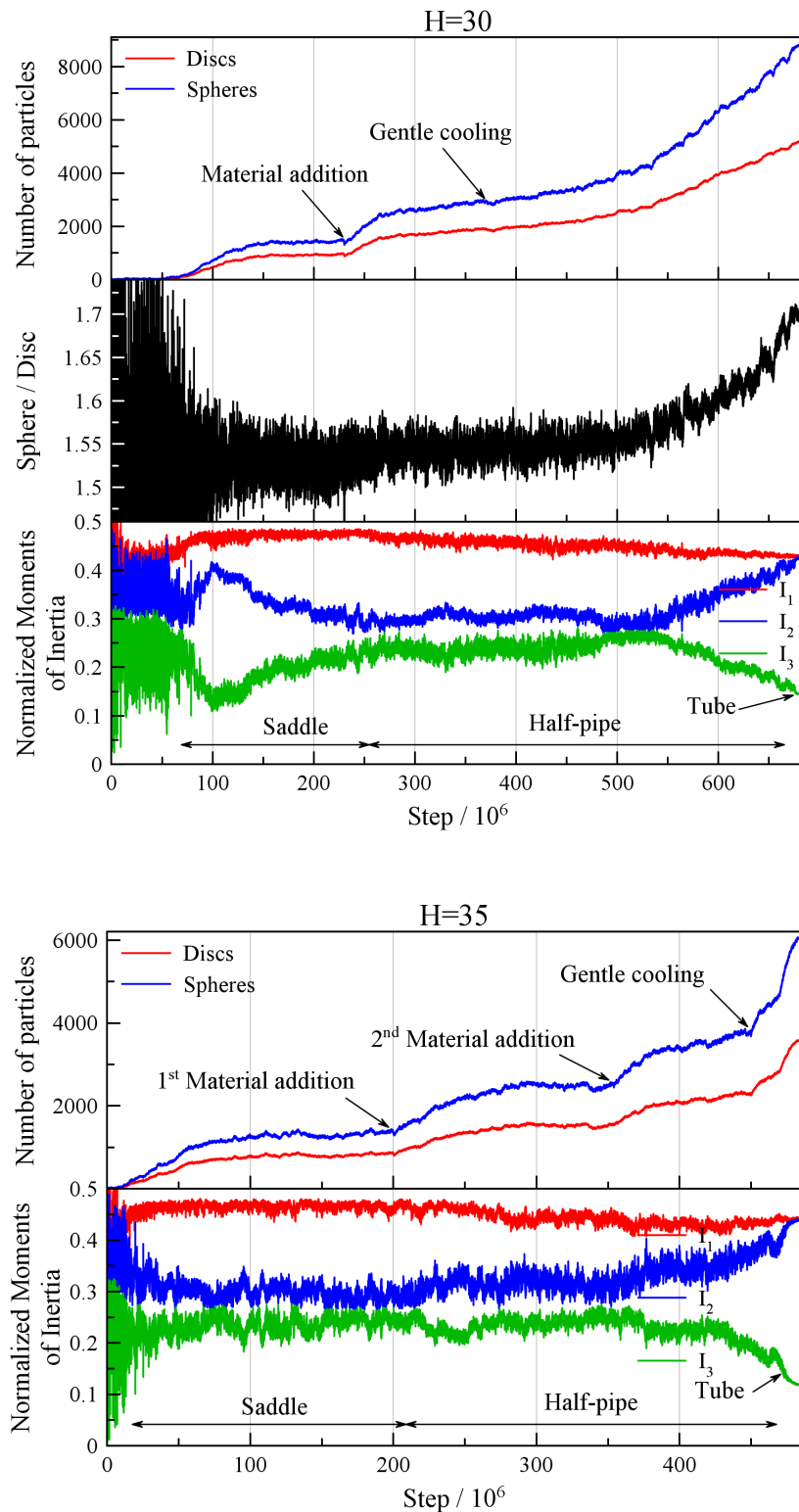


Figure 6.10: Time lines of the parameters of the systems with $H=30$ (top) and $H=35$ (bottom). The beginning of performed modifications were marked in each figure. Different stages of the tube formation pathway were also labelled. For the $H=30$ system, the formation temperature and the final one after gentle cooling runs were $T=4.37$ and $T=4.04$, respectively, while those were, respectively, $T=4.45$ and $T=4.35$ for the $H=35$ system.

6.3 Controlling Tube Size

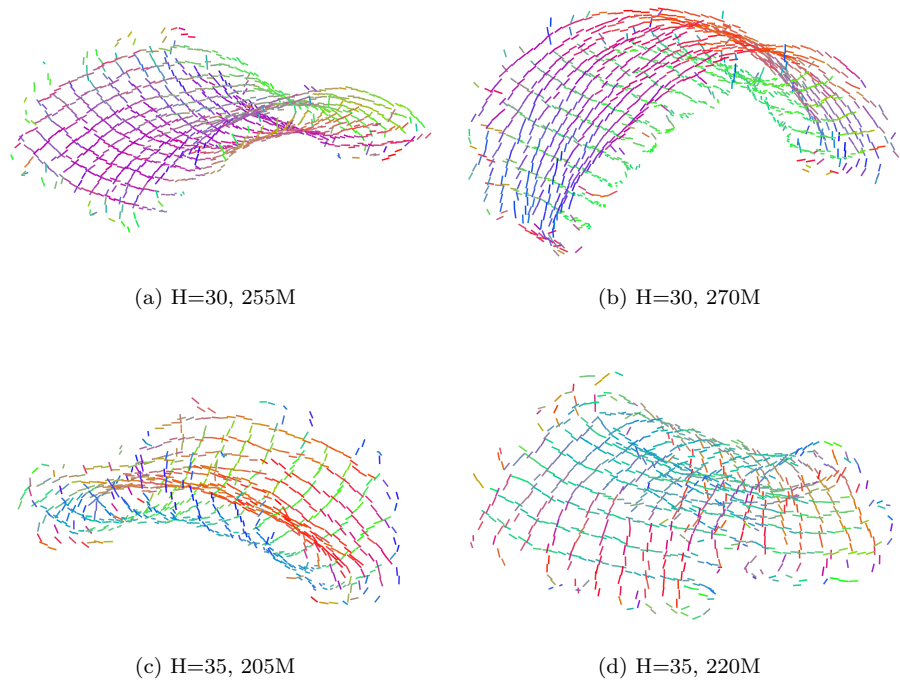


Figure 6.11: Snapshots of two systems with $H=30$ (top panel) and $H=35$ (bottom panel) before (left panel) and after (right panel) transition into half-pipe structure. Short axes of discs were coloured based on the particle orientation. The time steps associated with each configurations were written in the captions.

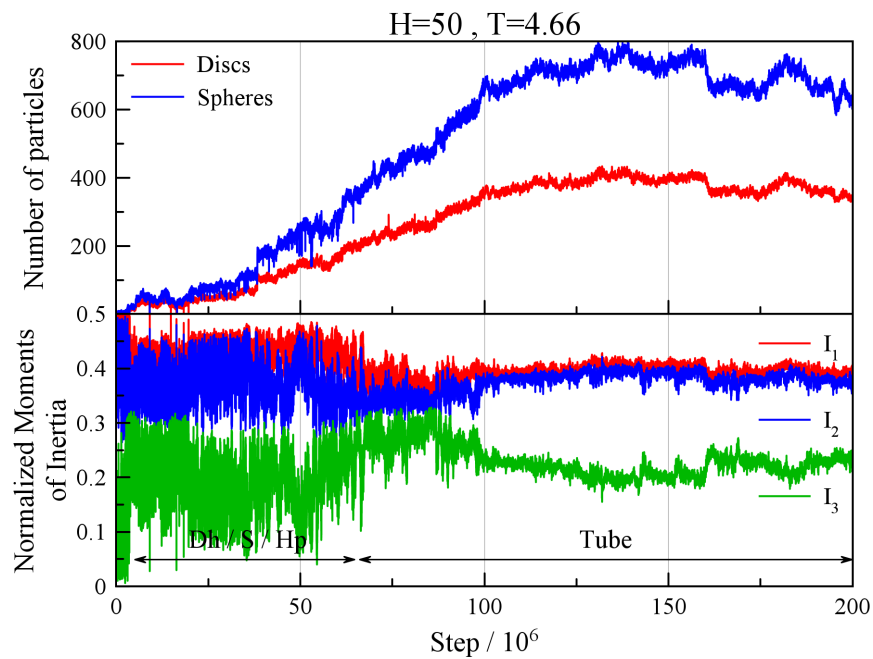


Figure 6.12: Time lines of number of particles and normalized Moments of Inertia in the system with $H=50$ at $T=4.66$. Before tube formation, the differences between double-helix (Dh), saddle (S) and half-pipe (Hp) were not so clear because the object was very small.

6.3 Controlling Tube Size

system. The formed tubes are illustrated in Figure 6.13 from two viewpoints. A bilayer structure with orthogonal arrangement, sandwiching a layer of sphere, was the common character of the formed tubes. However, the gross structural properties of the self-assembled tubes were different. With increase in H , the number of threads in the inner layer (inner diameter of the tube) decreased. Correspondingly, the curvature of the outer threads in the systems with larger H was higher. For the $H=45$ and 50 systems, this high curvature caused the outer threads to develop some defect points and to break up into discrete straight sections. The number of these sections was approximately the same as the number of threads in their inner layers, so the tube resembled a 6 or 7 faceted prism. This behaviour is apparent by the sharp change of colour in the outer threads of these systems (Figure 6.13c-d). For lower H parameters (also see Figure 6.3e), as the curvature was lower, the structure did not form these defect points to localize the bend energy and the change of orientation of particles was smooth.

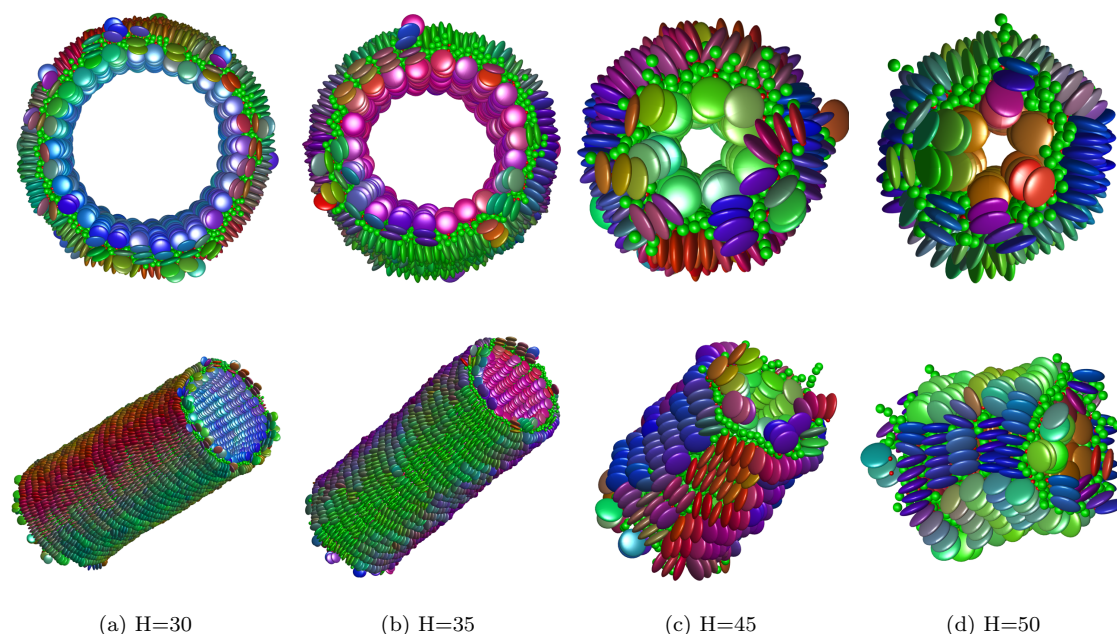


Figure 6.13: Snapshots of the final self-assembled tubes in the systems with different H values. The discs are colour coded based on their orientations.

For the systems with $H=45$ and 50, after formation of the tube, the simulations were run on for at least 140 million extra MD steps in order to confirm the stability of the the self-assembled structure and record any further growth. The results show

6.3 Controlling Tube Size

that, the self-assembled small tubes did not change their character in these long simulations, although the length of the tubes increased through addition of 2-3 threads to the outer layers (see Figure 6.12 for H=50 system). In addition, repeated transitions between the helical outer threads and separate rings arrangement were observed for these two small tubes. For the lower H systems, with larger aggregates and significantly larger numbers of separate rings, this transition was not seen, at least, in the short 5-10 million step run-on simulations performed after the complete merging of the outer threads.

Figure 6.14 compares the structural properties of the self-assembled tubes through the suggested pathway in systems with different H values. The inner diameter of the formed tubule structure was a strong function of the hot-spot size: on increasing H from 30 to 50, the inner diameter dropped from about 8 to only one disc diameter. The inner diameters were consistent with the numbers of threads in the inner layer, which also decreased when the H went up - for systems with H=30, 35, 40, 45 and 50, the numbers of inner threads were 30, 22, 11, 7 and 6, respectively. The length of the formed tube also showed the same trend and decreased from 28 to about 6.5 disc diameter. This decrease in the dimensions of the tubes can be also concluded from the number of particle curves. The largest tube contained about 5200 discs, whereas the size of the object dropped sharply with increase in H and reached only 370 particles in the smallest structure.

However, the sphere/disc ratio showed a different trend and, as expected, with increase in the hot-spot size, this ratio generally increased. The deviation of the H=30 system from the linear trend, in Figure 6.14, was possibly due to the artificial cooling down sequence required for this system. For the H=30 system, the direct cooling of the initial system with 3000 discs led to the formation of the initial aggregate at temperature $T=4.37$. This system had to be cooled down to $T=4.04$, for complete tube formation to be observed. Such cooling would be expected to cause the sphere/disc ratio to increase. The time line of this ratio is shown in Figure 6.10, where the sphere/disc ratio increase due to the cooling down sequence is apparent. The gentle cooling procedure required for the H=35 system involved a smaller decrease from $T=4.45$ (formation temperature) to $T=4.35$ and thus, the

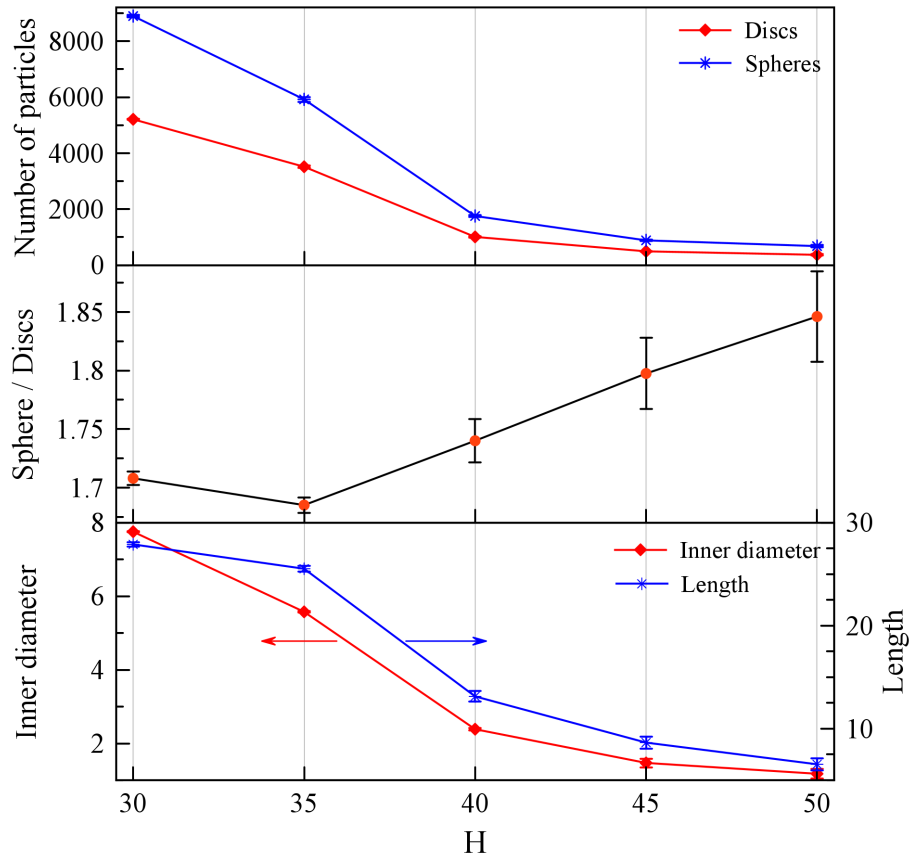


Figure 6.14: Averaged properties of the tubes self-assembled in the systems with different H values, sampled in the last 5-20 million MD steps of the simulations. The error bars show \pm Standard Deviation of data.

impact on the sphere/disc ratio was not significant. The formation temperature for $H=45$ and $H=50$ systems were $T=4.59$ and $T=4.66$, respectively, and were found by direct cooling of isotropic configurations.

6.4 Conclusions

In this chapter, the self-assembly of tubule structures has been studied in a bipartite system consisting of amphiphilic discotic particles and Lennard-Jones spheres. It has been shown that, by simulating thinner discs and smaller spheres than those employed in the previous chapter on twisted ribbon formation, a new class of bilayers form in which the threads of discs in the two leaflets are in a mutually orthogonal arrangement.

6.4 Conclusions

A pathway for self-assembly of tubes formed in the amphiphilic chromonic systems, illustrated in Figure 6.15, has been suggested. At the very early stages, the aggregate took the form of a small double-helix. Then, additional threads joined the existing two thread structure and a bilayer with orthogonal threads developed. The strain of these orthogonal leaflets along the threads of this bilayer caused the structure to bend in two opposite and perpendicular directions, leading to the formation of a saddle-shape configuration. The addition of threads to the two leaflets of this structure was not symmetric and, therefore, an anisotropy was introduced into the aggregate. One leaflet consistently had a smaller number of longer threads, while the other had a larger number of shorter threads. The energy cost associated with the growth of the saddle bilayer and also the difference in the mechanical properties of the anisotropic leaflets caused the aggregate to morph into a half-pipe structure with zero Gaussian curvature. In this, the two leaflets were very different, one involving parallel threads and the other a concerted bend. Eventually, the number of straight inner threads grew and the outer threads lengthened so that they could join to form a complete tube.

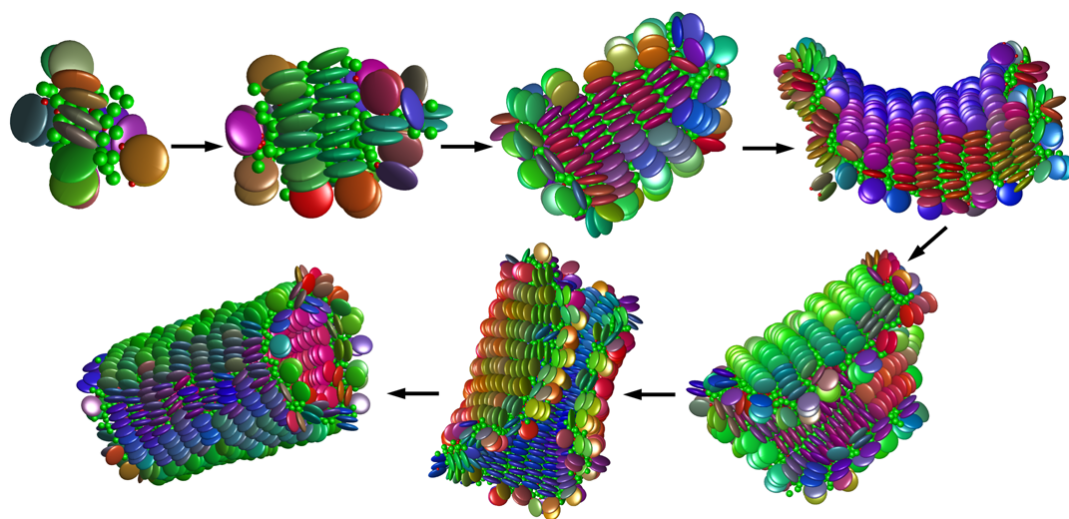


Figure 6.15: The suggested pathway for the self-assembly of tubes in the studied amphiphilic chromonic systems.

The observed pathway for self-assembly of tubes was not limited to a specific set of input parameters, but held for a range of hot-spot sizes. By an increase in the extent of solvophilicity, the flexibility of threads forming the structure increased and,

6.4 Conclusions

therefore, they could maintain higher curvature. As a consequence, the transition into the half-pipe occurred at smaller aggregate sizes for larger H values. For smaller hot-spot sizes, the curvature of the outer leaflet threads was limited and, as a result, tubes with significantly larger dimensions were formed. As before, the sphere/disc ratio, a significant parameter in the bipartite systems, generally increased with increase in the hot-spot size.

The literature suffers from lack of detailed information on the self-assembly of tubes by discotic particles. The results of this chapter hopefully provide more insight into the mechanisms of this complicated process by introducing a clear hierarchical pathway for self-assembly of tubule structures, in which the size of the object is controllable by particle-level parameters. The observed mechanism of tube self-assembly resides next to the other experimental and computational works [89, 93, 97] in the rolling-up category which was reviewed in section 2.3.2.

Chapter 7

Self-assembly of Other Structures

The results presented in the preceding chapters have demonstrated that the simple developed model can be used to investigate the self-assembly of a range of structures using chromonic and amphiphilic chromonic interactions. The coarse-grained model has proven capable of capturing physical phenomena, such as emergent chirality, which have eluded more coarse-grained models, whilst also accessing large time- and length-scale behaviours, such as geometrical frustration, that are not yet achievable by atomistic simulation. A very broad range of supramolecular structures, from twisted and straight fibres to twisted bilayers and multi-layers to tubes, has been obtained by applying a single methodology with minimal change of input parameters. Thus, modification of the main model in order to achieve each new behaviour has proved to be quite straight-forward. These observations justify the choice of coarse-grained modelling to study the aspects of self-assembly considered here.

In the course of this research, we observed that, this same approach has led to observations of spontaneous formation of several other fascinating supramolecular structures. In this chapter, we present some of these structures in order to show the wider capabilities of the model used and to open the route for further investigations. These include double-helices, multi-bilayers and a few structures formed in the double hot-spot systems. Within this, the focus is on presenting the structural/morphological features of the observed objects in each system, rather than full quantitative data.

7.1 Self-assembly of Double-helix

In simulating thinner amphiphilic discs with smaller spherical particles than those employed in Chapters 5 and 6, a new class of self-assembling structure was observed. Here, the shape parameter of the discs was $\kappa = 0.25$ and the diameter of the spheres was the same as the thickness of discs, $d_{sphere} = 0.25$. The energy anisotropy of $\kappa' = 0.075$ was used for the discs. The disc-sphere potential well-depth at edge-sphere configuration (before applying the Tanh potential) was the same as that of the disc-disc potential in the edge-edge configuration (see Table 5.1). The single hot-spot version of the Tanh potential was applied, and its parameters were the same as those used for previous chapters in investigations of bilayers and tubes. In summary, the potential well-depths for edge-edge and face-face configurations of disc-disc interaction and also for spheres interacting with the hot-spot zone at the rim of the discs were, 4.516, 60.21 and 22.58, respectively. A range of hot-spot sizes between $H=20$ and $H=40$ were employed for the results being presented here.

In a direct cooling of a mixture of discs and spheres equilibrated at a relatively high temperature ($T=6.5$), it was found that, for this set of building-block sizes and interaction parameters, a “double-helix” structure spontaneously formed. This comprised two helices of discs, with a very short pitch length (roughly 2 disc diameter), wrapped around a central elongated sphere cluster, as illustrated in Figure 7.1. In contrast with the rope structure of Chapter 5, here, the adjacent discs in each thread were not parallel, but had an angle with each other. Their hot-spot cores were, though, directed towards the centre of the cluster. This behaviour is analogous to that of the threads at the very early stages of tube growth studied in Chapter 6.

Figure 7.2 shows time lines of some properties of a double-helix formed in a mixture of 3000 discs with $\kappa' = 0.075$ and $H=20$ and 10,000 spheres at temperature $T=5.48$. It should be noted that, several clusters formed in this system and the figure only gives information on the biggest one. Figure 7.3 shows all double helices finally formed in this systems. Several instances of coalesce of double-helices of the same handedness was observed in this simulation, so leading to formation of a longer cluster. However, the lateral interaction of objects (similar to that of the ropes) was

7.1 Self-assembly of Double-helix

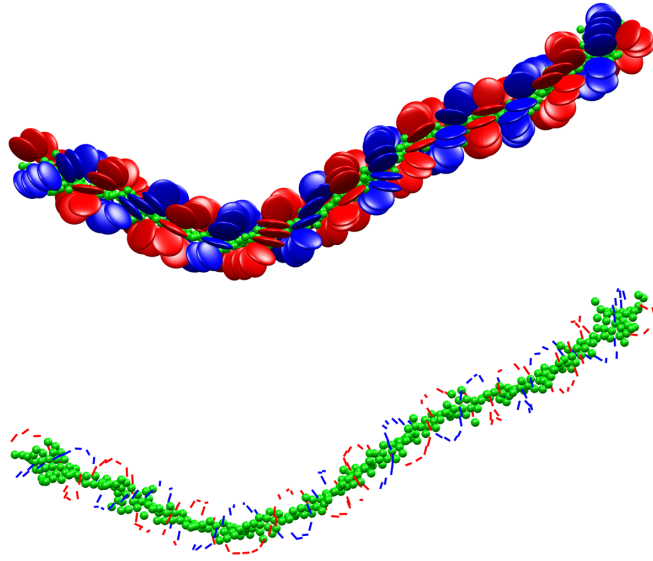


Figure 7.1: A double-helix structure formed in a system with $\kappa = 0.25$ and $H=30$. The helices were coloured differently. In the bottom panel, the same structure was illustrated by drawing the short axes of the discs.

rarely seen. Therefore, except the longitudinal merging of formed clusters, the only growth mechanism was via addition of discs and spheres to the two ends of each double-helix structure. At the early stages, the length of the object was in the order of its width (similar to the small double-helix at the early stages of tube formation illustrated in Figure 6.2b) and, therefore, the normalized moments of inertia had 3 close components. Then, through the growth of object, it became a 1D rod-like structure with two very big principal moments of inertia and a very small one. Figure 7.4a illustrates a nearly straight cluster formed in this system.

The results also show that, as the structure grew, the sphere/disc ratio dropped to a steady value of about 1, significantly smaller than the values seen in the previously investigated systems. The energy plots of the double-helix (Figure 7.2), however, indicate that the sphere-disc interaction was a dominant factor in formation of the structure, 8 times stronger than the disc-disc potential energy. This is, therefore, similar to a situation in which the discs have edge-edge preference and, indeed, the double-helix structure observed here is all consistent with the zero temperature prediction of Fejer *et al.* [99, 103] for such a condition. For a twisted bilayer with the same H parameter, data of Figure 5.7 show that the sphere-disc interaction was only

7.1 Self-assembly of Double-helix

55% of the total potential energy of the structure. This confirms the significance of the sphere-disc interaction into the double-helix formation. Considering the maximum possible potential energy gain by a single disc-sphere interaction for the system studied here (the hot-spot potential well-depth), the normalized energy plots reveal that, on average, each disc interacted with 6 spheres in the formed double-helix. For the twisted bilayers studied in Chapter 5, where the sphere diameter was $d_{sphere} = 0.345$, this number was about 4. Thus, the size of spheres and their packing approach in the hot-spot zone can be a significant factor in deriving the structure of self-assembling objects. Running on the simulation of this $H=20$ system led to formation of several double-helices, the biggest of which contained about 500 discs (see Figure 7.3).

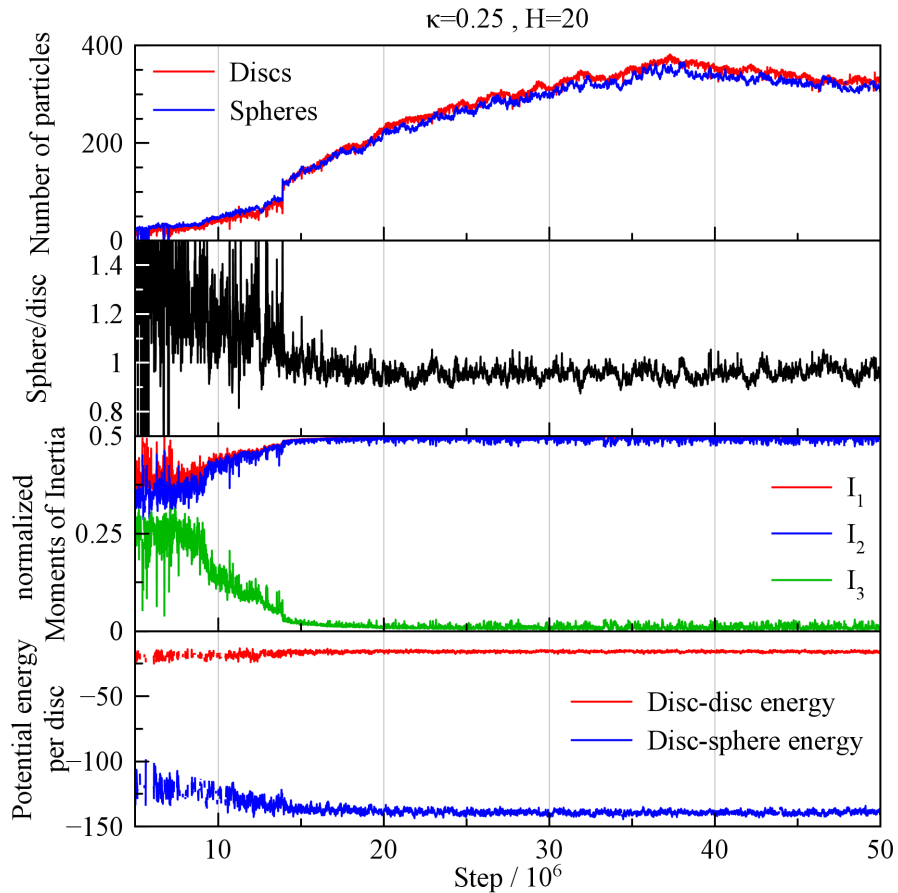


Figure 7.2: Time lines of the structural properties of the biggest double-helix formed in a system with $H=20$.

7.1 Self-assembly of Double-helix

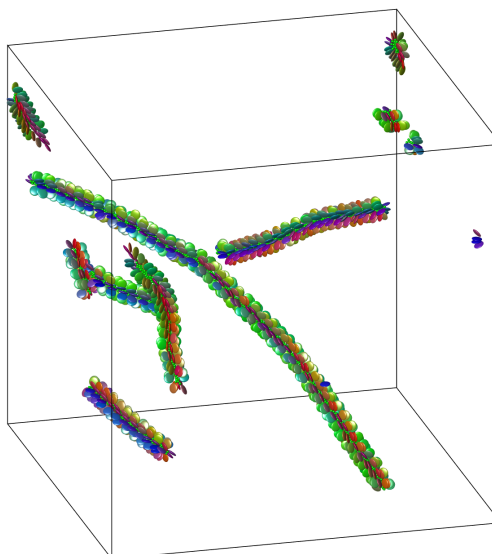


Figure 7.3: Double-helices formed in the system with $H=20$ at $T=5.48$ after 200 million steps.

Increasing the H parameter caused the formed double-helix to be more flexible (see Figure 7.1 as an example of the $H=30$ system) and, therefore, more able to interact with other clusters. In $H=30$ systems, for example, a very long curved double-helix with about 1700 discs formed after about 175 million MD steps at temperature $T=5.75$ - it ran through the simulation box boundaries at least 3-4 times. The extended hot-spot size led to an increase in the sphere/disc ratio to about 1.3. For $H=40$ systems at $T=5.95$, the formed double helix was even more flexible (see Figure 7.4b), and the sphere/disc ratio was even higher, around 1.55. For this system, the normalized disc-sphere potential energy of the double-helix was about -170 units per disc, although the disc-disc energy was in the same order as that of $H=20$ system.

The self-assembled double-helices were occasionally subject to defect and particle dislocation in the helix, particularly where the structure was highly curved. An interesting behaviour, observed in more flexible systems, was the interaction of one double-helix through one of its ends with the side of another structure. A stable triple junction, an example of which illustrated in Figure 7.5a, was the result of this merging process. It should be noted that both left- and right-handed double-helices were observed with equal likelihood in the simulations. In systems with lower H

7.1 Self-assembly of Double-helix

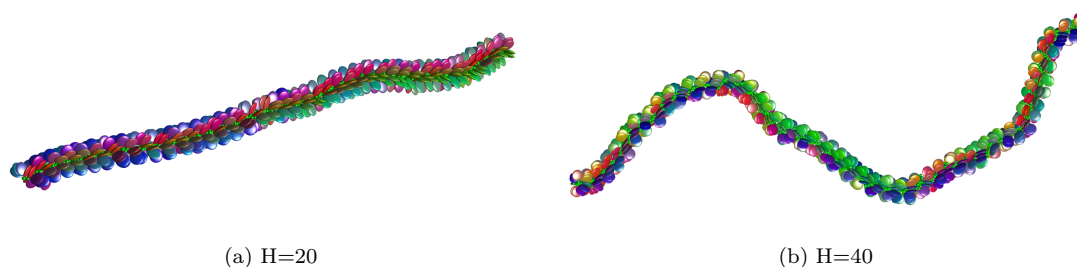


Figure 7.4: A comparison between the flexibility of the self-assembled double-helices in two systems with different hot-spot sizes. The particles are colour-coded based on their orientations.

values, forming less flexible double-helices, the difference in handedness prevented aggregates from coalescing - several individual clusters are apparent in Figure 7.3 showing the $H=20$ system. For larger H , however, the flexibility of helices made it possible for the aggregates to join with different handedness. That is, two structures with opposite handedness merged longitudinally by development of defects at the joint point. This is exemplified in Figure 7.5b which shows a double-helix with two parts having different handedness states.

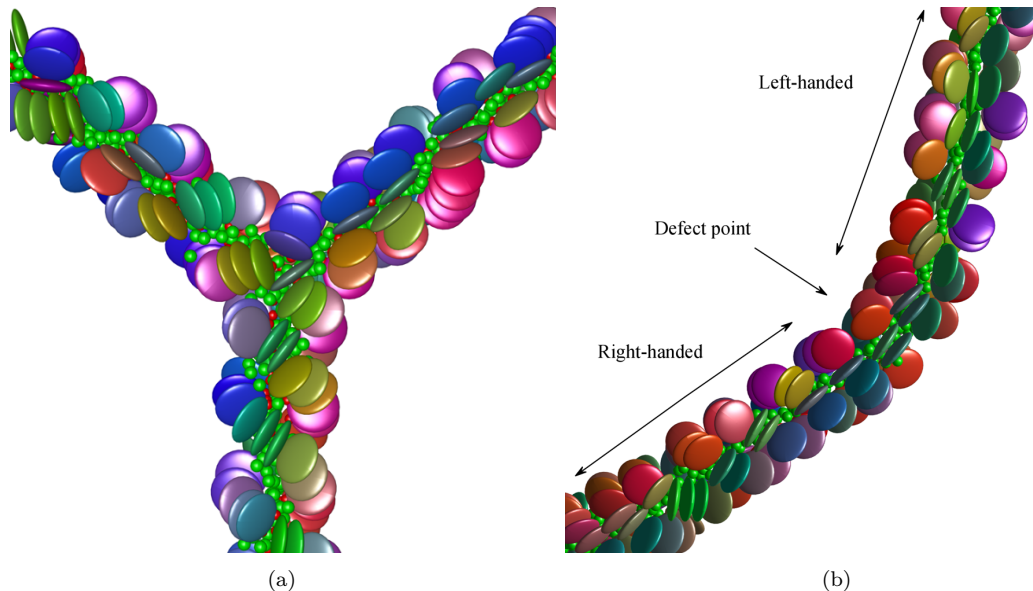


Figure 7.5: a) A triple-junction structure formed by coalescing of two double-helices in $H=40$ system at $T=5.6$. b) A double-helix having two parts with different handedness formed in $H=30$ system at $T=5.75$. The bottom section is right-handed, while the top section is left-handed.

7.2 Multi-bilayer Formation

In Chapter 5, it was shown that twisted bundles with several layers can form either through simulation of disc-sphere mixtures with 2 opposite hot-spots, or by the morphing of a multi-rope structure, formed by the discs with a small, single hot-spot, into a double-bilayer. In the former, each leaflet of discs was separated by a layer of spheres (the reason for calling it multi-layer), while the latter had disc bilayers between each sheet of spheres. Here, we report another pathway for the formation of structures consisted of a few bilayers formed through attachments of their disc leaflets.

In the simulation of a mixture of 3000 discs with $\kappa = 0.345$, $\kappa' = 0.1$ and $H=20$ and 10,000 spheres with $d_{sphere} = 0.345$ (the same as the bilayer system studied in section 5.2, but with a different κ' parameter) at the temperature $T=2.56$ (found by direct cooling), a twisted bilayer became the main aggregate in the system. It was verified that this temperature was the highest at which a cluster could be initiated - no self-assembly was seen for $T=2.57$ after 30 million steps. However, when the initial bilayer formed, a few small clusters also developed in this system. After about 14.7 million MD steps, one of these small bilayers joined the main aggregate and never dissociated. Figure 7.6a illustrates the attachment of the small cluster to the main bilayer. This point could be identified by a jump in the number of particle curves for this system, shown in Figure 7.7. Before the attachment, the bilayer had about 26 threads and its radius and length were about 6 and 15 disc diameters, respectively. The gradual untwisting process, observed in the other systems due to the lateral growth of the twisted object, did not alter by the joining of the small cluster, as the pitch length data suggests. Although, the number of particle curves do not indicate any change in the growth trend of the object, the other curves illustrated in Figure 7.7 show that the mechanism by which the structure grew changed.

After attachment of the second bilayer, the growth of the initial cluster slowed down and then paused, but the second object grew. This can be observed from Figure 7.8 which illustrates the number of particles in the outermost leaflets of the growing double-bilayer, one a part of the bigger bilayer and the other from the

7.2 Multi-bilayer Formation

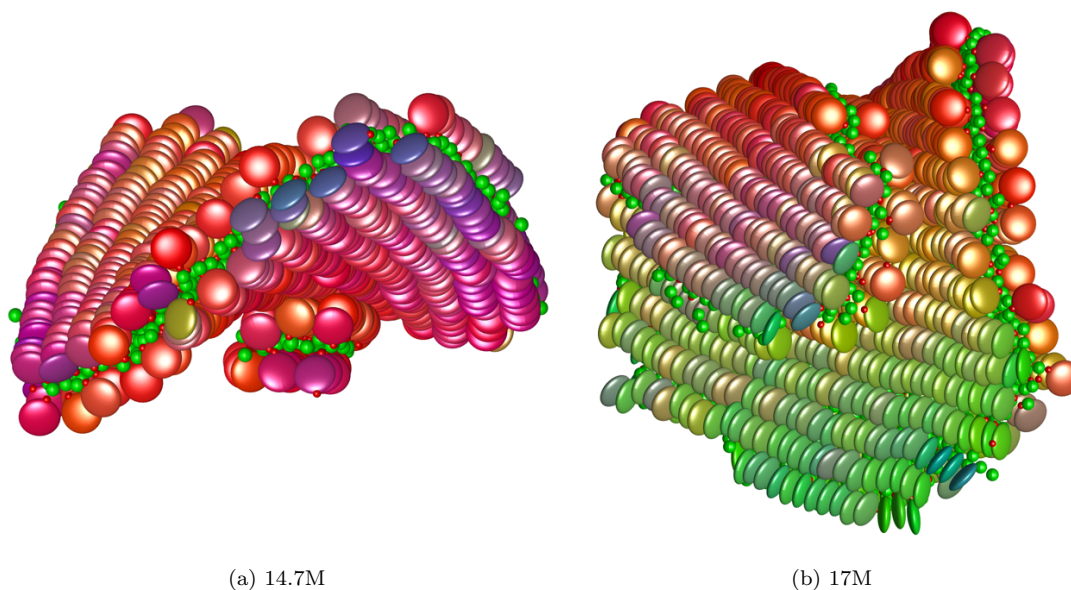


Figure 7.6: Snapshots of the system forming a double-bilayer by coalescing of two bilayers. a) Attachment of the small bilayer to the main one after 14.7 million steps. b) The attached small cluster grows on top of the main one.

smaller one. The size of the bigger leaflet, after an initial increase, remained nearly unchanged, until the number of particles in both became identical and then they grew together. After about 20 million MD steps, a twisted double-bilayer, with no difference between its bilayers had formed. The disc leaflets of the two bilayers attached to each other were parallel (Figure 7.6b), and due to the growth of the small bilayer, the number of particles with the same direction increased and, therefore, the expected drop in the orientational order parameter due to the growth stopped and slightly recovered. The potential energy plots in Figure 7.7, show that the cluster mostly benefited from the inter-thread interaction of two attached leaflets of the two bilayers, and the intra-thread energy was not significantly affected by the joining process of the two objects. The subsequent growth of the formed double-bilayer was mainly longitudinal and final object reached 32 disc diameters in length. The sphere/disc ratio of this system eventually levelled-off at about 1.23. Figure 7.9 shows two views of the self-assembled double-bilayer after 38.3 million MD steps.

The simulation of similar systems with even weaker face-face interaction ($\kappa' = 0.15$) and $H=25$ also led to the formation of multi-bilayers. At the temperature $T=2.43$, several clusters self-assembled in this system, and two of these remained

7.2 Multi-bilayer Formation

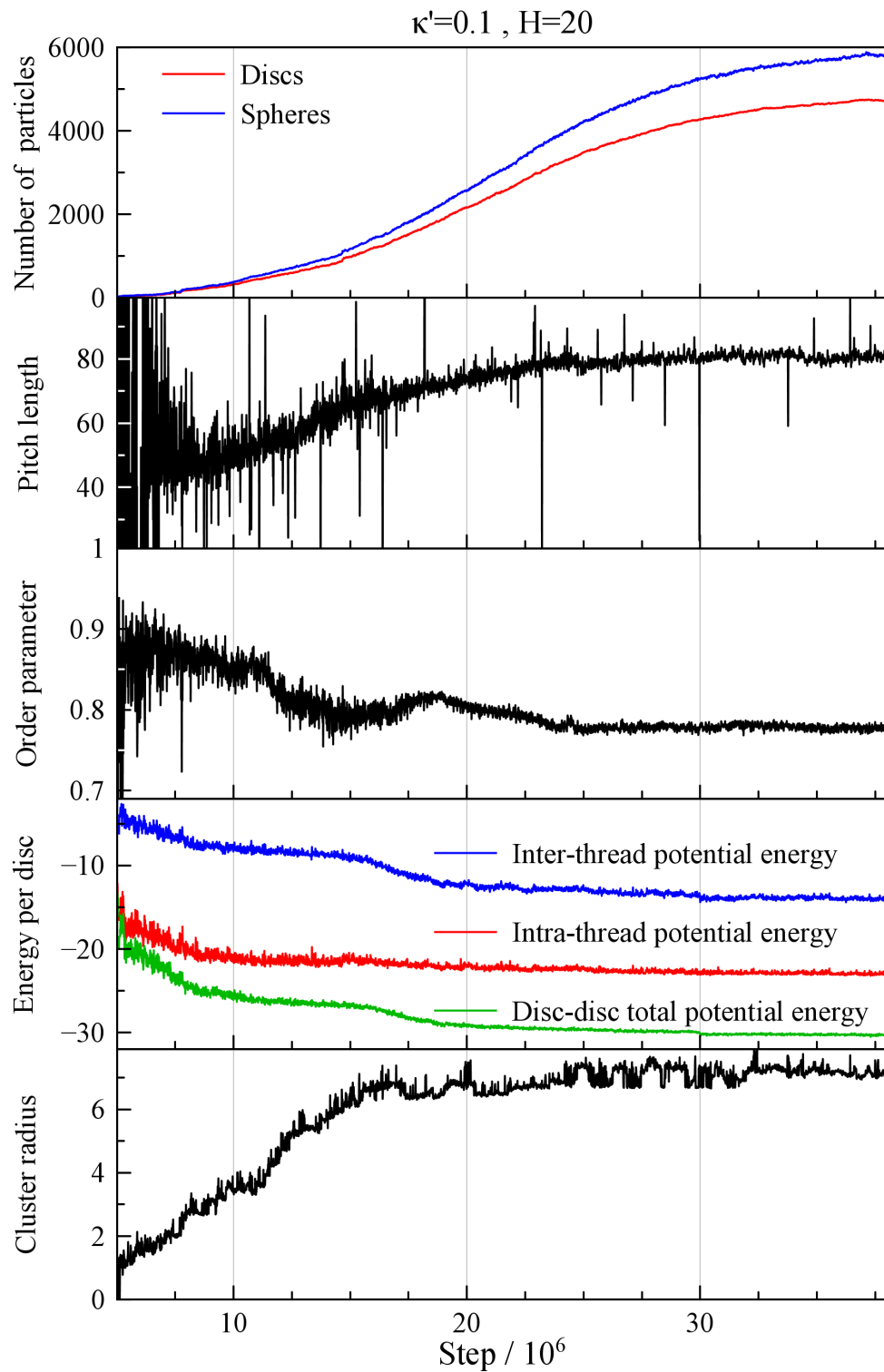


Figure 7.7: Time lines of different properties of the double-bilayer structure formed in a system with $\kappa' = 0.1$ and $H=20$.

7.2 Multi-bilayer Formation

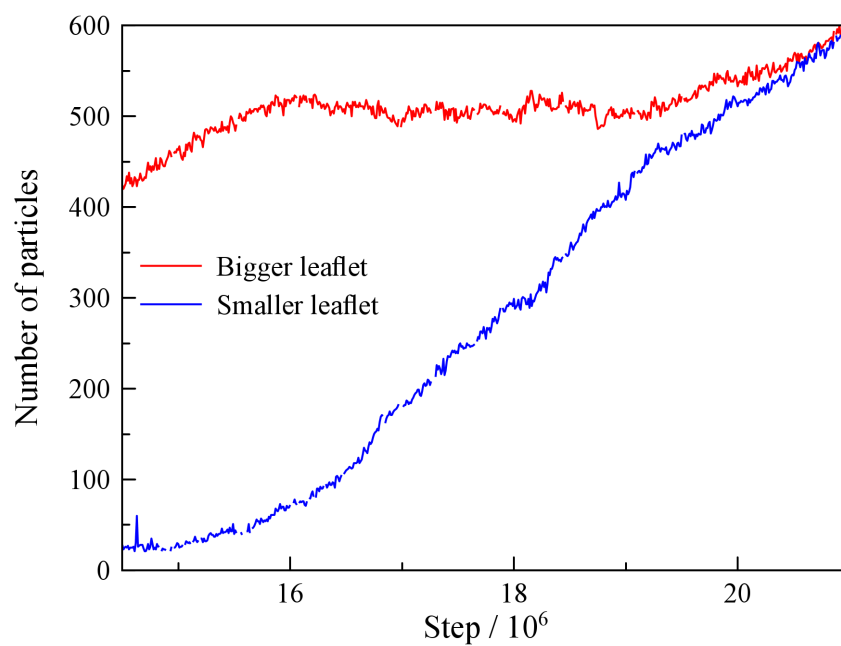


Figure 7.8: Number of particles in the outermost disc leaflets of the double-bilayer in the time window at which the attached small cluster grows.

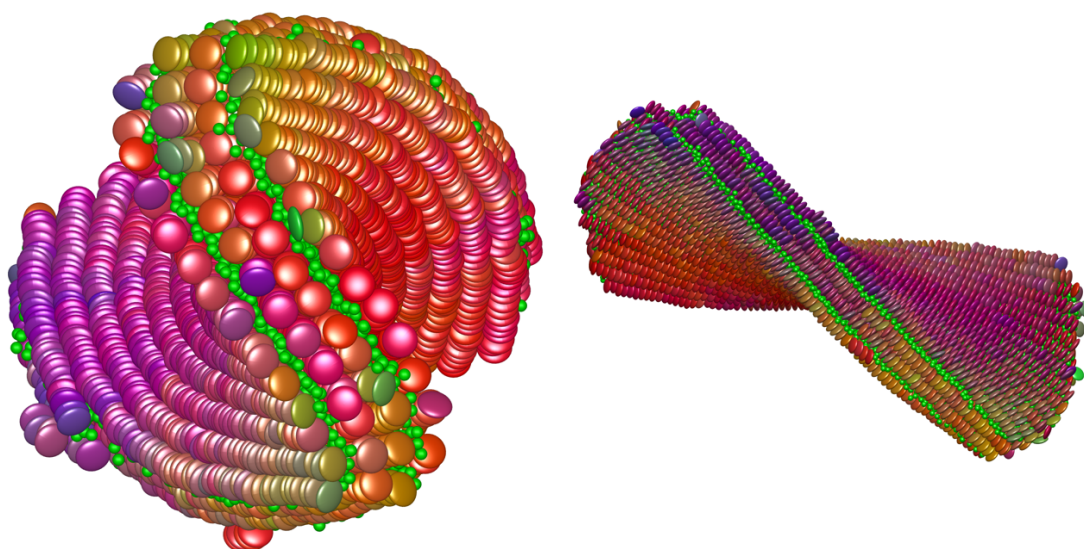


Figure 7.9: Two views of the self-assembled twisted double-bilayer in the system with $\kappa = 0.345$, $\kappa' = 0.1$ and $H=20$ after 38.3 million MD steps.

7.2 Multi-bilayer Formation

as long-lived objects. One had 4 leaflets and the other had 6 layers of discs (Figure 7.10). The growth mechanism of these twisted multi-bilayer objects was similar to that discussed above - attachment of a small bilayer to an existing bigger twisted bilayer cluster.

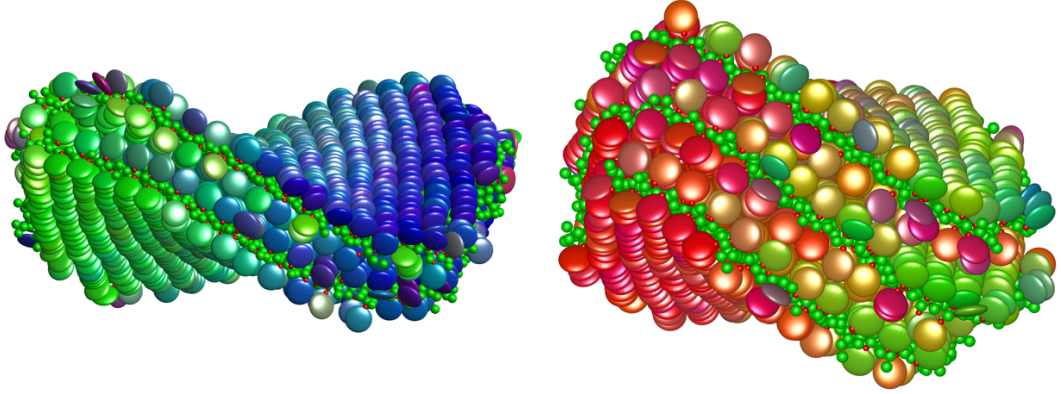


Figure 7.10: Two twisted multi-bilayer structures formed in a single system with $\kappa = 0.345$, $\kappa' = 0.15$ and $H=25$.

In Chapter 6, where the self-assembly of tubes was studied, it was shown that for a disc-sphere mixture with relatively thinner discs and smaller spheres, a bilayer structure in which the two leaflets of discs are in orthogonal arrangement can develop. With decrease in the size of the hot-spot, the emergent curvature in the final structure reduced - tubes with bigger diameter formed. For the same particle sizes, it was observed that reducing the H parameter even further resulted in formation of an orthogonal bilayer that was not capable of maintaining any curvature and, thus, a flat bilayer were formed.

In simulation of a mixture of discs having $\kappa = 0.3$, $\kappa' = 0.075$ and $H=20$ and spheres with $d_{sphere} = 0.3$ at temperature $T=4.08$ (other parameters being the same as those in the previous chapter), several small flat orthogonal bilayers formed. The very early stages of this self-assembly involved formation of aggregates comprising two orthogonal threads which had a tennis ball configuration (see Figure 7.11a). This resembled to the prediction of Fejer *et al.* [99, 103] discussed in Chapter 2. However, on further growth, the curvature of these threads disappeared and flat bilayers formed (Figure 7.11b). The discussed anisotropy in the orthogonal bilayers was also observed here, one leaflet had 4 short threads and the other had 3 longer

7.3 Flat Bilayer Formation

threads. The growth of the main formed bilayer and also a few other flat bilayers continued and, after about 59 million MD steps, similarly to the scenario described for twisted multi-bilayer, one of these bilayers attached to the biggest cluster, with the adhering leaflets parallel with each other (Figure 7.11c). The resultant structure then grew in both lateral directions and became a flat double-bilayer with orthogonal thread arrangement in both bilayers (Figure 7.11d). In the final structure, the inner leaflets had 12 threads, while the outer layers had 14 threads each.

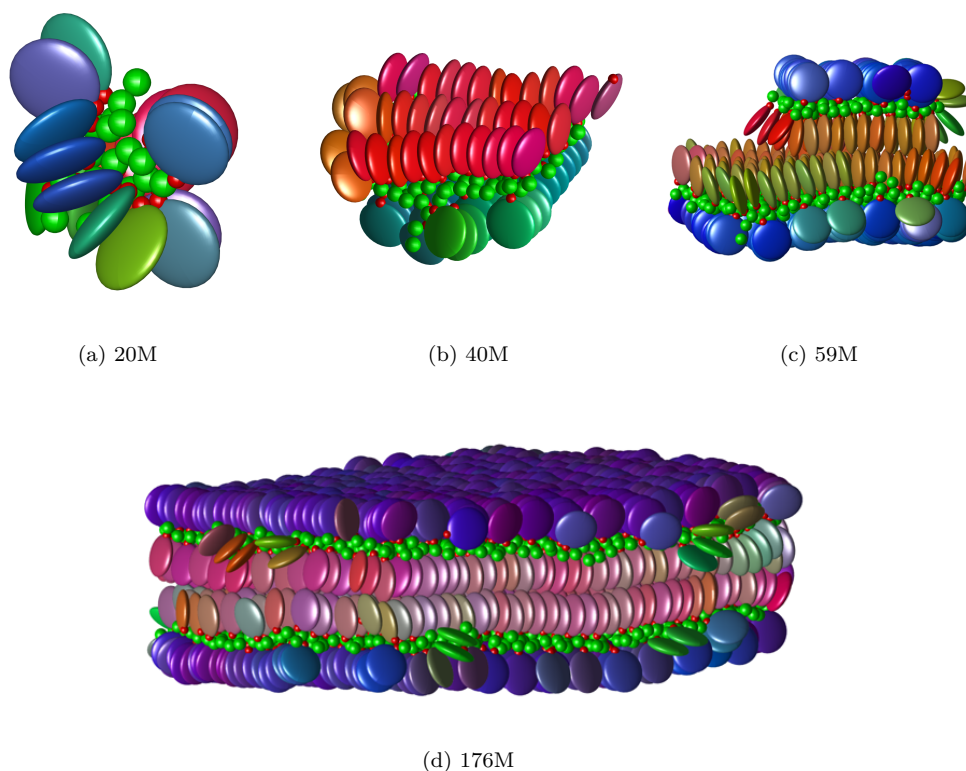


Figure 7.11: Different snapshots of the system with $\kappa = 0.3$, $\kappa' = 0.075$ and $H=20$, in which a flat multi-bilayer self-assembled. The discs are colour-coded based on their orientation. The time steps at which the configurations were taken are written in the caption of each part.

7.3 Flat Bilayer Formation

Simulation of an amphiphilic chromonic system with slightly thicker discs and larger spheres than those previously presented led to formation of an interesting structure. A mixture of 600 discs and 3400 spheres with total number density of 0.22 was

7.3 Flat Bilayer Formation

simulated. Here, the aspect ratio of discs was set to be $\kappa = 0.45$ and the energy anisotropy was $\kappa' = 0.075$. The sphere diameter was the same as the thickness of the discs, $d_{sphere} = 0.45$. The edge-sphere potential well-depth in GB disc-sphere potential was set to be the same as that of edge-edge configuration of discs, as given in Table 5.1. The other input parameters were similar to those used for the simulation of twisted bilayers in Chapter 5.

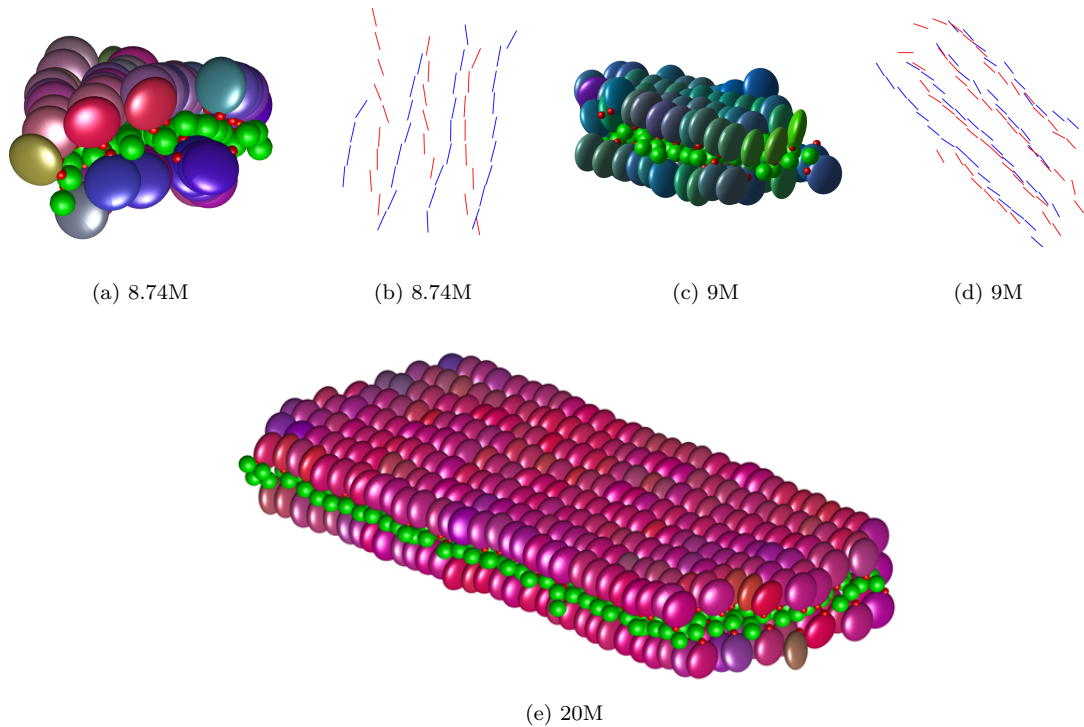


Figure 7.12: Different snapshots of the system with $\kappa = 0.45$, $\kappa' = 0.075$ and $H=20$, in which a flat bilayer self-assembled. The discs are colour coded based on their orientation. In parts b and d, the short axes of the threads in two leaflets were drawn with different colours and the view is normal to the bilayer plane. The time steps at which the configurations were taken are written in the caption of each part.

The results showed that, in $H=20$ system, a bilayer structure, consisting of 2 leaflets of discs and a layer of spheres, self-assembled at temperature $T=2.25$. At the early stages of growth, when the structure consisted of 6-7 threads, an angle was apparent between the threads of two leaflets, as was the case in the assembly of twisted bilayers (see Figure 7.12a-b). As the aggregate grew, however, the chirality disappeared and the twisted structure straightened into a flat bilayer with parallel leaflets (Figure 7.12c-d). This straightening of threads was similar to that observed

7.4 Self-assembly in Double Hot-spot Systems

in fibres with thicker particles, in which the structure unwound to relax elastic stress associated with being twisted. This flat bilayer remained stable, going on to comprise about 85% of the discs in the simulated system (Figure 7.12e). The sphere/disc ratio reached a steady value of 1.02 for this flat bilayer. However, simulations using the same input parameters (particle sizes), but with $H=30$, yielded a stable twisted bilayer. This suggests that, both the sizes of the interacting particles and the extent of solvophilicity (hot-spot size) have an effect on the stable structures which can form in a particular system.

7.4 Self-assembly in Double Hot-spot Systems

In Section 5.3, it was shown that the double hot-spot variant of the Tanh potential can lead to the formation of twisted multi-layer bundles, in which the structure had 3 different directions of growth. In the simulation of the similar systems with weaker face-face interaction, other structures were observed. These are briefly described here.

A mixture of 1200 discs with two equal opposite hot-spots and 6800 spheres at total number density of 0.22 with most interaction parameters identical to those used in the system studied for formation of twisted multilayer bundle in Section 5.3 was simulated. Here, however, a weaker face-face interaction, $\kappa' = 0.2$ was employed for the disc-disc interaction. That is, a face-face potential well-depth of 13.15 units was applied, while that of hot-spot for disc-sphere interaction was 10 units.

In this simulation, a system with $H_1 = H_2 = 25$ was considered at temperature $T=2.7$. A multilayer structure with several leaflets of discs separated by layers of spheres self-assembled. However, the formed structure here was not twisted, but had flat layers (see Figure 7.13). The cross-section of the object, perpendicular to the thread axes, was faceted, a characteristic which was also seen in the straight fibres studied in Chapter 4. An interesting feature of this structure was that, within the disc layers, where the particles in each thread had a common tilt with respect to the thread axis, neighbouring threads adopted alternative tilt angles. This behaviour is apparent in bottom panel of Figure 7.13, where the adjacent threads have different colours,

7.4 Self-assembly in Double Hot-spot Systems

but next-nearest neighbours have the same colour. Although the reason for this behaviour is unclear, a similar structure for columnar multilayer Langmuir-Blodgett films of triphenylene-based molecules was speculated from a set of experimental observations [154].

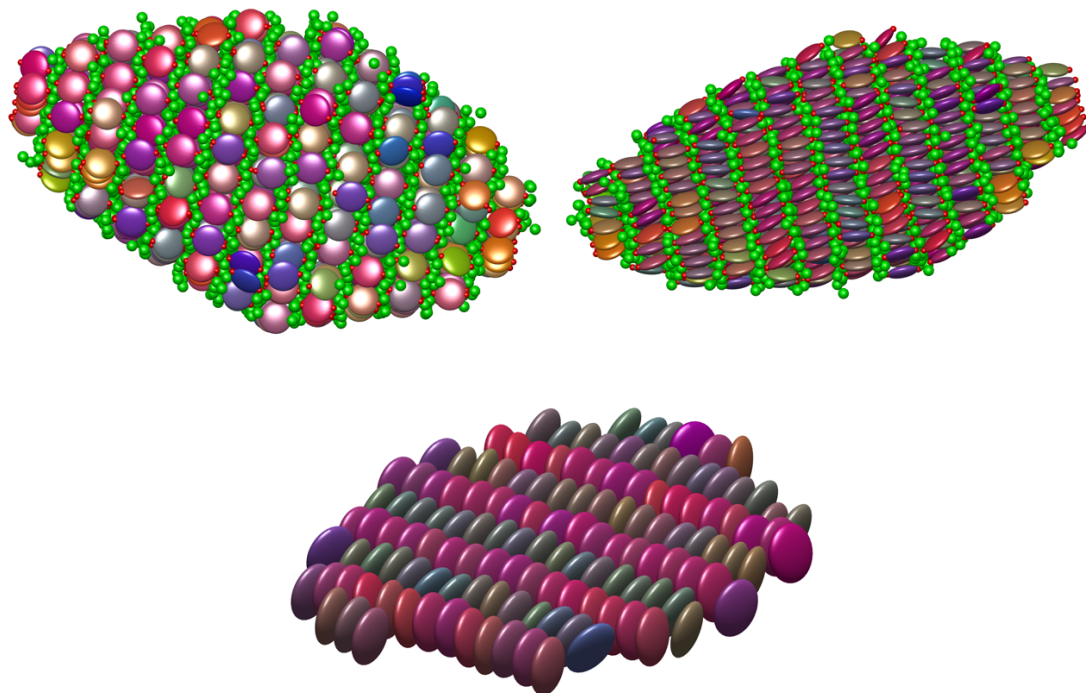


Figure 7.13: Snapshots of the flat multilayer structure formed in a system with $\kappa = 0.345$, $\kappa' = 0.2$ and $H_1 = H_2 = 25$. In the bottom panel, the biggest disc layer in the centre of structure was shown. The different colours of adjacent threads indicate their antisymmetric tilt angle.

In simulation of a similar system but with smaller hot-spot, $H_1 = H_2 = 15$, at temperature $T=2.42$, a very fascinating structure, illustrated in Figure 7.14, self-assembled. This very porous structure consisted of parallel columns of spheres connected to each other by scaffold of discs with a spacing of about one disc diameter. Here, the sphere columns were distributed in a distorted hexagonal arrangement. Four of the inter-connections were through a stacks of 2 discs locating in edge-edge configuration normal to the plane of the figure. The two other connections were by a single disc. The observed structure is analogous to a so-called “flower of life” pattern, a 2D geometrical design, produced by repeating, overlapping circles of equal radii [155].

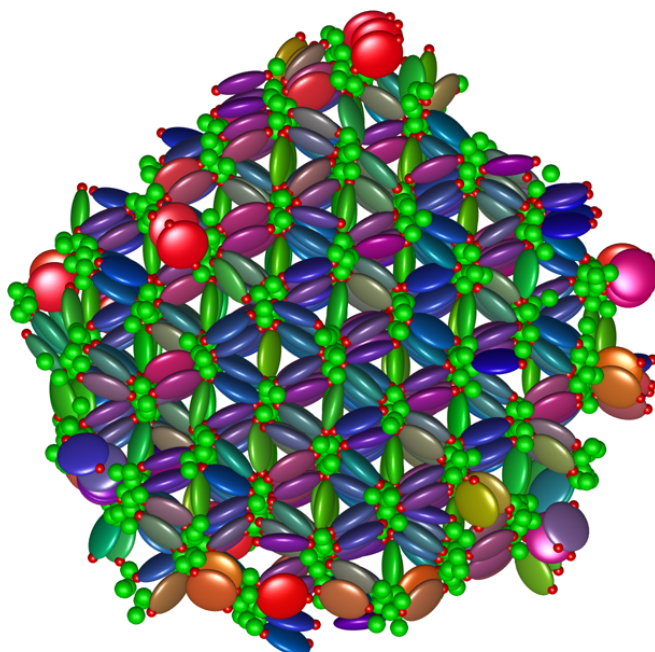


Figure 7.14: The structure self-assembled in a system with $\kappa = 0.345$, $\kappa' = 0.2$ and $H_1 = H_2 = 15$. The spheres are in green and the discs are colour-coded based on their orientations.

7.5 Conclusions

In this chapter, a series of other supramolecular structures, whose self-assembly can be investigated through the developed coarse-grained model for amphiphilic chromonic systems, were explored. The aim was to show the further capabilities of the model in studying different objects with very different characteristics. It was also demonstrated that the sizes of the interacting particles and their energy parameters can be employed to tune the bipartite system toward self-assembly of a range of objects.

For the thinnest studied discs and smallest spheres, double-helix structures, consisting of 2 helices of discs and a central sphere cluster, self-assembled. Smaller spheres could be efficiently packed into the hot-spot regions of the thin discs and, so leading to the observation of this structure. The flexibility of the formed double-helices was controllable by selecting the size of hot-spot, smaller H values giving more straight, more rigid structures.

7.5 Conclusions

It was also shown that the time- and length-scales accessible to the coarse-grained model were sufficiently large for the interaction of self-assembled aggregates to become accessible to molecular simulations. For example, formed bilayers were able to couple with each other to yield multi-bilayer structures. The effects of the newcomer on the growth of the existing bilayer and also the imprinting of chirality onto the small cluster were striking observations of these simulations.

The double hot-spot model was also shown to be promising in respect of studying further the structures with three independent directions of growth. In addition to the twisted multilayer bundle described in Chapter 5, flat multilayer with tilted threads and a new structure, resembling the flower of life pattern, were obtained simply by changing the energy anisotropy parameter and the hot-spots size.

Chapter 8

Conclusions and Future Work

In this chapter, the main results of this research is summarised and suggestions for future work are also made.

8.1 Conclusions

The aim of this work, as specified in chapter 1, was to use computer simulations of coarsed-grained discotic and spherical particles to achieve greater understanding of the mechanisms of spontaneous formation of some chiral supramolecular structures and, so, gain insight into the properties of these self-assembled objects. This approach has proven capable of capturing physical phenomena such as emergent chirality, which has eluded more coarse-grained models, whilst also accessing large time- and length-scale behaviours, such as geometrical frustration, that are not yet achievable by atomistic simulation.

We found that “anisotropy” is crucial in the processes which lead to formation of such structures. The shapes of the building-blocks and their interactions were two of the anisotropies introduced to the systems studied here. By simulating discotic particles, shape anisotropy was included in all simulations performed in this work. It was shown that the extent of this anisotropy (particle aspect ratio) has also a significant impact on the pathway of the self-assembly and, consequently, the final structure. The asymmetry in the interaction of particles was considered by giving a preference to the face-face configuration over the edge-edge relative orientation for

8.1 Conclusions

pairs of interacting discs. By this, the building-blocks tended to stack and, therefore, to form elongated structures, e.g. threads and, thus, fibres.

The simulations of disc-only systems led to self-assembly of multi-thread, chiral fibres. The fibre pitch lengths, a fully emergent supramolecular length-scale observed in this work, arose due to a combination of two factors: 1) the tilt of particles in interdigitating, helical threads; 2) untwisting due to radius-dependent stresses. By minimizing the free energy of clusters of GB discs, Chakrabarti *et al.* [100] previously showed that the chirality of a self-assembled multi-filament fibre changes with the shape anisotropy of the particles. Here, by exploring the growth of such objects, we could shed light on this process and show that the straight fibres either are straight from the very early stages of the growth, or become untwisted in response to the extended bending stresses associated with the helical threads at larger radii. In the latter scenario, the multi-step untwisting was dependent on the both shapes and energy anisotropies of the building-blocks, i.e. for different systems, the ultimate size of twisted fibre, before straightening, was a function of thread bending rigidity - fibres formed by more rounded discs, having higher face-face interaction strength, underwent the unwinding scenario at smaller radial sizes.

The simulations also showed that the fibre forming systems are kinetically trapped into isotropic states and that the metastable state needs to be super cooled 10-20% below its temperature of thermodynamic stabilities to form the fibre. This thermal hysteresis effect has been also observed in experimental works, e.g., in polymerization of perylene bisimide into a long 1D aggregate [141], where the thermal hysteresis was shown to be in the range of 3.1% and 8.6% above the formation temperature, depending upon concentration and the nature of the solution.

Detailed analysis showed that, in the fibre assembling systems, making and breaking of the intermediate clusters was always seen in the early stages of the hierarchical spontaneous formation. This, together with the observation that there was no threshold size for the start of assembly, suggests that the fibre pre-assembly phase can be categorised as isodesmic assembly [143], in which the free energy change of addition or dissociation of a molecule from a thread is independent of the thread length. Although lateral assembly of such threads then adds to the complexity

8.1 Conclusions

of the process, features observed in the presented mosaic plots for the probability of different object sizes show isodesmic character. Having established a complete first layer around the central thread, however, the aggregate grew monotonically in all systems. It was also shown that, by seeding, the early stages of the formation pathway can be biased and, as a result, fibres can form at temperatures at which, without seeds, the system would be trapped in the isotropic phase. An experimental evidence for the effectiveness of seeding in such a self-assembly process was provided by Gosal *et al.* [37] who have successfully used seeding to steer the aggregation product of β_2 -Microglobulin systems. Seeding effects observed in this thesis may also have a link to the infectious Prion diseases [156] in which amyloid fibre formation is boosted after consumption of small fibres.

A third type of anisotropy was introduced into our simulations by considering amphiphilic discs which were attracted to simple spheres. The disc-sphere interaction symmetry around the rim of the disc was broken by having hot-spot zones with a controllable interaction strength. The size of the attractive regions was also tunable through the parameters of the Tanh potential which was used to implement the interactions between discs and spheres. Results showed that this very simple model can be used to investigate spontaneous formation of a very broad range of supramolecular chiral structures in which the spheres play a key role. An experimental example of this type of situation is the observation of solvent-assisted self-assembly of an aromatic compound into helical bundles [157].

By changing the sizes of the particles and, therefore, their interaction parameters and also the extent of solvophilicity, different supramolecular structures self-assembled, some of which are illustrated in Figure 8.1. The horizontal axis of this plot is the H parameter (size of hot-spot), while the vertical axis is a measure of the availability of hot-spot volume into which spheres might pack. Explicitly, this is calculated as the volume of the hot-spot region around a disc with the minimum potential value of 80% of the maximal disc-sphere well-depth divided by the volume of a sphere. This packing parameter is, then, an estimate of the number of spheres which can be packed in the hot-spot zone of each disc.

8.1 Conclusions

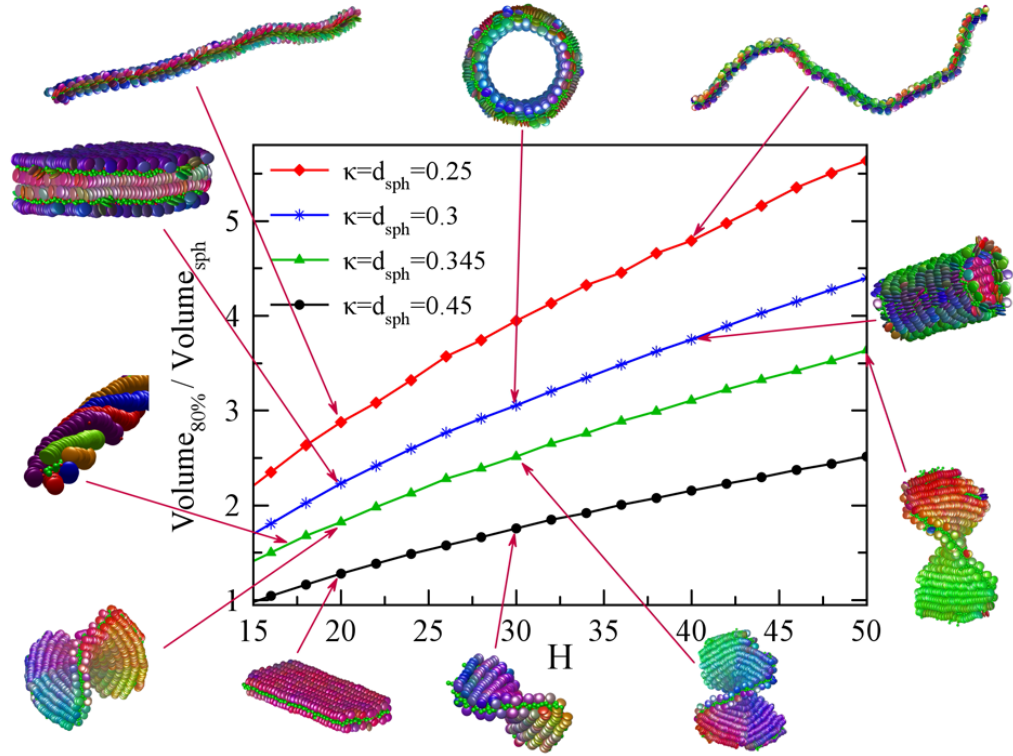


Figure 8.1: The packing parameter for the particle sizes studied here versus the size of hot-spot. The volume of hot-spot region with the strength of at least 80% of disc-sphere potential well-depth is defined as $\text{Volume}_{80\%}$. All the snapshots presented here belong to the systems with $\kappa' = 0.075$. The ϵ_0 parameter in the disc-sphere interaction is the same as the edge-edge potential well-depth for disc-disc interaction, except for the systems with $\kappa = d_{sph} = 0.345$, in which $\epsilon_0 = 2$ instead of 2.63. The symbols on each curve show the results of analytical calculations and the arrows point toward some simulated systems.

Although many-body effects and, also, the overlapping of hot-spots were not considered in Figure 8.1, it is still very effective at mapping out the structures observed here. On each line in this figure, different classes of structure are self-assembled. For the thickest discs, at small size of hot-spot, a flat bilayer formed, while by an increase in the H parameter, twist emerged in the structure. For the particles with $\kappa = 0.345$, a survey was performed on the self-assembly of twisted bilayers and it was found that the response of the system to the bending stresses of the outer threads was the development of radial defect lines with a mismatch in particle orientations. For relatively small hot-spot sizes, rope structures with 5 helical threads of discs wrapped around a sphere cluster were observed. The lateral growth of such objects was through addition or formation of further ropes. Geometrical

8.2 Future Work

frustration in such a multi-bundle object, then, led to a transition to a double-bilayer which had greater capacity for lateral growth.

For systems with $\kappa = 0.3$, bilayer structures also self-assembled, but with a different arrangement of threads in each leaflet. Here, the threads had a 90° angle with each other. Anisotropy emerged into the bilayer by the development of threads with different lengths in each leaflet. This anisotropy was the key to the new pathway for the formation of tubes observed in this work. For a range of H parameters, a saddle bilayer self-assembled in the systems which, then, morphed into a half-pipe structure. This half-pipe then, by rolling, became a tube in which the inner layer had threads that were parallel to the axis of the tube. By decreasing the size of the hot-spot, the flexibility of the outer threads decreased and, therefore, they could sustained less curvature in the self-assembled structure - this gave control over the diameter of the tube formed. This is analogous to the simulations of Han *et al.* [93], in which it was also observed that the diameter of scrolled tubes can be tuned with the fraction of building-blocks mimicking hydrogen bonding in the structure. For the smallest investigated size of hot-spot on this curve, no curvature was seen in the formed aggregate and flat orthogonal bilayers self-assembled. The further interaction of pairs of these bilayers led to formation of multi-bilayer objects.

By reducing the thickness of the discs and diameter of spheres ($\kappa = d_{sph} = 0.25$) and, therefore, further increasing the packing parameter, the type of self-assembled structures completely changed again and double-helices spontaneously formed in the system. Similar to the other systems, the flexibility of the threads and, consequently, the formed structures was tunable with the size of the disc hot-spots.

8.2 Future Work

Apart from the fascinating features of each supramolecular structure found here, the results of this thesis prove the capabilities of such a simple coarse-grained approach in the simulation of self-assembly of these complicated structures. This can open new routes in investigation of spontaneous formation of larger-scale structures. These, together with other suggestions for future work, are listed here:

8.2 Future Work

- The effects of having a chiral term in the interaction of particles on the straightening of twisted fibres can be studied. By this, it can be verified whether twisted fibres have limited radii, provided that the chiral interaction prevents unwinding.
- The data of mosaic plots in the pre-assembly phase of fibres may be used for development of a theoretical model for 2D isodesmic assembly similar to what is suggested in reference [143] for 1D aggregates.
- The system size effects on the formation temperature, which were observed for some of the systems studied here, need to be further investigated.
- The response of twisted bilayers observed in chapter 5 to heating can be a part of future research.
- Bigger systems can be simulated for the formation of multi-layer structures with double hot-spots and, then, the possible straightening of the structure with three different modes of twist may lead to interesting outcomes.
- The self-assembly in the multi hot-spot systems with different hot-spot sizes can be studied.
- The reversibility of the suggested pathway for tube formation should be investigated. That is, on heating, does the tube open up or simply shrink from its ends?
- The double-helices introduced in this research are fascinating structures and their formation, stability and properties warrant an extensive investigation.
- Some of the structures explored in chapter 7 were formed via the interaction of smaller objects. This signals that higher orders of hierarchy can also be studied with the methods of this research. Therefore, the interaction of supramolecular structures with each other, e.g. multi-fibre assemblies, could be the focus of future work.

8.2 Future Work

- In the simulations of this work, it was observed that threads at larger radii with increased bending stresses had shorter length than those in the centre and, therefore, curved ends were apparent for most of multi-thread, twisted assemblies. The length of tubes were also limited. An investigation of length-limiting factors in such self-assembling systems could shed some light on these observations.
- The approaches presented in Appendix C for breaking the symmetry of disc-disc interaction should be employed in order to determine their capabilities in studying similar systems.

Appendix A

Forces and Torques for Intermolecular Potentials

In this appendix, the derivation of forces and torques from the discussed potentials by applying equations (3.4-3.6) are presented. In these equations, the derivative of potential with respect to a vector needs to be calculated. By applying the chain rule this derivation can be simplified:

$$\frac{\partial U}{\partial \mathbf{a}} = \sum_{\mathbf{s}} \frac{\partial U}{\partial(\mathbf{s} \cdot \mathbf{a})} \frac{\partial(\mathbf{s} \cdot \mathbf{a})}{\partial \mathbf{a}} \quad (\text{A.1})$$

where \mathbf{a} is the vector with respect to which the derivation should be performed, and \mathbf{s} is any vector that its scalar product with \mathbf{a} appears in the potential U . That is, \mathbf{s} can be any directional vectors of the particles or their separation vector. Therefore the scalar product term, $(\mathbf{s} \cdot \mathbf{a})$, may be either A, B, C or D parameters introduced in equations (3.36 or 3.50). The second term in the R.H.S of equation (A.1) can be simplified to:

$$\frac{\partial(\mathbf{s} \cdot \mathbf{a})}{\partial \mathbf{a}} = \left(\frac{\partial}{\partial a_x}(s_x a_x), \frac{\partial}{\partial a_y}(s_y a_y), \frac{\partial}{\partial a_z}(s_z a_z) \right) = (s_x, s_y, s_z) = \mathbf{s}$$

And then the equation (A.1) reads:

$$\frac{\partial U}{\partial \mathbf{a}} = \sum_{\mathbf{s}} \frac{\partial U}{\partial(\mathbf{s} \cdot \mathbf{a})} \mathbf{s} \quad (\text{A.2})$$

A.2 Disc-disc Interaction

In order to this equation be generally used, the separation distance between particles, r , can be written as:

$$r = \mathbf{r}_{ij} \cdot \hat{\mathbf{r}}_{ij} \quad (\text{A.3})$$

where $\hat{\mathbf{r}}_{ij}$ is the unit separation vector.

As discussed in chapter 3, to have a smooth transition of potential to zero at cut-off radius, after which the potentials are assumed to be zero, they are shifted up as much as the value of potential at cut-off distance. For LJ interaction, the subtracted value is constant and therefore does not appear in the force equation, but for the other potentials discussed in this work, the attention should be paid to the shifted potentials in derivation of forces and torques.

With this introduction we can discuss the torques and forces applied on each particle due to the potentials presented in chapter 3.

A.1 Lennard-Jones Interaction

For spherical particles, the interacting force can be derived by applying equation (3.4) on the shifted Lennard-Jones potential given by equation (3.34) based on the points discussed above:

$$\mathbf{F}_i = 24 \frac{\epsilon_0}{r} \left[2 \left(\frac{\sigma_0}{r} \right)^{12} - \left(\frac{\sigma_0}{r} \right)^6 \right] \hat{\mathbf{r}}_{ij} \quad (\text{A.4})$$

A.2 Disc-disc Interaction

The shifted Gay-Berne potential for discotic particles takes the form of:

$$U^{sh} = U^{GB} - U_c^{GB} \quad (\text{A.5})$$

where U^{GB} is given by equation (3.42) and U_c^{GB} is the value of potential at cut-off radius. By replacing the potential into the above equation, it reads:

$$U^{sh} = 4\epsilon(\hat{\mathbf{u}}_i, \hat{\mathbf{u}}_j, \mathbf{r}_{ij}) \left\{ \left[R^{12} - R^6 \right] - \left[R_c^{12} - R_c^6 \right] \right\} \quad (\text{A.6})$$

A.2 Disc-disc Interaction

Where

$$R = \frac{\sigma_f}{r - \sigma(\hat{\mathbf{u}}_i, \hat{\mathbf{u}}_j, \mathbf{r}_{ij}) + \sigma_f} \quad (\text{A.7})$$

And R_c is achieved from equation (A.7) by replacing the r with the cut-off radius. As discussed in chapter 3, two approaches for applying the cut-off radius were considered in this work. In the standard approach, a constant cut-off radius, r_c , is applied, while we can also apply a variable cut-off distance, r_c^{var} , given by equation (3.48):

$$R_c^{const} = \frac{\sigma_f}{r_c - \sigma(\hat{\mathbf{u}}_i, \hat{\mathbf{u}}_j, \mathbf{r}_{ij}) + \sigma_f} \quad (\text{A.8})$$

$$R_c^{var} = \frac{\sigma_f}{\sigma_{cut} + \sigma_f} \quad (\text{A.9})$$

For disc-disc interaction, the potential is a function of one principal axis of each particle and, therefore, the matrices \mathbf{A}_{im} and \mathbf{A}_{jm} in equations (3.5) and (3.6) reduces to $\hat{\mathbf{u}}_i$ and $\hat{\mathbf{u}}_j$, respectively.

By applying the equations (3.4-3.6) on the shifted potential and recalling equation (A.2), the forces and torques for disc-disc interaction become:

$$\mathbf{F}_i = - \left[\frac{\partial U^{sh}}{\partial r} \hat{\mathbf{r}}_{ij} + \frac{\partial U^{sh}}{\partial A} \hat{\mathbf{u}}_i + \frac{\partial U^{sh}}{\partial B} \hat{\mathbf{u}}_j \right] \quad (\text{A.10})$$

$$\boldsymbol{\tau}_i = -\hat{\mathbf{u}}_i \times \left[\frac{\partial U^{sh}}{\partial A} \mathbf{r}_{ij} + \frac{\partial U^{sh}}{\partial C} \hat{\mathbf{u}}_j \right] \quad (\text{A.11})$$

$$\boldsymbol{\tau}_j = -\hat{\mathbf{u}}_j \times \left[\frac{\partial U^{sh}}{\partial B} \mathbf{r}_{ij} + \frac{\partial U^{sh}}{\partial C} \hat{\mathbf{u}}_i \right] \quad (\text{A.12})$$

A.2 Disc-disc Interaction

Where for the constant cut-off radius, we have:

$$\frac{\partial U^{sh}}{\partial A} = 4\epsilon \left[-m_1 \alpha' (p_1 + p_2) R_{12-6}^{\cos nt} + m_2 \alpha (p_3 + p_4) R_{13-7}^{\cos nt} \right] \quad (\text{A.13})$$

$$\frac{\partial U^{sh}}{\partial B} = 4\epsilon \left[-\frac{m_1}{\alpha'} (p_1 - p_2) R_{12-6}^{\cos nt} + \frac{m_2}{\alpha} (p_3 - p_4) R_{13-7}^{\cos nt} \right] \quad (\text{A.14})$$

$$\begin{aligned} \frac{\partial U^{sh}}{\partial C} = 4\epsilon \left[\frac{m_1 \chi'}{2} (p_1^2 - p_2^2) R_{12-6}^{\cos nt} - \frac{m_2 \chi}{2} (p_3^2 - p_4^2) R_{13-7}^{\cos nt} \right. \\ \left. + \nu \epsilon_1^2 \chi^2 C \right] \end{aligned} \quad (\text{A.15})$$

$$\begin{aligned} \frac{\partial U^{sh}}{\partial r} = 4\epsilon \left[\frac{m_1}{r} \left[p_1 \left(\alpha' A + \frac{B}{\alpha'} \right) + p_2 \left(\alpha' A - \frac{B}{\alpha'} \right) \right] R_{12-6}^{\cos nt} \right. \\ \left. - \frac{12R^{13} - 6R^7}{\sigma_f} \right. \\ \left. - \frac{m_2}{r} \left[p_3 \left(\alpha A + \frac{B}{\alpha} \right) + p_4 \left(\alpha A - \frac{B}{\alpha} \right) \right] R_{13-7}^{\cos nt} \right] \end{aligned} \quad (\text{A.16})$$

where:

$$\begin{aligned} m_1 &= \frac{\mu \chi'}{r^2 \epsilon_2}, & m_2 &= \frac{\sigma^3 \chi}{2r^2 \sigma_0^2 \sigma_f} \\ p_1 &= \frac{\alpha' A + \frac{B}{\alpha'}}{1 + \chi' C}, & p_2 &= \frac{\alpha' A - \frac{B}{\alpha'}}{1 - \chi' C} \\ p_3 &= \frac{\alpha A + \frac{B}{\alpha}}{1 + \chi C}, & p_4 &= \frac{\alpha A - \frac{B}{\alpha}}{1 - \chi C} \\ R_{12-6}^{\cos nt} &= [R^{12} - R^6] - [R_c^{\text{const}12} - R_c^{\text{const}6}] \\ R_{13-7}^{\text{const}} &= [12R^{13} - 6R^7] - [12R_c^{\text{const}13} - 6R_c^{\text{const}7}] \end{aligned} \quad (\text{A.17})$$

By applying the variable cut-off radius, the form of equations (A.13-A.16) remains unchanged, but the parameters $R_{12-6}^{\cos nt}$ and $R_{13-7}^{\cos nt}$ should be replaced by R_{12-6}^{var} and R_{13-7}^{var} , respectively:

$$\begin{aligned} R_{12-6}^{\text{var}} &= [R^{12} - R^6] - [R_c^{\text{var}12} - R_c^{\text{var}6}] \\ R_{13-7}^{\text{var}} &= [12R^{13} - 6R^7] \end{aligned} \quad (\text{A.18})$$

A.3 Disc-sphere Interaction

As the interaction of discs and spheres given by equation (3.47) is governed by a generalized GB potential, then the forms of equations for forces and torques will not be so different with what was discussed in the previous section. Here, the torque on spherical particles with index i is neglected. The force on particles and the torques on the disc are then given by:

$$\mathbf{F}_i = - \left[\frac{\partial U^{sh}}{\partial r} \hat{\mathbf{r}}_{ij} + \frac{\partial U^{sh}}{\partial B} \hat{\mathbf{u}}_j \right] \quad (\text{A.19})$$

$$\boldsymbol{\tau}_j = -\hat{\mathbf{u}}_j \times \left(\frac{\partial U^{sh}}{\partial B} \mathbf{r}_{ij} \right) \quad (\text{A.20})$$

where, U^{sh} is the shifted disc-sphere potential:

$$U^{sh} = 4\beta\epsilon^{ds}(\hat{\mathbf{u}}_j, \mathbf{r}_{ij}) \left\{ [R^{12} - R^6] - [R_c^{12} - R_c^6] \right\} \quad (\text{A.21})$$

And

$$R = \frac{\sigma_f}{r - \sigma^{ds}(\hat{\mathbf{u}}_j, \mathbf{r}_{ij}) + \sigma_f} \quad (\text{A.22})$$

In a similar way to the previous section, the derivatives of the potential for constant cut-off radius read:

$$\frac{\partial U^{sh}}{\partial B} = 4\beta\epsilon^{ds} \left[-m_1 R_{12-6}^{\cos nt} + m_2 R_{13-7}^{\cos nt} \right] \quad (\text{A.23})$$

$$\frac{\partial U^{sh}}{\partial r} = 4\beta\epsilon^{ds} \left[\frac{m_1 B}{r} R_{12-6}^{\cos nt} - \frac{12R^{13} - 6R^7}{\sigma_f} - \frac{m_2 B}{r} R_{13-7}^{\cos nt} \right] \quad (\text{A.24})$$

where $R_{12-6}^{\cos nt}$ and $R_{13-7}^{\cos nt}$ is the same as equation (A.17), but R is given by equation (A.22), R_c is its value at cut-off radius, and:

$$m_1 = \frac{2\mu B(\chi' \alpha'^{-2})}{r^2 - B^2(\chi' \alpha'^{-2})} \quad (\text{A.25})$$

$$m_2 = \frac{\sigma^{ds^3} B(\chi \alpha^{-2})}{r^2 \sigma_0^2 \sigma_f} \quad (\text{A.26})$$

A.3 Disc-sphere Interaction

For variable cut-off radius, the terms R_{12-6}^{var} and R_{13-7}^{var} given by equation (A.18) should be used instead of R_{12-6}^{cosnt} and R_{13-7}^{cosnt} , respectively.

Tanh potential

In this subsection, the forces and torques applied on the particles interacting through the Tanh model used for breaking the symmetry of disc-sphere potential will be discussed. For single hot-spot model, the potential is a function of two principal axes of the discotic particle, $\hat{\mathbf{u}}_j$ and $\hat{\mathbf{u}}^{hs}$, and, therefore, the matrix \mathbf{A}_{jm} in equation (3.6) has two rows. By extending this to the multi hot-spot model, the forces and torques for shifted version of equation (3.49) take the form of:

$$\mathbf{F}_i = - \left[\frac{\partial U^{sh}}{\partial r} \hat{\mathbf{r}}_{ij} + \frac{\partial U^{sh}}{\partial B} \hat{\mathbf{u}}_j + \sum_{k=1}^{n^{hs}} \frac{\partial U^{sh}}{\partial D_k} \hat{\mathbf{u}}^{hs}_k \right] \quad (\text{A.27})$$

$$\boldsymbol{\tau}_j = - \left[\hat{\mathbf{u}}_j \times \left(\frac{\partial U^{sh}}{\partial B} \mathbf{r}_{ij} \right) + \sum_{k=1}^{n^{hs}} \hat{\mathbf{u}}^{hs}_k \times \left(\frac{\partial U^{sh}}{\partial D_k} \mathbf{r}_{ij} \right) \right] \quad (\text{A.28})$$

where U^{sh} is the shifted Tanh potential:

$$U^{sh} = 4\beta\epsilon^{ds}(\hat{\mathbf{u}}_j, \mathbf{r}_{ij}) \left[\sum_{k=1}^{n^{hs}} \epsilon_k \tanh(\hat{\mathbf{u}}^{hs}_k, \mathbf{r}_{ij}) \right] \{ [R^{12} - R^6] - [R_c^{12} - R_c^6] \} \quad (\text{A.29})$$

And R is given by equation (A.22). The derivatives of the potential can be calculated through:

$$\frac{\partial U^{sh}}{\partial B} = 4\beta\epsilon^{ds} \sum_{k=1}^{n^{hs}} \epsilon_k \tanh \left[-m_1 R_{12-6}^{cosnt} + m_2 R_{13-7}^{cosnt} \right] \quad (\text{A.30})$$

$$\frac{\partial U^{sh}}{\partial r} = 4\beta\epsilon^{ds} \sum_{k=1}^{n^{hs}} \epsilon_k \tanh \left[\left(\frac{m_1 B}{r} - \frac{1}{r} \frac{\sum_{k=1}^{n^{hs}} m_{3k} D_k}{\sum_{k=1}^{n^{hs}} \epsilon_k \tanh} \right) R_{12-6}^{cosnt} - \frac{12R^{13} - 6R^7}{\sigma_f} - \frac{m_2 B}{r} R_{13-7}^{cosnt} \right] \quad (\text{A.31})$$

$$\frac{\partial U^{sh}}{\partial D_k} = 4\beta\epsilon^{ds} \sum_{k=1}^{n^{hs}} \epsilon_k \tanh \left[\frac{m_{3k}}{\sum_{k=1}^{n^{hs}} \epsilon_k \tanh} R_{12-6}^{cosnt} \right] \quad (\text{A.32})$$

A.3 Disc-sphere Interaction

where m_1 and m_2 are given by equations (A.25 and A.26), R_{12-6}^{cosnt} and R_{13-7}^{cosnt} are treated as discussed for disc-sphere interaction and:

$$m_{3k} = \frac{b_k}{rl_k} \left[1 - \tanh^2 \left(\frac{(D_k/r) - s_k}{l_k} \right) \right] \quad (\text{A.33})$$

As before, for variable cut-off approach, the parameters R_{12-6}^{var} and R_{13-7}^{var} should be replaced in the above equations.

Appendix B

NOSQUISH Algorithm

In this appendix, the details of the NOSQUISH algorithm for integration of rotational equations of motion, presented in chapter 3, will be discussed. As introduced in section 3.2, the algorithm has three main variables, these being the quaternions, \mathbf{q} , quaternion momenta, $\bar{\mathbf{p}}$, and quaternion torques, $\bar{\boldsymbol{\tau}}$. The derivation of the NOSQUISH algorithm from the Hamiltonian of the system given by equation (3.19) has been discussed in references [108, 112].

In this algorithm, the standard time step of the simulation, Δt , is split into m_{rot} sub-steps ($\delta t = \frac{\Delta t}{m_{rot}}$) such that the free rotation of particles can be integrated accurately. By knowing the values of quaternions, \mathbf{q} , rotational velocities, $\boldsymbol{\omega}$, and torques, $\boldsymbol{\tau}$, at the current time step (n), and applying the following scheme, the orientation and rotational velocities of the particles at the next time step ($n + 1$) can be achieved:

1. The torque is transformed to the body-fixed coordinate system by equation (3.18).
2. The quaternion momenta and quaternion torques are calculated by equations (3.16 and 3.17).
3. The quaternion momenta is updated to the half-step ($n + \frac{1}{2}$):

$$\bar{\mathbf{p}}^{n+\frac{1}{2}} = \bar{\mathbf{p}}^n + \frac{\Delta t}{2} \bar{\boldsymbol{\tau}}^n$$

Appendix B. NOSQUISH Algorithm

4. Three free rotation operations ($\hat{L}_1, \hat{L}_2, \hat{L}_3$) are applied in this part in a loop of m_{rot} steps (see reference [112]). That is, the following steps are repeated m_{rot} times in order to complete the first half-step of the algorithm:

- (a) The first half of the third operator: $RotationFunction(3, \frac{\delta t}{2})$
- (b) The first half of the second operator: $RotationFunction(2, \frac{\delta t}{2})$
- (c) The first operator: $RotationFunction(1, \delta t)$
- (d) The second half of the second operator: $RotationFunction(2, \frac{\delta t}{2})$
- (e) The second half of the third operator: $RotationFunction(3, \frac{\delta t}{2})$

where the $RotationFunction$ is a function which gradually updates the quaternions and their momenta based on two input parameters of k and $\Delta t'$:

$$\begin{aligned}
 &RotationFunction(k, \Delta t')\{ \\
 &\quad \zeta_k = \frac{1}{4I_k} (\bar{\mathbf{p}}^T \mathbf{P}_k \mathbf{q}) \\
 &\quad \mathbf{q} = \cos(\zeta_k \Delta t') \mathbf{q} + \sin(\zeta_k \Delta t') \mathbf{P}_k \mathbf{q} \\
 &\quad \bar{\mathbf{p}} = \cos(\zeta_k \Delta t') \bar{\mathbf{p}} + \sin(\zeta_k \Delta t') \mathbf{P}_k \bar{\mathbf{p}} \\
 &\quad \}
 \end{aligned}$$

where $\bar{\mathbf{p}}$ is initially the quaternion momenta calculated in the step 3 of this scheme (the subscript dropped for simplicity) and is updated in each sub-step mentioned above. The term \mathbf{P}_k is an operator such that when it acts on a vector like $\mathbf{a} = [a_0, a_1, a_2, a_3]$, then we have:

$$\mathbf{P}_1 \mathbf{a} = [-a_1, a_0, a_3, -a_2]$$

$$\mathbf{P}_2 \mathbf{a} = [-a_2, -a_3, a_0, a_1]$$

$$\mathbf{P}_3 \mathbf{a} = [-a_3, a_2, -a_1, a_0]$$

At the end of this step, the quaternions at the next time step ($n + 1$) are calculated and, therefore, the orientation of the particle and the rotation matrix,

Appendix B. NOSQUISH Algorithm

\mathbf{A} , is known. However, the quaternion momenta need another half-step of integration which is performed after the movement of particles.

5. Consistent with the velocity-Verlet scheme, at this step, the forces and torques on the particles can be calculated based on their new positions and orientations.
6. The new calculated torques are transformed to the body-fixed coordinate and then the new quaternion torques can be achieved from equation (3.17).
7. The second half of the integration of quaternion momenta is performed:

$$\bar{\mathbf{p}}^{n+1} = \bar{\mathbf{p}}^{n+\frac{1}{2}} + \frac{\Delta t}{2} \bar{\boldsymbol{\tau}}^{n+1}$$

8. For calculation of rotational kinetic energy or application of any thermostat or barostat, as discussed in section 3.3, we may need to have the values of rotational velocities. These can be achieved from equation (3.16).

The choice of m_{rot} may have an effect on the NOSQUISH algorithm. Smith [112] suggested that $m_{rot} = 10$ can be an ideal choice. However, since computational cost grows linearly with this parameter, choosing larger values might be inefficient. Investigations performed in this work showed that the efficacy of this choice may vary from one system to the other. For example, for one of the investigated systems, $m_{rot} = 5$ led to the least energy drift among all values of $m_{rot} = 1 - 10$. Given an increase in the complexity of the governing interaction potential, it seems that larger value of m_{rot} should be chosen for simulation to maintain the required accuracy. Therefore, it is suggested that for each set of simulations, a study on the value of this parameter should be performed. In this work, $m_{rot} = 10$ was chosen for the most of simulations.

Appendix C

Symmetry Breaking of Disc-Disc Interaction

There is full rotational symmetry around the short axis of discs in the original GB potential for disc-disc interaction. This means that, all the points at the edge are equivalent. However, for many chromonic molecules, this is not the case [131–133]. This asymmetry is usually due to the presence of different functional groups at the peripheries of discotic particles. Here, two different approaches are suggested for breaking the symmetry of the coarse-grained GB disc-disc interaction. In the first, the axis of energy profile is slightly shifted with respect to the axis of particle. In the second, a hot-spot zone is considered at the edges of discs.

C.1 Internally-Shifted Gay-Berne Potential

By investigating the GB potential for disc-disc interaction given in equation (3.42), one may conclude that the shape and energy parameter functions, σ and ϵ , are responsible for bringing the effects of shape of interacting particles and their energy distribution to the potential, respectively. Centres of particles are considered as the centre of actions for these two functions. By moving the centre for the energy parameter function, then the short axis of particle is not the symmetry axis of potential any more, and the internally-shifted GB potential (ISGB) can be coarse-

C.1 Internally-Shifted Gay-Berne Potential

grained. This may represent the molecules in which the in-plane aromatic rings being responsible for $\pi - \pi$ interaction are not distributed evenly around the centre of mass of the particle.

Figure C.1 shows a schematic of the configuration of two discs with indices i and j interacting through ISGB potential. The vector \mathbf{r}_{ij} is the standard separation vector of particles. Two vectors \mathbf{d}_i and \mathbf{d}_j are the displacement vectors for two particles. It is supposed that the center of energy function is shifted to the end of each vector. The vector \mathbf{r}'_{ij} is, in fact, the separation vector of these two imaginary centres.

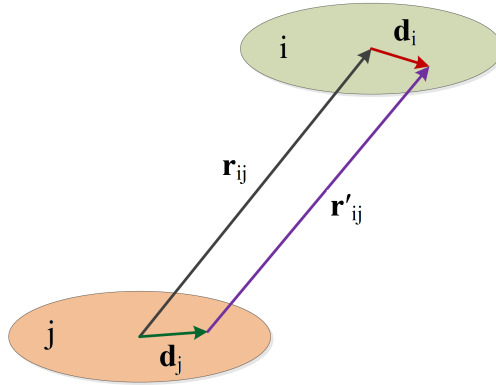


Figure C.1: A schematic view of two particles interacting through ISGB potential.

The displacement vectors can be written as:

$$\mathbf{d}_i = d\hat{\mathbf{d}}_i$$

$$\mathbf{d}_j = d\hat{\mathbf{d}}_j$$

where d is the displacement distance of energy centres and $\hat{\mathbf{d}}_i$ and $\hat{\mathbf{d}}_j$ are the unit vectors pointing to the energy centre from the gravity centre of each particles. Therefore, these two unit vectors are in symmetry plane of the discs and can be, for example, one of the in-plane principal axes of particles.

According to Figure C.1, the vector \mathbf{r}'_{ij} can be rewritten to:

$$\mathbf{r}'_{ij} = \mathbf{r}_{ij} + d(\hat{\mathbf{d}}_i - \hat{\mathbf{d}}_j)$$

C.1 Internally-Shifted Gay-Berne Potential

and its length would be:

$$r' = \sqrt{(\mathbf{r}'_{ij} \cdot \mathbf{r}'_{ij})}$$

Then the ISGB potential for disc-disc interaction is introduced as:

$$U^{\text{ISGB}} = 4\epsilon'(\hat{\mathbf{u}}_i, \hat{\mathbf{u}}_j, \mathbf{r}'_{ij}) \left[\left(\frac{\sigma_f}{r - \sigma(\hat{\mathbf{u}}_i, \hat{\mathbf{u}}_j, \mathbf{r}_{ij}) + \sigma_f} \right)^{12} - \left(\frac{\sigma_f}{r - \sigma(\hat{\mathbf{u}}_i, \hat{\mathbf{u}}_j, \mathbf{r}_{ij}) + \sigma_f} \right)^6 \right] \quad (\text{C.1})$$

where the σ function is the same as the one for original disc-disc GB potential given in equation (3.36), and ϵ' is the new energy parameter function:

$$\epsilon'(\hat{\mathbf{u}}_i, \hat{\mathbf{u}}_j, \mathbf{r}'_{ij}) = \epsilon_0 [\epsilon_1(\hat{\mathbf{u}}_i, \hat{\mathbf{u}}_j)]^\nu [\epsilon_2'(\hat{\mathbf{u}}_i, \hat{\mathbf{u}}_j, \mathbf{r}'_{ij})]^\mu \quad (\text{C.2})$$

The function ϵ_1 is given by equation (3.41) and we re-write the ϵ_2 function by replacing the \mathbf{r}_{ij} vector with \mathbf{r}'_{ij} :

$$\epsilon_2'(\hat{\mathbf{u}}_i, \hat{\mathbf{u}}_j, \mathbf{r}'_{ij}) = 1 - \frac{\chi'}{2r'^2} \left[\frac{[\alpha'(\mathbf{r}'_{ij} \cdot \hat{\mathbf{u}}_i) + \frac{1}{\alpha'}(\mathbf{r}'_{ij} \cdot \hat{\mathbf{u}}_j)]^2}{1 + \chi' C} + \frac{[\alpha'(\mathbf{r}'_{ij} \cdot \hat{\mathbf{u}}_i) - \frac{1}{\alpha'}(\mathbf{r}'_{ij} \cdot \hat{\mathbf{u}}_j)]^2}{1 - \chi' C} \right] \quad (\text{C.3})$$

Figure C.2 shows the contour plot for the absolute value of ISGB potential around a disc interacting with another disc while their short axes are parallel and the displacement vectors are opposite. The parameters of GB potential is $GB(0.345, 0.15, 1, 2)$, similar to those of Figure 3.2. Here, the displacement length is $d = 0.1$. The areas with high absolute value of potential at bellow and top of the disc, being shifted to the right, are, in fact, the favourable places for the centre of the interacting particle, such that the tips of displacement vectors meet each other.

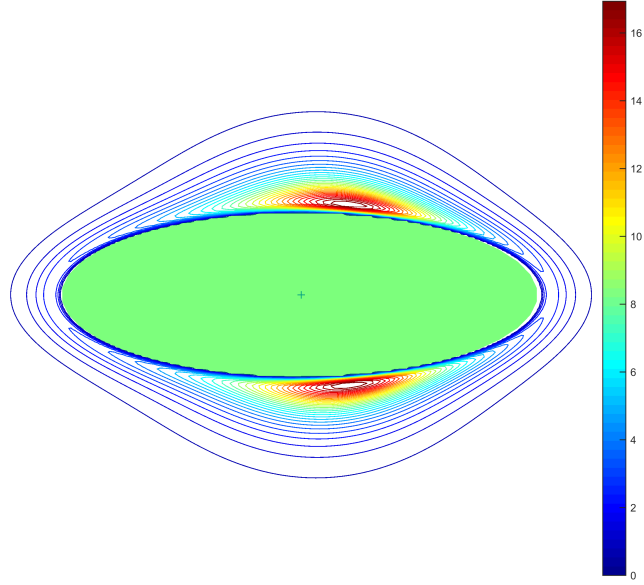


Figure C.2: Contour plot for absolute value of ISGB potential at central plane of a disc interacting with another parallel disc, while their displacement vectors are opposite. The GB parameters are $GB(0.345, 0.15, 1, 2)$ and the displacement length is $d = 0.1$. The green ellipse shows the area with repulsion.

C.2 Hot-spot for Disc-Disc Interaction

In this section, similar to what was performed for the disc-sphere interaction, we try to introduce a hot-spot zone at the rim of a disc interacting with another discotic particle. However, as the standard disc-disc and disc-sphere interactions have some differences, the hot-spot models introduced for each have to be also different. For the disc-sphere interaction the favourable configuration is edge-sphere which causes the applying of hot-spot at the rim to be easier than the disc-disc interaction in which the favourable configuration is face-face. In spite of this, we still use a ‘‘Tanh’’ function to act as a digital switch for turning the hot-spot model on or off.

Here the GB disc-disc potential with a hot-spot region at the rim is introduced:

$$U^{dd-hs} = 4 \left(\epsilon(\hat{\mathbf{u}}_i, \hat{\mathbf{u}}_j, \mathbf{r}_{ij}) + \epsilon^{hs}(\hat{\mathbf{v}}_i, \hat{\mathbf{v}}_j, \mathbf{r}_{ij}) \right) \left[R^{12} - R^6 \right] \quad (\text{C.4})$$

where ϵ is the standard energy parameter function for disc-disc interaction given by equation (3.40), $\hat{\mathbf{v}}_i$ and $\hat{\mathbf{v}}_j$ are two unit vectors for each discs which point at the core

C.2 Hot-spot for Disc-Disc Interaction

of hot-spot zones from their centres, R introduced with equation (A.7), and ϵ^{hs} is the new hot-spot energy parameter function for disc-disc interaction:

$$\epsilon^{hs}(\hat{\mathbf{v}}_i, \hat{\mathbf{v}}_j, \mathbf{r}_{ij}) = \epsilon_{min} + \frac{\epsilon_{max} - \epsilon_{min}}{4} \left[1 + \tanh\left(\frac{-(F_i/r) - s}{l}\right) \right] \times \left[1 + \tanh\left(\frac{(F_j/r) - s}{l}\right) \right] \quad (\text{C.5})$$

where

$$\begin{aligned} F_i &= \hat{\mathbf{v}}_i \cdot \mathbf{r}_{ij} \\ F_j &= \hat{\mathbf{v}}_j \cdot \mathbf{r}_{ij} \\ s &= 1 - 0.02H \end{aligned}$$

and ϵ_{max} and ϵ_{min} are the maximum and minimum values of ϵ^{hs} , H is the size of hot-spot area around the rim in percentage and l controls the shape of cross-over between inside and outside of the hot-spot zone.

It should be mentioned that by this approach of applying the hot-spot model, it is assumed that, the interacting discs see the hot-spot zone of each other when they are in the edge-edge configuration and, therefore, $\hat{\mathbf{v}}_i$ and $\hat{\mathbf{v}}_j$ point toward each other. Depending on the value of H (size of hot-spot region), the hot-spot energy function gradually vanishes when these two vectors depart from opposite direction.

Figure C.3 shows two views of the potential contour around a disc interacting with a parallel disc whose hot-spot vector is toward left, in opposite direction of that of the shown disc. It should be mentioned that the domain of action of the hot-spot zone is a cone whose axis is the hot-spot unit vector. The anisotropy in the shape of discs causes this cone to cover more area on the surface of the disc than its peripheries.

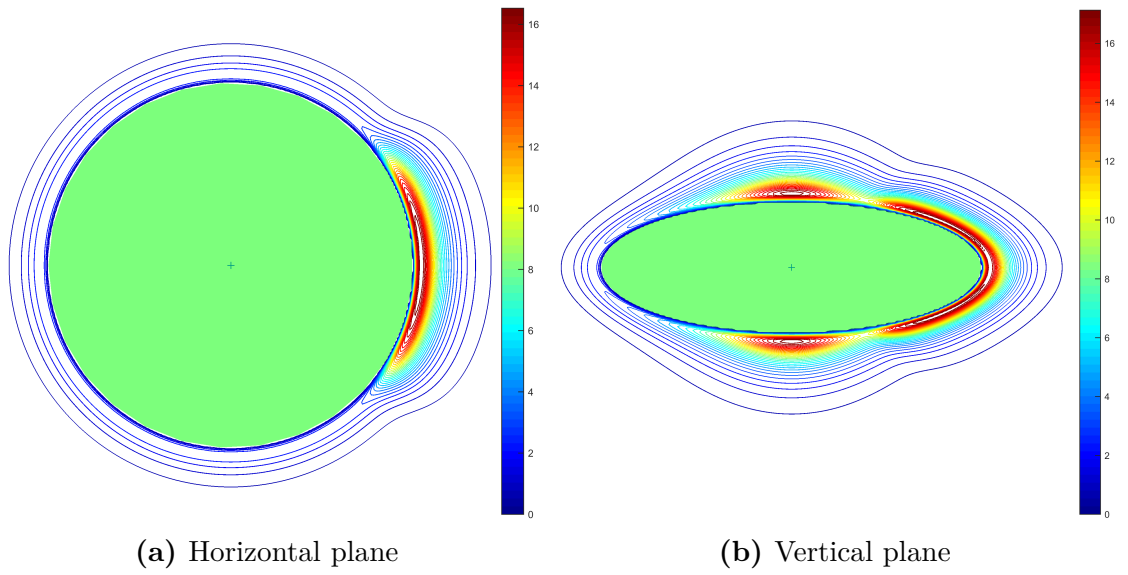


Figure C.3: Contour plot of the absolute value of disc-disc potential with hot-spot at two different symmetry planes of a disc interacting with another parallel disc. The hot-spot vector of shown disc is toward right, while that of the other disc is to the left. The disc-disc GB parameters are $GB(0.345, 0.15, 1, 2)$, and the hot-spot model parameters are: $\epsilon_{min} = 0$, $\epsilon_{max} = 15$, $H = 10$ and $l = 0.1$. The repulsion zone of the potential is coloured green.

Appendix D

Videos

In this appendix, the videos supporting the descriptions of various systems discussed within the thesis are presented. The associated files are available on a sharing website called “Figshare” which provides a permanent link to the files.

Video1:FibreFormation

In this video [158], the self-assembly of a twisted fibre in the system with $\kappa = 0.345$, $\kappa' = 0.15$ and 600 discs at $T=1.51$, discussed in Section 4.2, is visualized. In this video, only the clusters of at least 2 threads and 4 particles are shown. The particles are coloured based on their orientations. The biggest cluster in the simulation is always drawn at the centre of the box.

Video2:FibreUntwisting

In this video [159], the initiation and growth of a fibre in a system with $\kappa = 0.345$, $\kappa' = 0.15$ and 20,000 discs at $T=1.57$, discussed in Section 4.5, is shown. In this system, a multi-step untwisting process was observed and the final fibre was straight. For visualization, a plane at the centre of the straight fibre at the step of 13 million was identified and different colours are assigned to each thread of particles in this plane. The particles being a part of the identified threads at the final configuration are drawn with their true colour in the course of self-assembly. Other particles in

Appendix D. Videos

the cluster are shown by their short axes. This illustrates how the threads maintain their integrity during the untwisting scenario.

Video3: Bilayer Formation

In this video [160], the self-assembly of a twisted bilayer in a system of 3000 discs with $\kappa = 0.345$ and $H=20$ and 10,000 spheres at $T=2.77$, studied in Section 5.2, is illustrated. At the early stages, all the threads and cluster which formed in the system are shown. After initiation of the bilayer, however, the focus is given to the biggest cluster. The particles are colour-coded based on their orientations and the sphere are in green.

Video4: Tube Formation

In this video [161], the self-assembly of a tube in a system of 3000 discs with $\kappa = 0.3$ and $H=40$ and 10,000 spheres at $T=4.5$, studied in Section 6.2, is illustrated. The particles are coloured based on their locations in the formed tube at step of 120 millions. Particles which finally reside at the inner layer of tube are in blue and those at the outer layer are coloured in red. The particles which are not in the final configuration but appear in the growing cluster are shown in white. The particles which are present in final tube but are dissolved in the solution are shown by their short axes and the associated colour.

References

- [1] J. Lehn, “Perspectives in supramolecular chemistry—from molecular recognition towards molecular information processing and self-organization,” *Angewandte Chemie International Edition*, vol. 29, no. 11, pp. 1304–1319, 1990.
- [2] G. M. Whitesides, J. P. Mathias, and C. T. Seto, “Molecular self-assembly and nanochemistry: a chemical strategy for the synthesis of nanostructures,” tech. rep., DTIC Document, 1991.
- [3] S. Zhang, “Fabrication of novel biomaterials through molecular self-assembly,” *Nature biotechnology*, vol. 21, no. 10, pp. 1171–1178, 2003.
- [4] T. G. Barclay, K. Constantopoulos, and J. Matison, “Nanotubes self-assembled from amphiphilic molecules via helical intermediates,” *Chemical reviews*, vol. 114, no. 20, pp. 10217–10291, 2014.
- [5] P. Prybytak, *Coarse-grained computer simulation of fibre self-assembly*. PhD thesis, Sheffield Hallam University, 2012.
- [6] J. P. Hill, L. K. Shrestha, S. Ishihara, Q. Ji, and K. Ariga, “Self-assembly: From amphiphiles to chromophores and beyond,” *Molecules*, vol. 19, no. 6, pp. 8589–8609, 2014.
- [7] G. M. Whitesides and B. Grzybowski, “Self-assembly at all scales,” *Science*, vol. 295, no. 5564, pp. 2418–2421, 2002.
- [8] H. Bayley, “Designed membrane channels and pores,” *Current opinion in biotechnology*, vol. 10, no. 1, pp. 94–103, 1999.
- [9] K. Wen, R. Maoz, H. Cohen, J. Sagiv, A. Gibaud, A. Desert, and B. M. Ocko, “Postassembly chemical modification of a highly ordered organosilane multilayer: New insights into the structure, bonding, and dynamics of self-assembling silane monolayers,” *ACS nano*, vol. 2, no. 3, pp. 579–599, 2008.
- [10] F. Simon, J. Combet, M. Schmutz, P. J. Mésini, *et al.*, “Modification of self-assembled nanotubes by click chemistry generates new nanotubes by an out-of equilibrium process,” *Soft Matter*, vol. 7, no. 3, pp. 1121–1128, 2011.
- [11] H. K. Bisoyi and S. Kumar, “Liquid-crystal nanoscience: an emerging avenue of soft self-assembly,” *Chemical Society Reviews*, vol. 40, no. 1, pp. 306–319, 2011.
- [12] R. Koynova and B. Tenchov, “Transitions between lamellar and non-lamellar phases in membrane lipids and their physiological roles,” *OA Biochemistry*, vol. 1, pp. 1–9, 2013.

References

- [13] A. Mahler, M. Reches, M. Rechter, S. Cohen, and E. Gazit, "Rigid, self-assembled hydrogel composed of a modified aromatic dipeptide," *Advanced Materials*, vol. 18, no. 11, pp. 1365–1370, 2006.
- [14] C. A. Hunter and J. K. Sanders, "The nature of $\pi - \pi$ interactions," *Journal of the American Chemical Society*, vol. 112, no. 14, pp. 5525–5534, 1990.
- [15] C. R. Martinez and B. L. Iverson, "Rethinking the term pi-stacking," *Chemical Science*, vol. 3, no. 7, pp. 2191–2201, 2012.
- [16] S. E. Wheeler and J. W. Bloom, "Toward a more complete understanding of noncovalent interactions involving aromatic rings," *The Journal of Physical Chemistry A*, vol. 118, no. 32, pp. 6133–6147, 2014.
- [17] L. Smith and P. Ma, "Nano-fibrous scaffolds for tissue engineering," *Colloids and surfaces B: biointerfaces*, vol. 39, no. 3, pp. 125–131, 2004.
- [18] J. Guo, H. Su, Y. Zeng, Y.-X. Liang, W. M. Wong, R. G. Ellis-Behnke, K.-F. So, and W. Wu, "Reknitting the injured spinal cord by self-assembling peptide nanofiber scaffold," *Nanomedicine: Nanotechnology, Biology and Medicine*, vol. 3, no. 4, pp. 311–321, 2007.
- [19] H. Hosseinkhani, M. Hosseinkhani, F. Tian, H. Kobayashi, and Y. Tabata, "Osteogenic differentiation of mesenchymal stem cells in self-assembled peptide-amphiphile nanofibers," *Biomaterials*, vol. 27, no. 22, pp. 4079–4086, 2006.
- [20] N. M. Sangeetha and U. Maitra, "Supramolecular gels: functions and uses," *Chemical Society Reviews*, vol. 34, no. 10, pp. 821–836, 2005.
- [21] M. Zhou, A. M. Smith, A. K. Das, N. W. Hodson, R. F. Collins, R. V. Ulijn, and J. E. Gough, "Self-assembled peptide-based hydrogels as scaffolds for anchorage-dependent cells," *Biomaterials*, vol. 30, no. 13, pp. 2523–2530, 2009.
- [22] S. Zhang, M. A. Greenfield, A. Mata, L. C. Palmer, R. Bitton, J. R. Mantei, C. Aparicio, M. O. De La Cruz, and S. I. Stupp, "A self-assembly pathway to aligned monodomain gels," *Nature materials*, vol. 9, no. 7, pp. 594–601, 2010.
- [23] R. Rambaran and L. Serpell, "Amyloid fibrils: abnormal protein assembly.," *Prion*, vol. 2, no. 3, pp. 112–117, 2008.
- [24] M. R. Nilsson, "Techniques to study amyloid fibril formation in vitro," *Methods*, vol. 34, no. 1, pp. 151–160, 2004.
- [25] M. Fändrich, "On the structural definition of amyloid fibrils and other polypeptide aggregates," *Cellular and Molecular Life Sciences*, vol. 64, no. 16, p. 2066, 2007.
- [26] S. K. Maji, M. H. Perrin, M. R. Sawaya, S. Jessberger, K. Vadodaria, R. A. Rissman, P. S. Singru, K. P. R. Nilsson, R. Simon, D. Schubert, *et al.*, "Functional amyloids as natural storage of peptide hormones in pituitary secretory granules," *Science*, vol. 325, no. 5938, pp. 328–332, 2009.
- [27] M. S. Dueholm, M. Albertsen, D. Otzen, and P. H. Nielsen, "Curli functional amyloid systems are phylogenetically widespread and display large diversity in operon and protein structure," *PLoS One*, vol. 7, no. 12, p. e51274, 2012.

References

- [28] D. M. Ridgley, C. M. Rippner, and J. R. Barone, “Design and construction of large amyloid fibers,” *Fibers*, vol. 3, no. 2, pp. 90–102, 2015.
- [29] T. P. Knowles and R. Mezzenga, “Amyloid fibrils as building blocks for natural and artificial functional materials,” *Advanced Materials*, vol. 28, no. 31, pp. 6546–6561, 2016.
- [30] J.-X. Lu, W. Qiang, W.-M. Yau, C. D. Schwieters, S. C. Meredith, and R. Tycko, “Molecular structure of β -amyloid fibrils in Alzheimer’s disease brain tissue,” *Cell*, vol. 154, no. 6, pp. 1257–1268, 2013.
- [31] E. H. Bromley, K. J. Channon, P. J. King, Z. N. Mahmoud, E. F. Banwell, M. F. Butler, M. P. Crump, T. R. Dafforn, M. R. Hicks, J. D. Hirst, *et al.*, “Assembly pathway of a designed α -helical protein fiber,” *Biophysical journal*, vol. 98, no. 8, pp. 1668–1676, 2010.
- [32] P. Prybytak, W. Frith, and D. Cleaver, “Hierarchical self-assembly of chiral fibres from achiral particles,” *Interface focus*, vol. 2, no. 5, pp. 651–657, 2012.
- [33] J. A. Elemans, A. E. Rowan, and R. J. Nolte, “Mastering molecular matter. Supramolecular architectures by hierarchical self-assembly,” *Journal of Materials Chemistry*, vol. 13, no. 11, pp. 2661–2670, 2003.
- [34] A. Aggeli, I. A. Nyrkova, M. Bell, R. Harding, L. Carrick, T. C. McLeish, A. N. Semenov, and N. Boden, “Hierarchical self-assembly of chiral rod-like molecules as a model for peptide β -sheet tapes, ribbons, fibrils, and fibers,” *Proceedings of the National Academy of Sciences*, vol. 98, no. 21, pp. 11857–11862, 2001.
- [35] Y. Huang, D. Wang, L. Xu, Y. Cong, J. Li, and L. Li, “Multiscale fibers via supramolecular self-assembly of a fully rigid, discotic aromatic aramid molecule,” *European Polymer Journal*, vol. 49, no. 6, pp. 1682–1687, 2013.
- [36] H. Engelkamp, S. Middelbeek, *et al.*, “Self-assembly of disk-shaped molecules to coiled-coil aggregates with tunable helicity,” *Science*, vol. 284, no. 5415, pp. 785–788, 1999.
- [37] W. S. Gosal, I. J. Morten, E. W. Hewitt, D. A. Smith, N. H. Thomson, and S. E. Radford, “Competing pathways determine fibril morphology in the self-assembly of β_2 -microglobulin into amyloid,” *Journal of molecular biology*, vol. 351, no. 4, pp. 850–864, 2005.
- [38] M. Allen and D. Tildesley, *Computer simulation of liquids*. Oxford U.P, 1987.
- [39] P. Hoogerbrugge and J. Koelman, “Simulating microscopic hydrodynamic phenomena with dissipative particle dynamics,” *EPL (Europhysics Letters)*, vol. 19, no. 3, p. 155, 1992.
- [40] C. A. Hauser, R. Deng, A. Mishra, Y. Loo, U. Khoe, F. Zhuang, D. W. Cheong, A. Accardo, M. B. Sullivan, C. Riek, *et al.*, “Natural tri- to hexapeptides self-assemble in water to amyloid β -type fiber aggregates by unexpected α -helical intermediate structures,” *Proceedings of the National Academy of Sciences*, vol. 108, no. 4, pp. 1361–1366, 2011.

References

- [41] P. Tamamis, K. Terzaki, M. Kassinosopoulos, L. Mastrogiannis, E. Mossou, V. T. Forsyth, E. P. Mitchell, A. Mitraki, and G. Archontis, “Self-assembly of an aspartate-rich sequence from the adenovirus fiber shaft: insights from molecular dynamics simulations and experiments,” *The Journal of Physical Chemistry B*, vol. 118, no. 7, pp. 1765–1774, 2014.
- [42] N.-V. Buchete, R. Tycko, and G. Hummer, “Molecular dynamics simulations of Alzheimer’s β -amyloid protofilaments,” *Journal of molecular biology*, vol. 353, no. 4, pp. 804–821, 2005.
- [43] T. Yu, O.-S. Lee, and G. C. Schatz, “Steered molecular dynamics studies of the potential of mean force for peptide amphiphile self-assembly into cylindrical nanofibers,” *The Journal of Physical Chemistry A*, vol. 117, no. 32, pp. 7453–7460, 2013.
- [44] S. Izrailev, S. Stepaniants, B. Isralewitz, D. Kosztin, H. Lu, F. Molnar, W. Wriggers, and K. Schulten, “Steered molecular dynamics,” in *Computational molecular dynamics: challenges, methods, ideas*, pp. 39–65, Springer, 1999.
- [45] O.-S. Lee, S. I. Stupp, and G. C. Schatz, “Atomistic molecular dynamics simulations of peptide amphiphile self-assembly into cylindrical nanofibers,” *Journal of the American Chemical Society*, vol. 133, no. 10, pp. 3677–3683, 2011.
- [46] M. L. Klein and W. Shinoda, “Large-scale molecular dynamics simulations of self-assembling systems,” *Science*, vol. 321, no. 5890, pp. 798–800, 2008.
- [47] M. Levitt and A. Warshel, “Computer simulation of protein folding,” *Nature*, vol. 253, no. 5494, pp. 694–698, 1975.
- [48] S. Kmiecik, D. Gront, M. Kolinski, L. Wieteska, A. E. Dawid, and A. Kolinski, “Coarse-grained protein models and their applications,” *Chem. Rev.*, vol. 116, no. 14, pp. 7898–7936, 2016.
- [49] C. Avendaño and E. A. Müller, “Liquid crystalline behavior of a coarse-grained model of shape-persistent macrocycles with flexible attractive chains,” *Soft Matter*, vol. 7, no. 5, pp. 1694–1701, 2011.
- [50] C. Avendaño and E. A. Müller, “Liquid crystalline and antinematic behavior of shape-persistent macrocycles from molecular-dynamics simulations,” *Physical Review E*, vol. 80, no. 6, p. 061702, 2009.
- [51] K. R. Hadley and C. McCabe, “Coarse-grained molecular models of water: a review,” *Molecular simulation*, vol. 38, no. 8-9, pp. 671–681, 2012.
- [52] S. J. Marrink, A. H. De Vries, and A. E. Mark, “Coarse grained model for semiquantitative lipid simulations,” *The Journal of Physical Chemistry B*, vol. 108, no. 2, pp. 750–760, 2004.
- [53] Y. S. Velichko, S. I. Stupp, and M. O. de la Cruz, “Molecular simulation study of peptide amphiphile self-assembly,” *The journal of physical chemistry B*, vol. 112, no. 8, pp. 2326–2334, 2008.

References

- [54] H. D. Nguyen and C. K. Hall, "Molecular dynamics simulations of spontaneous fibril formation by random-coil peptides," *Proceedings of the National Academy of Sciences of the United States of America*, vol. 101, no. 46, pp. 16180–16185, 2004.
- [55] O.-S. Lee, V. Cho, and G. C. Schatz, "Modeling the self-assembly of peptide amphiphiles into fibers using coarse-grained molecular dynamics," *Nano letters*, vol. 12, no. 9, pp. 4907–4913, 2012.
- [56] M. Schor, B. Ensing, and P. G. Bolhuis, "A simple coarse-grained model for self-assembling silk-like protein fibers," *Faraday discussions*, vol. 144, pp. 127–141, 2010.
- [57] Z.-W. Li, Z.-Y. Sun, and Z.-Y. Lu, "Simulation model for hierarchical self-assembly of soft disklike particles," *The Journal of Physical Chemistry B*, vol. 114, no. 7, pp. 2353–2358, 2010.
- [58] X.-X. Jia, Z.-W. Li, Z.-Y. Sun, and Z.-Y. Lu, "Hierarchical self-assembly of soft disklike particles under shear flow," *The Journal of Physical Chemistry B*, vol. 115, no. 46, pp. 13441–13448, 2011.
- [59] J. Gay and B. Berne, "Modification of the overlap potential to mimic a linear site–site potential," *The journal of chemical physics*, vol. 74, no. 6, pp. 3316–3319, 1981.
- [60] N. Nakashima, S. Asakuma, J.-M. Kim, and T. Kunitake, "Helical superstructures are formed from chiral ammonium bilayers," *Chemistry Letters*, vol. 13, no. 10, pp. 1709–1712, 1984.
- [61] K. Yamada, H. Ihara, T. Ide, T. Fukumoto, and C. Hirayama, "Formation of helical super structure from single-walled bilayers by amphiphiles with oligo-l-glutamic acid-head group," *Chemistry Letters*, vol. 13, no. 10, pp. 1713–1716, 1984.
- [62] J. P. Hill, W. Jin, A. Kosaka, T. Fukushima, H. Ichihara, T. Shimomura, K. Ito, T. Hashizume, N. Ishii, and T. Aida, "Self-assembled hexa-perihexabenzocoronene graphitic nanotube," *Science*, vol. 304, no. 5676, pp. 1481–1483, 2004.
- [63] T. Barclay, K. Constantopoulos, and J. Matison, "Self-assembled lipid nanotubes by rational design," *Journal of Materials Research*, vol. 26, no. 02, pp. 322–335, 2011.
- [64] T. Kunitake, Y. Okahata, M. Shimomura, S. Yasunami, and K. Takarabe, "Formation of stable bilayer assemblies in water from single-chain amphiphiles. Relationship between the amphiphile structure and the aggregate morphology," *Journal of the American Chemical Society*, vol. 103, no. 18, pp. 5401–5413, 1981.
- [65] T. Shimizu, M. Masuda, and H. Minamikawa, "Supramolecular nanotube architectures based on amphiphilic molecules," *Chemical reviews*, vol. 105, no. 4, pp. 1401–1444, 2005.

References

- [66] N. Kameta, H. Minamikawa, and M. Masuda, "Supramolecular organic nanotubes: how to utilize the inner nanospace and the outer space," *Soft Matter*, vol. 7, no. 10, pp. 4539–4561, 2011.
- [67] A. Weitkamp, "The acidic constituents of degrass. A new method of structure elucidation1," *Journal of the American Chemical Society*, vol. 67, no. 3, pp. 447–454, 1945.
- [68] D. S. Chung, G. B. Benedek, F. M. Konikoff, and J. M. Donovan, "Elastic free energy of anisotropic helical ribbons as metastable intermediates in the crystallization of cholesterol," *Proceedings of the National Academy of Sciences*, vol. 90, no. 23, pp. 11341–11345, 1993.
- [69] N. Nakashima, S. Asakuma, and T. Kunitake, "Optical microscopic study of helical superstructures of chiral bilayer membranes," *Journal of the American Chemical Society*, vol. 107, no. 2, pp. 509–510, 1985.
- [70] J. N. Israelachvili, D. J. Mitchell, and B. W. Ninham, "Theory of self-assembly of lipid bilayers and vesicles," *Biochimica et Biophysica Acta (BBA)-Biomembranes*, vol. 470, no. 2, pp. 185–201, 1977.
- [71] T. Lubensky and J. Prost, "Orientational order and vesicle shape," *Journal de Physique II*, vol. 2, no. 3, pp. 371–382, 1992.
- [72] C.-M. Chen, "Theory for the bending anisotropy of lipid membranes and tubule formation," *Physical Review E*, vol. 59, no. 5, p. 6192, 1999.
- [73] W. Helfrich and J. Prost, "Intrinsic bending force in anisotropic membranes made of chiral molecules," *Physical Review A*, vol. 38, no. 6, p. 3065, 1988.
- [74] F. Konikoff, D. Chung, J. Donovan, D. Small, and M. Carey, "Filamentous, helical, and tubular microstructures during cholesterol crystallization from bile. evidence that cholesterol does not nucleate classic monohydrate plates.," *Journal of Clinical Investigation*, vol. 90, no. 3, p. 1155, 1992.
- [75] J. V. Selinger, M. S. Spector, and J. M. Schnur, "Theory of self-assembled tubules and helical ribbons," *The Journal of Physical Chemistry B*, vol. 105, no. 30, p. 7157–7169, 2001.
- [76] J. Selinger, F. MacKintosh, and J. Schnur, "Theory of cylindrical tubules and helical ribbons of chiral lipid membranes," *Physical Review E*, vol. 53, no. 4, p. 3804, 1996.
- [77] B. K. Mishra, C. C. Garrett, and B. N. Thomas, "Phospholipid tubelets," *Journal of the American Chemical Society*, vol. 127, no. 12, pp. 4254–4259, 2005.
- [78] L. Ziserman, A. Mor, D. Harries, and D. Danino, "Curvature instability in a chiral amphiphile self-assembly," *Physical review letters*, vol. 106, no. 23, p. 238105, 2011.
- [79] L. Ziserman, H.-Y. Lee, S. R. Raghavan, A. Mor, and D. Danino, "Unraveling the mechanism of nanotube formation by chiral self-assembly of amphiphiles," *Journal of the American Chemical Society*, vol. 133, no. 8, pp. 2511–2517, 2011.

References

- [80] S. Pakhomov, R. P. Hammer, B. K. Mishra, and B. N. Thomas, "Chiral tubule self-assembly from an achiral diynoic lipid," *Proceedings of the National Academy of Sciences*, vol. 100, no. 6, pp. 3040–3042, 2003.
- [81] Anuradha, D. D. La, M. Al Kobaisi, S. V. Bhosale, *et al.*, "Right handed chiral superstructures from achiral molecules: self-assembly with a twist," *Scientific reports*, vol. 5, p. srep15652, 2015.
- [82] Anuradha, D. D. La, M. Al Kobaisi, A. Gupta, and S. V. Bhosale, "Chiral assembly of AIE-active achiral molecules: An odd effect in self-assembly," *Chemistry-A European Journal*, vol. 23, no. 16, pp. 3950–3956, 2017.
- [83] B. N. Thomas, C. M. Lindemann, and N. A. Clark, "Left-and right-handed helical tubule intermediates from a pure chiral phospholipid," *Physical Review E*, vol. 59, no. 3, p. 3040, 1999.
- [84] S. Cheng, A. Aggarwal, and M. J. Stevens, "Self-assembly of artificial microtubules," *Soft Matter*, vol. 8, no. 20, pp. 5666–5678, 2012.
- [85] S. Cheng and M. J. Stevens, "Self-assembly of chiral tubules," *Soft matter*, vol. 10, no. 3, pp. 510–518, 2014.
- [86] M. Bachand, N. Bouxsein, S. Cheng, S. J. von Hoyningen-Huene, M. Stevens, and G. Bachand, "Directed self-assembly of 1D microtubule nano-arrays," *RSC Advances*, vol. 4, no. 97, pp. 54641–54649, 2014.
- [87] G. Srinivas and M. L. Klein, "Molecular dynamics simulations of self-assembly and nanotube formation by amphiphilic molecules in aqueous solution: a coarse-grain approach," *Nanotechnology*, vol. 18, no. 20, p. 205703, 2007.
- [88] Y. Yamamoto, T. Fukushima, W. Jin, A. Kosaka, T. Hara, T. Nakamura, A. Saeki, S. Seki, S. Tagawa, and T. Aida, "A glass hook allows fishing of hexaperi-hexabenzocoronene graphitic nanotubes: Fabrication of a macroscopic fiber with anisotropic electrical conduction," *Advanced Materials*, vol. 18, no. 10, pp. 1297–1300, 2006.
- [89] Y. Chen, B. Zhu, F. Zhang, Y. Han, and Z. Bo, "Hierarchical supramolecular self-assembly of nanotubes and layered sheets," *Angewandte Chemie International Edition*, vol. 47, no. 32, pp. 6015–6018, 2008.
- [90] E. Lee, J.-K. Kim, and M. Lee, "Reversible scrolling of two-dimensional sheets from the self-assembly of laterally grafted amphiphilic rods," *Angewandte Chemie International Edition*, vol. 48, no. 20, pp. 3657–3660, 2009.
- [91] D.-J. Hong, E. Lee, H. Jeong, J.-k. Lee, W.-C. Zin, T. D. Nguyen, S. C. Glotzer, and M. Lee, "Solid-state scrolls from hierarchical self-assembly of T-shaped rod-coil molecules," *Angewandte Chemie International Edition*, vol. 48, no. 9, pp. 1664–1668, 2009.
- [92] M. Han and E. Sim, "Formation of tubular scrolls with controlled internal cavity," *The Journal of Physical Chemistry B*, vol. 116, no. 6, pp. 1796–1801, 2012.

References

- [93] M. Han, J. Hyun, and E. Sim, "Formation of rigid organic nanotubes with controlled internal cavity based on frustrated aggregate internal rearrangement mechanism," *The Journal of Physical Chemistry B*, vol. 117, no. 25, pp. 7763–7770, 2013.
- [94] M. Han, J. Hyun, and E. Sim, "Self-rolled nanotubes with controlled hollow interiors by patterned grafts," *Soft matter*, vol. 11, no. 18, pp. 3714–3723, 2015.
- [95] L. Radzihovsky and J. Toner, "A new phase of tethered membranes: tubules," *Physical review letters*, vol. 75, no. 26, p. 4752, 1995.
- [96] S. J. Marrink, H. J. Risselada, S. Yefimov, D. P. Tieleman, and A. H. De Vries, "The MARTINI force field: coarse grained model for biomolecular simulations," *The journal of physical chemistry B*, vol. 111, no. 27, pp. 7812–7824, 2007.
- [97] C. Guo, Y. Luo, R. Zhou, and G. Wei, "Probing the self-assembly mechanism of diphenylalanine-based peptide nanovesicles and nanotubes," *ACS nano*, vol. 6, no. 5, pp. 3907–3918, 2012.
- [98] X. Yan, Y. Cui, Q. He, K. Wang, J. Li, W. Mu, B. Wang, and Z.-c. Ou-yang, "Reversible transitions between peptide nanotubes and vesicle-like structures including theoretical modeling studies," *Chemistry—A European Journal*, vol. 14, no. 19, pp. 5974–5980, 2008.
- [99] S. N. Fejer, D. Chakrabarti, and D. J. Wales, "Self-assembly of anisotropic particles," *Soft Matter*, vol. 7, no. 7, pp. 3553–3564, 2011.
- [100] D. Chakrabarti, S. N. Fejer, and D. J. Wales, "Rational design of helical architectures," *Proceedings of the National Academy of Sciences*, vol. 106, no. 48, pp. 20164–20167, 2009.
- [101] Z. Li and H. A. Scheraga, "Monte Carlo-minimization approach to the multiple-minima problem in protein folding," *Proceedings of the National Academy of Sciences*, vol. 84, no. 19, pp. 6611–6615, 1987.
- [102] D. Chakrabarti and D. J. Wales, "Tilted and helical columnar phases for an axially symmetric discoidal system," *Physical review letters*, vol. 100, no. 12, p. 127801, 2008.
- [103] S. N. Fejer and D. J. Wales, "Helix self-assembly from anisotropic molecules," *Physical review letters*, vol. 99, no. 8, p. 086106, 2007.
- [104] L. Paramonov and S. N. Yaliraki, "The directional contact distance of two ellipsoids: Coarse-grained potentials for anisotropic interactions," *The Journal of chemical physics*, vol. 123, no. 19, p. 194111, 2005.
- [105] H. Goldstein, *Classical mechanics*. Reading, Massachusetts: Addison-Wesley, 1980.
- [106] M. P. Allen and G. Germano, "Expressions for forces and torques in molecular simulations using rigid bodies," *Molecular Physics*, vol. 104, no. 20-21, pp. 3225–3235, 2006.

References

- [107] N. S. Martys and R. D. Mountain, “Velocity Verlet algorithm for dissipative-particle-dynamics-based models of suspensions,” *Physical Review E*, vol. 59, no. 3, p. 3733, 1999.
- [108] T. Miller Iii, M. Eleftheriou, P. Pattnaik, A. Ndirango, D. Newns, and G. Martyna, “Symplectic quaternion scheme for biophysical molecular dynamics,” *The Journal of chemical physics*, vol. 116, no. 20, pp. 8649–8659, 2002.
- [109] D. Fincham, “Leapfrog rotational algorithms,” *Molecular Simulation*, vol. 8, no. 3-5, pp. 165–178, 1992.
- [110] M. Svanberg, “Research note: An improved leap-frog rotational algorithm,” *Molecular physics*, vol. 92, no. 6, pp. 1085–1088, 1997.
- [111] R. Berardi, L. Muccioli, and C. Zannoni, “Field response and switching times in biaxial nematics,” *The Journal of chemical physics*, vol. 128, no. 2, p. 024905, 2008.
- [112] W. Smith, *Elements of Molecular Dynamics*. 2014.
- [113] H. J. Berendsen, J. P. M. Postma, W. F. van Gunsteren, A. DiNola, and J. Haak, “Molecular dynamics with coupling to an external bath,” *The Journal of chemical physics*, vol. 81, no. 8, pp. 3684–3690, 1984.
- [114] W. G. Hoover, *Computational statistical mechanics*. Elsevier, 1991.
- [115] G. J. Martyna, M. L. Klein, and M. Tuckerman, “Nosé–Hoover chains: the canonical ensemble via continuous dynamics,” *The Journal of chemical physics*, vol. 97, no. 4, pp. 2635–2643, 1992.
- [116] G. J. Martyna, D. J. Tobias, and M. L. Klein, “Constant pressure molecular dynamics algorithms,” *The Journal of Chemical Physics*, vol. 101, no. 5, pp. 4177–4189, 1994.
- [117] M. Parrinello and A. Rahman, “Strain fluctuations and elastic constants,” *The Journal of Chemical Physics*, vol. 76, no. 5, pp. 2662–2666, 1982.
- [118] H. Kamberaj, R. Low, and M. Neal, “Time reversible and symplectic integrators for molecular dynamics simulations of rigid molecules,” *The Journal of chemical physics*, vol. 122, no. 22, p. 224114, 2005.
- [119] W. Shinoda and M. Mikami, “Rigid-body dynamics in the isothermal-isobaric ensemble: A test on the accuracy and computational efficiency,” *Journal of computational chemistry*, vol. 24, no. 8, pp. 920–930, 2003.
- [120] M. Ikeguchi, “Partial rigid-body dynamics in NPT , $NPAT$ and $NP\gamma T$ ensembles for proteins and membranes,” *Journal of computational chemistry*, vol. 25, no. 4, pp. 529–541, 2004.
- [121] D. Eberly, “Fitting 3D data with a helix,” Available: <http://www.geometrictools.com/Documentation>, 1999.
- [122] The CGAL Project, *CGAL User and Reference Manual*. CGAL Editorial Board, 4.10 ed., 2017.

References

- [123] M. Meyer, M. Desbrun, P. Schröder, and A. H. Barr, “Discrete differential-geometry operators for triangulated 2-manifolds,” in *Visualization and mathematics III*, pp. 35–57, Springer, 2003.
- [124] D. J. Cleaver, C. M. Care, M. P. Allen, and M. P. Neal, “Extension and generalization of the Gay-Berne potential,” *Physical Review E*, vol. 54, no. 1, p. 559, 1996.
- [125] F. Barmes, M. Ricci, C. Zannoni, and D. Cleaver, “Computer simulations of hard pear-shaped particles,” *Physical Review E*, vol. 68, no. 2, p. 021708, 2003.
- [126] G. Luckhurst, R. Stephens, and R. Phippen, “Computer simulation studies of anisotropic systems. XIX. Mesophases formed by the Gay-Berne model mesogen,” *Liquid Crystals*, vol. 8, no. 4, pp. 451–464, 1990.
- [127] A. Emerson, G. Luckhurst, and S. Whatling, “Computer simulation studies of anisotropic systems: XXIII. The Gay-Berne discogen,” *Molecular Physics*, vol. 82, no. 1, pp. 113–124, 1994.
- [128] M. Bates and G. Luckhurst, “Computer simulation studies of anisotropic systems. XXVI. Monte Carlo investigations of a Gay-Berne discotic at constant pressure,” *The Journal of chemical physics*, vol. 104, no. 17, pp. 6696–6709, 1996.
- [129] D. Michel, *Computer simulation of self-assembling amphiphilic systems*. PhD thesis, Sheffield Hallam University, 2006.
- [130] J. Lydon, “Chromonic liquid crystal phases,” *Current opinion in colloid & interface science*, vol. 3, no. 5, pp. 458–466, 1998.
- [131] J. Reiche, R. Dietel, D. Janietz, H. Lemmetyinen, and L. Brehmer, “Edge-on Langmuir-Blodgett multilayers derived from disc-shaped multiyne mesogens,” *Thin Solid Films*, vol. 226, no. 2, pp. 265–269, 1993.
- [132] D. Janietz, D. Hofmann, and J. Reiche, “Molecular organization of amphiphilic disc-shaped penta-alkynes in LB-mono-and multilayers,” *Thin Solid Films*, vol. 244, no. 1-2, pp. 794–798, 1994.
- [133] M. Lee, J.-W. Kim, S. Peleshanko, K. Larson, Y.-S. Yoo, D. Vaknin, S. Markutsya, V. V. Tsukruk, *et al.*, “Amphiphilic hairy disks with branched hydrophilic tails and a hexa-peri-hexabenzocoronene core,” *Journal of the American Chemical Society*, vol. 124, no. 31, pp. 9121–9128, 2002.
- [134] F. C. Meldrum and H. Colfen, “Controlling mineral morphologies and structures in biological and synthetic systems,” *Chemical reviews*, vol. 108, no. 11, pp. 4332–4432, 2008.
- [135] A. K. Buell, A. Dhulesia, D. A. White, T. P. Knowles, C. M. Dobson, and M. E. Welland, “Detailed analysis of the energy barriers for amyloid fibril growth,” *Angewandte Chemie International Edition*, vol. 51, no. 21, pp. 5247–5251, 2012.
- [136] L. C. Hsiao, B. A. Schultz, J. Glaser, M. Engel, M. E. Szakasits, S. C. Glotzer, and M. J. Solomon, “Metastable orientational order of colloidal discoids,” *Nature communications*, vol. 6, p. 8507, 2015.

References

- [137] G. M. Grason, “Perspective: Geometrically frustrated assemblies,” *The Journal of Chemical Physics*, vol. 145, no. 11, p. 110901, 2016.
- [138] A. Laio and F. L. Gervasio, “Metadynamics: a method to simulate rare events and reconstruct the free energy in biophysics, chemistry and material science,” *Reports on Progress in Physics*, vol. 71, no. 12, p. 126601, 2008.
- [139] R. J. Allen, C. Valeriani, and P. R. ten Wolde, “Forward flux sampling for rare event simulations,” *Journal of physics: Condensed matter*, vol. 21, no. 46, p. 463102, 2009.
- [140] B. Huisman, P. Bolhuis, and A. Fasolino, “Phase transition to bundles of flexible supramolecular polymers,” *Physical Review Letters*, vol. 100, no. 18, p. 188301, 2008.
- [141] S. Ogi, V. Stepanenko, K. Sugiyasu, M. Takeuchi, and F. Würthner, “Mechanism of self-assembly process and seeded supramolecular polymerization of perylene bisimide organogelator,” *Journal of the American Chemical Society*, vol. 137, no. 9, pp. 3300–3307, 2015.
- [142] E. A. Mills, M. H. Regan, V. Stanic, and P. J. Collings, “Large assembly formation via a two-step process in a chromonic liquid crystal,” *The Journal of Physical Chemistry B*, vol. 116, no. 45, pp. 13506–13515, 2012.
- [143] P. J. Collings, J. N. Goldstein, E. J. Hamilton, B. R. Mercado, K. J. Nieser, and M. H. Regan, “The nature of the assembly process in chromonic liquid crystals,” *Liquid Crystals Reviews*, vol. 3, no. 1, pp. 1–27, 2015.
- [144] D. M. Hall, I. R. Bruss, J. R. Barone, and G. M. Grason, “Morphology selection via geometric frustration in chiral filament bundles,” *Nature materials*, vol. 15, no. 7, pp. 727–732, 2016.
- [145] T. Gibaud, E. Barry, M. J. Zakhary, M. Henglin, A. Ward, Y. Yang, C. Berciu, R. Oldenbourg, M. F. Hagan, D. Nicastro, *et al.*, “Reconfigurable self-assembly through chiral control of interfacial tension,” *Nature*, vol. 481, no. 7381, pp. 348–351, 2012.
- [146] A. Uesaka, M. Ueda, A. Makino, T. Imai, J. Sugiyama, and S. Kimura, “Morphology control between twisted ribbon, helical ribbon, and nanotube self-assemblies with his-containing helical peptides in response to ph change,” *Langmuir*, vol. 30, no. 4, pp. 1022–1028, 2014.
- [147] C. J. Forman, S. N. Fejer, D. Chakrabarti, P. D. Barker, and D. J. Wales, “Local frustration determines molecular and macroscopic helix structures,” *The Journal of Physical Chemistry B*, vol. 117, no. 26, pp. 7918–7928, 2013.
- [148] S. Armon, E. Efrati, R. Kupferman, and E. Sharon, “Geometry and mechanics in the opening of chiral seed pods,” *Science*, vol. 333, no. 6050, pp. 1726–1730, 2011.
- [149] A. S. Gladman, E. A. Matsumoto, R. G. Nuzzo, L. Mahadevan, and J. A. Lewis, “Biomimetic 4D printing,” *Nature materials*, vol. 15, no. 4, pp. 413–418, 2016.

References

- [150] R. Oda, I. Huc, and S. J. Candau, “Gemini surfactants as new, low molecular weight gelators of organic solvents and water,” *Angewandte Chemie International Edition*, vol. 37, no. 19, pp. 2689–2691, 1998.
- [151] H. Cramér, *Mathematical Methods of Statistics*. Princeton university press, 1946.
- [152] D. M. Ridgley, E. C. Claunch, and J. R. Barone, “The effect of processing on large, self-assembled amyloid fibers,” *Soft Matter*, vol. 8, no. 40, pp. 10298–10306, 2012.
- [153] N. C. Maliszewskyi, P. A. Heiney, J. Y. Josefowicz, J. P. McCauley Jr, and A. B. Smith III, “Unexpected square symmetry seen by atomic force microscopy in bilayer films of disk-like molecules,” *Science*, vol. 264, no. 5155, pp. 77–80, 1994.
- [154] P. Henderson, D. Beyer, U. Jonas, O. Karthaus, H. Ringsdorf, P. A. Heiney, N. C. Maliszewskyj, S. S. Ghosh, O. Y. Mindyuk, and J. Y. Josefowicz, “Complex ordering in thin films of di-and trifunctionalized hexaalkoxytriphenylene derivatives,” *Journal of the American Chemical Society*, vol. 119, no. 20, pp. 4740–4748, 1997.
- [155] B. Rawles, *Sacred geometry design sourcebook*. Elysian Publishing, Eagle Point, Oregon, 1997.
- [156] J. D. Wadsworth, S. Joiner, J. M. Linehan, M. Desbruslais, K. Fox, S. Cooper, S. Cronier, E. A. Asante, S. Mead, S. Brandner, *et al.*, “Kuru prions and sporadic Creutzfeldt–Jakob disease prions have equivalent transmission properties in transgenic and wild-type mice,” *Proceedings of the National Academy of Sciences*, vol. 105, no. 10, pp. 3885–3890, 2008.
- [157] P. Jonkheijm, P. van der Schoot, A. P. Schenning, and E. Meijer, “Probing the solvent-assisted nucleation pathway in chemical self-assembly,” *Science*, vol. 313, no. 5783, pp. 80–83, 2006.
- [158] A. Dastan, “Video1:FibreFormation,” Available: <https://goo.gl/Zg1ebz>, 2017. doi: 10.6084/m9.figshare.5492614.
- [159] A. Dastan, “Video2:FibreUntwisting,” Available: <https://goo.gl/h3dnH4>, 2017. doi: 10.6084/m9.figshare.5492629.
- [160] A. Dastan, “Video3:BilayerFormation,” Available: <https://goo.gl/MYMfUB>, 2017. doi: 10.6084/m9.figshare.5492641.
- [161] A. Dastan, “Video4:TubeFormation,” Available: <https://goo.gl/m5iP42>, 2017. doi: 10.6084/m9.figshare.5492659.